Characterising Seismic Hazard with InSAR Measurements: cases over large length scales

Lin Shen

School of Earth and Environment

University of Leeds

A thesis submitted for the degree of

Doctor of Philosophy

March, 2021

Declaration

The candidate confirms that the work submitted is her own, except where work which has formed part of jointly authored publications has been included. The contribution of the candidate and the other authors to this work has been explicitly indicated below. The candidate confirms that appropriate credit has been given within the thesis where reference has been made to the work of others.

The work in Chapter 3 of the thesis has mostly been published in a jointly authored publication: Lin Shen, Andrew Hooper, John Elliott (2019), A Spatially Varying Scaling Method for InSAR Tropospheric Corrections Using a High-Resolution Weather model, *Journal of Geophysical Research: Solid Earth*. https://doi.org/10.1029/2018JB016189. The candidate worked on the method development, the data processing and the discussion of the results. Andy Hooper and John Elliott provided comments and suggestions on the work.

The candidate carried out the work in Chapter 4 of the thesis. Andy Hooper, John Elliott and Tim Wright provided comments and suggestions on the work.

The work in Chapter 5 of the thesis is a collective contribution. The candidate worked on the data reduction, the derivation of the fault model, the Bayesian inversion, the determination of the finite fault model and the discussion of the results. The GPS data was processed by Wim Simons at the Delft University of Technology. The ALOS-2 SAR data was processed by Yu Morishita when he was at the University of Leeds. The tsunami data was processed by Olga Kleptsova at the Delft University of Technology. Andy Hooper provided comments and suggestions on the work.

Acknowledgements

The PhD journey is bumpy but fascinating, and I have gained a lot over the last four years. I am proud of myself, but I could never complete this journey successfully without the support of many people. Here I would like to express my heartfelt thanks to them.

First and foremost, I would like to express my deep and sincere gratitude to my primary supervisor, Prof. Andy Hooper, for his invaluable guidance and support throughout my research and writing of this thesis. His vision, sincerity, motivation and immense knowledge have deeply inspired me. I am extremely grateful for his support during the last year of my PhD research. It was a great privilege and honour to work and study under his guidance.

I would like to say special thanks to my co-supervisors, Dr. John Elliott and Prof. Tim Wright, for their consistent support and guidance throughout this project. They were always willing and enthusiastic to assist in all the time of the research. I am extremely grateful for what they have offered me.

The overall project was supported by the University of Leeds and the Chinese Scholarship Council Joint Scholarship. I also received support from the Centre for Observation and Modelling of Earthquakes, volcanoes and Tectonics (COMET).

I would like to express my thanks to research colleagues at the School of Earth and Environment, especially to my office mates: Pawan Piromthong, Jeanne Giniaux, Matthew Gaddes, Huw Goodall, Katy Willis, Ita Alvarez, Maeve Murphy Quinlan, Peidong Shi, Hardianshah Saleh and Patrick Sugden. It truly has been a wonderful time in this office. Many thanks to Ruth Amey, Tom Ingleby, Ekbal Hussain and Karsten Spaans, especially for their kind help and support during the beginning of my PhD study. I would like to say thanks to Milan Lazecky and Yu Morishita. They have been highly supportive of my research questions. To Richard Rigby for his kind and professional help in computer issues. I would like to thank Prof. Gregory Houseman and Prof. Graham Stuart for their genuine guidance and advice during my PhD Transfer. I thank colleagues and staffs at the COMET for their support during my research work. I would like to express my big thanks to research colleagues from the Netherlands, especially to Taco Broerse, Olga Kleptsova, Julie Pietrzak and Wim Simons, for their collaborations on the project of the Palu earthquake. I also would like to show sincere thanks to Dr. Romain Jolivet and Prof. Gregory Houseman for examining this thesis.

I thank my friends from Leeds and China, for their accompanying and encouragements over these few years.

Finally, I cannot thank my parents enough for their unconditional love, understanding and caring throughout my life.

Abstract

Seismic hazard, a natural hazard that is associated with potential earthquakes in a particular area, can lead to human casualties, damage to infrastructure and substantial economic losses. We can assess the potential level of seismic hazard that a region is exposed to by studying previous seismic events or measuring strain build-up on a fault.

As a space geodetic tool, Interferometric Synthetic Aperture Radar (InSAR) offers great potential to measure surface deformation in nearly all weather conditions day and night. As most earthquakes result from the long-term accumulation of strain in the crust, there are two ways to analyse seismic hazard using InSAR measurements: i) investigating the seismic deformation during earthquakes; ii) studying the long time-series of crustal displacement in between earthquakes.

However, variation in the phase delay, caused by the spatiotemporal variability of tropospheric properties, is still a major limiting factor in InSAR measurements, particularly when deriving long wavelength deformation signals that are partially correlated with topography. To improve the retrieval of deformation signals from InSAR measurements, in this thesis, I present a spatially varying scaling method for reducing tropospheric effects that combines the use of both external weather model data and the interferometric phase. I assume that vertical refractivity profiles calculated from a high-resolution weather model data can generally describe the form of the relationship between tropospheric delay and height but that the magnitude can be incorrect. I estimate a magnitude correction by scaling the original delays to best match the interferometric phase. I validate the new method using simulated data and demonstrate that both coseismic and interseismic

signals can be separated from strong tropospheric delays. I also apply the new algorithm to the central portion of the Altyn Tagh Fault (ATF) in northern Tibet, where deformation correlates strongly with topographic relief of 6,000 m. The derived velocity map from the interferograms after correction using the scaled tropospheric delays is more internally consistent and agrees better with independent Global Positioning System (GPS) measurements. Furthermore, the results for Taal Volcano in the Philippines demonstrate that the method can be applied to volcanic activities, for which deformation signals are sometimes correlated with topography.

Motivated by the aim of providing an overall picture of the seismic risk along the 1600 km-long Altyn Tagh Fault in the Northern Tibetan Plateau, in this thesis, I present an interseismic velocity field along the fault between 80°E to 95°E, from Sentinel-1 interferograms spanning the period between late 2014 and 2019, and show results of the inverted slip rate and strain rate based on the velocity field. It is the first time such a large-scale analysis has been carried out for this fault with InSAR. I use the spatially varying scaling method to reduce the tropospheric effects in the interferograms and derive a clearer deformation signal over the ATF. I present a new scheme for stitching InSAR LOS velocities estimated from multiple satellite tracks and derive a consistent velocity field over an extensive spatial scale. Using a modified elastic half-space model, I find a systemic decrease of the slip rate along the ATF from 12 mm/yr to 8 mm/yr over the western portion to the central portion, whereas it increases again to 10 mm/yr over the eastern portion. I find strain accumulation occurs on the southern strand of the ATF to the west of 83 °E, which is structurally linked to the Longmu-Gozha Co strike-slip fault. This demonstrates that the generation of the NS-trending normal faulting events in this region, such as the 2008 M_w 7.2 Yutian earthquake, is ascribed to the EW-trending extensional stress at a step-over between the two left-lateral faults. The inverted width of shear zones along the fault reveals two broad shear zones along the fault, where the strain is distributed over multiple strands rather than concentrates on a single strand. The broad shear zones also explain the seismic activities on the strands away from the ATF in these areas. This work shows significant strain accumulation along the 1500 km length of the ATF, and that it is fast at about 10 mm/yr and quite localised along the fault. Since no major earthquake ($M_w > 7.0$) has occurred along the ATF since the 1924 events, a slip deficit of $\sim$1 m has been accumulated over the last century. Consequently, the ATF is capable of rupturing along its entire length with the potential for some of the largest earthquakes on the continents. Furthermore, I find a high strain rate greater than 0.4 μstrain yr^{-1} along the south-western segment of the ATF, implying that there might be a relatively greater earthquake potential in this region compared to other portions.

To provide insights into analysing seismic deformation over large length scales using InSAR measurements, in this thesis, I present a finite fault solution to measure the coseismic surface deformation field for the 2018 M_w 7.5 Palu earthquake, which ruptured approximately 200 km. This earthquake caused tsunami waves of surprisingly large magnitudes for a strike-slip faulting earthquake. The coseismic displacement field is crucial to explain the direct cause of the tsunami and can shed light on the tsunami potential generated from strike-slip earthquakes. To derive a high-resolution 3-D coseismic surface deformation field, I use the coseismic GPS displacement fields and multiple types of SAR-derived displacement fields to constrain a coseismic model through a Bayesian inversion framework. The finite fault solution reveals a dominance of shallow strike-slip for most of the rupture, mostly limited to the upper 10 km. The results show that the large slip (> 5 m) on the segments south of the bay continues up to the surface, whereas the segments north of the bay feature no, or minor, slip on the upper segments, implying that the rupture does not reach the surface there. Besides the main rupture, I find two additional normal faults that accommodate the notable dip-slip motions in the east of the main fault in the Sulawesi Neck and Northwest of the main fault in the Balaesang peninsula. As parts of the fault strand run below Palu bay, there are no surface observations that precisely locate the course of the rupture. To provide better constraints on surface displacement over the Palu bay, I investigate four different scenarios that cover possible fault geometries in the region, where the rupture has the key tsunami potential. All four models reproduce displacements observed by the surrounding GPS sites well, and reveal that dip-slip motions below the Palu bay are required to characterise the displacements observed by the GPS data around the bay. The models generally predict consistent runup heights and arrival times of the leading waves compared to the observed field surveys. While it is not possible to rule out contributions from landslides, this study shows that displacements due to coseismic slip are the leading cause of the major tsunami source in and around Palu.

Contents

List of Figures xiv

List of Tables xviii

1 Introduction 1

1.1 Seismic hazard . . . 1

1.2 Crustal deformation associated with the seismic cycle . . . 2

1.2.1 Interseismic deformation . . . 4

1.2.2 Coseismic deformation . . . 7

1.3 InSAR tropospheric corrections . . . 9

1.4 Characterising large-scale crustal deformation . . . 14

1.4.1 Case study: Altyn Tagh Fault, Northern Tibet . . . 15

1.4.2 Case study: the 2018 M_w 7.5 Palu earthquake, Sulawesi . . . 16

1.5 Aims and objectives . . . 17

1.6 Thesis structure . . . 18

2 Methods 19

2.1 Interferometric Synthetic Aperture Radar (InSAR) . . . 19

2.1.1 Basics of InSAR . . . 20

2.1.2 InSAR processing from SLC products to time-series . . . 21

2.2 Tropospheric delay modelling . . . 23

2.3 An elastic half-space model for interseismic deformation modelling . 25

2.4 An elastic dislocation model for coseismic deformation modelling . . 26

2.5 A Bayseian Markov chain Monte Carlo approach . . . 28

3 A spatially varying scaling method for InSAR tropospheric corrections using a high resolution weather model 29
3.1 Introduction 29
3.2 Spatially varying scaling method 30
3.2.1 Phase delay anomaly 31
3.2.2 Estimation of scaling factors 32
3.2.3 Scaling factor smoothing 34
3.3 Simulated test cases 38
3.4 Case study: central portion of the Altyn Tagh Fault, Tibet 43
3.5 Discussion 52
3.6 Conclusions 55

4 Interseismic strain accumulation along the Altyn Tagh Fault determined from Sentinel-1 InSAR 56
4.1 Introduction 56
4.2 InSAR data processing 63
4.3 Velocity mosaicking over adjacent tracks 65
4.4 Interseismic strain accumulation along the ATF 72
4.4.1 Fault-parallel velocities 76
4.4.2 Interseismic deformation modelling 78
4.4.3 Strain rate inversion 82
4.5 Discussion 82
4.5.1 Strain accumulation in broad shear zones 82
4.5.2 Comparisons to the published slip rates 84
4.5.3 Slip rates on a strike-slip fault in Central Tibet 86
4.5.4 High strain rate over the south-western portion 87
4.6 Conclusions 90

5 Constraints on the 2018 M_w 7.5 Palu earthquake from coseismic surface deformation 91
5.1 Introduction 91
5.2 Geodetic data acquisitions 95
5.2.1 SAR-derived dataset 95
5.2.2 GPS dataset 96

5.3 Data reduction and errors . . . 99
5.4 Derivation of the fault model . . . 102
5.4.1 Fault trace . . . 102
5.4.2 Fault segmentation and discretization . . . 104
5.5 Bayesian inversion . . . 105
5.5.1 Determining 3-D displacement . . . 106
5.5.2 Model parameter priors . . . 106
5.5.3 Moment regularisation . . . 108
5.5.4 Inversion efficiency . . . 108
5.6 Finite fault model . . . 108
5.7 Discussion . . . 124
5.7.1 Comparisons to published results . . . 124
5.7.2 Fault geometries over the Palu bay . . . 125
5.7.3 Tsunami modelling . . . 127
5.8 Conclusions . . . 131

6 Conclusions 133
6.1 Chapter 3 . . . 133
6.2 Chapter 4 . . . 134
6.3 Chapter 5 . . . 136
6.4 Future work . . . 137
6.4.1 Enhancing the scaling tropospheric correction method . . . 137
6.4.2 Improved seismic hazard evaluation for both the Altyn Tagh fault and other faults within Tibet . . . 137
6.4.3 Applying a joint inversion of geodetic dataset and tsunami observations to the 2018 M_w 7.5 Palu earthquake . . . 138
6.5 Concluding remarks . . . 138

A Supplementary materials for Chapter 3 139
A.1 Figures . . . 139
A.2 Tables . . . 156
A.3 Package for A Spatially Varying Scaling (ASVS) Method . . . 160
A.3.1 Introduction . . . 160

A.3.2 Configuration 160
A.3.3 Data preparation 160
A.3.4 Programs 163
A.3.4.1 Step 1: Getting a grid overlapped with the Region of Interest (ROI) 163
A.3.4.2 Step 2: Estimating spatially varying scaling factors 163

B Supplementary materials for Chapter 4 **164**
B.1 Figures 164

C Supplementary materials for Chapter 5 **184**
C.1 Figures 185

References **196**

List of Figures

1.1 Illustration of Reid's elastic rebound model of the seismic cycle. . . 4

1.2 Illustrations of elastic strain build-up and shallow creep on a strike-slip fault during the interseismic period. 5

1.3 Illustration of tropospheric delays 11

1.4 Relative tropospheric delays estimated from the HRES-ECMWF products over northern Tibet. 13

2.1 A work flow diagram illustrating the main steps of InSAR processing. 22

2.2 A schematic of the elastic dislocation model for the interseismic deformation modelling. 26

2.3 A schematic of the Okada model for the coseismic deformation modelling. 27

3.1 Spatially varying scaling method. 33

3.2 Example results of the scaling method applied to the testing area across the Altyn Tagh Fault. 34

3.3 Map of the scaling method study region over the Altyn Tagh Fault zone. 37

3.4 Tropospheric correction results for the simulated coseismic case. . . 41

3.5 Tropospheric correction results for the simulated interseismic case. . 42

3.6 The performance of the scaling method for three selected epochs. . 45

3.7 Histograms of the InSAR phase delay anomalies versus topography for the same three epochs. 46

3.8 Comparisons of the original and scaled weather model phase delay anomalies to the InSAR phase delay anomalies. 47

3.9 RMS comparisons of deramped single master interferograms before and after tropospheric corrections. 48
3.10 LOS annual velocity maps derived from the single master interferograms. 50
3.11 LOS InSAR velocities for profiles and the comparison to GPS data. 51
3.12 Testing results of the scaling method on volcanic deformation. . . . 54

4.1 Tectonic setting of the Altyn Tagh Fault (ATF) zone and other major features in Tibet. 59
4.2 Published slip rate estimates along the ATF. 62
4.3 RMS comparisons of interferograms in individual track before and after tropospheric corrections 64
4.4 Mosaicked InSAR LOS velocity fields after removing the average offsets in overlapping areas and the corresponding standard deviation of velocities. 66
4.5 GPS velocity map. 69
4.6 The fit of the model to data points in the inversion of long wavelength trends. 70
4.7 Mosaicked InSAR LOS velocity fields in the Tarim reference. 71
4.8 Comparison of the LOS velocity differences in the overlapping region between adjacent tracks before and after velocity mosaicking. 72
4.9 Decomposed east-west velocity map. 74
4.10 Decomposed sub-vertical velocity map. 75
4.11 Fault-parallel velocity profiles along the ATF. 78
4.12 Estimates of slip rate and strain rate along the ATF. 82
4.13 Estimated shear zones along the ATF. 84
4.14 Comparisons of slip rates between along the ATF previous measurements and the estimates derived in this study. 85
4.15 Slip rates on a strike-slip fault in Central Tibet. 87
4.16 Temporal evolution of LOS displacement between two sites on either side of the south-western segment of the ATF. 89

5.1 Tectonic setting of Sulawesi island. 94

5.2 The SAR-derived data and the GPS data used in the coseismic modelling. 98
5.3 Subsampled SAR-derived datasets from an adaptive quadtree sampling algorithm. 100
5.4 3-D displacement fields derived from the pixel-offset tracking data. Positive values in each panel indicate eastward motion, northward motion and uplift, respectively. 103
5.5 Fault trace and segmentation in the model. 105
5.6 Azimuth offsets profiles perpendicular to the fault south of the Palu bay. 107
5.7 Estimated maximum a posterior (MAP) model of strike-slip and dip-slip. 110
5.8 Estimated maximum a posterior (MAP) model of fault slip. 111
5.9 Estimated posterior mean model of fault slip. 112
5.10 Estimated posterior median model of fault slip. 113
5.11 Fit of the MAP model to geodetic surface observations. 114
5.12 Estimated 2σ uncertainties of slip from the posterior solutions. 120
5.13 Posterior PDF for the dip angle of each segment. 121
5.14 The mean of 3D displacements estimated from a sample of all posterior solutions. 122
5.15 Probability distributions of the estimated vertical displacement over the bay. 123
5.16 Differences of the derived vertical displacement between the selected extremes and the MAP solution. 124
5.17 Estimated maximum a posterior (MAP) solutions of three bay segments in four scenarios. 126
5.18 RMSE comparisons of four models between geodetic observations and the model predictions. 127
5.19 Comparisons of runup between models and observations from surveys along the Palu bay. 129

A.1 Small baseline subset network of interferograms. 140
A.2 InSAR phase delay anomalies for all 19 epochs. 141

A.3 Tropospheric phase delay anomalies for all 19 epochs. 142
A.4 Histograms of the InSAR phase delay anomalies versus topography for all 19 epochs before tropospheric corrections. 143
A.5 Spatial distributions of the smoothed scaling factor. 144
A.6 Scaled tropospheric phase delay anomalies for all 19 epochs. 145
A.7 Histograms of the InSAR phase delay anomalies after correction using the scaled weather model anomalies versus topography for all 19 epochs. 146
A.8 Comparison of the correlation coefficient between the InSAR phase delay anomalies and scaled weather model anomalies to the value between the original weather model anomalies and scaled weather model anomalies for all 19 epochs. 147
A.9 Scaling results for an atypical epoch 5 April 2015. 148
A.10 Original weather model anomaly against scaling factor. 149
A.11 LOS annual velocity maps derived from the deramped single master interferograms. 151
A.12 Changes in tropospheric phase delay anomalies. 152
A.13 Tropospheric correction results using the power law method. 153
A.14 Temporal evolution of deformation between two distant points. . . . 154
A.15 Postseismic signals across the Manyi south branch. 155

B.1 Sentinel-1 data frames across the ATF. 165
B.2 Small baseline subset networks of all tracks. 166
B.3 The MAP solution for each fault-perpendicular profile. 170
B.4 Marginal probability distributions of each profile. 171
B.5 The MAP solution of the shear zone model. 183

C.1 SAR-derived datasets at page size. 185
C.2 Posterior PDF of the strike-slip component on three segments over the Palu bay. 189
C.3 Posterior PDF of the dip-slip component on three segments over the Palu bay. 192
C.4 Posterior PDF of the strike for segment G over the bay. 195

List of Tables

3.1 Parameters of the simulated earthquake used. 38
3.2 InSAR Processing Parameters. 39

5.1 SAR-derived dataset from the ALOS-2 used in this study. 96
5.2 Estimates of the semivariogram for SAR-derive data. 102

A.1 Tropospheric phase delay anomalies for each epoch in the LOS direction estimated from continuous GPS data. 157
A.2 Randomized weather model. 158
A.3 Parameters of the power law method used. 159
A.4 Processing parameters used in the package. 162

Abbreviations

List of Acronyms

3-D	Three Dimensional
ALOS-2	Advanced Land Observing Satellite 2
ATF	Altyn Tagh Fault
BLUE	Best Linear Unbiased Solution
DEM	Digital Elevation Model
GNSS	Global Navigation Satellite System
GAMIT	GNSS at MIT
GPS	Global Positioning System
HRES-ECMWF	High Resolution European Centre for Medium-Range Weather Forecasts
InSAR	Interferometric Synthetic Aperture Radar
ITRF08	International Terrestrial Reference Frame 2008
ITRF2014	International Terrestrial Reference Frame 2014
LGCF	Longmu-Gozha Co Fault
LiCSAR	Looking inside the Continents from Space SAR
LOS	Line of Sight
MAI	Multiple Aperture InSAR
MAP	Maximum a Posterior
MCMC	Markov chain Monte Carlo
MERIS	Medium Resolution Imaging
MODIS	Moderate Resolution Imaging Spectroradiometer
PDF	Probability Density Function
PS	Persistent Scatterer
RMSE	Root Mean Square Error
SABS	Small Baseline Subset
SAR	Synthetic Aperture Radar
ScanSAR	Scanning Synthetic Aperture Radar
SLC	Simple Look Complex
SRTM	Shuttle Radar Topography Mission
StaMPS	Stanford Method for Persistent Scatterers
STD	Standard Deviation

TRAIN	Toolbox for Reducing Atmospheric InSAR Noise
USGS	United States Geological Survey
WRF	Weather Research and Forecasting Model
ZTD	Zenith Tropospheric Delay

List of Symbols

λ	Wavelength
M_{w}	Moment magnitude
μ	A unit prefix denoting a factor of 10^{-6}
Φ	InSAR phase
ϕ	Azimuth direction of satellite
θ	Radar incidence angle
σ	Standard Deviation

Chapter 1

Introduction

1.1 Seismic hazard

Natural hazards have significant adverse effects on the environments in which humans build communities. Seismic hazard, a natural hazard that is associated with potential earthquakes in a particular area, can lead to human casualties, damage to infrastructure and substantial economic losses (Sawires et al., 2015). Whilst the fatality rate from other natural hazards, such as flooding and drought, has declined significantly in the past century, the death rate from seismic hazard has remained persistent (Elliott, 2020).

Since the early 20th century, we have gained more insights about seismogenesis: recognising that earthquakes represent the sudden release of strain energy that has continuously accumulated around tectonic faults (Lawson, 1908). Based on our knowledge, we are aiming to forecast the possibility of when and where the next earthquake might occur (Jena et al., 2020). However, due to the complexity of continental tectonics and the indeterminacy of the location of active faults, existing assessment methods often fail when estimating seismic hazard, particularly in areas with low seismicity (Wright, 2016). We are often surprised by earthquakes that occur in unexpected areas (e.g., Hamling et al., 2017), reminding us of the importance of continuing to study on continental faults.

Studying previous seismic events is critical to understand the overall earthquake process, including the size, exact locations and rupture processes (Elliott, 2020).

These past earthquakes represent areas where strain has accumulated in the lead up to seismic rupture (Biggs and Wright, 2020). Since a region that had earthquakes before is likely to host them in the future (Elliott, 2020), past earthquakes are essential data for assessing seismic hazard (Lin et al., 2020).

However, the record of past earthquakes is incomplete. Measuring strain build-up on a fault is an alternative way to provide the potential level of seismic hazard, as we expect that long-term strain accumulation can eventually lead to an earthquake. For instance, a Global Strain Rate Model based on crustal measurements from over 22,000 locations (Kreemer et al., 2014) has been used to forecast shallow seismicity globally (Bird and Kreemer, 2015). Therefore, mapping strain accumulation, which can be related to seismicity rates (Ader et al., 2012; Michel et al., 2018; Molnar, 1979; Rollins and Avouac, 2019), can shed light on long-term forecasts of seismic hazard (Biggs and Wright, 2020).

1.2 Crustal deformation associated with the seismic cycle

Although earthquakes happen within a short time period, stress accumulates on a fault in long intervals of decades to millennia. When the accumulated strain exceeds the frictional forces that are preventing slip, the elastic strain is released in the brittle upper crust suddenly causing an earthquake. This process has been considered as a quasi-cyclical reoccurrence (Thatcher et al., 1993), which is usually termed as the "seismic cycle". According to Reid's elastic rebound model of earthquakes (Reid et al., 1910), elastic strain accumulates over a long period between two earthquakes, known as the interseismic period, followed by a sudden rupture when a breaking point is reached, known as the coseismic period (Fig. 1.1). Both processes produce ground displacement at the surface that can be observed by Interferometric Synthetic Aperture Radar (InSAR), which offers great potential to measure surface deformation in nearly all weather conditions and during day and night (Wright, 2016).

There are two ways to analyse crustal deformation associated with the seismic cycle using InSAR measurements. Firstly, we can use InSAR to investigate seismic deformation during earthquakes. Since the first map of ground deformation caused by the 1992 Landers earthquake (Massonnet et al., 1993), InSAR has been used to characterise hundreds of coseismic displacement fields caused by earthquakes (e.g., Elliott et al., 2010; Wang et al., 2007). Accurate measurements of seismic deformation from InSAR can help with the identification of earthquake location (e.g., the 2004 Tabuk earthquake in Saudi Arabia, Xu et al. (2015)) and to determine if earthquakes rupture the surface or not (e.g., the 2018 Palu earthquake in Sulawesi, Socquet et al. (2019)). They can be used to solve for complex fault geometry and segmentation (e.g., the 2016 Kaikōura earthquake in New Zealand, Hamling et al. (2017)) and to invert for a reliable slip distribution on the fault plane (e.g., the 2015 Nepal earthquake, Ingleby et al. (2020)). Secondly, multi-temporal InSAR has been used to estimate interseismic strain accumulation along faults to identify aseismic deformation transients between two earthquakes (e.g., Cavalié et al., 2008; Hussain et al., 2018). Using this method, we can determine if the fault is rapidly accumulating strain and so should be considered more hazardous (Elliott, 2020).

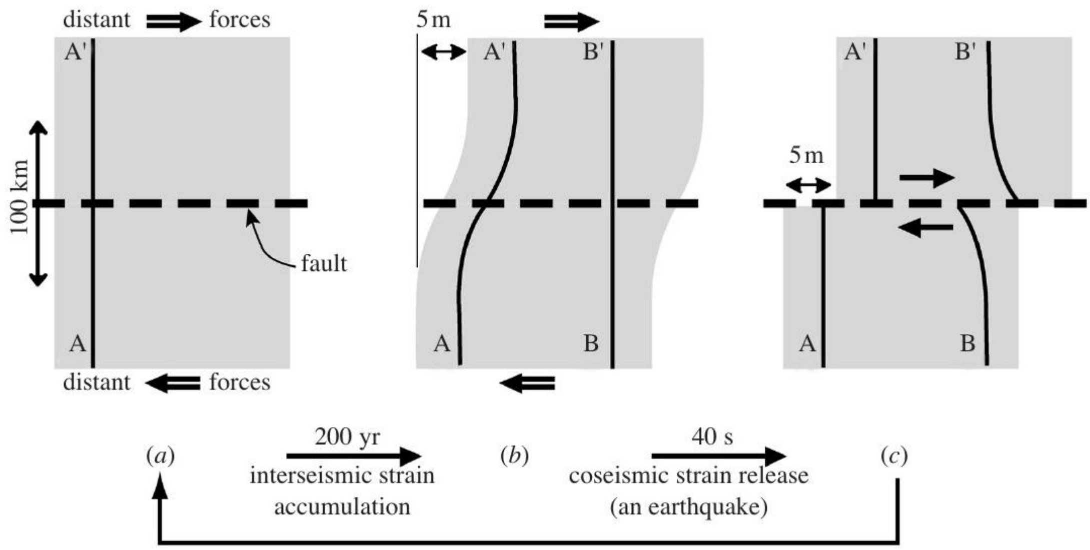

Figure 1.1: Illustration of Reid's elastic rebound model of the seismic cycle (adapted from Wright (2002)). The profile A-A' is straight when the cycle begins (a) and then is gradually distorted as the interseismic strain is accumulated over 200 years (b). 40s after the earthquake, the profile A-A' is straight again immediately, but with an offset of 5 m at the fault (c). The profile B-B', which is straight before the earthquake occurs (b), is distorted with an offset of 5 m at the fault in the near field, whereas the displacement decays in the far field (c). This scheme assumes that the upper crust, on which most earthquakes occur, behaves elastically and does not consider the heterogeneous properties of rocks at the deeper fault zone.

1.2.1 Interseismic deformation

During the interseismic period, strain accumulates steadily on either side of the fault (Thatcher and Rundle, 1979). At this stage, the upper crust is locked, whereas the deformation continues in the lower crust (Fig. 1.2) and mantle, and the shape of the deformation in the upper crust reflects the slip rate and the range of earthquake focal depths, commonly known as the seismogenic thickness. Using survey markers in a trilateral network, Savage et al. (1979b) first estimated the interseismic deformation for the San Andreas Fault. Laser ranging (e.g., Wang et al., 2003) and GNSS measurements (e.g., Bettinelli et al., 2006) have also been applied to measure the deformation signals. As most earthquakes occur after long-term strain accumulation, characterising the interseismic deformation is significant for assessing the earthquake potential.

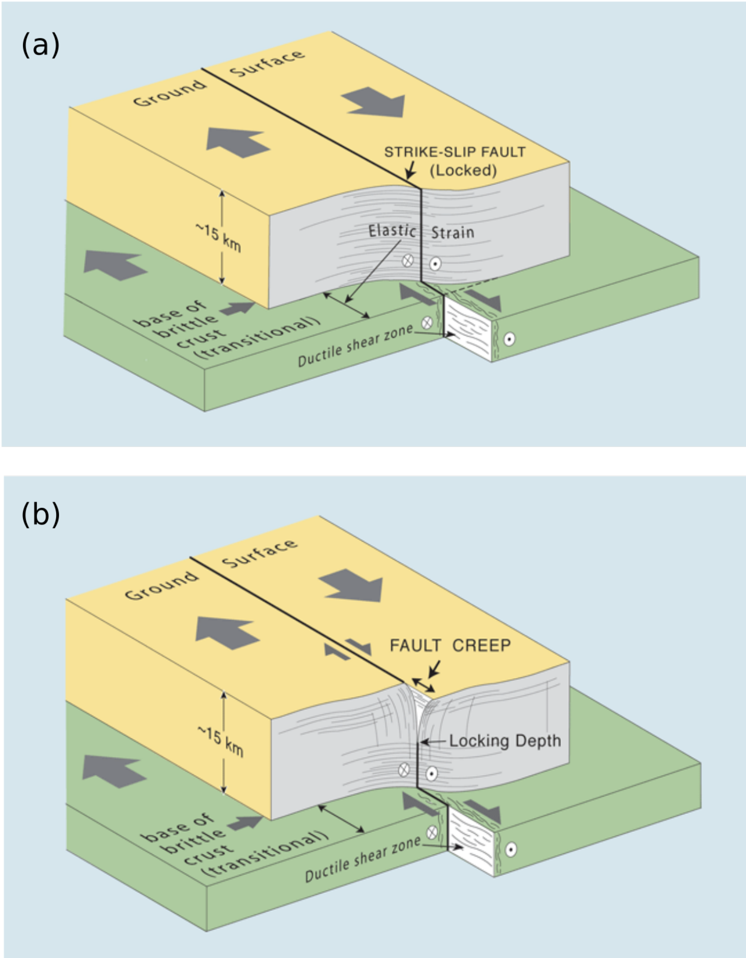

Figure 1.2: Illustration of elastic strain build-up (a) and shallow creep (b) on a strike-slip fault during the interseismic period (Funnel, 2006). At this stage, the brittle upper crust (yellow blocks) is locked, whereas the motion in the ductile shear zone of the lower crust (green blocks) continues. Fault creep occurs in the uppermost part of the brittle upper crust, and the locking depth is always greater than the creep depth.

With the significant improvement of quality and rapid accumulation in data volume over the last three decades, InSAR can now be used routinely to provide precise interseismic measurements with uncertainties in the level of mm/yr (e.g., Walters et al., 2014). Since InSAR was first used to estimate the interseismic strain accumulation in high-spatial resolution across the North Anatolian Fault in Turkey (Wright et al., 2001), the technique has been applied to measure the interseismic deformation for over 25 fault zones worldwide (Wright et al., 2013). The derived interseismic velocity fields were used to investigate variations in deformation style between the segment that ruptured recently and seismic gaps further along the fault (e.g., Cavalié et al., 2008) and assess seismogenic potential over fault zones (e.g., Fialko, 2006; Hussain et al., 2016a; Karimzadeh et al., 2013). Additionally, the measurements were used to investigate the variation of rheology and frictional properties on faults (e.g., Kaneko et al., 2013; Lindsey et al., 2014). The estimates were used to extract interseismic coupling signals in subduction zones to understand the earthquake potential of the megathrust (e.g., Béjar-Pizarro et al., 2013; Lin et al., 2015). The data can also be used to measure long-term mountain growth shedding light on the evolution of orogeny (e.g., Grandin et al., 2012). Moreover, the high-resolution interseismic velocity fields that were derived recently have a much wider spatial coverage (e.g., Tong et al., 2013), even crossing an entire plate boundary fault (e.g., Hussain et al., 2016a).

Despite some studies that favour the use of more complex models to characterise the interseismic velocity field (e.g., Jiang et al., 2015), the elastic dislocation model is commonly applied to estimate the fault slip rate and the locking depth at the interseismic stage (Elliott et al., 2016). The dislocation model has the strong assumption that the motion is steady in a homogeneous elastic half-space below a locked lid of the fault (Savage and Burford, 1973), which is not necessarily consistent with our understanding about the characteristics of the seismic cycle. However, the recent studies on the development of seismic cycle models reveal that the velocities are generally steady after the transient postseismic deformation has decayed (Takeuchi and Fialko, 2012; Yamasaki et al., 2014). Moreover, the continuing success of the dislocation model in hundreds of applications over the last three decades has demonstrated its effectiveness (Wright et al., 2013). It suggests that the uncertainties in the geodetic measurements may hamper better performance with the more complex models (Elliott et al., 2016).

Besides the accumulated elastic shear strain, aseismic slip is another important component of measuring fault strain accumulation (Jin and Funning, 2017). Fault creep occurs in the uppermost part of the crust during the interseismic period

(Fig. 1.2). Identifying characteristics of creeping areas on major faults can provide constraints on whether these slowly slipping sections can act as barriers to seismic ruptures (Jolivet et al., 2013). Fault creep has been observed along sections of the San Andreas Fault (e.g., Johanson and Bürgmann, 2005), North Anatolian Fault (e.g., Cakir et al., 2005), Chaman Fault (e.g., Barnhart, 2017), Haiyuan Fault (e.g., Jolivet et al., 2013), the Leyte fault (e.g., Duquesnoy et al., 1994) and the Longitudinal Valley Fault (e.g., Champenois et al., 2012). The occurrence of fault creep indicates that the values of normal stress or the geometric irregularity is low or absent on a fault so that the uppermost part is not able to be locked during the interseismic stage. The creep rate at the surface depends on the rate of stress accumulation in the lower crust, the creep depth and the fault's resistance to the shear stress (Savage and Lisowski, 1993). As aseismic slip, fault creep usually deforms much more quickly at the beginning, and then the rate gradually decays. Sometimes fault creep occurs as a series of discrete creeping events that may last from several days to years (Wesson, 1988). Burford (1988) and Lienkaemper and Galehouse (1997) showed that creep rate along a fault is sensitive to the tectonic loading of its surrounding region, and changes in creep rates are often ascribed to local earthquakes. Simpson et al. (2001) also revealed that variations of the locking depth along the fault are associated with changes in the creep rate, which means that locking depth is a key parameter when assessing seismic hazard.

1.2.2 Coseismic deformation

Since the first successful use of InSAR to map the surface displacement caused by the 1992 M_w 7.3 Landers earthquake (Massonnet et al., 1993), it has become routine to apply this space geodetic technique to measure coseismic deformation (more than 100 earthquake events are referenced in (Wright et al., 2013)). With high-spatial resolution and wide spatial coverage, InSAR can provide remote measurements at large scale with exquisite detail for continental earthquakes with moderate to large magnitude (M_w 5+) (Elliott et al., 2016).

Based on an interferogram covering the rupture, source geometry and fault slip distributions at depth can be inverted using elastic dislocation theory to explain the observed surface displacement fields (Segall, 2010). For instance, Okada

(1992) used a rectangular dislocation to represent a fault in an elastic half-space. Comparison of observed surface motion with that computed for a rectangular dislocation, thereby constrains the slip distribution on that patch (e.g., Thatcher et al., 1997). For larger events, multiple planes are incorporated to characterise the segmentation of faulting (e.g., Bie et al., 2017; Sreejith et al., 2016). The detailed slip distributions at depth inverted from InSAR measurements can allow us to investigate which portions of the fault failed and which did not, providing insights on the possible sections of future failure (e.g., Zhao et al., 2018). Furthermore, the inverted slip distributions can be used to calculate the Coulomb stress to identify the stress changes caused by the failure on surrounding faults. This enables the prediction of the approximate location of strong aftershocks following a large mainshock (e.g., King et al., 1994; Martínez-Díaz et al., 2012; McCloskey et al., 2005), which is significant for the seismic hazard assessment (Zhao et al., 2018).

Using InSAR measurements, previous studies show that the derived fault geometry, such as strike, dip and rake, and seismic moment values are generally consistent with that of the seismological observations (e.g., Weston et al., 2010). For shallow earthquakes, the estimated location from InSAR is very accurate because of the high-spatial resolution, which shows good agreement with seismic locations from regional catalogues (Weston et al., 2012). It can support field geologists to locate the surface rupture after earthquakes occur (e.g., Hamling et al., 2017).

By analysing the published InSAR coseismic modelling results of 78 continental earthquakes (M_w 5.5+) globally, Wright et al. (2013) found that the average thickness of the seismogenic layer is 14 $\pm$ 5 km, which is consistent with 187 estimates of interseismic locking depth. However, the earthquake depth determined by InSAR is slightly shallower compared with the estimates using seismic source models (e.g., Lohman and Simons, 2005; Weston et al., 2011). This can be caused by the poorer depth resolution of seismic techniques (Weston et al., 2012) or the bias introduced by the homogeneous elastic half-space model used in InSAR modelling, as Lohman et al. (2002) found that the depths estimated from the elastic half-space model are systemically shallower than the seismic waveform modelling results.

InSAR can measure the deformation in the line-of-sight (LOS) direction with high precision, but due to the polar-orbiting direction (Wright et al., 2004), it is not sensitive to the motion in the azimuth direction and thus has limitations when measuring the north-south movement caused by crustal motion (e.g., Himematsu and Furuya, 2016; Merryman Boncori and Pezzo, 2015). Alternatively, at lower spatial resolution and measurement accuracy, pixel-offset tracking can provide unambiguous estimates of deformation in both the range and azimuth direction, even if the interferogram is decorrelated (Tobita et al., 2001). The Multiple Aperture Interferometry (MAI) method is developed based on the split-beam InSAR method using bandpass filters to create geometrically symmetric forward- and backward-looking interferograms (Bechor and Zebker, 2006), which has improved accuracy compared to the pixel-offset tracking (e.g., Jo et al., 2015; Jung et al., 2009). The differences between the two interferograms characterise the along-track displacements. As the troposphere in the forward- and backward-looking interferograms are almost identical, the MAI technique is nearly insensitive to tropospheric effects. Therefore, the pixel-offset tracking and the MAI can be considered as complementary to InSAR measurements when deriving 3-D surface displacement field, especially for the north-south striking strike-slip faults (e.g., Socquet et al., 2019) and east-west striking dip-slip faults.

Besides InSAR, Global Navigation Satellite System (GNSS) provides highly accurate measurements for crustal deformation and are often used to invert for the fault slip distributions if the data is dense enough to characterise the surface displacements (e.g., Dreger et al., 2015; Tung and Masterlark, 2016). The constraints on the slip distributions at depth with multi-sources can provide a more robust picture for the fault rupture (Delouis et al., 2002).

1.3 InSAR tropospheric corrections

The accuracy of measurements in InSAR is limited by coherence loss due to the changes of scattering properties, errors in the determination of satellite orbit and surface elevation, and variations in atmospheric properties. The former three contaminations are less of problems in the recently launched Sentinel-1 constellation, which has improved the coherence of interferograms due to its high spatial resolution, short revisit times and good orbital control (Elliott et al., 2016). However, variation in the phase delay, caused by the spatiotemporal variability of atmospheric properties, is still a remaining limiting factor in Sentinel-1 InSAR measurements (Parker et al., 2015).

Atmospheric delays are caused by dispersive effects of free electrons in the ionosphere and by changes in refractive index in the troposphere. Ionospheric delays in interferograms are usually observed as azimuth distortions or shifts with length-scales generally larger than 100 km (Meyer et al., 2006). Moreover, ionospheric effects in interferograms are more significant for larger wavelengths, such as L-band and P-band (Gray et al., 2000; Mattar and Gray, 2002). Tropospheric delays depend on temperature, pressure and relative humidity and can cause variations of up to 15-20 cm in magnitude over a distance on the order of 100 km (Fig. 1.3), which would overwhelm most slowly accumulating deformation or time-dependent signals (Bekaert et al., 2015b; Fournier et al., 2011; Heleno et al., 2010; Hooper et al., 2012). This can limit our ability to measure low-amplitude deformation fields such as interseismic strain accumulation (e.g., Daout et al., 2018; Fialko, 2006; Hussain et al., 2016a; Jolivet et al., 2008; Walters et al., 2013; Wei et al., 2010), small magnitude coseismic deformation (e.g., Yu et al., 2018a) and urban subsidence (e.g., Chaussard et al., 2014; Perissin and Wang, 2011).

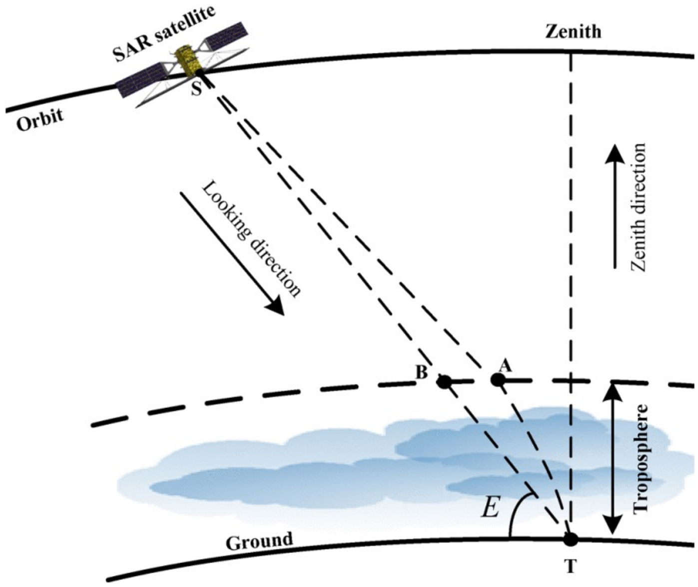

Figure 1.3: Illustration of tropospheric delays (adapted from Yu et al. (2015)). The line AT and BT represent the actual propagation path of electromagnetic signals through the troposphere at two different epochs. The relative tropospheric delays between the two epochs depend on the variability of tropospheric properties during the spanning time.

To reduce the tropospheric effects, various approaches have been tried, using either external data or the interferometric phase itself. External datasets that have been utilized include local meteorological data (e.g., Delacourt et al., 1998; Pinel et al., 2011), continuous Global Positioning System (GPS) zenith delay measurements (e.g., Li et al., 2006; Onn and Zebker, 2006; Yu et al., 2017), spectrometer measurements (e.g., Li et al., 2009), numerical metrological products such as the local weather research and forecasting (WRF) model (e.g., Puysségur, Béatrice and Michel, Rémi and Avouac, Jean-Philippe, 2007; Yun et al., 2015) and global atmospheric reanalysis products (e.g., Doin et al., 2009; Jolivet et al., 2014; Walters et al., 2013). However, local meteorological data, spectrometer and continuous GPS stations are rarely available for the time of each SAR acquisition: continuous GPS stations are often absent and are generally distributed with a coarse spatial density when considered globally; spectrometer observations from the Medium Resolution Imaging Spectrometer (MERIS) or the Moderate Resolution Imaging Spectroradiometer (MODIS) are not available at night, or over areas with cloud cover, and in the case of MERIS, were only available between 2002 and 2012. More importantly, spectrometer data can only be used to estimate the wet delay. Studies that have used regional numerical weather prediction models have found that although they have high temporal and spatial resolutions and can account for both the hydrostatic and wet delay, it has not been possible to obtain consistently robust results in a wide range of settings (Bekaert et al., 2015b; Cimini et al., 2012; Foster et al., 2013). In contrast, global weather models have the benefits of complete spatial coverage and data availability (Dee et al., 2011), and can also account for both the hydrostatic and wet delay. The latest High Resolution European Centre for Medium-Range Weather Forecasts (HRES-ECMWF) analysis products (ECMWF, 2016) have a much higher spatial resolution when compared with previous global weather models. However, they are models that are still limited by the assimilation of observations to constrain their boundary conditions (Dee et al., 2016). In regions with sparse input data such as Western China, Africa, Western South America and the polar regions, it is unclear of the performance of the models at their highest resolution. In addition, global weather models including the HRES-ECWMF suffer from timing issues as they are not sampled simultaneously with SAR acquisitions. This lack of synchronisation is likely a contributing factor to the lack of consistently robust results from global weather models (Gong et al., 2015) due to the relatively rapidly changing state of the troposphere.

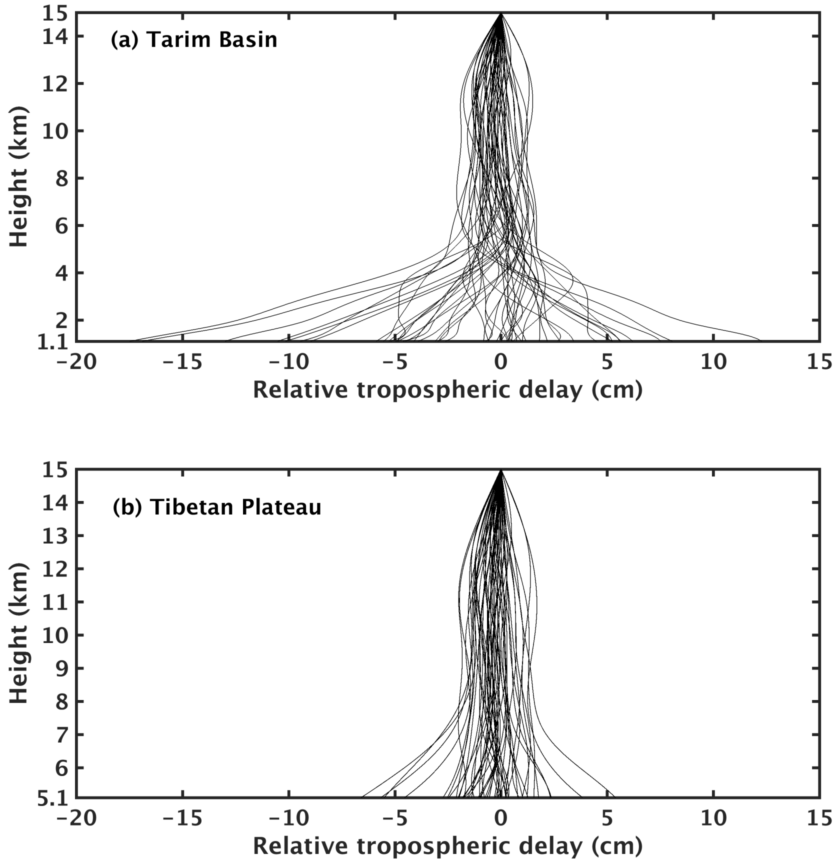

Figure 1.4: Relative tropospheric delays estimated from the HRES-ECMWF products for 53 small baseline interferograms over northern Tibet in Chapter 3. Each curve shows the relative tropospheric delays for a point in (a) the Tarim Basin (85.6°E, 38.3°N) or (b) the Tibetan Plateau (86.1°E, 36.8°N) from the surface (note difference in surface elevation of 1.1 km vs 5.1 km).

There are numerous approaches to using the interferometric phase itself. Linear approaches assume a single relationship between phase and topography over the whole interferogram (e.g., Elliott et al., 2008; Lin et al., 2010; Wicks et al., 2002). Liang et al. (2018) proposed a quad-tree aided joint model that can estimate the deformation, tropospheric delays and delay-to-elevation ratio simultaneously. The method characterises both the long wavelength delay and the turbulent delay, whereas it assumes a simple linear relationship between phase and topography. The second approach assumes a power law correction relationship between phase and height (Bekaert et al., 2015a; Hanssen, 2001), which allows for a spatial variability in tropospheric properties and estimation of long wavelength tropospheric signals as well as the topographically correlated component. This is particularly important for larger interferograms, where the assumption of consistent atmospheric properties across the whole image breaks down. However, measurements derived from balloon-sounding data (Bekaert et al., 2015a) and weather model data (Fig. 1.4) show that the actual observed and predicted patterns of differential tropospheric delays with height are more variable than a simple power law can sufficiently describe. A third set of approaches are available for multi-interferogram stacking (e.g., Ferretti et al., 2011) and spatial-temporal filtering of the time series (e.g., Ferretti et al., 2011, 2001; Hooper et al., 2004) are applied to mitigate the tropospheric delays. However, those methods ignore that tropospheric delays are not Gaussian distributed and can decrease the temporal resolution of InSAR measurements and discard useful geophysical signals (Yu et al., 2018b). Also, applying temporal filtering to a time series with uneven acquisition program can introduce long temporal wavelength biases (Doin et al., 2009).

Therefore, to address the limitations of using either approach individually, I present a new approach for InSAR tropospheric corrections that combines the use of both external high resolution weather model data and the interferometric phase in Chapter 3 (Shen et al., 2019).

1.4 Characterising large-scale crustal deformation

Crustal deformation processes associated with seismic cycle often have large spatial scales spanning several hundred thousand square kilometres, such as interseismic fault processes on large-scale continental faults (e.g., Cavalié and Jónsson, 2014; Hussain et al., 2018; Tong et al., 2013) and large earthquakes that cross plate boundary zones (e.g., Wang et al., 2020). Limited by the operational nature and radar characteristics of previous SAR sensors, the first studies on crustal deformation using InSAR have relatively small areas. Thanks to recently launched radar satellites, such as the Sentinel-1 constellation and the Advanced Land Observing Satellite 2 (ALOS-2), we now have InSAR datasets with wide spatial coverage that have accumulated six years of data, to constrain deformation for large regions. The sensors can achieve high spatial resolution and short revisit times, which have improved the coherence of interferograms.

1.4.1 Case study: Altyn Tagh Fault, Northern Tibet

Large continental strike-slip faults have the potential of large earthquakes that rupture long segments at very fast speeds (Robinson et al., 2010). By investigating the long-term crustal deformation for large continental strike-slip faults, of which the deformation acts as a reflection of the deep motion in the region (Bourne et al., 1998), we can better understand how the continent deforms and the kinematics of tectonic processes there.

However, the detection of slowly accumulated interseismic deformation over large length scales remains challenging (Parker et al., 2015). Firstly, contamination caused by the spatiotemporal variability of tropospheric properties can easily mask low amplitude deformation signals (Walters et al., 2013). Furthermore, variation in satellite geometry (e.g., azimuth direction and incidence angle) and long wavelength errors between tracks lead to velocity inconsistencies in the overlapping regions, which is non-negligible in studies of large E-W trending faults.

The 1600 km-long Altyn Tagh Fault (ATF) is a major intra-continental strike-slip fault in Northern Tibet, the slip rate of which has significant implications for our understanding of the tectonic processes of the Tibetan Plateau region. The ATF trends approximately ENE-WSW between 80°E and 96°E (Searle et al., 2011), and splits into three sub-parallel strands at around 85°E eastward. The initial motion of the ATF is estimated to have occurred between the Eocene and the Miocene epochs (Robinson et al., 2003). Three palaeo-trenches along the fault have suggested three major earthquakes in the Holocene, between AD 60–980 and AD 1456–1775 respectively, indicating that the earthquake repeat cycle of the ATF is around 700–900 years. Historic earthquake records show several major earthquakes ($M_w > 6.9$) have occurred on the fault zone since 1900, including a pair of earthquakes along the western portion in 1924 with the magnitude of M_w 7.0 and M_w 7.2, respectively, the 1932 M_w 7.9 Gansu earthquake at the easternmost end, and the 2014 M_w 6.9 Yutian earthquake at the southwestern segment.

In contrast to the San Andreas Fault and the North Anatolian Fault, where the seismic risks have been well described (e.g., Tong et al., 2013; Weiss et al., 2020), previous studies of interseismic deformation over the ATF have only focused on specific portions. Of particular note, the western portion of the fault is hardly covered by previous measurements, although several studies have warned of an earthquake potential over this region (Bie and Ryder, 2014; Li et al., 2020). Consequently, to improve our understanding of the seismic hazard of this region, it is necessary to produce an overall picture of strain localisation along the ATF to investigate if the fault is capable of rupturing along its entire length.

In addition, as the ATF is located at the border between the low Tarim Basin and the high Tibetan Plateau, the interseismic deformation signals correlate strongly with the 6000 m topographic relief across it. Therefore, tropospheric correction is crucial to the accuracy of interseismic measurements in this region.

1.4.2 Case study: the 2018 M_w 7.5 Palu earthquake, Sulawesi

The Sulawesi block is located at the triple junction, marking the convergence of the India-Australia, Sunda and Pacific-Philippines plates. The Palu-Koro fault is a major active tectonic feature in Central Sulawesi (Bellier et al., 2006). It is straddled by Palu city, which has a population of 370,000. This left-lateral strike-slip fault has a NNW-SSE trend and passes from the SW corner of the Celebes Sea to the northern end of Bone Bay, a distance of 220 km onshore (Watkinson and Hall, 2017). To the north, the fault continues offshore and terminates at the western end of the North Sulawesi Trench (Hall and Wilson, 2000). To the south, the fault connects to another left-lateral strike-slip fault, the Matano Fault (Socquet et al., 2006). The Palu-Koro Fault Zone is interpreted as a cross-basin fault system (Watkinson and Hall, 2017). The dynamics of the Palu-Koro Fault are associated with the eastward migration of faulting activity from the western oblique-normal sidewall fault to an intra-basin strike-slip fault in Palu Valley (Patria and Putra, 2020).

Previous studies suggest that the fault can generate some of the largest earthquakes in Eastern Indonesia (Cummins, 2017; Watkinson and Hall, 2017).

Geological (Bellier et al., 2006), geomorphological (Bellier et al., 1998, 2001) and geodetic observations (Socquet et al., 2006; Walpersdorf et al., 1998) clearly indicate that the Palu-Koro fault is a very active fault system. Bellier et al. (2001) estimated that the Holocene slip rate of the fault is 35 $\pm$ 8 mm/year. Geodetic observations indicate that the current slip rate along the fault is fast at around 40 mm/yr (Bellier et al., 2001; Walpersdorf et al., 1998). Significant earthquakes ($M_w > 6.7$) occurred along the Palu-Koro Fault in 1905, 1907, 1909, 1927, 1934 and 1968, respectively (Katili, 1970). More recently, damaging earthquakes were recorded close to the fault in 2005 (M_w 6.3), 2012 (M_w 6.3) and 2018 (M_w 7.5), based on the United States Geological Survey (USGS) catalogue.

The 2018 M_w 7.5 Palu earthquake ruptured approximately 200 km on the segment of the Palu-Koro fault (USGS, 2018). The earthquake shows the intra-basin strike-slip faulting activity in Palu Valley (Patria and Putra, 2020). For a strike-slip faulting earthquake, this earthquake caused tsunami waves with surprisingly large amplitudes. Constraints on the fault slip from the surface deformation can provide insights into the earthquake mechanics and shed light on the tsunami potential generated from strike-slip earthquakes.

1.5 Aims and objectives

In this thesis, I aim to improve the retrieval of deformation signals from InSAR in different aspects of seismic hazard. I also aim to shed light on determining short-term seismic deformation and long-term crustal displacement leading up to earthquakes over large length scales, to provide insights into analysing seismic hazard using InSAR.

To achieve the aims, the following are specific objectives:

1. Develop a novel method for InSAR tropospheric corrections to address the limitations of previous correction approaches. Apply this new method to reduce InSAR tropospheric delays in different aspects of seismic hazard.

2. Derive long time-series InSAR velocity fields along the Altyn Tagh Fault from multiple satellite tracks, and develop a new scheme to stitch these velocity fields and derive a consistent velocity field over an extensive length scale.

3. Invert slip rate and strain rate along the Altyn Tagh Fault from the InSAR velocity field obtained by the second objective, and provide an overall picture of the seismic risk along the Altyn Tagh Fault.

4. Provide a finite fault solution to characterise the coseismic surface deformation field for the 2018 M_w 7.5 Palu earthquake.

1.6 Thesis structure

In **Chapter 2**, I provide background information on InSAR, and present a work flow of InSAR processing that I use to derive InSAR time-series from Sentinel-1 SLC products. I explain the method for deriving tropospheric delays from the latest high-resolution weather model. I describe core models for modelling the interseismic deformation along the Altyn Tagh Fault and the coseismic deformation of the 2018 M_w 7.5 Palu earthquake, respectively. I also explain a Bayesian Markov chain Monte Carlo approach that is used in later modelling inversions.

In **Chapter 3**, I address the first objective of this thesis, by presenting a new method for InSAR tropospheric corrections using high-resolution weather model products.

In **Chapter 4**, I address the second and third objectives of this thesis, by presenting the interseismic strain localisation along the Altyn Tagh Fault, over a spatial scale of approximately 1500 km. In this chapter, I apply the novel tropospheric correction method that I describe in Chapter 3 to improve the retrieval of interseismic deformation signals.

In **Chapter 5**, I address the fourth objective of this thesis, by presenting a finite fault solution to characterise the coseismic surface deformation field for the 2018 M_w 7.5 Palu earthquake that ruptured approximately 200 km.

In **Chapter 6**, I summarise the key findings of this thesis and provide suggestions for future work.

Chapter 2

Methods

In this chapter, I provide background information on InSAR techniques, and present a work flow of InSAR processing that I use to derive InSAR time-series from Sentinel-1 SLC products. I explain the method for deriving tropospheric delays from the latest high-resolution weather model. I describe core models for modelling the interseismic deformation along the Altyn Tagh Fault and the coseismic deformation of the 2018 M_w 7.5 Palu earthquake, respectively. I also explain a Bayesian Markov chain Monte Carlo approach for model inversion.

2.1 Interferometric Synthetic Aperture Radar (InSAR)

In the last three decades, Interferometric Synthetic Aperture Radar (InSAR) has emerged as a significant space geodetic tool to measure surface deformation (Curlander and McDonough, 1991; Pepe and Calò, 2017; Simons and Rosen, 2007). In contrast to most remote sensing satellites that measure the sun's radiation reflected back from the ground, Synthetic Aperture Radar (SAR) satellites transmit electromagnetic waves to illuminate an area of the Earth's surface and record the amplitude and phase of the waves that bounce back, which enables measurements of the illuminated target in nearly all weather conditions and during day and night.

2.1.1 Basics of InSAR

The interferogram is generated by the complex conjugate multiplication of two co-registered SAR acquisitions (Massonnet and Feigl, 1998), and the phase shift in the interferogram, $\delta\Phi_{InSAR}$, includes the following information:

$$\delta\Phi_{InSAR} = \delta\Phi_{flat} + \delta\Phi_{topo} + \delta\Phi_{atm} + \delta\Phi_{def} + \delta\Phi_{noise} \tag{2.1}$$

where $\delta\Phi_{flat}$ is the flatten phase caused by the satellite geometry; $\delta\Phi_{topo}$ is the topographic phase; $\delta\Phi_{atm}$ is the phase shift caused by the different atmospheric delay between passes; $\delta\Phi_{def}$ is the phase change from the ground deformation; $\delta\Phi_{noise}$ is the noise term corresponding to thermal noise and any other errors unaccounted for. In a wrapped interferogram, the coloured contours indicate the interference fringes between the two SAR images and the phase is measured as an angle from 0 to 360 degrees (or 0 to 2π radians). After correcting for $\delta\Phi_{flat}$ and $\delta\Phi_{topo}$, phase unwrapping is applied to solve the ambiguity of phase by adding integer multiples of 2π to the phase of each pixel thereby transforming the wrapped phase to the cumulative phase change. Then the unwrapped phase, $\delta\Phi_{unw}$, is made up by the following contributions as:

$$\delta\Phi_{unw} = \delta\Phi_{def} + \delta\Phi_{atm} + \delta\Phi_{DEM} + \delta\Phi_{orbit} + \delta\Phi_{noise} + \xi_{unw} \tag{2.2}$$

where $\delta\Phi_{DEM}$ and $\delta\Phi_{orbit}$ are the remaining DEM and orbital errors due to the inaccuracy in the determination of surface elevation and satellite orbit, respectively, and ξ_{unw} are the unwrapping errors. The $\delta\Phi_{unw}$ can be converted to the ground displacement along the light-of-sight (LOS) direction, D_{LOS}, as

$$D_{LOS} = -\frac{\lambda}{4\pi}\delta\Phi_{unw} \tag{2.3}$$

where λ is the wavelength of the SAR signal.

Since changes of scattering properties can easily cause phase noise in conventional InSAR (Hooper et al., 2012), to improve the accuracy of measurements, multi-temporal InSAR techniques are applied to derive deformation signals in time. Multi-temporal InSAR techniques can be divided into two broad categories, the persistent scatterer (PS) technique (Ferretti et al., 2001; Hooper et al., 2004; Kampes, 2005) and the small baseline subset (SBAS) approach

(Berardino et al., 2002; Hooper, 2008). In the PS-InSAR scheme, PS pixels with high signal-to-noise ratio, which remain coherent over long time periods, are selected from multiple single master interferograms using the amplitude variations of the interferograms (Ferretti et al., 2001) or the phase characteristics (Hooper et al., 2004). The technique derives deformation signals based on the selected stable PS pixels only to reduce the errors and has been successfully applied to urban areas where man-made structures are dominant. The PS-InSAR technique can achieve 1 mm/year accuracy if the region deforms linearly in time (Hooper et al., 2012; Vallone et al., 2008).

On the other hand, the SBAS approach uses a network that consists of multiple short temporal and perpendicular baseline interferograms to limit spatial decorrelation effects. A singular value decomposition or least-squares algorithm is applied in this technique to invert the phase for the distributed stable scatters, or so-called Slowly-Decorrelating Filter Phase (SDFP) pixels, at each epoch. The SBAS method can achieve similar accuracy as the PS-InSAR technique in urban areas(Lanari et al., 2007), whereas it has greater capability in non-urban areas which are dominated by distributed scatterers.

2.1.2 InSAR processing from SLC products to time-series

Figure 2.1 shows the main steps that I use to derive InSAR time-series from Sentinel-1 Simple Look Complex (SLC) products.

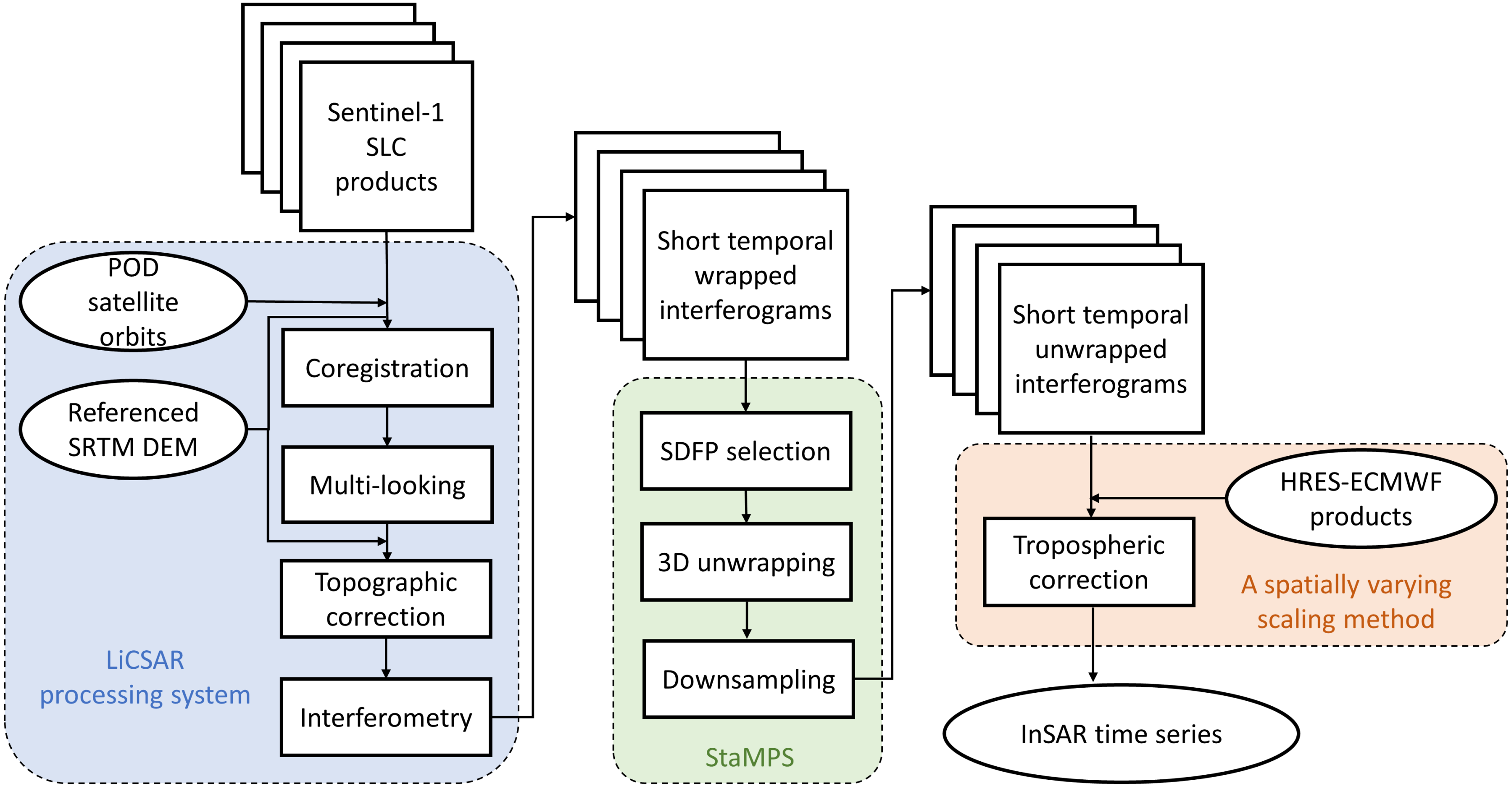

Figure 2.1: A work flow diagram illustrating the main steps of InSAR processing from Sentinel-1 Simple Look Complex (SLC) products to time-series.

I use the Sentinel-1 processing system Looking inside the Continents from Space SAR (LiCSAR) software package to generate short temporal baseline wrapped interferograms (Gonzalez et al., 2016; Lazecký et al., 2020). In the LiCSAR, processing a spectral diversity method is applied to co-register the interferograms (Scheiber and Moreira, 2000), and differences in satellite position are corrected by the precise orbit determination (POD) precise satellite orbits. The topographic contributions are corrected using the 3 arc sec Shuttle Radar Topography Mission (SRTM) DEM (Farr et al., 2007). The wrapped interferograms are multilooked 4 and 20 times in the azimuth and range directions, respectively, to improve the signal-to-noise ratio.

I then use the Stanford Method for Persistent Scatterers (StaMPS) software (Hooper, 2008; Hooper et al., 2012) to select high coherent Slowly-Decorrelating Filter Phase (SDFP) scatterers from the wrapped interferograms, downsample and unwrap the interferometric phase of the stable scatterers using a 3-D unwrapping approach (Hooper, 2010; Hooper and Zebker, 2007). I then perform a phase closure check to the unwrapped scatterers (Hussain et al., 2016a) and correct unwrapping errors in each interferogram manually.

Based on the short temporal baseline unwrapped interferograms, I use a spatially varying scaling method that I present in Chapter 3 to mitigate tropospheric effects before deriving InSAR time-series.

2.2 Tropospheric delay modelling

The phase delay through the troposphere depends on the refractivity, N, which can be divided into hydrostatic and wet components. In flat regions, hydrostatic delays are usually smooth in space as they are predominately pressure dependent. However, in areas of significant relief, spatial variations in hydrostatic delays are strong and can lead to a correlation between phase and topography (Elliott et al., 2008). For instance, whilst it has been possible to measure relatively small interseismic signals in flat regions of the Tibetan Plateau (Bell et al., 2011; Taylor and Peltzer, 2006), it has previously been hard to measure such deformation with high accuracy at the steep margins of the Plateau, where low-amplitude tectonic signals are strongly masked by the tropospheric delays resulting from the 6000 m topographic relief across it. In contrast to hydrostatic signals, the magnitude of wet delays, which are caused by the lateral variation in water vapour, is several times smaller (Hanssen, 2001) whereas the spatial pattern is much more variable (Zebker et al., 1997). The turbulent mixing process is strong in the near-ground surface (up to about 2 km above ground) and can cause localized variation in apparent phase of up to 10-15 cm (Ding et al., 2008) which often dominate the troposphere in interferograms (Hanssen, 1998; Tarayre and Massonnet, 1996; Yu et al., 2018b). Therefore, both the hydrostatic and wet delays should be accounted for to fully describe the tropospheric delays (Doin et al., 2009; Elliott et al., 2008).

At a specific height, h, the tropospheric phase delay Φ_{tropo} corresponds to the integration of the refractivity between h and the top of the troposphere h_T in the radar line-of-sight (LOS) direction (Berrada Baby et al., 1988; Hanssen, 2001) as

$$N = N_{hydr} + N_{wet} = (k_1 \frac{P}{T})_{hydr} + (k_2^{'} \frac{e}{T} + k_3 \frac{e}{T^2})_{wet} \tag{2.4}$$

$$\Phi_{tropo} = \frac{-4\pi}{\lambda} \frac{10^{-6}}{cos\theta} \int_{h}^{h_T} N dh \tag{2.5}$$

Where P is total tropospheric pressure, T the temperature, e the partial pressure of water vapor, θ the radar incidence angle, λ the radar wavelength, k_1, $k_2^{'}$ and k_3 the constants which are empirically taken as 77.6 K hPa^{-1}, 23.3 K hPa^{-1} and 3.75 $\cdot\ 10^5$ K^2 hPa^{-1} (Smith and Weintraub, 1953) respectively.

The latest High Resolution European Centre for Medium-Range Weather Forecasts (HRES-ECMWF) analysis products in pressure levels (ECMWF, 2016), assimilated from surface and satellite observations, provide meteorological data (such as temperature, relative humidity and geo-potential) along 25 pressure levels from the surface (1000, 950, 925, 900, 850, 800, 700, 600, 500, 400, 300, 250, 200, 150, 100, 70, 50, 30, 20, 10, 7, 5, 3, 2, 1 hPa). Note that some pressure levels are below the local surface height and the values there are given by extrapolations. The analysis data has four base time per day (00, 06, 12 and 18) and a spatial resolution of 0.125° by 0.125°, which is a much higher spatial resolution when compared with previous global weather models (e.g., the spatial resolution of ERA-Interim re-analysis products is 1.125°).

Thus given an HRES-ECMWF model, it is possible to derive a model LOS tropospheric delay for a given time, and its high resolution could be beneficial for describing smaller-scale variation in tropospheric delays.

2.3 An elastic half-space model for interseismic deformation modelling

In the elastic half-space model (Savage and Burford, 1973), the upper crust is locked during the interseismic period (Fig. 2.2), whereas the dislocation slip, S, continues steadily on a narrow fault plane below the locking depth, d_1. The locked part respond elastically to the screw dislocation beneath and the strike-slip displacement is reflected as the long wavelength signals at the surface as

$$v_p = \frac{S}{\pi} arctan(\frac{x+l}{d_1}) + a \tag{2.6}$$

where v_p is the fault parallel velocities, x is the perpendicular distance to the fault trace, l is the horizontal shift between the fault trace and buried dislocation and a is a static offset.

To account for possible fault creep during the interseismic period (Fig. 2.2), a short wavelength signal is incorporated into the Eq. 2.6 to represent the creep. Using a back slip algorithm (e.g., Hussain et al., 2016b; Savage, 1983), the fault creep that occurs at the uppermost part between the surface and the creep depth, d_2, can be modelled as the sum of creep at a rate, C, on the whole fault plane plus a screw dislocation in the opposite sense to the fault motion below the creep depth as

$$\begin{aligned} v_p &= \frac{S}{\pi} arctan(\frac{x+l}{d_1}) \\ -C(\frac{1}{\pi} arctan(\frac{x+l}{d_2}) &- H(x+l)) + a \\ where \quad H(x+l) &= \begin{cases} 1 & \text{if x+l} \geq 0 \\ 0 & \text{if x+l} < 0 \end{cases} \end{aligned} \tag{2.7}$$

where $H(x)$ is the Heaviside function.

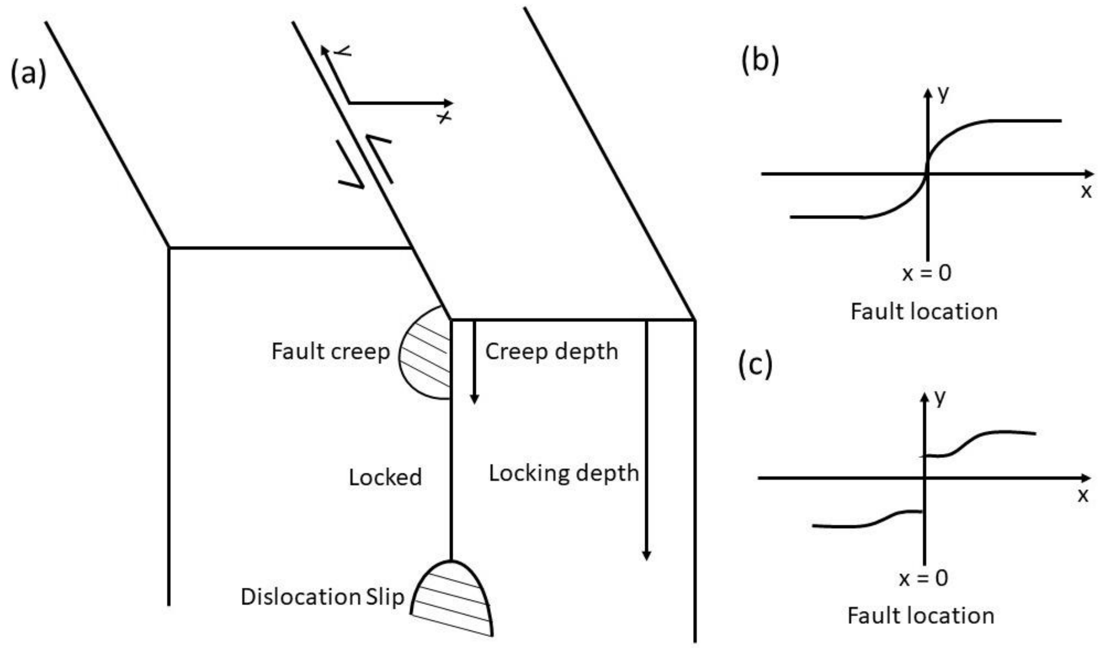

Figure 2.2: (a) A schematic of the elastic dislocation model for the interseismic deformation modelling. (b) Strike-slip displacement at the surface. (c) Strike-slip displacement plus creeping displacement at the surface.

2.4 An elastic dislocation model for coseismic deformation modelling

In coseismic deformation modelling, the dislocation, which is considered as a 2-D manifold with vector fields that represent motions on it (Van Zwieten et al., 2013), is often used for quantitative analyses of the elastic response to earthquakes (Steketee, 1958). Based on the dislocation theory, Okada (1992) proposed analytical expressions to model the surface displacement by providing solutions for surface displacements caused by rectangular dislocations in an elastic half-space.

Following up Chinnery (1961), which used a vertical rectangular dislocation to characterize a pure strike-slip earthquake, Okada (1992) presented a complete set of solutions for finite rectangular sources at arbitrary depth and dip angle in a homogeneous half-space, which is a good first-order approximation of reality. Illustrating by figure 2.3, nine parameters are incorporated to characterize the dislocation's geometry, including two horizontal coordinates of the centre of the upper edge, orientation angle, dip angle, length, width, depth and two components of the slip vector (strike-slip and dip-slip). Due to the linearity of the homogeneous half-space, multiple sources can be incorporated to characterize the spatial variation of a rupture. The inverted distributed slip using the solution is discontinuous, and the geometrical continuity of a curved dislocation is lost as the actual geometry is approximately represented by planes in rectangular shapes. As the equations of the solution are lengthy, I refer the reader to Okada (1985) and Okada (1992) for more details, with codes written by Peter Cervelli (Cervelli, 2000).

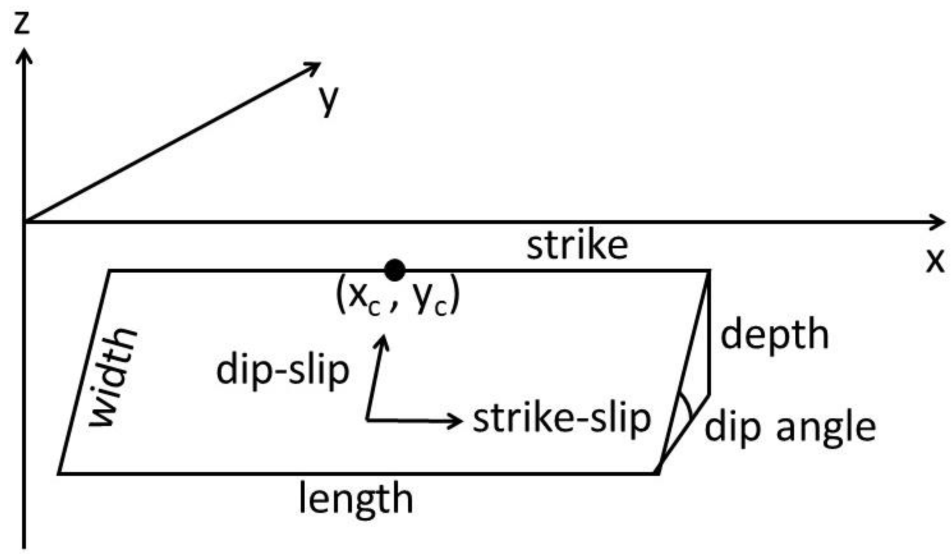

Figure 2.3: A schematic of the Okada model for the coseismic deformation modelling.

2.5 A Bayseian Markov chain Monte Carlo approach

A Bayesian approach provides a posterior probability density function (PDF) of each model parameter given observed data and prior information. The posterior PDF forms the basis for statistical inference, such as point estimates (e.g., mean and median). An optimal set of source parameters can also be extracted from the posterior PDF by finding the maximum a posteriori (MAP) probability solution.

The Bayesian method can sample the PDF through a Markov chain Monte Carlo (MCMC) scheme. In each iteration of the MCMC, the algorithm draws a random walk step from a uniform prior PDF and then scales this step by an optimized maximum step (different for each parameter), defined by an automatic step size selection process (Bagnardi and Hooper, 2018), to ensure an appropriate acceptance/rejection ratio for all parameters. The optimized maximum step is estimated in the first phase of the inversion, and should balance the speed of convergence and the possibility of escaping local maxima. The likelihood $p(\mathbf{d}|\mathbf{m})$ of the model parameter vector $\mathbf{m}$, given data vector $\mathbf{d}$, at each iteration is:

$$p(\mathbf{d}|\mathbf{m}) = \exp(-\frac{1}{2}(\mathbf{d} - \mathbf{G_m})^T \mathbf{\Sigma_d}^{-1}(\mathbf{d} - \mathbf{G_m})); \tag{2.8}$$

where $\mathbf{\Sigma_d}$ is the data covariance matrix, and $\mathbf{G_m}$ is the model function. The new likelihood is compared to the likelihood of the previous solution using the Metropolis-Hastings algorithm (Hastings, 1970; Metropolis et al., 1953) to determine whether the new trial should be accepted or rejected. While the model parameter vector is updated during the MCMC iterations, the inversion scheme populates the posterior PDF.

Chapter 3

A spatially varying scaling method for InSAR tropospheric corrections using a high resolution weather model

This chapter addresses the first objective of the thesis, by presenting a new empirical method for InSAR tropospheric corrections using high-resolution weather model products. I apply this novel method to reduce InSAR tropospheric delays in different aspects of seismic hazard and use it to improve the retrieval of interseismic deformation signals along the Altyn Tagh Fault in Chapter 4. The work in this chapter has mostly been published (Shen et al., 2019), except for the application to Taal Volcano, which is more recent work.

3.1 Introduction

Interferometric Synthetic Aperture Radar (InSAR) is used to measure ground deformation such as interseismic slip (e.g., Fialko, 2006; Hussain et al., 2016a; Jolivet et al., 2008; Walters et al., 2013; Wei et al., 2010), earthquake deformation (e.g., Ainscoe et al., 2017; Delouis et al., 2010; Hamling et al., 2017; Lindsey et al., 2015), volcanic dike intrusions (e.g., Sigmundsson et al., 2015), landslides (e.g., Yin et al., 2010) and urban subsidence (e.g., Chaussard et al., 2014; Perissin and Wang, 2011). The recently launched Sentinel-1 constellation can achieve high spatial resolution and short revisit times with a wide spatial coverage, which has improved the coherence of interferograms and so increased the potential of precise and large-scale InSAR studies of tectonic processes (Elliott et al., 2016). However, variation in the phase delay, caused by the spatiotemporal variability of tropospheric properties, is still a major limiting factor in Sentinel-1 InSAR measurements (Parker et al., 2015), particularly when deriving long wavelength deformation signals that are partially correlated with topography.

As I summarise in Chapter 1, numerous approaches have been tried to mitigate the tropospheric effects, whereas each of the approaches has limitations. In this chapter, I describe a new approach for InSAR tropospheric corrections to address the limitations of using either approach individually. I validate the new method using simulated data and demonstrate that both coseismic and interseismic signals can be separated from strong tropospheric delays. I also apply the algorithm to the central portion of the Altyn Tagh Fault in northern Tibet, where deformation correlates strongly with topographic relief of 6000 m, and show that the derived velocity field is more internally consistent and agrees better with independent GPS measurements.

3.2 Spatially varying scaling method

As I describe in Chapter 2, it is possible to derive a model LOS tropospheric delay for a given time, given an HRES-ECMWF model. I use the approach of the triangle-based linear interpolation in space and linear interpolation in time to interpolate the weather model to every pixel of the master image and every acquisition time. I assume that vertical refractivity profiles calculated from a high-resolution weather model data can generally describe the form of the relationship between tropospheric delay and height, but that the magnitude can be incorrect. With a much higher spatial resolution, interferograms are more sensitive to the spatial variability in tropospheric properties. Therefore, I estimate a magnitude correction by scaling the original tropospheric delays estimated from the weather model to best match the interferometric phase.

3.2.1 Phase delay anomaly

As the interferometric phase represents the difference in signal delay, it is only sensitive to the variability of the tropospheric delay with time, and not the overall magnitude of the tropospheric delay. It is therefore the difference from the mean tropospheric delay that I aim to scale, where the mean delay is the average tropospheric delay in time for any given height (Fig. 3.1a). For all epochs, I derive this difference from the mean phase delay, which I term the phase delay "anomaly", using a minimum norm inversion, noting that there can be contributions other than the tropospheric delay in the resulting single epoch phase:

$$\delta\Phi_{InSAR} = G^T(GG^T)^{-1}\Phi_{InSAR} \tag{3.1}$$

where Φ_{InSAR} is the vector of interferometric phase delays for a single pixel, $\delta\Phi_{InSAR}$ the vector of estimated phase delay anomalies for every epoch, and G is the design matrix relating the relevant observation epochs for each interferogram. Note that throughout this manuscript, I use the term "phase delay anomaly" to refer to the portion of the interferometric phase allocated to a single epoch, whereas "phase delay" alone indicates the phase delay between two epochs. I incorporate only small baseline interferograms so as to minimise any decorrelation noise and contributions from deformation. The regularisation of the minimum norm inversion of the interferograms will introduce smearing of the phase between epochs, due to imperfect resolution. To give the same smearing, I derive the single epoch anomalies from the weather model in the same way, by first calculating estimates of the phase delay for each interferogram from the single epoch delays, and then inverting these using the minimum norm approach as

$$\delta\hat{\Phi}_{tropo} = G^T(GG^T)^{-1}\hat{\Phi}_{tropo} \tag{3.2}$$

where $\hat{\Phi}_{tropo}$ is the vector of tropospheric phase delays for a single pixel in each interferogram, derived from the weather model, and $\delta\hat{\Phi}_{tropo}$ is the vector of estimated phase delay anomalies for every epoch.

I assume that

$$\delta\Phi_{tropo}(x, y, h) \approx K(x, y)\delta\hat{\Phi}_{tropo}(x, y, h) \tag{3.3}$$

where $\delta\Phi_{tropo}(x, y, h)$ is the actual tropospheric phase delay anomaly, and $K(x, y)$ is a spatially-varying scaling factor that is spatially smooth. I estimate values for $K(x, y)$ empirically using the single epoch phase delay anomalies derived from the interferograms, on the assumption that other interferometric components such as tectonic deformation, DEM errors and other sources of noise are not correlated with the scaled weather model phase anomalies.

3.2.2 Estimation of scaling factors

For each epoch, I divide the image into smaller windows and estimate the scaling factor, K, for each window. Because these single epoch phase maps ($\delta\Phi_{InSAR}$) are relative to a local spatial reference, I cannot substitute them directly for $\delta\Phi_{tropo}(x, y, h)$ in Eq. 5, but must include the unknown phase of the reference point. I estimate this reference independently for each patch, which has the effect of ignoring correlations between the InSAR and weather model anomalies at long spatial wavelengths. Whilst using the correlation at long wavelengths could potentially improve the accuracy of the scaling, the long wavelength signals are often contaminated by non-tropospheric errors from the ionosphere and orbital inaccuracy, which can bias the estimation.

For each patch I have

$$\delta\Phi^n_{InSAR} = K_n\delta\hat{\Phi}^n_{tropo} + C_n \quad (n \in \mathbb{N}) \tag{3.4}$$

where K_n and C_n are the scaling factor and the constant shift for the patch n that I estimate using least squares. To ensure a sufficient number of scatterers for the inversion, I set the square window size as 50 km (Fig. 3.2a). However, as I smooth the scaling factor spatially in the next step, the final result is not strongly dependent on the choice of window size. Fig. 3.2c shows the estimated scaling factors for a representative single epoch.

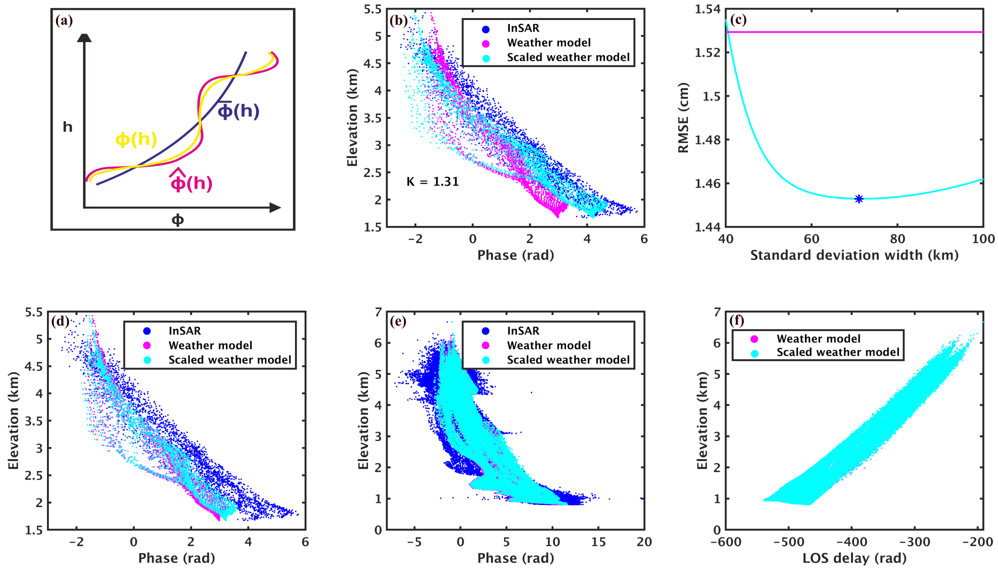

Figure 3.1: (a) an interpretive cartoon showing how the scaling operates. The blue curve represents the mean tropospheric delay for any given height. The magenta curve is the estimated tropospheric delay for a single acquisition time, and the yellow curve shows the same delay after scaling. Note that it is only the difference between the magenta and blue curves that is scaled. (b) shows the comparison between the weather model phase delay anomalies and the InSAR phase delay anomalies for the red patch in Fig. 3.2a before and after scaling using the scaling factor estimated for the whole patch. (c) shows the RMSE variation between the scaled weather model phase delay anomalies (cyan curve) and the tropospheric phase delay anomalies estimated from two continuous GPS stations in Fig. 3.3 when varying the standard deviation width of the Gaussian filter used for the scaling factor smoothing. The blue star indicates the optimal value of the standard deviation, which is 71 km and the corresponding RMSE is 1.45 cm. The magenta line represents the RMSE between the non-scaled weather model phase delay anomalies and the GPS anomalies, which is 1.53 cm. (d) shows the comparison between the weather model phase delay anomalies and the InSAR phase delay anomalies for the red patch in Fig. 3.2a before and after scaling using the smoothed scaling factor. (e) indicates the comparison between the InSAR phase delay anomalies and the weather model phase delay anomalies over the whole image. (f) shows the weather model delays in the LOS direction over the whole image before and after scaling.

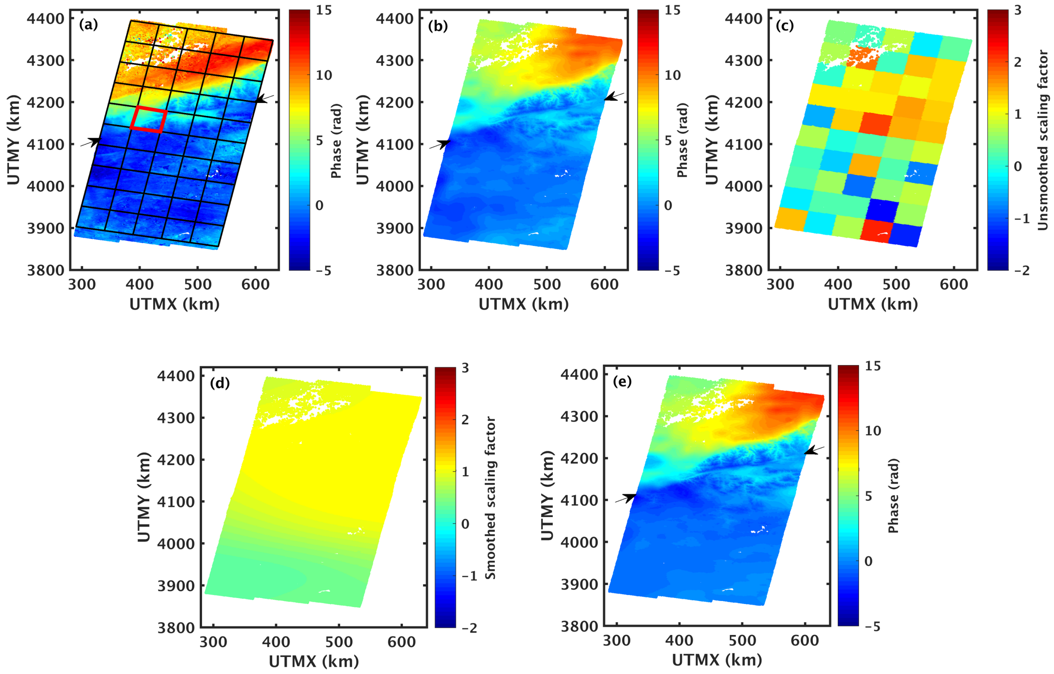

Figure 3.2: Example results of the scaling method applied to the testing area across the Altyn Tagh Fault. (a) and (b) are, respectively, the InSAR phase delay anomalies and weather model tropospheric phase delay anomalies, estimated using the minimum norm approach for a typical epoch, that of 17 May 2016. The black arrows indicate the fault orientation. The overlapped grid in (a) is rotated to the heading direction of the satellite, and each patch is completely within the SAR area so as to make sure the number of points in each patch is similar. (c) shows the scaling factors of all patches. (d) shows the spatial pattern of the spatially-varying smoothed scaling factors. (e) shows the scaled tropospheric phase delay anomalies.

3.2.3 Scaling factor smoothing

The accuracy of the estimated scaling factor depends on the signal-to-noise ratio of the weather model anomalies. Therefore, I define a variance ratio to weight each patch as

$$W_{var}^{n} = \frac{\sigma_{tropo}^{2}(n)}{\sigma_{res}^{2}(n)} \quad (n \in \mathbb{N}) \tag{3.5}$$

where $\sigma_{tropo}^{2}(n)$ is the variance of the weather model delay anomalies in the patch n, representing the signal, and $\sigma_{res}^{2}(n)$ is the variance of the differences between the weather model delay anomalies and the InSAR phase delay anomalies in the patch n, representing the noise. For $\sigma^2_{res}(n)$, I also tried using the variance of the difference after scaling of the weather model, but this led to an increase in the mean velocity standard deviation from 2.6 mm/yr to 3.4 mm/yr.

As the scaling is expected to vary spatially, I also estimate a distance weight for each pixel using a Gaussian filter as

$$W^n_{dis}(x,y) = \frac{1}{2\pi\sigma_d^2} \exp^{-\frac{(x-X_n)^2+(y-Y_n)^2}{2\sigma_d^2}} \quad (n \in \mathbb{N}) \tag{3.6}$$

where (X_n, Y_n) is the central coordinate of the window n and σ_d is the standard deviation width of the Gaussian filter. I then determine a scaling factor for each pixel as

$$K(x,y) = \sum_{n=1}^{N} \{K_n \cdot W^n_{var} \cdot W^n_{dis}(x,y)\} \quad (n \in \mathbb{N}) \tag{3.7}$$

Since the spatial pattern of the smoothed scaling factors is strongly dependent upon the Gaussian smoothing width σ_d, I optimise it using the tropospheric delays estimated from two continuous GPS stations (Fig. 3.3). The total zenith tropospheric delay (ZTD) was processed with the GAMIT software (Liang et al., 2013), which parametrises the ZTD for each station as a stochastic variation from the Saastamoinen model, with a piecewise-linear function over the span of the observations (Herring et al., 2015). Taking the 2-hourly estimates of the ZTD, I estimate the delay at each SAR acquisition time using spline interpolation and transform into LOS delay. I then difference the single epoch values to give the delay for each interferogram time span, and invert using the minimum norm approach to give anomaly values for each epoch (Table A.1). I scale the tropospheric delay anomalies estimated from the HRES-ECMWF data using different values for σ_d and compare these to the delay anomalies derived from the GPS data. Note that in the comparison, I select a continuous GPS station as the reference point and so the comparison is based on the relative tropospheric delay. The optimal σ_d is chosen as the value with a minimum Root Mean Square (RMS) difference (Fig. 3.1c). For regions without any continuous GPS stations, it will not be possible to estimate the optimal Gaussian smoothing width. However, the RMSE between the weather model and the GPS measurements varies little when the smoothing width changes over a broad range between 50 km to 100 km, so using a default value of 71 km is likely to be fine in most cases. Fig. 3.1b and Fig. 3.1d show the scaled results for the red patch in Fig. 3.2a before and after smoothing of the scaling factor. Although the scaling factors estimated for a single patch can have large errors with absolute values much greater than one (Fig. 3.2c), these patches are down-weighted in the smoothing process, leading to smoothed factors close to one (Fig. 3.2d).

Using the smoothed spatially-varying scaling factors, I scale the tropospheric phase delay anomalies estimated from the HRES-ECMWF for each epoch (Fig. 3.2e) and calculate the scaled interferometric tropospheric delays from these. The scaled tropospheric phase delay anomalies are more consistent with the InSAR phase delay anomalies (Fig. 3.1e), as is to be expected. As the scaling is implemented on the tropospheric phase delay anomalies, the absolute change to the total weather model delay resulting from the scaling is small (Fig. 3.1f). In the next section, I test how robust the approach is in the presence of tectonic deformation.

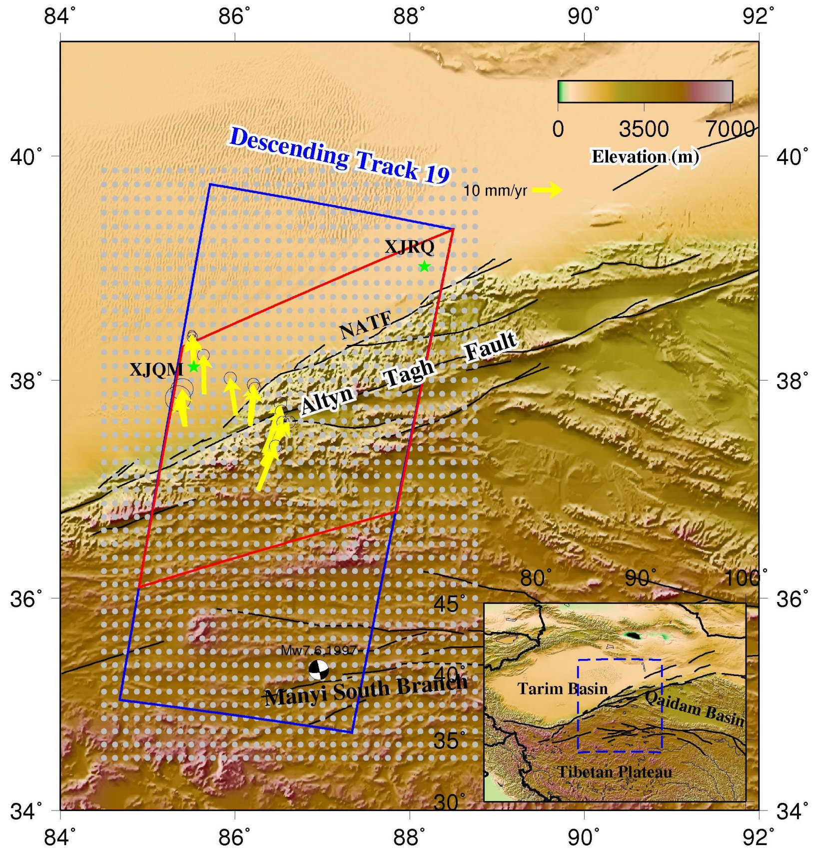

Figure 3.3: Map of the scaling method study region over the Altyn Tagh Fault zone, Tibet. The blue rectangle represents the extent of SAR data coverage. Grey dots indicate the HRES-ECMWF points used for tropospheric delay corrections of which the spatial resolution is 16 km. Green stars show the location of the only two available continuous GPS stations within the SAR image area (Liang et al., 2013). Yellow arrows indicate velocities of available campaign GPS stations near the fault within the InSAR area (He et al., 2013a; Liang et al., 2013). All of the GPS velocities are within the Eurasia reference frame, with uncertainties plotted at 95% confidence level. The red parallelogram indicates the outline of deforming region that I mask out before estimating phase ramps. The background shows the elevation of the study region derived from the Shuttle Radar Topography Mission (SRTM) 3-arc seconds data (Farr et al., 2007), which is also applied to the subsequent figures.

3.3 Simulated test cases

To test the ability of the method to separate deformation from tropospheric signals, I simulate a sub-vertical, strike-slip (M_w 6.7) earthquake (details in Table 3.1) on the northern strand of the Altyn Tagh Fault in Northern Tibet (Fig. 3.3), a region that is strongly contaminated by the variation in tropospheric delay across the step in relief. I choose a sub-vertical, strike-slip earthquake because the Altyn Tagh fault is of this type. I determine the depth of rupture based on the previous measurements for the locking depth of the fault (Elliott et al., 2008; He et al., 2013a). I set the earthquake magnitude to be sufficiently large that the spatial coverage of the simulated signal would be larger than the applied Gaussian smoothing size. I add an example of real noise to the simulated deformation, including tropospheric signal, as described in the following paragraph.

Table 3.1: Parameters of the simulated earthquake used.

Parameter	**Value**
Fault centre	87.3°E, 38.3°N
Magnitude (M_w)	6.7
Strike	66°
Top depth	2 km
Dip	60°
Bottom depth	15 km
Rake	0°
Slip	1 m
Length	25 km
LOS vector unit (E, N, U)	[0.6557, -0.1147, 0.7447]

Based on the work flow of InSAR processing that I describe in Chapter 2, I process 19 SAR images acquired by Sentinel-1 on descending track 19 between October 2014 and September 2016, and generate 53 small baseline interferograms. I then solve for InSAR phase delay anomalies for each epoch using the minimum norm approach with the small baseline interferograms(Fig. A.2). I add the simulated earthquake signal (Fig. 3.4a) to the InSAR phase delay anomaly for the 14 September 2016 and then generate a 24 day interferogram with the InSAR phase delay anomaly at the epoch 21 August 2016 (Fig. 3.4b). I select this interferometric pair because it is strongly influenced by tropospheric delays and the short interval of the interferometric plane limits contamination from any real interseismic tectonic deformation.

Table 3.2: InSAR Processing Parameters.

InSAR Processing		**Small Baseline Analysis**	
Parameter	**Value**	**Parameter**	**Value**
Wavelength	0.0555 m	Number of patches	27
SRTM DEM	90 m	Unwrap grid size	1200 m
Multilook factor	20×4	Merge resample size	1000 m
		Merge σ	1 rad

I process the HRES-ECMWF pressure level data using the Toolbox for Reducing Atmospheric InSAR Noise (TRAIN version 1) (Bekaert et al., 2015b). HRES-ECMWF has a spatial resolution of 16 km, at 6h intervals and provides parameters of temperature, pressure, relative humidity and geopotential on 25 pressure levels. Within the TRAIN software, the HRES-ECMWF integrated refractivity is linearly interpolated to match the SAR acquisition time. Fig. A.3 shows the estimated tropospheric phase delay anomalies for the two selected epochs. I then use the InSAR phase delay anomalies associated with the simulated interferogram to scale the weather model anomalies using a 50 km by 50 km grid. The simulated earthquake signal above 2 mm covers 27 of 50 square patches in total (Fig. 3.4a) and so the spatial coverage is much larger than the applied Gaussian smoothing size, which is 71 km. Finally, as the real interferometric phase that I added will also include long wavelength errors due to ionospheric signal and orbital inaccuracy, I estimate a phase ramp from the non-deforming region shown in Fig. 3.3, and subtract it.

Fig. 3.4c shows the results after correction using the original HRES-ECMWF. Much of the noise has been reduced when compared to Fig. 3.4b. However, when using the scaled tropospheric delays, shown in Fig. 3.4d, the noise is reduced still further, with the RMSE between the corrected signal and the deformation signal alone dropping from 1.9 to 0.8 radians. Importantly, the scaling estimation process does not result in an obvious reduction of the deformation signal.

As the magnitude and spatial extent of interseismic slip are very different to coseismic motion, I also simulate 10 mm left-lateral strike-slip motion from 15 km downwards along the central branch of the Altyn Tagh Fault, and add it to the same 24 day interferogram (Fig. 3.5). This simulation approximates a 1 year interferogram with a slip rate of 10 mm/yr. Although the corrected results are not as clean as in the seismic case, due to the lower magnitude of the signal, the isolation of deformation shows a marked improvement over the unscaled case with the RMSE between the corrected signal and the deformation signal alone dropping from 1.8 to 0.6 radians.

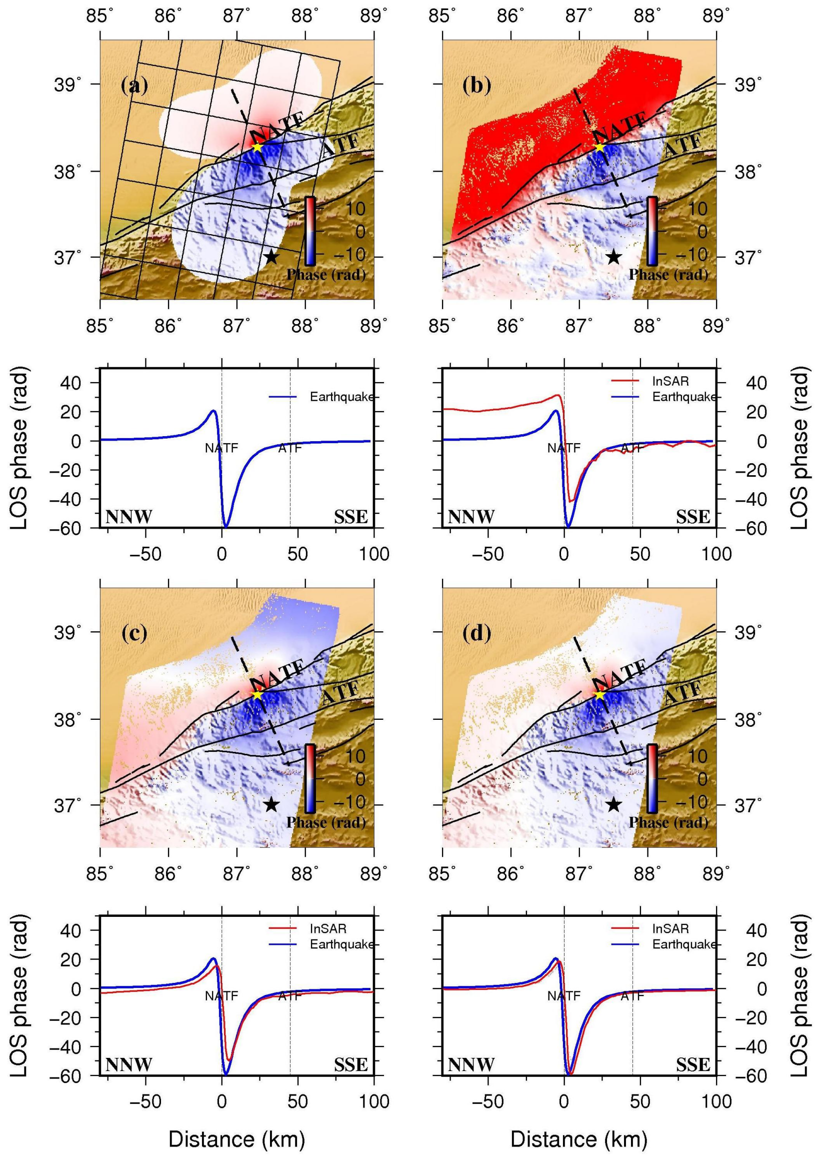

Figure 3.4: Tropospheric correction results for a 24 day interferogram to which deformation from a simulated earthquake has been added: (a) the simulated earthquake signal and the grid of windows used for calculating the scaling factor, K; (b) the uncorrected interferogram; (c) the interferogram corrected using the original HRES-ECMWF and with an estimated phase ramp subtracted; (d) the interferogram corrected with the scaled tropospheric delays from HRES-ECMWF and with an estimated phase ramp subtracted. For each panel, positive values indicate motion away from the satellite. The red lines in the panels below indicate the interferometric phase along the black dashed profile. The blue lines represent the simulated earthquake signals. The fault centre (yellow star) is at the 0 km profile distance. The black star indicates the InSAR reference point.

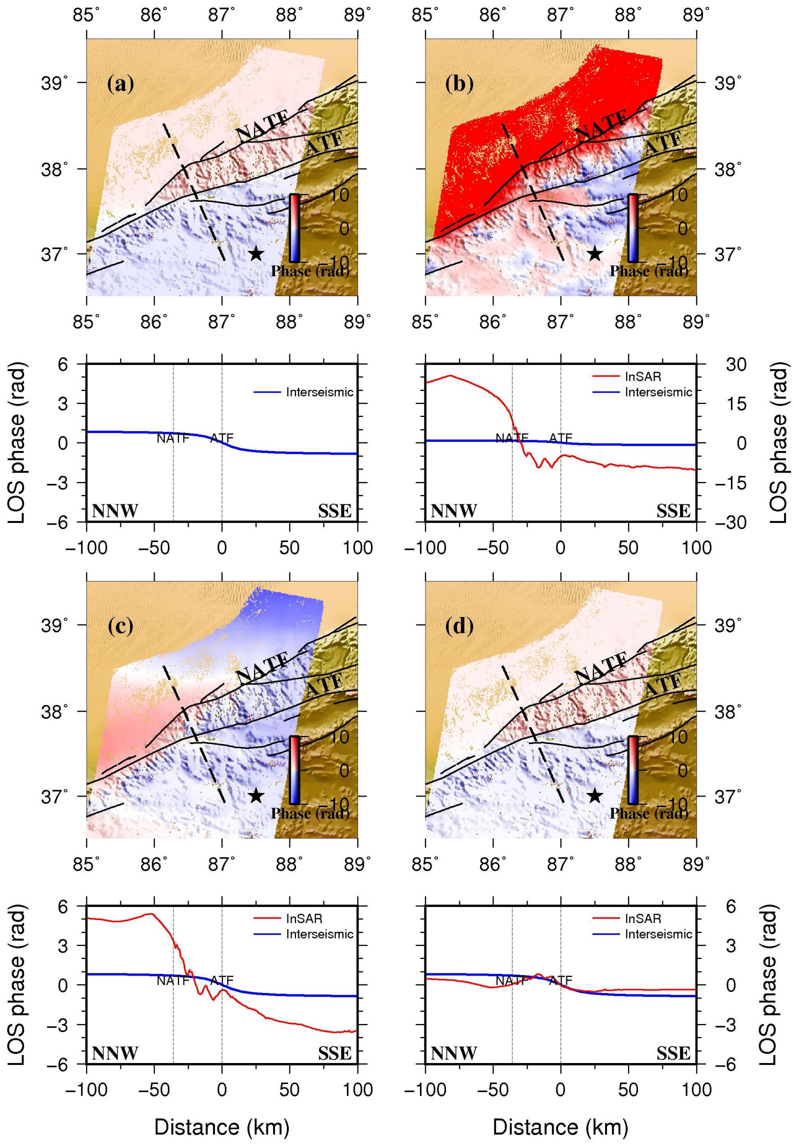

Figure 3.5: Tropospheric correction results for a 24 day interferogram to which deformation from a simulated interseismic signal has been added: (a) the simulated interseismic deformation signal. (b) the uncorrected interferogram; (c) the interferogram corrected with the original HRES-ECMWF and with an estimated phase ramp subtracted; (d) the interferogram corrected with the scaled tropospheric delays and with an estimated phase ramp subtracted. For each panel, positive values indicate motion away from the satellite. The red lines in the panels below indicate the interferometric phase along the black dashed profile. The blue line represents the simulated interseismic signals. The fault dislocation is at 0 km distance. The black star indicates the InSAR reference point.

3.4 Case study: central portion of the Altyn Tagh Fault, Tibet

To test the algorithm on real data, I apply the scaling method to interferograms over the central portion of the Altyn Tagh Fault (Fig. 3.3). The Altyn Tagh Fault is one of the major tectonic structures in northern Tibet, and accurate determination of its slip rate has significant implications for the interpretation of tectonic processes across the Tibetan Plateau region (Searle et al., 2011; Tapponnier et al., 2001). However, as the fault is located at the border between the low Tarim Basin and the high Tibetan Plateau, the interseismic deformation signals are strongly masked by the tropospheric delays resulting from the 6000 m topographic relief across it.

From the 19 SAR images that I processed (Fig. A.3), I select three epochs that are strongly influenced by the tropospheric delays as examples to show (Fig. 3.6), which are 31 October 2014, 23 May 2015 and 16 June 2015. The InSAR phase delay anomalies are highly correlated with the topography (Fig. 3.7a, b and c, Fig. A.4), which implies the existence of strong tropospheric delays. I estimate the smoothed spatially-varying scaling factor for every epoch (Fig. 3.6g, h and i, Fig. A.5) and then scaled the original weather model anomalies (Fig. 3.6j, k and l, Fig. A.6). After removing the scaled tropospheric delay anomalies from the InSAR phase delay anomalies in each epoch, the phase no longer has strong correlations with the topography (Fig. A.7, Fig. 3.7d, e and f). Although I deliberately omit the long wavelength component during the estimation of the scaling factors, this does not prevent the application of the scaling from resulting in a gradient in the tropospheric anomalies. Therefore, the long wavelength differences between InSAR phase delay anomalies and the scaled tropospheric phase delay anomalies suggests that non-tropospheric long wavelength signal exists in the InSAR data.

To investigate whether the scaled weather anomalies are simply mimicking the InSAR phase delay anomalies, I calculate the correlation coefficient between the InSAR phase delay anomaly and the scaled weather model anomaly for each epoch and compare them to the correlation coefficient between the weather model anomaly and scaled weather model anomaly. The results (Fig. A.8) show that the scaled weather model data are more correlated with the original weather model products than the InSAR phase delay anomalies, for 18 of the 19 epochs. Fig. 3.8 also indicates that the general characteristics of the weather model have been kept after the scaling.

I then generate 18 single master interferograms and subtracted the estimated tropospheric delays from each interferogram. For each tropospheric-corrected interferogram, I also subtract a ramp estimated from the non-deforming region (Fig. 3.3). The root-mean-square (RMS) variation of apparent LOS phase in the interferograms corrected using the scaled tropospheric delays drops 38% on average compared with the interferograms corrected using the original estimates derived from the HRES-ECMWF, with RMS drops of 60% on average compared with the uncorrected interferograms (Fig. 3.9).

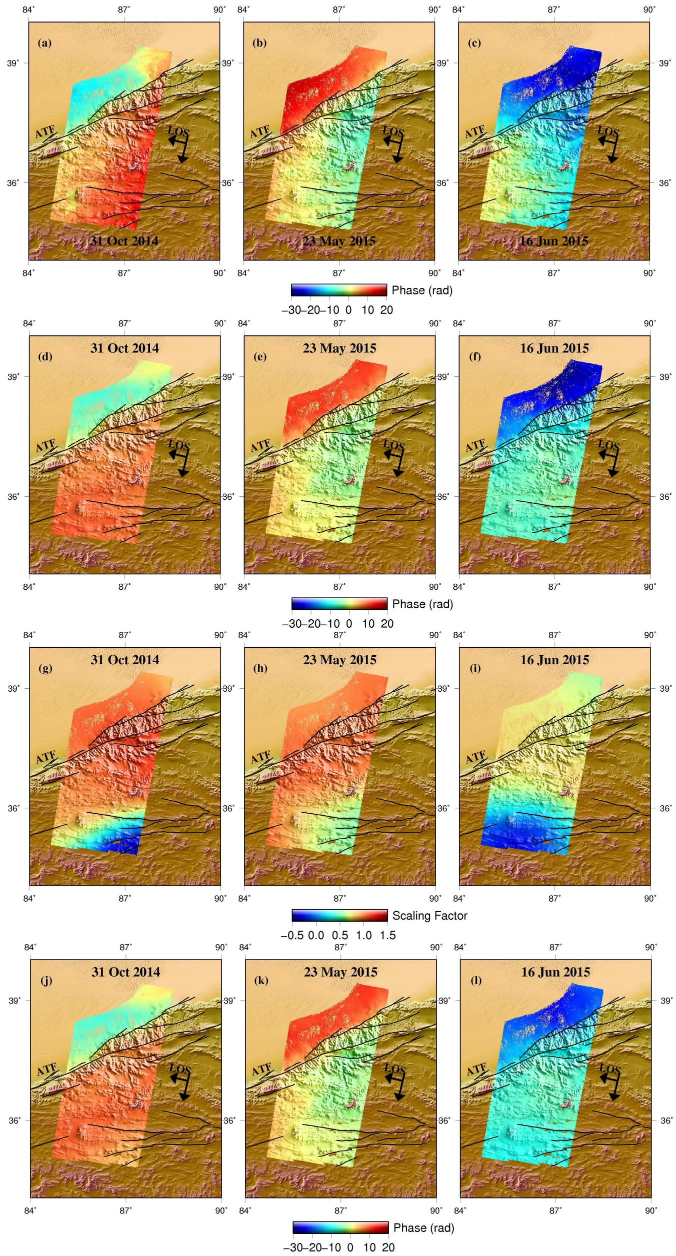

Figure 3.6: (a), (b) and (c) are InSAR phase delay anomalies for three selected epochs, estimated from a small baseline interferogram network using a minimum norm constraint. (d), (e) and (f) are tropospheric phase delay anomalies for the same epochs estimated from HRES-ECMWF using the minimum norm solution. (g), (h) and (i) are the smoothed scaling factor applied to the HRES-ECMWF correction, for the same epochs. (j), (k) and (l) are the scaled tropospheric phase delay anomalies for the same epochs. The phase value in each epoch is referenced to the InSAR phase delay anomaly of the corresponding epoch for the comparison.

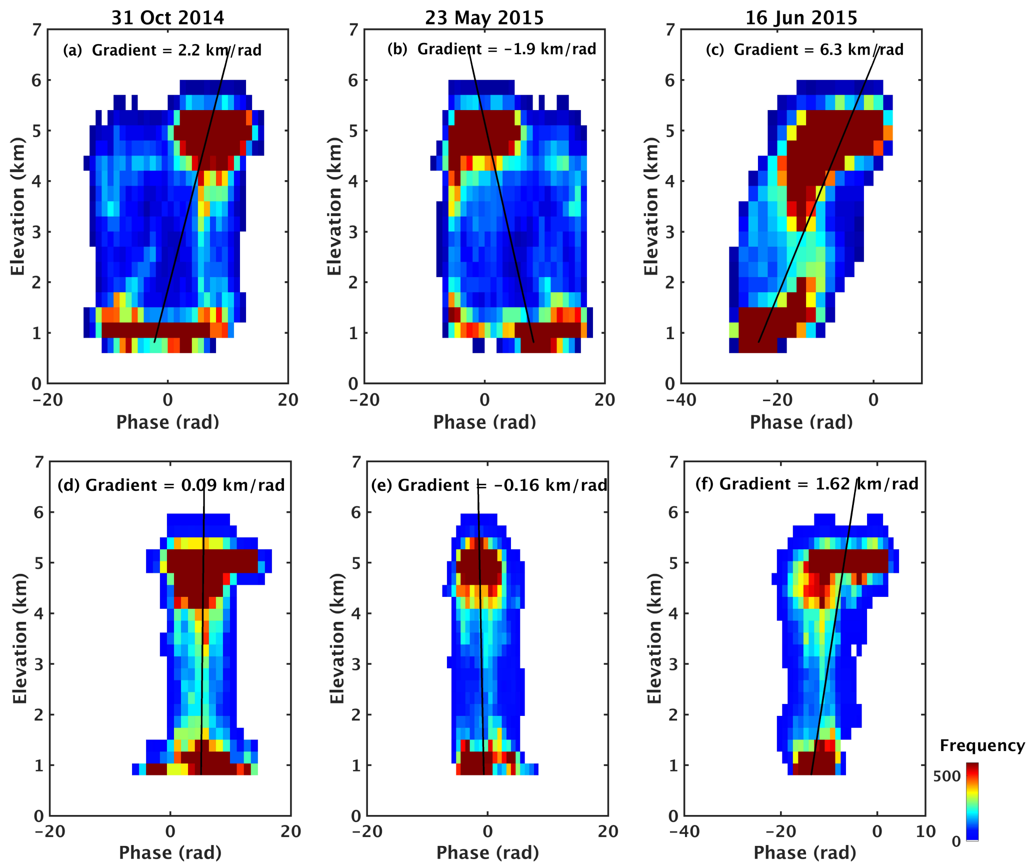

Figure 3.7: Histograms of the InSAR phase delay anomalies versus topography for the same three epochs shown in Fig. 3.6 before (a, b and c) and after (d, e and f) tropospheric corrections with the scaled weather model anomalies. The black lines are the best fitting linear function, shown for reference.

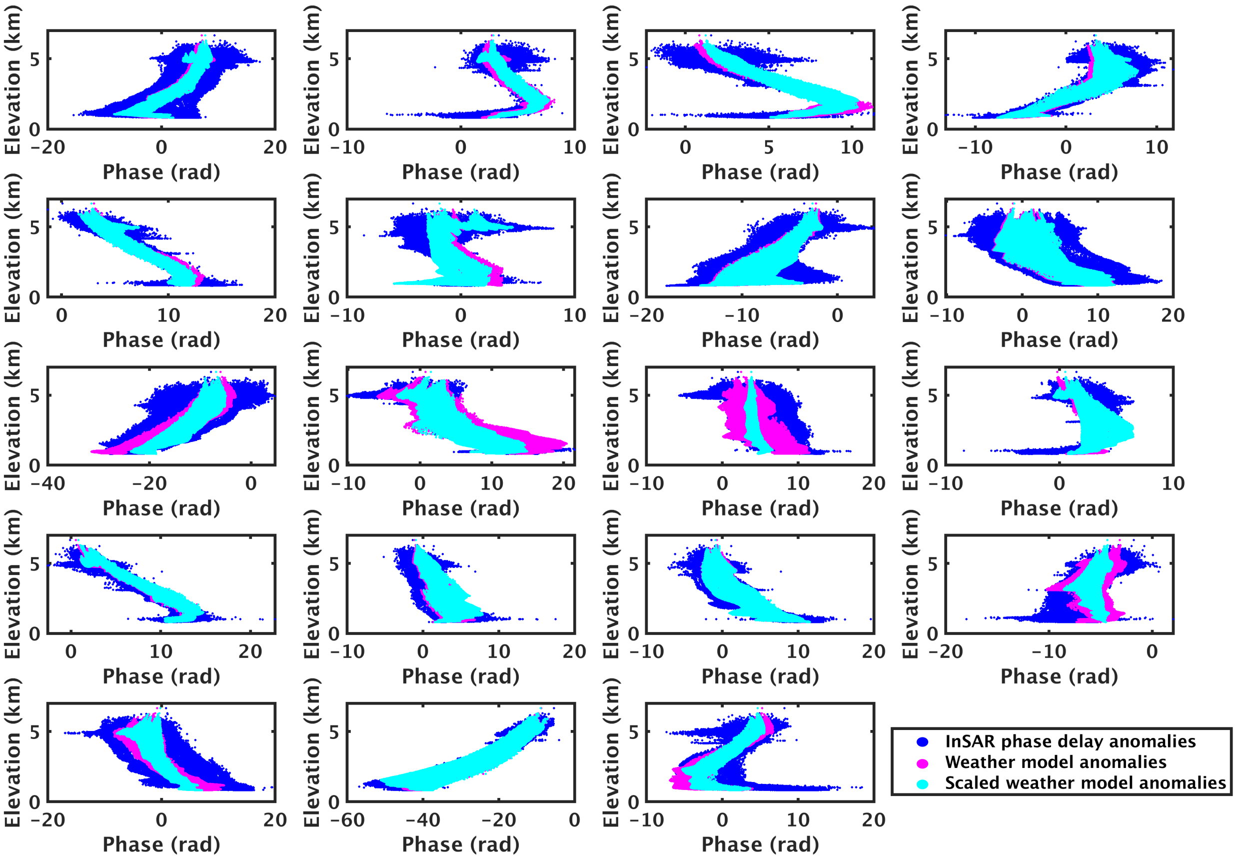

Figure 3.8: Comparisons of the original and scaled weather model phase delay anomalies to the InSAR phase delay anomalies, for each epoch.

Based on the 18 tropospheric corrected and deramped single master interferograms, I calculate LOS velocities using the Best Linear Unbiased Estimator (BLUE) (e.g., Puntanen et al., 2000). I calculate phase variances for each epoch from the variances of the tropospheric corrected and deramped short temporal interferograms by least squares inversion. I then use these variances as the elements on the principal diagonal of the variance-covariance matrix in the BLUE inversion. Off-diagonal elements are set to zero since the noise of each epoch is considered to be independent. The velocity map derived from the interferograms after correction using the scaled tropospheric delays (Fig. 3.10b) is clearly more consistent with left-lateral strike-slip deformation than that corrected using the original tropospheric delays, with motion north of the Altyn Tagh Fault more consistently away from the satellite and motion on the Plateau systematically towards. The mean standard deviation of velocities generated by bootstrapping the signal master time series also drops from 2.9 mm/yr (Fig. 3.10c) to 2.6 mm/yr (Fig. 3.10d).

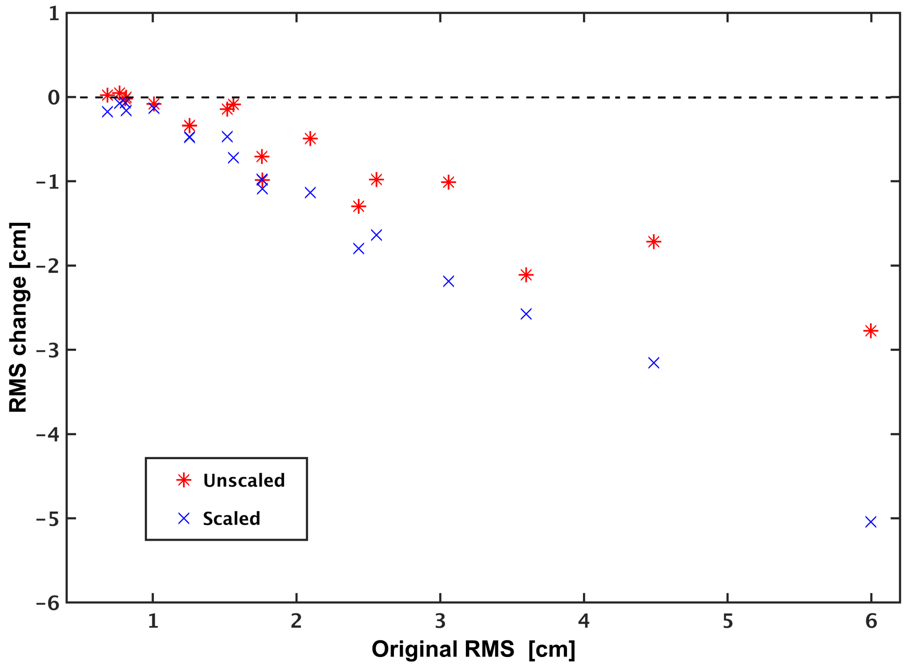

Figure 3.9: RMS comparisons of deramped single master interferograms before and after tropospheric corrections. The RMS of all interferograms reduces after correction with the scaled HRES-ECMWF, even for the two interferograms for which the RMS increases after correction with the original HRES-ECMWF. The master date of the interferograms is 17 November 2015.

As the campaign GPS data are not provided with vertical estimates, I project GPS velocities estimated from measurements made at sites shown in Fig. 3.10 to the LOS direction by assuming vertical deformation is negligible, and then calculate the weighted mean offset from the InSAR results. I then add the offset to the InSAR measurements to tie them to the same reference frame as the GPS data, with Eurasia fixed. I project the referenced InSAR velocities to two profiles, A-A' and B-B', which are perpendicular to the fault strike, within a 30 km width (Fig. 3.10a and b). I use the elastic half-space model that I described in Chapter

2 (Savage and Burford, 1973) to estimate the slip rate and the locking depth for profile A-A' and B-B'. Using the original HRES-ECMWF corrections, I find slip rates of 11.5 ± 1.8 mm/yr and 4.7 ± 1.2 mm/yr and 10.5 ± 3.2 km and 12.2 ± 2.6 km for the locking depth (Fig. 3.11a and b). Errors represent 2σ errors estimated using the percentile bootstrap method (e.g., Efron and Tibshirani, 1994). Using velocities estimated from the interferograms corrected using the scaled HRES-ECMWF, I find slip rates of 12.3 ± 1.5 mm/yr and 9.0 ± 1.3 mm/yr, and the locking depth of 10.0 ± 2.3 km and 11.2 ± 2.6 km (Fig. 3.11c and d), which are more consistent with the previous modelling of GPS measurements around this region, giving a slip rate of $9.0^{-3.2}/_{+4.4}$ mm/yr (He et al., 2013b).

I calculate the time series of relative LOS displacement between two points located 200 km apart, either side of the Altyn Tagh Fault along profile A-A' and B-B' respectively, from the interferograms corrected using both the original and the scaled tropospheric delays (Fig. 3.11e and f). Both time series show less scatter after scaling imply that the tropospheric delays have been reduced. The left-lateral strike-slip deformation across the fault also becomes apparent for the time series along the profile B-B', where the scaling has more impact. Comparing the InSAR estimates to the independent GPS measurements (He et al., 2013a; Liang et al., 2013), the RMS misfit drops from 3.0 mm/yr to 1.9 mm/yr with application of the additional scaling correction (Fig. 3.11g).

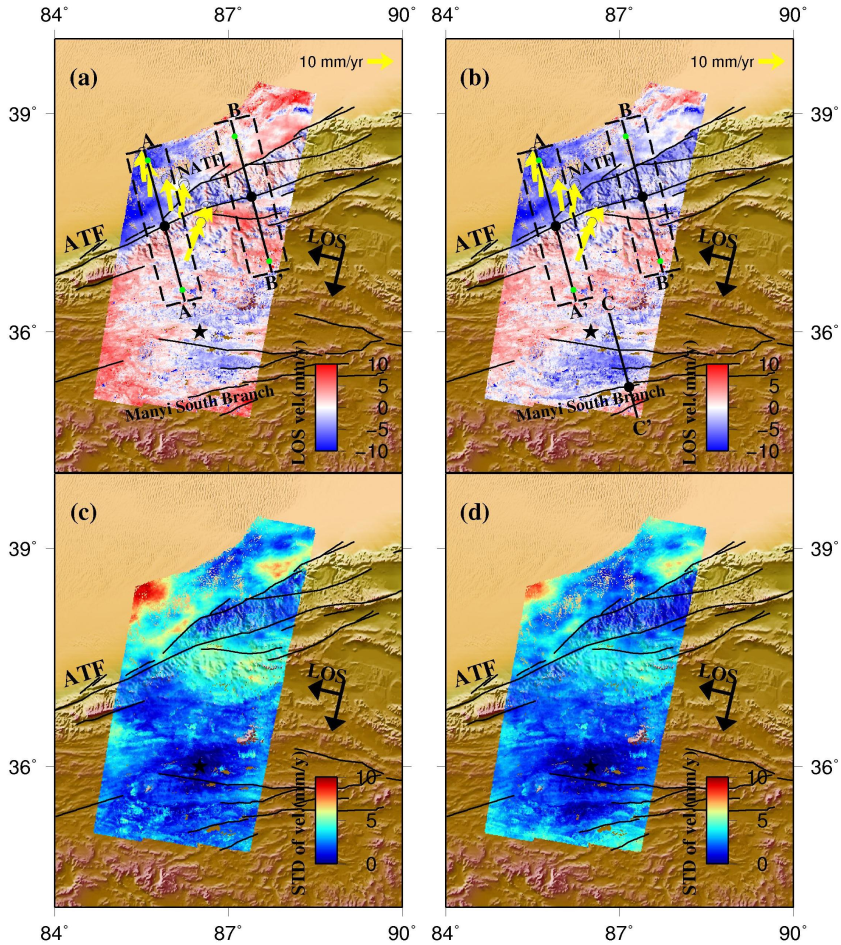

Figure 3.10: LOS annual velocity maps derived from the single master interferograms corrected with a, the original and b, the scaled tropospheric delays, and their respective standard deviations (c and d) estimated by the percentile bootstrapping technique (e.g., Efron and Tibshirani, 1994). Incoherent scatterers in the northern sandy area were masked out. Positive values indicate motion towards the satellite and negative values indicate motion away from the satellite relative to the reference region (black star). Black lines A-A' and B-B' represent profiles which are perpendicular to the strike of the Altyn Tagh Fault with the centre of 85.9°E, 37.5°N, 87.4°E, 37.9°N respectively and a 120 km extension of each side of the fault. The black dash line indicates the extent of the velocity projection (swath wides 30 km). Black line C-C' represents profile which is perpendicular to the Manyi south branch. Yellow arrows show velocities of available campaign GPS stations near the fault within the InSAR area (He et al., 2013a; Liang et al., 2013), which are in a Eurasia reference frame with uncertainties plotted at 95% confidence level.

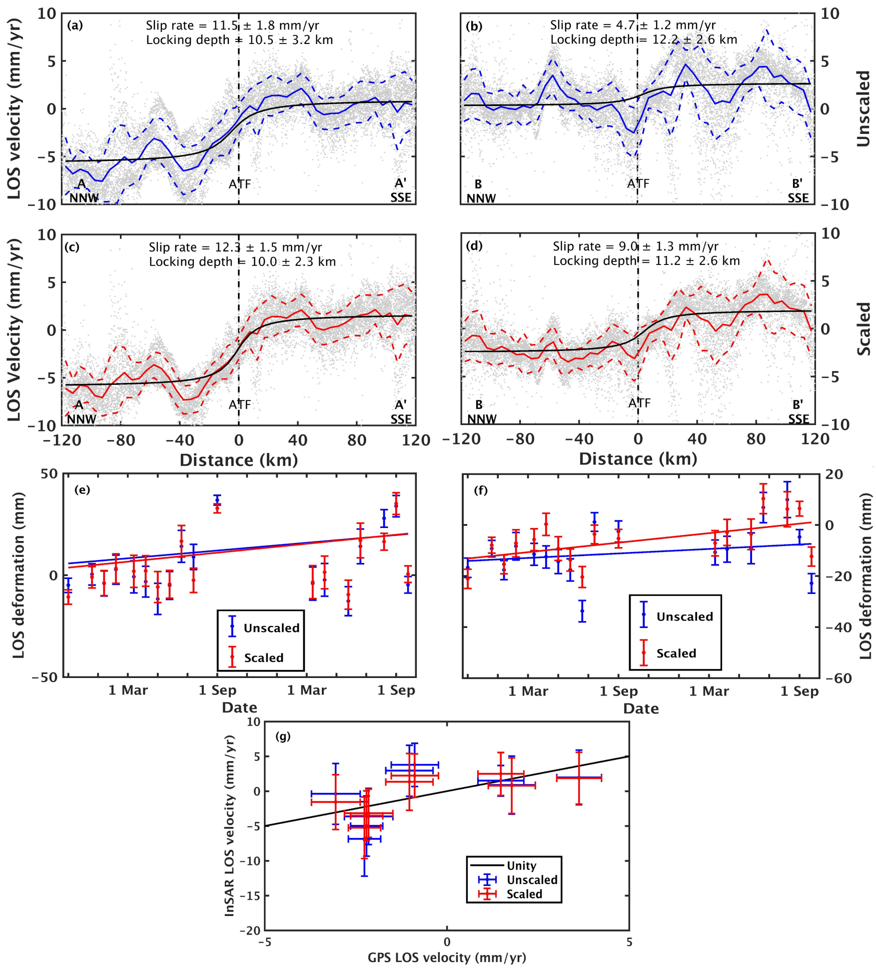

Figure 3.11: LOS InSAR velocities for profiles A-A' and B-B' in Fig. 3.10: (a) and (b) are estimated from interferograms corrected using HRES-ECMWF and (c) and (d) are corrected by the scaled tropospheric delays. The red and blue full line and dashed line represent the average values and the $\pm 1\sigma$ of the profiles, respectively, calculated from 5 km long bins. The black full line represents the maximum likelihood solution for the interseismic deformation modelling estimated using a simulated annealing inversion. (e) and (f) show the temporal evolution of deformation between two distant points along the profile A-A' and B-B' respectively (green points in Fig. 3.10a and b). Error bars represent the $\pm 1\sigma$ spread. The measurements are much closer to a linear model in time (indicated by the blue and red lines) when corrected using the scaled tropospheric delays. (g) shows the LOS velocity comparison between the InSAR and surrounding campaign GPS measurements. The horizontal errorbar represents the $\pm 1\sigma$ GPS errors and the vertical errorbar shows the InSAR errors from bootstrapping. Proximity to the black line, which marks equality between GPS and InSAR, implies that velocities match within error both before and after scaling, although errors are smaller after scaling.

3.5 Discussion

In this study, I use the HRES-ECMWF data rather than a power-law relationship to define the form of the relationship between tropospheric delay and height, and then scale the magnitude of the delay to best match the interferometric phase. The results demonstrate that the method is able to better isolate deformation across the Altyn Tagh Fault zone.

Although the magnitudes of the estimated scaling factors are generally close to one, indicating that significant information is being provided to the correction from the weather model, there are cases where it is very small (Fig. A.5). This tends to be where the HRES-ECMWF anomaly values are themselves small (Fig. A.10), and therefore have a lower signal-to-noise ratio. The effect of a small scaling factor is to reduce the influence of the HRES-ECMWF correction still further, which makes sense if it is dominated by the prediction error.

To investigate what proportion of the information contained in the weather model is still being used after the scaling, I randomise the weather model epochs (Table A.2) and reapply the method, using the randomised weather model products to derive the velocity map. The comparison between the InSAR results and the surrounding campaign GPS measurements show that randomising the weather model makes the result much worse (Fig. A.11). This demonstrates that important information from the weather model is being utilised in the scaling process, and that the method does not simply reduce all of the signals in the interferograms, which would include the deformation.

For some epochs, the difference between the scaled weather model anomalies and original weather model anomalies has a long wavelength component which could be contributed to by ionospheric effects, or orbital errors. To test whether the algorithm artificially removes long wavelength errors due to non-tropospheric contributions, I add a simulated ramp to the original InSAR phase delay anomalies and then re-estimate the scaled weather model anomaly. The results show that the added ramp does not dominate the values of the scaling factor (Fig. A.12).

I also apply the power law method (Bekaert et al., 2015a) to the same region within the TRAIN (Table A.3) and find that the average RMS of the 18 single master interferograms increases by 20% after tropospheric corrections. The LOS annual velocity derived from the interferograms corrected with the power law method shows that it is unable to separate the left-lateral strike-slip deformation across the Altyn Tagh Fault (Fig. A.13). I calculate the time series of relative LOS displacement derived from the interferograms corrected using the power law method between two distant points along the profile B-B' (Fig. 3.10a and b) whereas the results (Fig. A.14) indicate an opposite (right-lateral) motion trend across the fault. It is possible that the failure of the power law method is caused by the extremely high relief in this region.

As well as the motion across the Altyn Tagh Fault, the final LOS annual velocity map reveals an approximately 5 mm/yr velocity gradient across the Manyi south branch (Profile CC' in Fig. 3.10b), where a Mw 7.6 earthquake occurred in 1997 (Funning et al., 2007; Wang et al., 2007). I compare the LOS velocity profile (Fig. A.15) to the interseismic deformation estimates prior to the earthquake (Bell et al., 2011) and the measurements of the postseismic motion following the earthquake (Ryder et al., 2007) respectively. I find that the current deformation rate across the Manyi south branch is smaller than the rate during the 4 years immediately following the earthquake, which was around 1 cm/yr, but still larger than the estimated interseismic rate of 3 mm/yr, indicating that the elevated signals are caused by the postseismic motion, 20 years after the event.

The InSAR data (Fig. 3.10b) are noisy for some areas in the Plateau region, which is likely to be caused by the permafrost (Daout et al., 2017). The data also show a step in velocity over the southern Tarim, which may be associated with vertical deformation in this region.

For other applications such as volcanic activities, where the deformation signals are sometimes correlated with topography, I expect the correction method to also work well, as it does not estimate the troposphere directly from its correlation with topography, and the scaling factor is estimated from a wider area than just the volcano itself. To validate this, I test this method on Taal Volcano in the Philippines where an eruption occurred in January 2020. After tropospheric correction, the results show that more noise has been reduced using the scaling method compared to other approaches and the scaling estimation process does not result in a reduction of the deformation signal (Fig. 3.12).

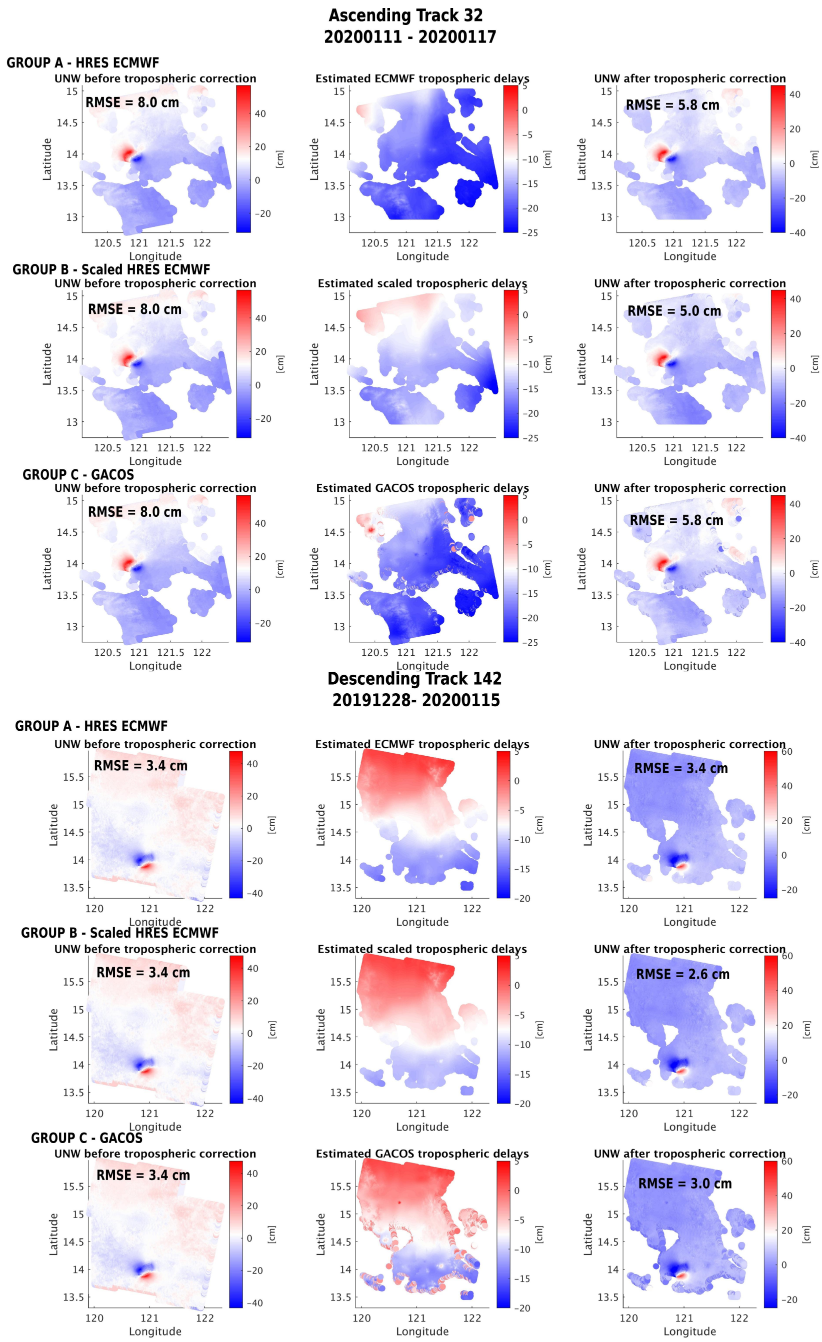

Figure 3.12: Comparison of tropospheric correction results for two Sentinel-1 interferograms spanning the period of the eruption of the Taal volcano in the Philippines, in January of 2020. The scaling method reduces more noise compared to both using the original weather model and the GACOS toolbox (Yu et al., 2018b). Positive values indicate motion towards the satellite, and negative values indicate motion away from the satellite.

3.6 Conclusions

In this chapter, I have developed a novel approach for reducing tropospheric effects in InSAR that combines the use of both external weather model data and the interferometric phase. I use the HRES-ECMWF data to define the form of the relationship between tropospheric delay and height, and then scale the magnitude of the delay to best match the interferometric phase. I test the new method on simulated data, and the results demonstrate that it can separate both coseismic and interseismic signals from an interferogram contaminated by strong tropospheric delays. I also apply the method to the central portion of the Altyn Tagh Fault in the northern Tibet. I find that the method better reduces the strong tropospheric delays in this region, leading to clearer long wavelength deformation signals. Furthermore, I find that the method has a better performance when reducing the tropospheric noise of the volcanic deformation compared to other correction algorithms. These results suggest that the extra scaling step should be applied wherever weather model data are being used to correct interferograms.

Chapter 4

Interseismic strain accumulation along the Altyn Tagh Fault determined from Sentinel-1 InSAR

This chapter addresses the second and third objectives of my thesis, by presenting the interseismic strain localisation along the Altyn Tagh Fault, over a spatial scale of approximately 1500 km. It is the first time such a large-scale analysis been carried out for this fault with InSAR.

4.1 Introduction

The Tibetan Plateau region, bordered by the Himalaya to the south, the Kun Lun and Altyn Tagh ranges to the north, the Tien Shan to the NW and Long Men Shan range to the east (Searle et al., 2011), has been created by the India-Eurasia collision over the past 50 million years, with deformation distributed from the Himalayas to Mongolia (Fig. 4.1). Tectonic processes in this region are not fully understood, and the debate about how continental deformation accommodates the Indo-Asian plate collision (Chen et al., 2017; England and Molnar, 2005; Thatcher, 2007; Yang and Liu, 2009) still continues.

From the perspective of 'rigid block' models, the Tibetan crust is regarded as a rigid block which is bounded by a small number of crustal-scale active strike-slip faults (Avouac and Tapponnier, 1993; Molnar and Tapponnier, 1975; Tapponnier and Molnar, 1976). The block is described as an elastic medium and will deform only when the inelastic changes of the shape are allowed by the slip of the block-bounding faults (Kong and Bird, 1994; Vilotte et al., 1982). Therefore, 'rigid block' models consider that a significant proportion of the Indo-Asian convergence is taken up by the eastward extrusion along block-bounding strike-slip faults, with around 20–30 mm/year of slip rate expected for these faults (Peltzer and Tapponnier, 1988; Replumaz and Tapponnier, 2003; Ryerson et al., 2006; Tapponnier et al., 1982, 2001).

On the other hand, continuum models consider that continents are elastic and viscous, and anticipate that the deformation is distributed throughout the lower continental lithosphere (England and Molnar, 1997; Houseman and England, 1993). Continuum models can provide self-consistent stress and strain-rate fields based on a simple physical model, whereas 'rigid block' models allow only a kinematic description of the measured velocity field. However, as rheology is uncertain, continuum models may place other sources of uncertainties within the physics of the model. In continuum models, it is thought that the Tibetan Plateau region deforms on a distributed fault network and the faults represent the near-surface localisation of distributed deformation at depth (England and McKenzie, 1982). Since a large portion of Indian convergence is considered to be absorbed by lithospheric thickening (England and Molnar, 1997), the slip rate for these major faults in the Tibetan Plateau region is anticipated to be around 10 mm/year (England and Molnar, 1990; Houseman and England, 1986), with the models suggesting that strain associated with 20–30 mm/year of slip rate on those faults is inconsistent with the strain distribution in surrounding regions.

However, Thatcher (2007) suggested that the behaviour of 'rigid block' models can approach that of the continuum system when introducing more faults, decreasing the sizes of blocks and using more comparable fault slip rates as constraints in the inversion. He argues that previous conclusions that low fault slip rates are not compatible with block motions in Tibet might not be correct as the high geological estimates used to constrain these block models (Peltzer and Tapponnier, 1988; Replumaz and Tapponnier, 2003) have been controversial (Thatcher, 2009). Recent estimates for the slip rates on Tibet's major strike-slip faults inverted from tectonic microplate models with GPS measurements are in a range of 5 to 12 mm/year (Loveless and Meade, 2011; Wang et al., 2017), which are consistent with the predictions from the continuum models. These studies show that the precision and the spatial coverage of slip rate constraints are crucial to the modelling results as very small differences in the data can translate into significant intrablock deformation and slip on faults. Consequently, accurate estimates of the slip rate for the major faults in Tibet are significant to explain how continents deform there.

The 1600 km-long Altyn Tagh Fault (ATF) is a major intra-continental strike-slip fault in the Northern Tibetan Plateau (Fig. 4.1), the slip rate of which has significant implications for our understanding of the tectonic processes of the Tibetan Plateau region. The long straight segments ($>$ 100 km) of the ATF are capable of sustaining supershear rupture speeds and have potential to reach compressional wave speeds over significant distances (Robinson et al., 2010), which indicates the potential of possible large earthquakes that rupturing long segments at very fast speeds on these faults in this region.

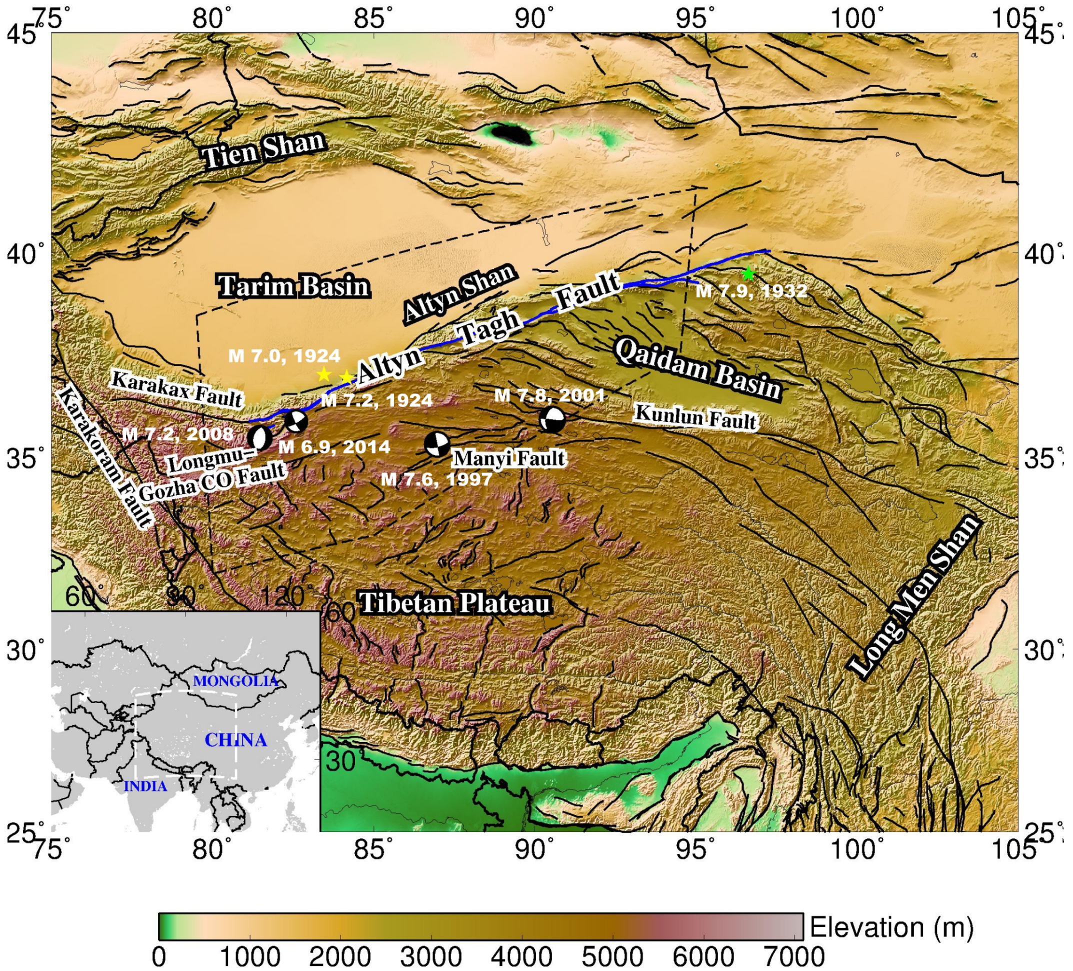

Figure 4.1: Tectonic setting of the Altyn Tagh Fault (ATF) zone and other major features in Tibet. The black dashed lines indicate the extent of the study region. Black solid lines represent fault traces in the region (Taylor and Yin, 2009). Blue lines highlight the high-resolution fault traces of the main strand of the ATF (Elliott et al., 2018, 2015), which I use in the later interseismic deformation modelling. Yellow stars represent a pair of earthquakes, which occurred along the western portion of the ATF in 1924 with a magnitude of M_w 7.0 (USGS, 1924a) and M_w 7.2 (USGS, 1924b), respectively. The green star shows the 1932 Gansu M_w 7.9 at the easternmost end of the ATF (USGS, 1932). Major earthquakes ($M_w > 6.9$) that occurred near the ATF recently are also featured in the map, including the 1997 M_w 7.6 Manyi earthquake, the 2001 M_w 7.8 Kokoxili earthquake, the 2008 M_w 7.2 Yutian earthquake and the 2014 M_w 6.9 Yutian earthquake. The background shows the elevation of the study region derived from the Shuttle Radar Topography Mission (SRTM) 3-arc seconds data (Farr et al., 2007), which is also applied to the subsequent figures.

Recent slip rate estimates along the ATF are generally determined by three methods over different time scales (Fig. 4.2): i) long-term geological measurements through the identification of offset (displaced) piercing points across the fault (e.g., Yin and Harrison, 2000); ii) Quaternary estimates from stream, terrace offsets, cosmogenic or ^{14}C dated offsets (e.g., Cowgill et al., 2009); iii) Geodetic modelling from GPS and InSAR measurements (e.g., Gan et al., 2007). Although these studies have provided valuable insights into the interseismic deformation along the ATF, some questions still remain. Firstly, published geodetic measurements along the ATF suggest 0–10 mm/year of slip rate over the western portion from 78°E to 80°E (Wang and Wright, 2012; Wright et al., 2004; Zheng et al., 2017), 5–15 mm/year for the central portion from 84°E to 90°E (Daout et al., 2018; Elliott et al., 2008; He et al., 2013b; Shen et al., 2019; Vernant, 2015; Wallace et al., 2004; Wang et al., 2017; Xu and Zhu, 2019; Zhu et al., 2016) and 4–10 mm/year over the eastern portion (Bendick et al., 2000; Jolivet et al., 2008; Liu et al., 2018; Qiu et al., 2019; Vernant, 2015; Zhang et al., 2007; Zheng et al., 2017), which are not always in agreement with those derived from the long-term geological measurements nor Quaternary. For instance, the geodetic measurements are generally 2–3 times less than some of the Quaternary measurements (Mériaux et al., 2004; Peltzer et al., 1989; Tapponnier et al., 2001). The discrepancy could be caused by the uncertainties of the measurements (Cowgill, 2007; Cowgill et al., 2009; Gold et al., 2011; Mohadjer et al., 2017), or may indicate a secular change in fault slip rates over distinct time scales (Wallace et al., 2004; Washburn et al., 2003), which leads to a controversy over whether the geodetic measurements are representative of the measurements over long time scales (Mériaux et al., 2012, 2005). Mohadjer et al. (2017) applied least squares regression to the pairs of published GPS and geological slip rates along the ATF and reveals that disagreements between the GPS and Quaternary rates are mainly ascribed to the incorrect geomorphic reconstructions of offset landforms used for estimating Quaternary slip rates. Furthermore, the results suggest a possibility of temporal variations in slip rates over the time scales as a third of the total variation in the Quaternary estimates can not be explained statistically by a linear relationship between the GPS measurements and the Quaternary rates. Alternatively, previous studies of interseismic deformation from geodetic measurements over the ATF have only focused on specific portions (e.g., Liu et al., 2018; Qiu et al., 2019), and may not provide an overall picture of the variation of localised strain accumulation along the fault. A third possibility is that although the conventional elastic half-space model (Savage and Burford, 1973) has been well applied to characterise interseismic deformation along the fault (e.g., Elliott et al., 2008; Zhu et al., 2016), modifications may need to be applied to the model.

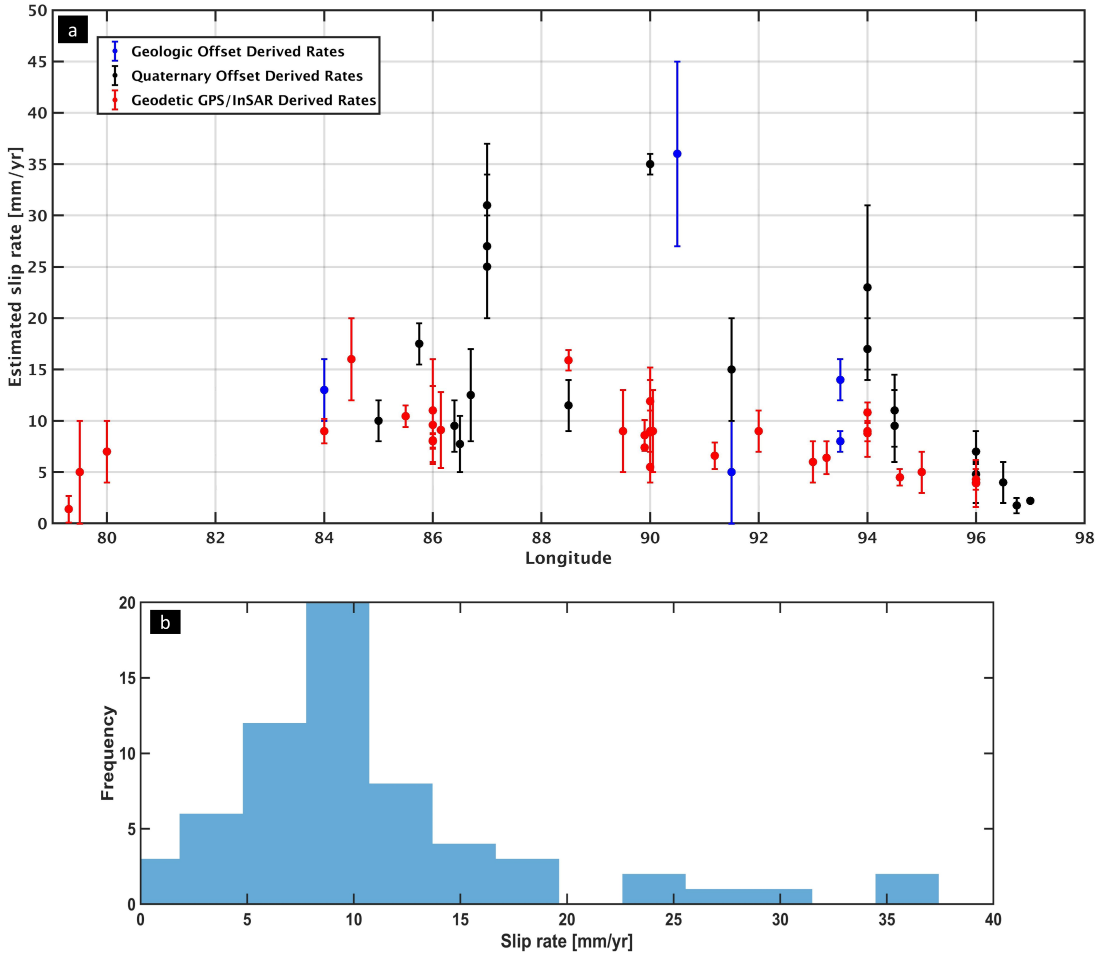

Figure 4.2: Published slip rate estimates along the ATF against the longitudinal position (a), including geologic offset derived rates (Chen et al., 2002; Cowgill et al., 2003; Yin et al., 2002; Yin and Harrison, 2000; Yue et al., 2003, 2001), Quaternary offset derived rates (Cowgill, 2007; Cowgill et al., 2009; Gold et al., 2011; Mériaux et al., 2004, 2005; Meyer et al., 1996; Peltzer et al., 1989; Tapponnier et al., 2001; Washburn et al., 2003; Xu et al., 2005; Zhang et al., 2007) and geodetic derived rates (Bendick et al., 2000; Chen et al., 2000; Daout et al., 2018; Elliott et al., 2008; Gan et al., 2007; He et al., 2013b; Jolivet et al., 2008; Liu et al., 2018; Qiu et al., 2019; Shen et al., 2019; Vernant, 2015; Wallace et al., 2004; Wang and Wright, 2012; Wang et al., 2017; Wright et al., 2004; Xu and Zhu, 2019; Zhang et al., 2007; Zheng et al., 2017; Zhu et al., 2016). (b) is a histogram of published slip rate estimates along the ATF.

In this chapter, I derive the InSAR velocity field over the ATF between 80°E to 95°E from Sentinel-1 interferograms spanning the period between late 2014 and 2019. To improve the retrieval of small tectonic signals, I use the spatially varying scaling method that I describe in Chapter 3, to reduce the tropospheric effects in the interferograms. To derive a consistent velocity field along the fault, I present a new scheme to link InSAR velocity fields estimated from different satellite tracks. I investigate the slip rate and locking depth along the ATF using a modified elastic half-space model. Furthermore, I provide the strain rate at the surface, calculated from the estimated slip rate and the locking depth, to assess seismic hazard along the fault.

4.2 InSAR data processing

In this study, I process 12 overlapping tracks (6 ascending and 6 descending) using the first 5 years of Sentinel-1 SAR data, spanning the period between late 2014 and 2019, to cover the ATF between 80 °E to 95 °E (Fig. B.1). The original InSAR data includes 21 frames (250 km by 250 km) defined by the Sentinel-1 processing system LiCSAR (Gonzalez et al., 2016; Lazecký et al., 2020) and I process the equivalent of 1–2 frames along each track (250–500 km long). To avoid possible inconsistent phase in the overlapping region of the same track during the construction, I merge frames within the same track to form a long track before generating interferograms using LiCSAR.

Based on the work flow of InSAR processing that I describe in Chapter 2, I generate short temporal baseline interferograms forming a small baseline network with sufficient redundancy, which has 200 interferometric pairs on average (Fig. B.2). As the ATF is located at the border between the low Tarim Basin and the high Tibetan Plateau, the expected long wavelength deformation signal is strongly masked by tropospheric delay variation across the 6 km topographic relief. As I present in Chapter 3, I have developed a new spatially varying scaling method for InSAR tropospheric corrections to improve the retrieval of small tectonic signals (Shen et al., 2019). In this chapter, I apply the method to remove the tropospheric delays in each interferogram, and the average Root Mean Square (RMS) for all tracks drops by 37 % after corrections (Fig. 4.3), implying significant reductions of tropospheric signals. Compared to descending tracks, the improvement on the ascending tracks, which have greater noise, is more significant after the correction is applied.

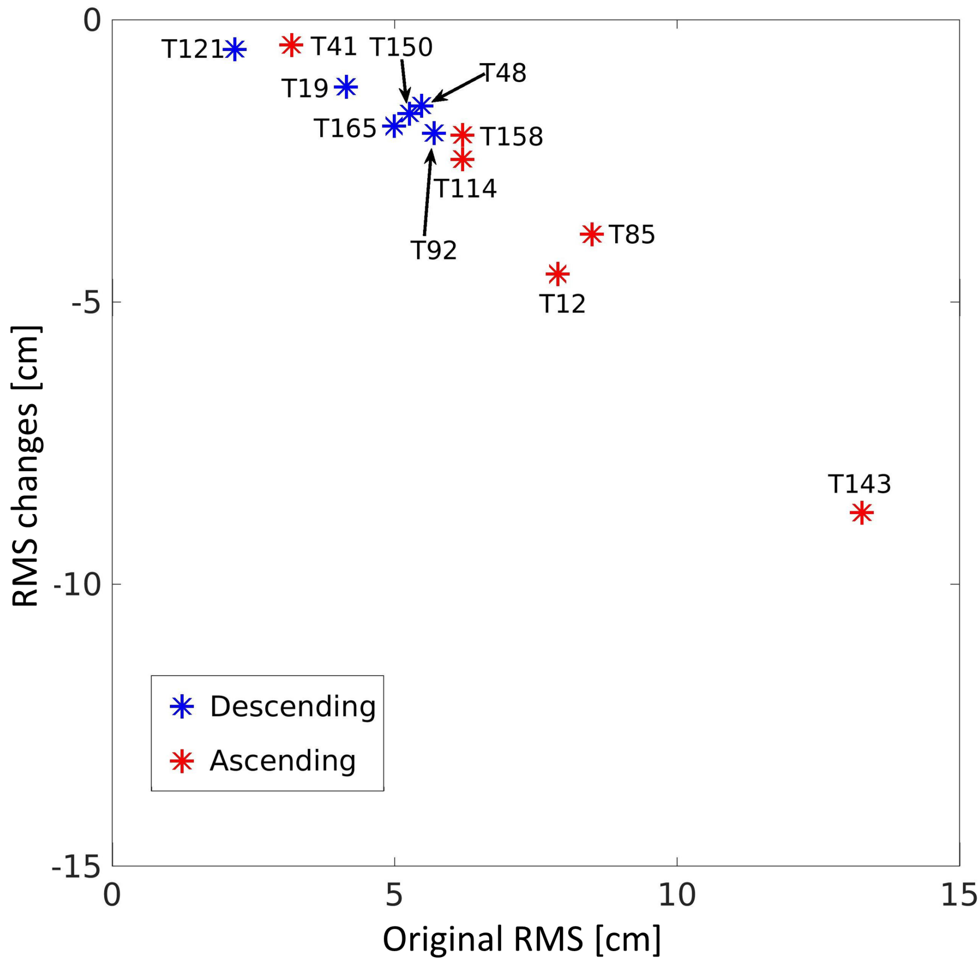

Figure 4.3: RMS comparisons of interferograms for individual tracks before and after tropospheric corrections. All tracks show a reduction in the RMS after the correction is applied.

I then derive the InSAR line-of-sight (LOS) velocity fields for each pixel from the tropospheric-corrected interferograms using the function

$$D_{LOS} = A\sin(\frac{2\pi}{365.25})t + B\cos(\frac{2\pi}{365.25})t + vt + C \tag{4.1}$$

where D_{LOS} is the InSAR LOS displacement, the sinusoidal term $A\sin(\frac{2\pi}{365.25})t$ and the cosinusoidal $B\cos(\frac{2\pi}{365.25})t$ term model signal subject to the annual seasonal freezing and thawing of the upper layer of the permafrost in Tibetan Plateau (Daout et al., 2017), $\sqrt{A^2 + B^2}$ is the amplitude of the seasonal signal, v is the annual LOS velocity, t is the time from the master date of interferograms of each track and C is a constant. I invert the solution using the best linear unbiased estimator (BLUE) (e.g., Puntanen et al., 2000). I calculate phase variances for each epoch from the variances of the tropospheric corrected short temporal interferograms by least squares inversion. I then use these variances as the elements on the principal diagonal of the variance-covariance matrix in the BLUE inversion. Off-diagonal elements are set to zero, since the noise of each epoch is considered to be independent.

4.3 Velocity mosaicking over adjacent tracks

After removing the average offset in each overlapping area between every two adjacent tracks in ascending and descending, respectively, the merged LOS velocity fields show clear left-lateral strike-slip deformation along the ATF (Fig. 4.4). The standard deviations of velocities, estimated using the percentile bootstrap method (e.g., Efron and Tibshirani, 1994), show the uncertainties in velocities (Fig. 4.4), which indicates the threshold for measuring tectonic signals (Morishita et al., 2020).

However, variation in satellite geometry (e.g., azimuth direction and incidence angle) and long wavelength errors between tracks lead to velocity inconsistencies in the overlapping regions, which is non-negligible in large-scale studies. To obtain a consistent velocity field across the region, I present a new scheme to estimate long wavelength trends from the InSAR velocity fields using GPS observations within the region and meanwhile minimising the differences between the adjacent tracks of the InSAR LOS velocity fields. I then remove the long wavelength trends from the InSAR LOS velocity fields and decompose the velocities into an east-west component and a sub-vertical component which I define below.

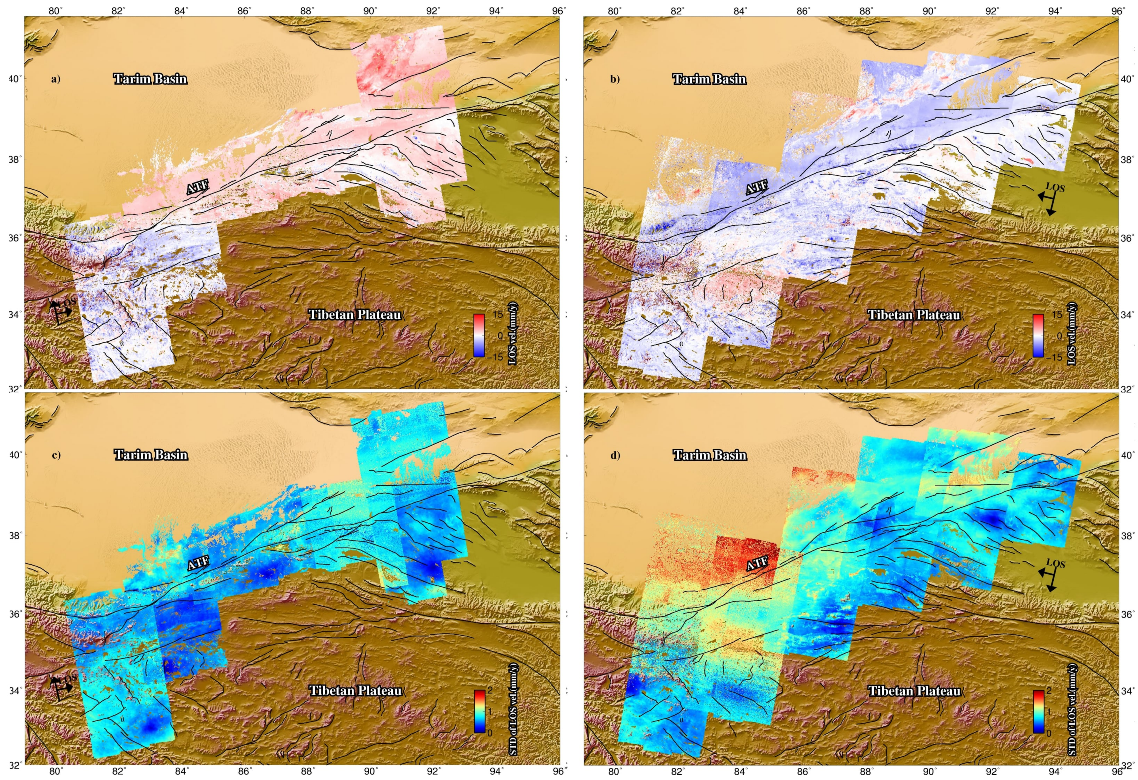

Figure 4.4: Mosaicked InSAR LOS velocity fields in ascending (a) and descending (b) after removing the average offsets in overlapping areas. Positive values indicate the motion towards the satellite, whereas negative values show the motion away from the satellite. (c) and (d) are the estimated standard deviation of velocities accordingly using the percentile bootstrap method (e.g., Efron and Tibshirani, 1994).

I incorporate three kinds of InSAR points in the inversion for long wavelength trends: i) points within the overlapping regions across tracks that have both ascending and descending measurements, which to minimise the velocities differences between adjacent tracks; ii) points have both ascending and descending measurements and are also overlapped (within a 1 km distance) by GPS observations of the horizontal components only; iii) points which are overlapped (within a 1 km distance) by GPS observations of both the horizontal and vertical components. Constraints from the latter two kinds of points reference the InSAR velocity field to the GPS reference frame. Each horizontal GPS point can provide one extra constraint in the inversion, and each GPS point with the vertical component can provide two extra constraints.

I remove the velocities resulting from continental rotation, before conducting the inversion. I first transform the GPS velocities from a Eurasia-fixed reference frame to a Tarim reference, by minimising the velocities of the GPS stations located in the Tarim Basin (Fig. 4.5). As I only have two observational InSAR inputs in the form of ascending and descending, it is not possible to incorporate the full 3-D velocity field in the inversion. Although previous studies along the ATF from InSAR measurements often ignore the north-south component due to the lack of evidence of fault shortening over this region (e.g., Zhu et al., 2016), the northern component can contribute ~11 % to the LOS measurements. Alternatively, some studies of the North Anatolian Fault use the interpolated north-south GPS velocities as the constraint (e.g., Hussain et al., 2018; Weiss et al., 2020), although the accuracy is highly dependent on the density and spatial distribution of the GPS sites. In this study, I consider an east-west striking plane, tilted to the south, representing the average plane defined by all LOS vectors. I estimate two components of the crustal velocity in this plane: the east-west direction and the "sub-vertical" direction, perpendicular to the east-west direction as

$$V_{subv} = (\frac{\sin\theta \sin\phi}{\Delta})V_n + (\frac{\cos\theta}{\Delta})V_u \tag{4.2}$$

$$where \quad \Delta = \sqrt{((\sin\theta \sin\phi)^2 + (\cos\theta)^2)} \tag{4.3}$$

where V_{subv} is the sub-vertical component, V_n and V_u are the northern and vertical motion, respectively, θ is the radar incidence angle, and ϕ is the azimuth direction of the satellite positive clockwise from the north.

Therefore, I can estimate the long wavelength trends from the InSAR LOS velocity fields as

$$
\begin{bmatrix} {V_{a_i}}^l \\ \vdots \\ {V_{a_i}}^m \\ \vdots \\ {V_{d_i}}^n \\ \vdots \\ {V_{d_i}}^p \\ \vdots \\ V_{ei} \\ \vdots \\ V_{ni} \\ \vdots \\ V_{vi} \\ \vdots \end{bmatrix}
=
\begin{bmatrix}
-\sin\theta_i^l\cos\phi^l & \dots & \Delta_i^l & \dots & 0 & \dots & 0 & \dots & x_i & y_i & 1 & 0 & 0 & 0 & 0 & 0 & 0 & 0 & 0 & 0 & \dots \\
\vdots \\
-\sin\theta_i^m\cos\phi^m & \dots & \Delta_i^m & \dots & 0 & \dots & 0 & \dots & 0 & 0 & 0 & x_i & y_i & 1 & 0 & 0 & 0 & 0 & 0 & 0 & \dots \\
\vdots \\
-\sin\theta_i^n\cos\phi^n & \dots & \Delta_i^n & \dots & 0 & \dots & 0 & \dots & 0 & 0 & 0 & 0 & 0 & 0 & x_i & y_i & 1 & 0 & 0 & 0 & \dots \\
\vdots \\
-\sin\theta_i^p\cos\phi^p & \dots & \Delta_i^p & \dots & 0 & \dots & 0 & \dots & 0 & 0 & 0 & 0 & 0 & 0 & 0 & 0 & 0 & x_i & y_i & 1 & \dots \\
\vdots \\
1 & \dots & 0 & \dots & 0 & \dots & 0 & \dots & 0 & 0 & 0 & 0 & 0 & 0 & 0 & 0 & 0 & 0 & 0 & 0 & \dots \\
\vdots \\
0 & \dots & 0 & \dots & 1 & \dots & 0 & \dots & 0 & 0 & 0 & 0 & 0 & 0 & 0 & 0 & 0 & 0 & 0 & 0 & \dots \\
\vdots \\
0 & \dots & 0 & \dots & 0 & \dots & 1 & \dots & 0 & 0 & 0 & 0 & 0 & 0 & 0 & 0 & 0 & 0 & 0 & 0 & \dots \\
\vdots
\end{bmatrix}
\times
\begin{bmatrix} V_{\hat{e}i} \\ \vdots \\ V_{s\hat{ubv}i} \\ \vdots \\ V_{\hat{n}i} \\ \vdots \\ V_{\hat{v}i} \\ \vdots \\ a^l \\ b^l \\ c^l \\ a^m \\ b^m \\ c^m \\ a^n \\ b^n \\ c^n \\ a^p \\ b^p \\ c^p \\ \vdots \end{bmatrix}
\quad (i, m, n, l, p \in \mathbb{N})
\tag{4.4}
$$

where ${V_{a_i}}^l$ and ${V_{a_i}}^m$ are the InSAR LOS velocity of the ith points in the lth and the mth ascending tracks, respectively; $V_{d_i}^n$ and $V_{d_i}^p$ are the InSAR LOS velocity of the ith points in the nth and the pth descending tracks, respectively; V_{ei}, V_{ni}, V_{vi} and V_{subvi} are the east-west, the north-south, the vertical and the sub-vertical components of the GPS velocity of the ith points, respectively; $V_{\hat{e}i}$, $V_{\hat{n}i}$, $V_{\hat{v}i}$ and $V_{s\hat{ubv}i}$ are the modelled east-west, north-south, vertical and sub-vertical components of the ith points, respectively; x_i and y_i are the location of the ith points; a, b, c are the modelled factors to determine the linear plane for each track.

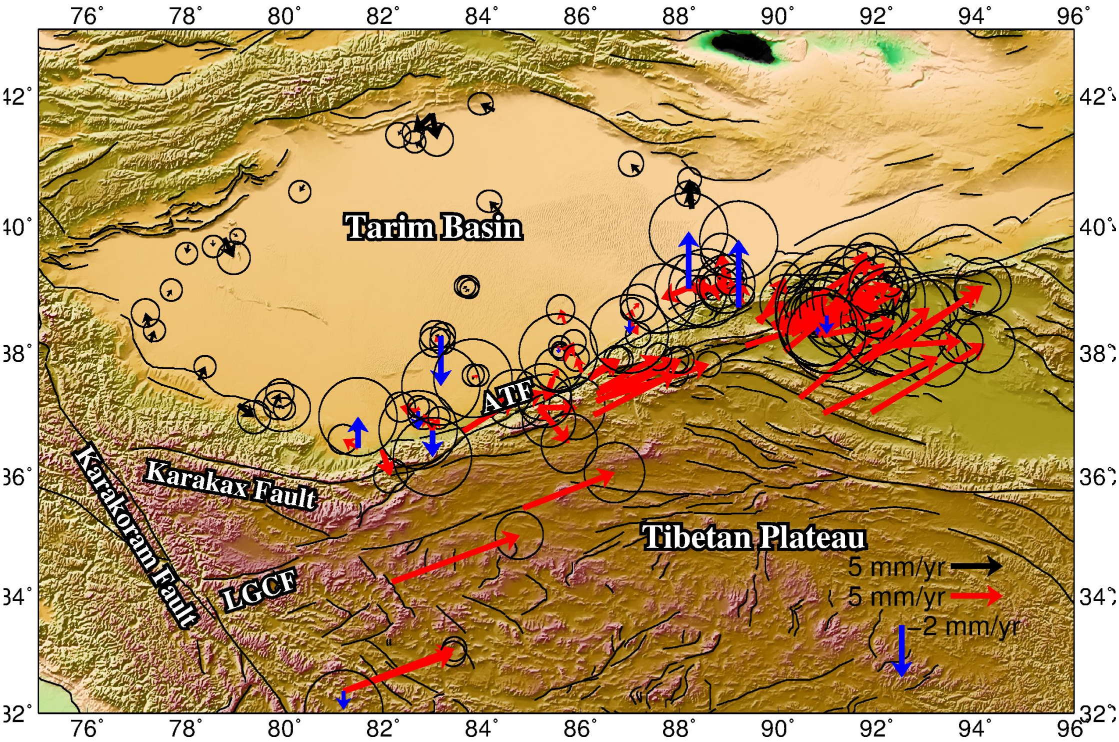

Figure 4.5: GPS velocity map. Black vectors show horizontal velocities of the 28 GPS sites used to define the Tarim Basin reference frame. Red vectors and blue vectors represent horizontal velocities of the 84 available GPS sites and vertical velocities of the 23 available GPS observations used to determine the linear planes for each track, respectively. All velocities are plotted in the defined Tarim Basin reference frame at 68 % confidence level.

I uniformly sample the InSAR points in the overlapping regions across tracks with a spacing of ∼10 km, and obtain 632 points that have two ascending and one descending measurements, and 840 points that have two descending and one ascending measurements. I also incorporate 84 available GPS points with the horizontal components and 23 GPS observations of both the horizontal and vertical components in the inversion (Fig. 4.5). I invert the solution using least squares with equal weight to each data point. The results show a good fit between the model and the observations (Fig. 4.6).

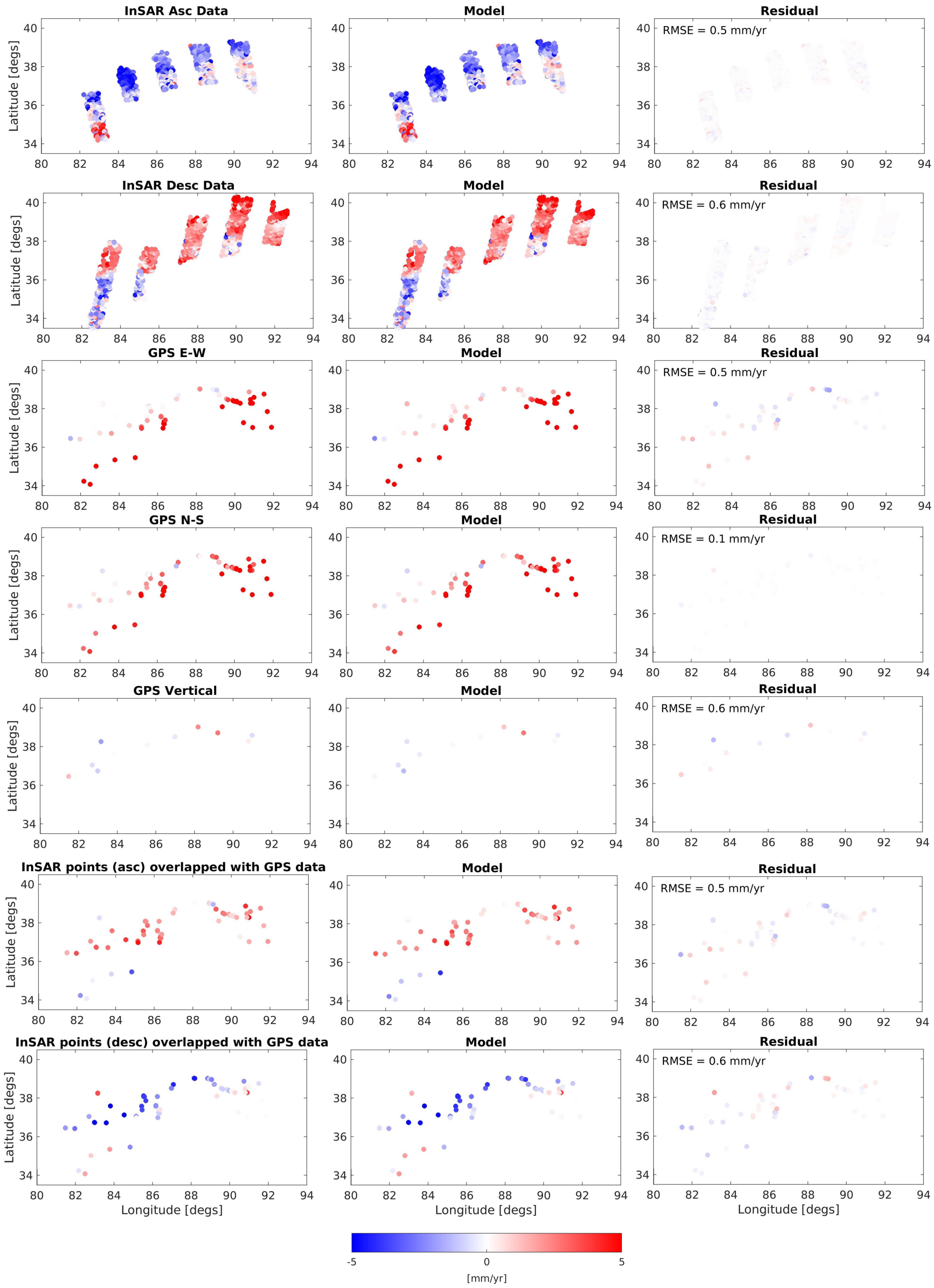

Figure 4.6: The fit of the model to the data points in the inversion for long wavelength trends. Panels in the first and the second rows show the fit of the model to the InSAR points selected from the overlapping region between adjacent tracks; Panels in the third to the fifth rows indicate the fit of the model to the GPS data; Panels in the last two rows show the fit of the model to the InSAR points covered by the GPS sites in ascending and descending, respectively.

I then remove the linear planes determined from the data points shown in figure 4.6 from each track to mosaic the InSAR velocity field and transform the merged LOS velocities to the Tarim reference frame (Fig. 4.7). The mosaicked LOS velocities are more consistent in the overlapping region between adjacent tracks (Fig. 4.8).

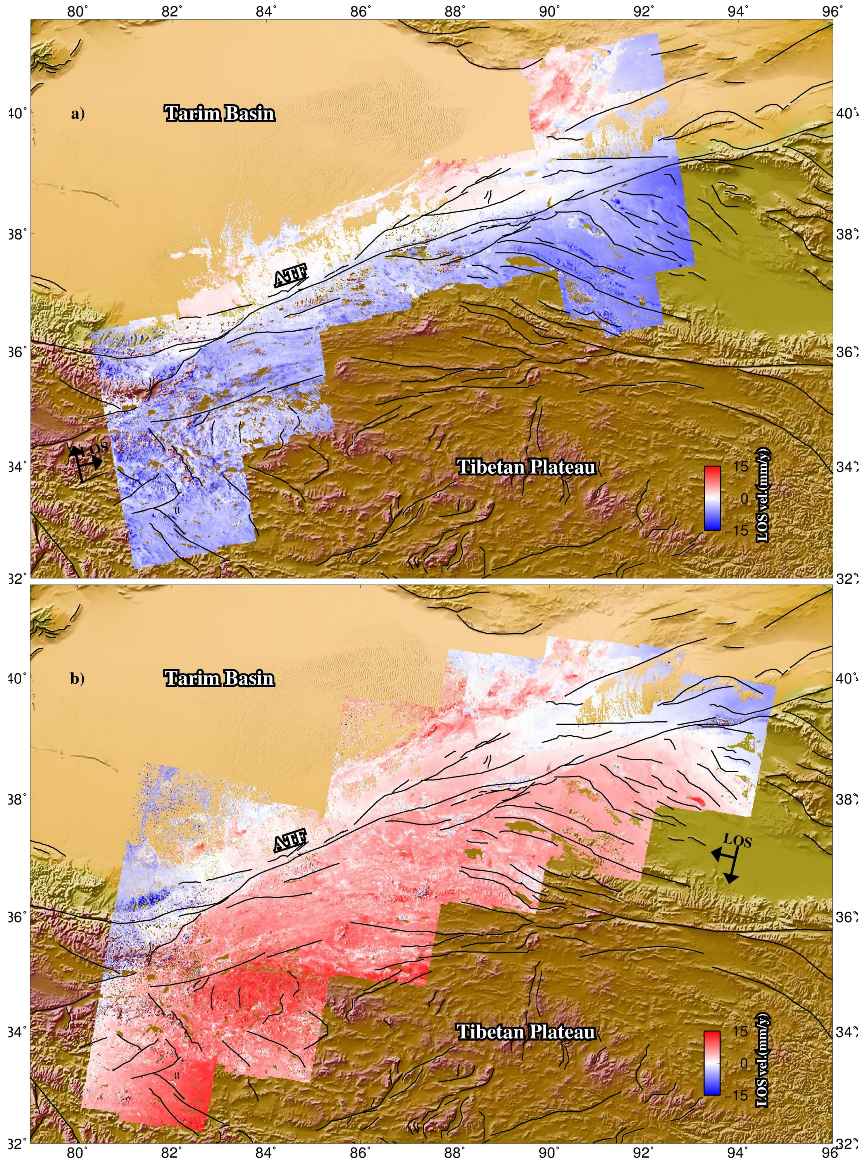

Figure 4.7: Mosaicked InSAR LOS velocity fields of ascending (a) and descending (b) in the Tarim reference after removing the inverted linear planes from each track. Positive values indicate motion towards the satellite.

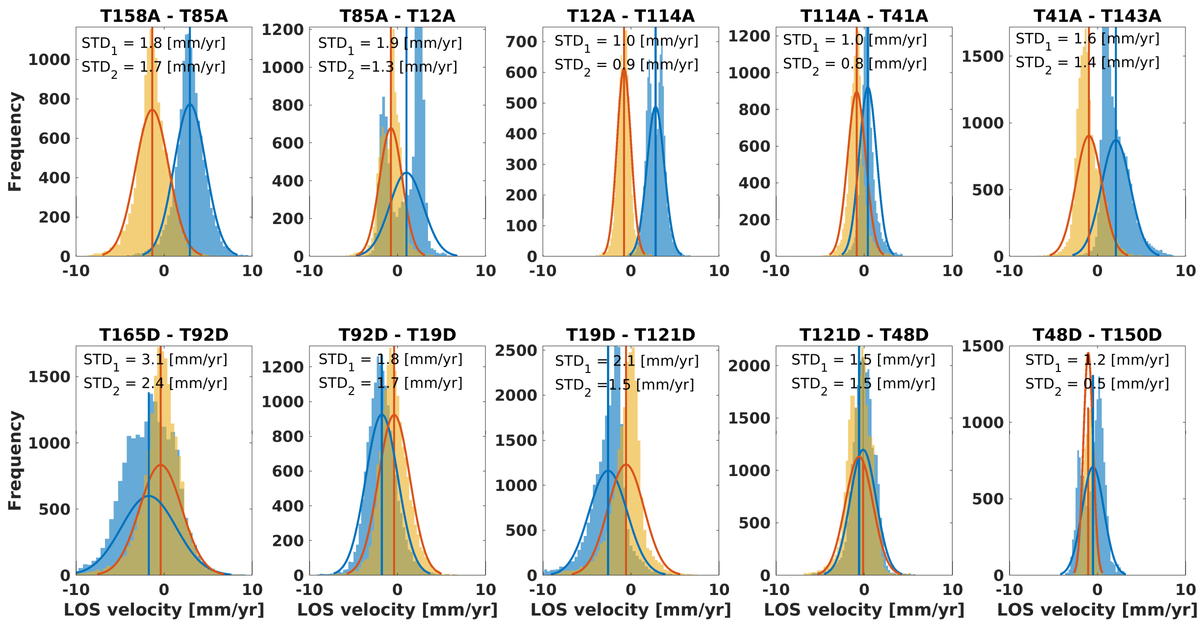

Figure 4.8: Comparison of the LOS velocity differences in the overlapping region between adjacent tracks before and after velocity mosaicking. Blue histograms show the original differences along with the Gaussian distribution fit (blue curves), whereas the yellow-orange colour features the differences after removing inverted linear planes. The blue and orange lines indicate the mean value of the corresponding Gaussian distribution. STD_1 and STD_2 show the standard deviation of each estimated Gaussian distribution before and after velocity mosaicking, respectively. The mean of each is expected to be non-zero due to the different incidence angles.

4.4 Interseismic strain accumulation along the ATF

To investigate the pattern of interseismic deformation along the ATF, I decompose the entire merged LOS velocity field into the east-west and the sub-vertical component, which includes contributions from any vertical or north-south movements, as

$$V_{LOS} = \begin{bmatrix} -\sin\theta\cos\phi, & \sqrt{((\sin\theta\sin\phi)^2 + (\cos\theta)^2)} \end{bmatrix} \begin{bmatrix} V_e \\ V_{subv} \end{bmatrix} \tag{4.5}$$

The decomposed east-west component shows a clear gradient across the ATF resulting from the eastward motion of the Tibetan Plateau with respect to the Tarim Basin (Fig. 4.9). Regions of uplift or northward motion observed to the north of ATF from 87 °E to 89 °E in the decomposed sub-vertical component (Fig. 4.10) can be ascribed to the south dipping Altyn Shan thrusts along the southern border of the Tarim Basin (Daout et al., 2018). The sub-vertical component also shows a signal over the eastern edge of the Tarim Basin that does not appear tectonic. I interpret this as being associated with the hydrological processes or effects from the sand dunes there.

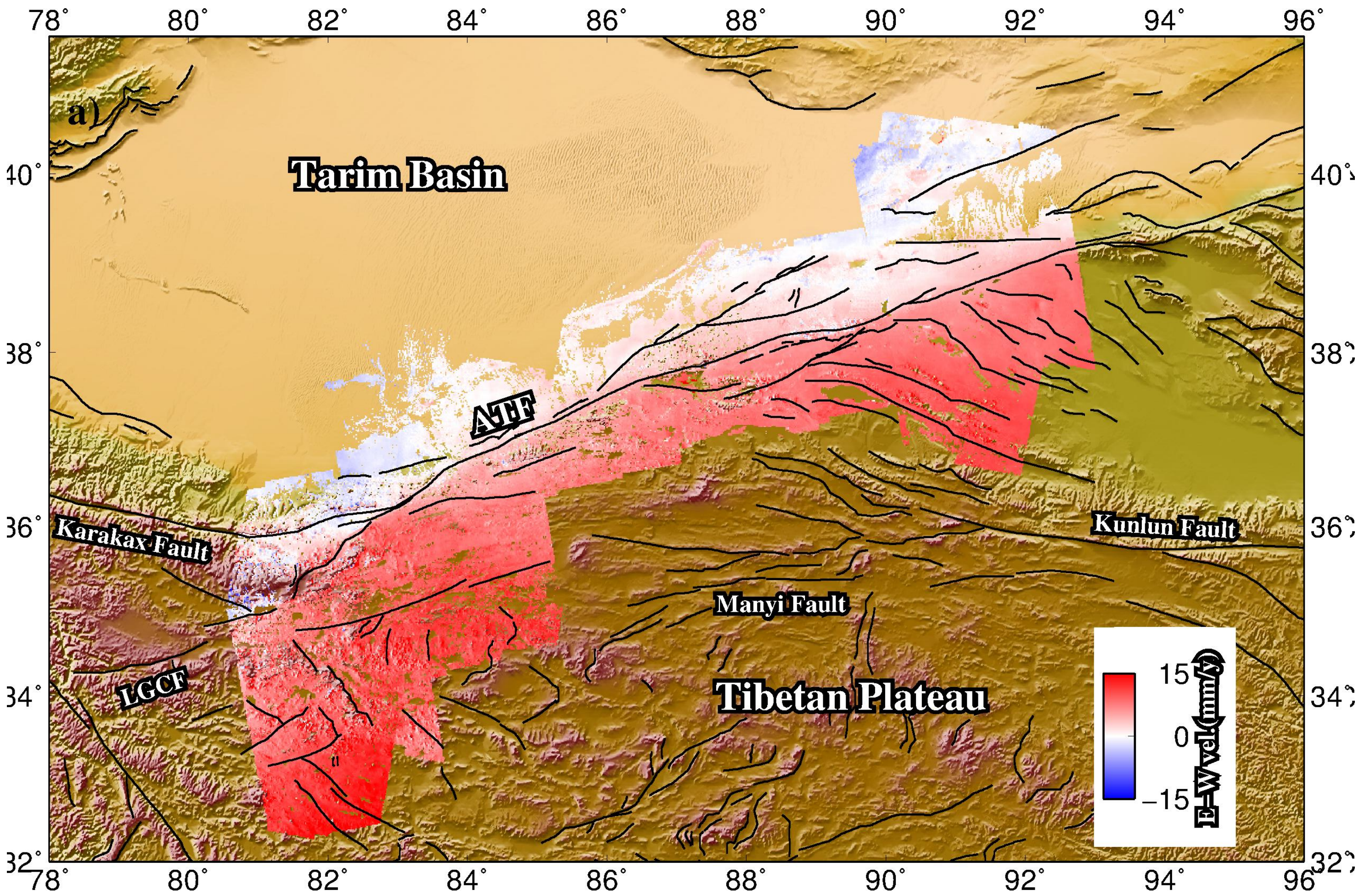

Figure 4.9: The east-west velocity map decomposed from the mosaicked InSAR LOS velocity fields in the Tarim reference. Positive values indicate the eastward motion.

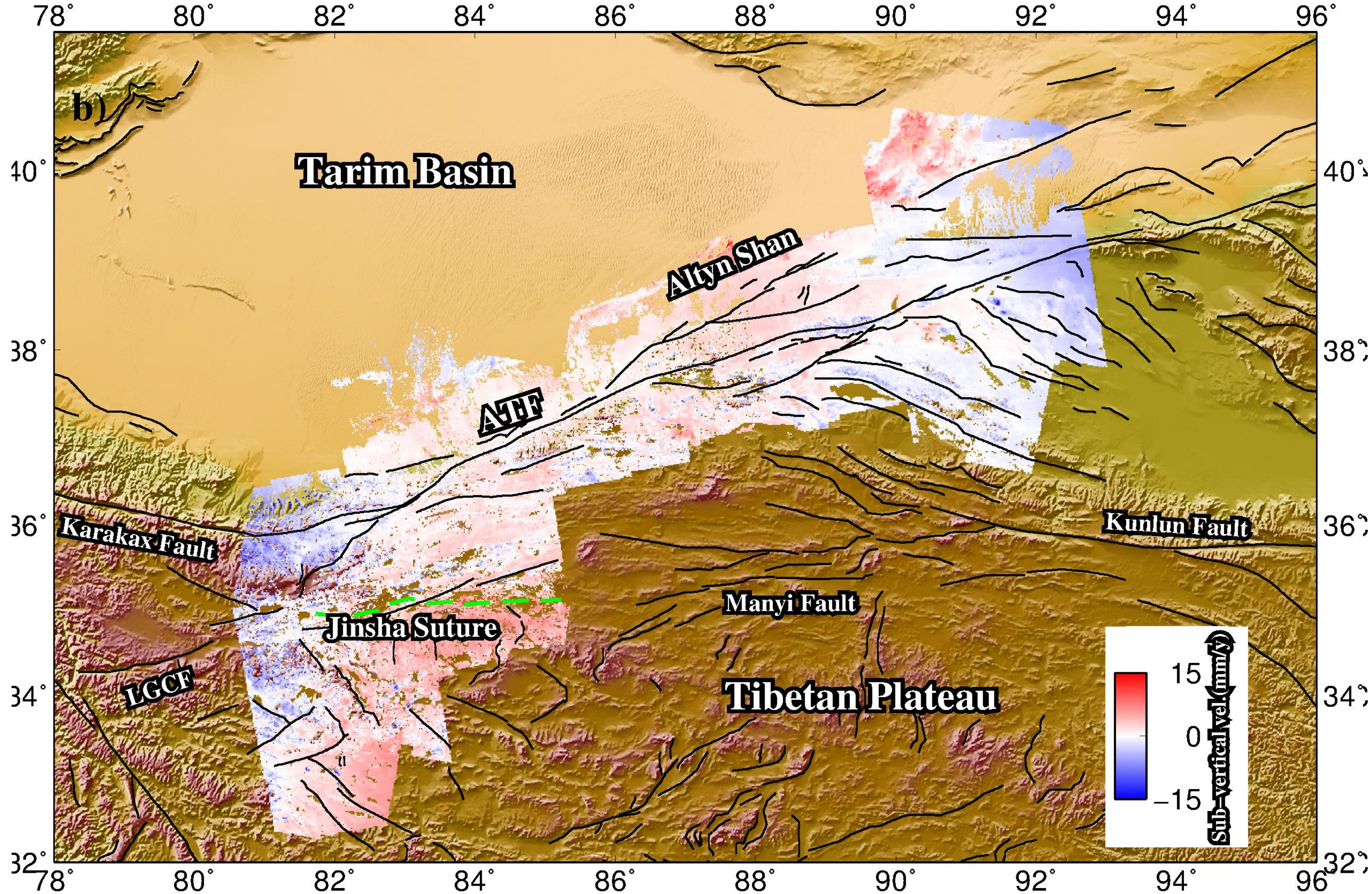

Figure 4.10: The sub-vertical velocity map decomposed from the mosaicked InSAR LOS velocity fields in the Tarim reference. Positive values indicate the northward or uplift motion. The green dashed line shows the trace of the Jinsha suture derived from Daout et al. (2018).

4.4.1 Fault-parallel velocities

Based on the estimated east-west velocity field, I derive 1-D fault-perpendicular profiles at intervals of 0.5° in a varying local strike perpendicular to the high-resolution fault trace of the ATF shown in Fig. 4.1. Each profile shows fault-parallel velocities projected from within a 50 km perpendicular distance. The profiles show visible strain accumulation on the ATF (Fig. 4.11). The asymmetric pattern of interseismic velocities shown in the profiles suggests a decrease in rigidity from the Tarim basin to the Tibetan Plateau (Jolivet et al., 2008; Zhang et al., 2007). The profiles also reveal that additional strain localisations are distributed over southern strands near the western portion of the ATF from 84°E to 85.5°E and the eastern portion from 91°E to 92°E. I also project previous modelling of GPS measurements into the fault-perpendicular profiles, and the results show that they are in good agreement (Fig. 4.11).

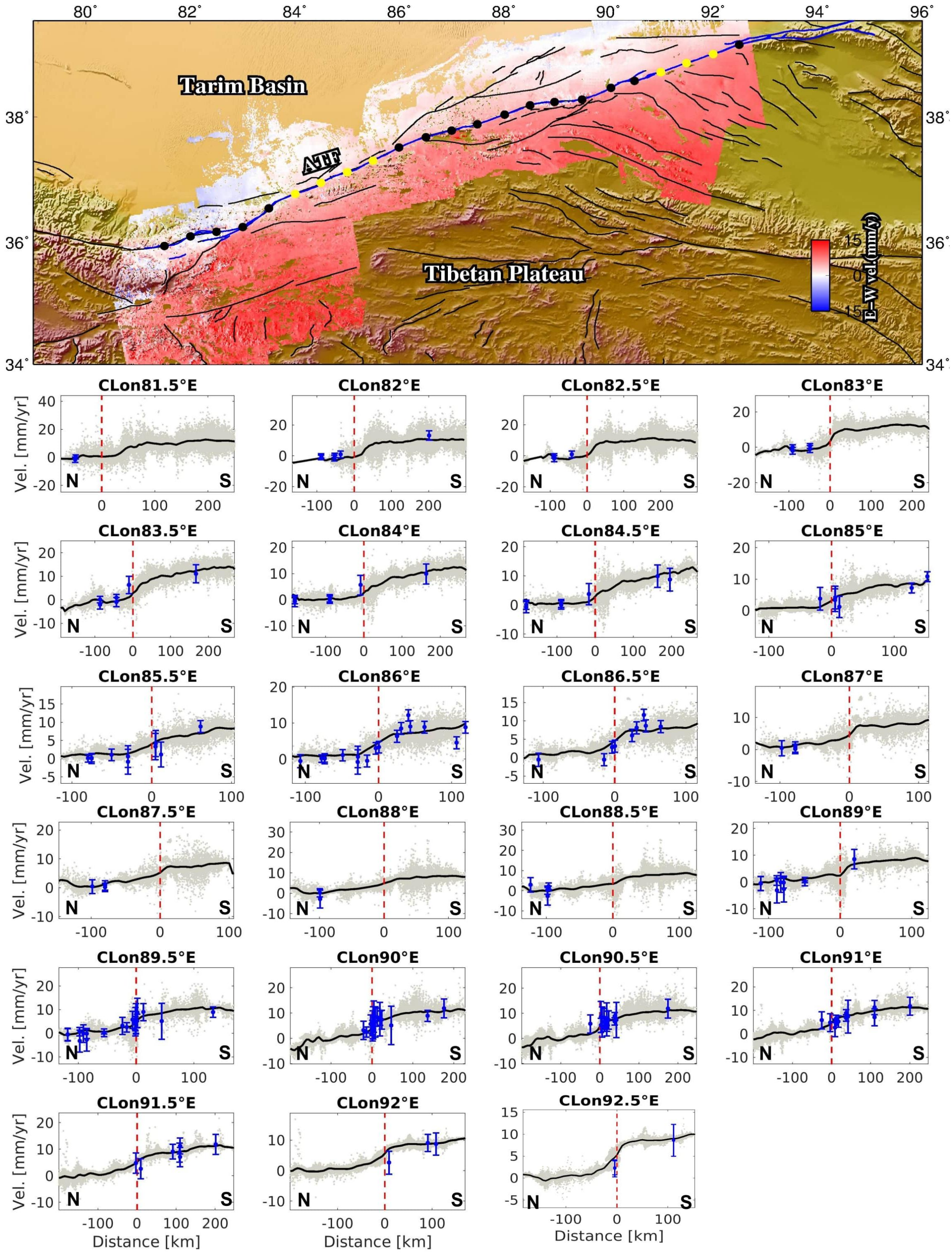
Tarim Basin
ATF
Tibetan Plateau
E-W vel.(mm/y)
CLon81.5°E
CLon82°E
CLon82.5°E
CLon83°E
CLon83.5°E
CLon84°E
CLon84.5°E
CLon85°E
CLon85.5°E
CLon86°E
CLon86.5°E
CLon87°E
CLon87.5°E
CLon88°E
CLon88.5°E
CLon89°E
CLon89.5°E
CLon90°E
CLon90.5°E
CLon91°E
CLon91.5°E
CLon92°E
CLon92.5°E
Vel. [mm/yr]
Distance [km]
N
S

Figure 4.11: Fault-parallel velocity profiles of the ATF derived from the east-west velocity field. The black and yellow points indicate the fault location of each profile on the high-resolution fault trace of the ATF (blue lines) (Elliott et al., 2018, 2015). The yellow points indicate locations for which the profiles show additional strain localisation south of the ATF. In the profile panels, the grey points are the mean fault-parallel velocities of points projected from within a 50 km perpendicular distance onto each profile; The black bold line represents the mean velocities binned by every 5 km along the profile; The red dashed lines show the mapped fault locations; The blue points are the resolved fault-parallel GPS velocities projected onto the profile with $\pm 2\sigma$ errorbars.

4.4.2 Interseismic deformation modelling

I derive the slip rate and locking depth for the individual fault-parallel velocity profiles along the ATF using the elastic half-space model (Savage and Burford, 1973) that I describe in Chapter 2. To explain the asymmetry in the interseismic velocities on each side of the fault, I incorporate an asymmetry coefficient in the model to characterise the different rigidity between the Plateau and the Tarim basin (e.g., Jolivet et al., 2008). As previous studies show that the proximity to the Euler pole of the rotation can lead to additional velocity variation in the fault-parallel velocity (e.g., Hussain et al., 2016a; Nocquet, 2012; Walters et al., 2014), I estimate a rotation rate for each profile south of the fault in the model to account for this. As profiles from 84°E to 85.5°E and profiles from 91°E to 92°E show additional strain localisation over strands south of the ATF (Fig. 4.11), I also solve for slip on secondary faults for these profiles. Therefore, the modified elastic half-space model for the profiles showing strain accumulated along the ATF can be expressed as

$$v_p = \begin{cases} \frac{2S\gamma}{\pi} arctan(\frac{x+l}{d_1}) - C(\frac{1}{\pi} arctan(\frac{x+l}{d_2}) \\ -H(x+l)) + \theta(x+l) + a, & \text{if x+l} \geq 0 \\ \frac{2S(1-\gamma)}{\pi} arctan(\frac{x+l}{d_1}) - C(\frac{1}{\pi} arctan(\frac{x+l}{d_2}) \\ -H(x+l)) + a, & \text{if x+l} < 0 \end{cases}$$
$$where \quad H(x+l) = \begin{cases} 1 & \text{if x+l} \geq 0 \\ 0 & \text{if x+l} < 0 \end{cases} \quad and \quad \gamma = \frac{R_b}{(R_p + R_b)} \tag{4.6}$$

where v_p is the fault parallel velocities, S is the slip rate, x is the perpendicular distance to the fault trace, l is the horizontal shift between the fault trace and buried dislocation, d_1 is the locking depth, C is the creep rate, d_2 is the creep depth, $H(x)$ is the Heaviside function, θ is solved to correct the rotation effect, γ represents the ratio of the rigidity in the Tibetan Plateau, R_p, and the Tarim block R_b, and a is a static offset.

For profiles showing strain localisation over other southern strands, I solve for the additional slip rate S_2, locking depth d_3 and buried dislocation shift l_2 as

$$v_p = \begin{cases} \frac{2S\gamma}{\pi} arctan(\frac{x+l}{d_1}) - C(\frac{1}{\pi} arctan(\frac{x+l}{d_2}) \\ -H(x+l)) + \theta(x+l) + \frac{S_2}{\pi} arctan(\frac{x+l_2}{d_3}) + a, & \text{if x+l} \geq 0 \\ \frac{2S(1-\gamma)}{\pi} arctan(\frac{x+l}{d_1}) - C(\frac{1}{\pi} arctan(\frac{x+l}{d_2}) \\ -H(x+l)) + \frac{S_2}{\pi} arctan(\frac{x+l_2}{d_3}) + a, & \text{if x+l} < 0 \end{cases} \tag{4.7}$$

$$where \quad H(x+l) = \begin{cases} 1 & \text{if x+l} \geq 0 \\ 0 & \text{if x+l} < 0 \end{cases} \quad and \quad \gamma = \frac{R_b}{(R_p + R_b)}$$

I find the optimal values for each model parameter through the Bayesian Markov chain Monte Carlo (MCMC) approach that I describe in Chapter 2. Prior constraints in the MCMC sampler for model parameters are: $0 < S < 30$ mm/yr, $0 < d_1 < 40$ km, -100 $< l <$ 100 km, -100 $< a <$ 100 mm/yr, 0.5 $< \gamma <$ 1, $0 < C <$ 10 mm/yr, $0 < d_2 < 40$ km, $0 < S_2 < 30$ mm/yr, $0 < d_3 < 10$ km, -300 $< l_2 <$ 0 km assuming a uniform probability distribution over each range. I fit a linear trend through the resolved fault-parallel far-field GPS velocities south of the fault and the estimated mean rotation rate is 0.0122 mm/yr/km. Therefore, I constrain the rotation rate, θ, between 0 and 0.03 mm/yr/km. In addition, I constrain the creep depth, d_2, to be shallower than the locking depth, d_1, and enforce the horizontal shift of the buried dislocation for the additional strain localisation in the south, l_2, to be greater than the shift to the strain along the ATF, l. The model runs over 300,000 iterations to arrive at a converged model that fits the data well (Fig. B.3) and to have a sufficiently sampled PDF (Fig. B.4).

The maximum a posteriori probability (MAP) solution reveals a systemic decrease in fault slip rate along the ATF (Fig. 4.12b), from 12 mm/yr to 8 mm/yr along the western portion (from 80 °E to 84 °E) to the central portion (from 84 °E to 88 °E) of the fault, whereas it increases to 10 mm/yr over the eastern portion (from 88 °E to 93 °E). The general eastward decrease in slip rate reveals that a significant proportion of the India-Asia convergence is not transferred into eastward extrusion of the Tibetan Plateau as expected in the 'rigid block' model (Zhang et al., 2007), whereas the increase in slip rate over the eastern portion is likely to ascribe to the strain distributed over the multiple conjugate strands in the south of this region.

The posterior probability distributions for the locking depth are generally lower than 20 km when the fault is shown as a single strand from 80 °E to 88 °E (Fig. 4.12c), which supports the small thickness of the elastic layer in the lithosphere (not exceeding ∼20 km) suggested by previous depth distribution of earthquakes in this region (Lasserre et al., 2005). The two high estimates explain the additional strain accumulation shown in the accordingly profiles. I interpret the higher estimates of locking depth from 88 °E eastward as a wider zone of strain localisation in this region where the fault breaks into three strands.

The slip results along the ATF reveals that, for most of the portions, the strain is generally accumulated along the main strand of the fault (Fig. 4.12b). However, results show that all strain accumulation occurs on the southern strand of the ATF to the west of 83 °E, which is structurally linked to the Longmu-Gozha Co strike-slip fault.

The additional buried dislocation for the profiles from 84°E to 85.5°E are ∼50 km to 150 km south of the ATF (Fig. 4.12a) in a location where other sinistral faults are located (Taylor and Yin, 2009). For the profiles over the eastern portion from 91°E to 92°E, the buried dislocation shifts ∼130 km southward to a region that features other multiple fault strands.

The modelling results also suggest that no significant creeping occurs along most portions of the ATF, except for ∼2 mm/yr of creep rate on the westernmost end of the fault and the region from 88.5°E to 90.5°E (Fig. 4.12d).

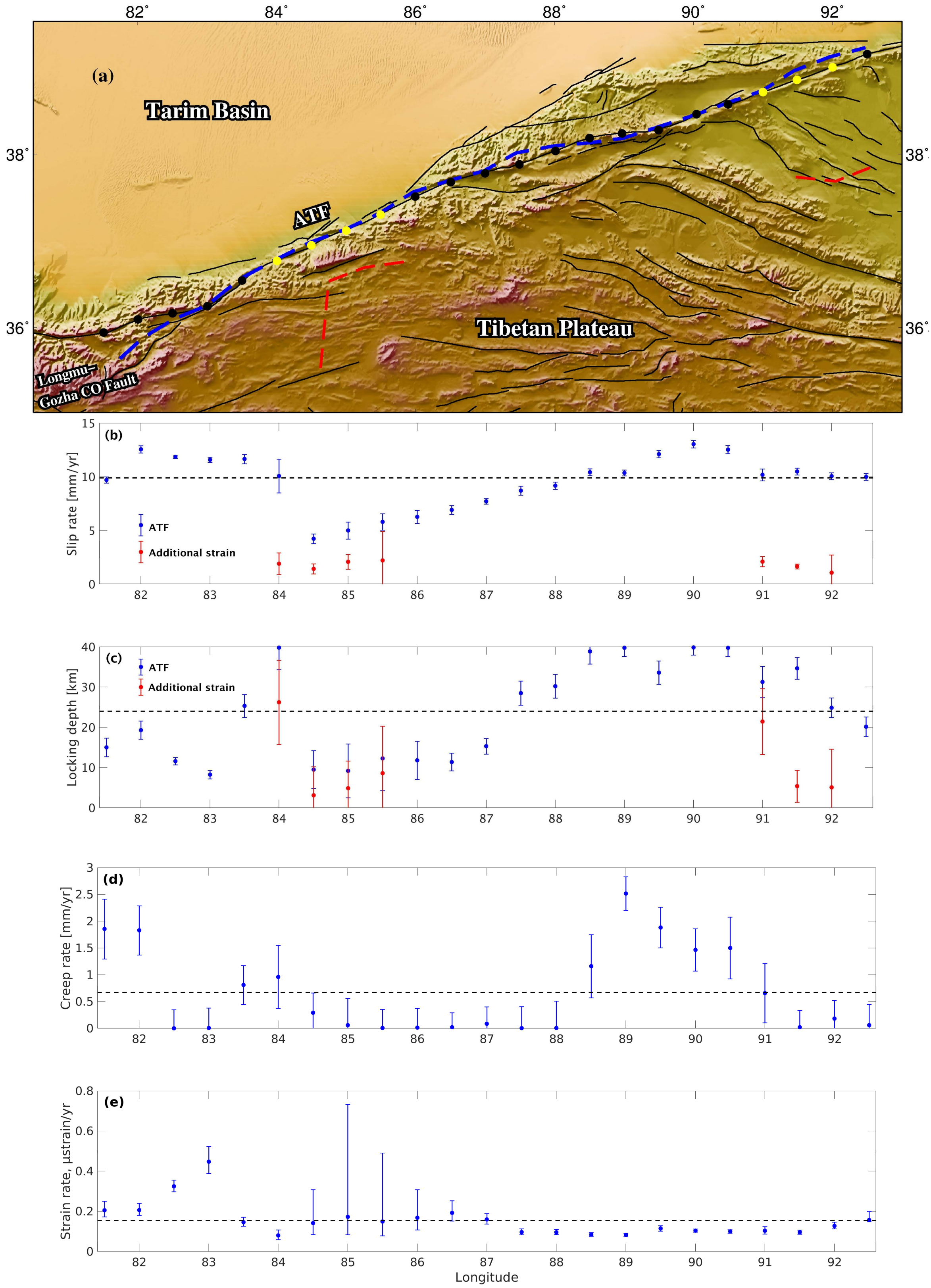

(a)
Tarim Basin
ATF
Tibetan Plateau
Longmu–Gozha CO Fault
82° 84° 86° 88° 90° 92°
36° 38°
(b)
Slip rate [mm/yr]
ATF
Additional strain
(c)
Locking depth [km]
ATF
Additional strain
(d)
Creep rate [mm/yr]
(e)
Strain rate, μstrain/yr
Longitude

Figure 4.12: Estimates of slip rate and strain rate along the ATF. The blue dashed line in the map (a) indicates the estimated locations of the buried dislocations along the ATF, and the red dashed lines show the estimated locations of the buried dislocations away from the ATF. The black dashed lines in (b) to (e) give the average estimate for each parameter. The errorbars represent the 68 % confidence bounds on the parameter estimates.

4.4.3 Strain rate inversion

To investigate the strain distribution along the ATF, I calculate the strain rate at the surface, $\dot{\varepsilon}$, from the estimated slip rate and locking depth along the main strand for each profile by differentiating the elastic half-space model as

$$\dot{\varepsilon} = \frac{S}{\pi d_1} \tag{4.8}$$

The results show a consistent strain rate along most of the fault (Fig. 4.12e), with an average value of 0.16 μstrain yr^{-1}. However, I find that high strain rate greater than 0.4 μstrain yr^{-1} is accumulating at the surface along the south-western strand of the ATF. Figure 4.12a and 4.12b indicate that the high strain rate is mainly caused by the high slip rate in this region, implying that there may be a relatively higher earthquake potential.

4.5 Discussion

4.5.1 Strain accumulation in broad shear zones

The field-based investigations of slip rates on the ATF show both strong strain localisation along the fault and an unquantified amount of distributed deformation across broader shear zones (Cowgill et al., 2009). The broad shear zones could result from multiple strands of the ATF itself or other fault strands that are away from the ATF, which has been observed in the San Andreas Fault system (e.g., Savage et al., 1979a) and the North Anatolian Fault (Hussain et al., 2018). To investigate the pattern of the strain localisation along the ATF, I fit a shear zone model (e.g., Prescott and Nur, 1981) to each fault-parallel velocity profile to derive the width of the shear zone individually.

In contrast to the elastic half-space model, which features stable sliding of a single narrow fault beneath a locked elastic lid, the shear zone model has a distributed deformation at depth. The distributed shear strain can result in a broader shear zone compared to the strain concentrated on the single master fault (Prescott and Nur, 1981). The velocity observed at the surface is modelled as

$$
\begin{aligned}
V_p = \frac{S}{2\pi(c-b)}\{(\pi(c-b) + 2((x+l)-b))\arctan\frac{((x+l)-b)}{d_1} \\
+2(c-(x+l))\arctan\frac{((x+l)-c)}{d_1} + d_1\log_{10}(d_1^2 + ((x+l)-c)^2) \\
-d_1\log_{10}(d_1^2 + ((x+l)-b)^2))\} + a \\
where \quad b = -c
\end{aligned}
\tag{4.9}
$$

where b and c are half of the shear zone width on each side of the solved buried dislocation.

I find the optimal values for each model parameter using the Bayesian MCMC approach that I describe in Chapter 2. Prior constraints in the MCMC sampler for model parameters are: $0 < S < 30$ mm/yr, $0 < d_1 < 40$ km, -150 $< l <$ 150 km, -100 $< a <$ 100 mm/yr and $0 < c < 200$ km assuming a uniform probability distribution over each range. The model runs over 300,000 iterations to arrive at a converged model that fits the data well (Fig. B.5) and to have a sufficiently sampled PDF.

The results reveal two sections with broad shear zone along the ATF: ∼122 km between 84°E to 85.5°E, and ∼94 km between 91°E to 91.5°E (Fig. 4.13), which are consistent with the region that I infer additional strain localisations from the fault-parallel velocity profiles. Over these areas, the results suggest that the strain is distributed over multiple strands rather than concentrates on a single strand. According to the USGS earthquake catalogue, strands in these areas have been active recently, recording four earthquakes ($M_w > 5.0$) in the year of 1960, 2000, 2007 and 2016, respectively. The wider shear zones explain the high estimates of the locking depth solved from the elastic half-space model in these areas. The modelling results also reveal a relatively wider shear zone of ∼62 km between 87.5°E to 88°E in the location where the ATF breaks into three parallel strands.

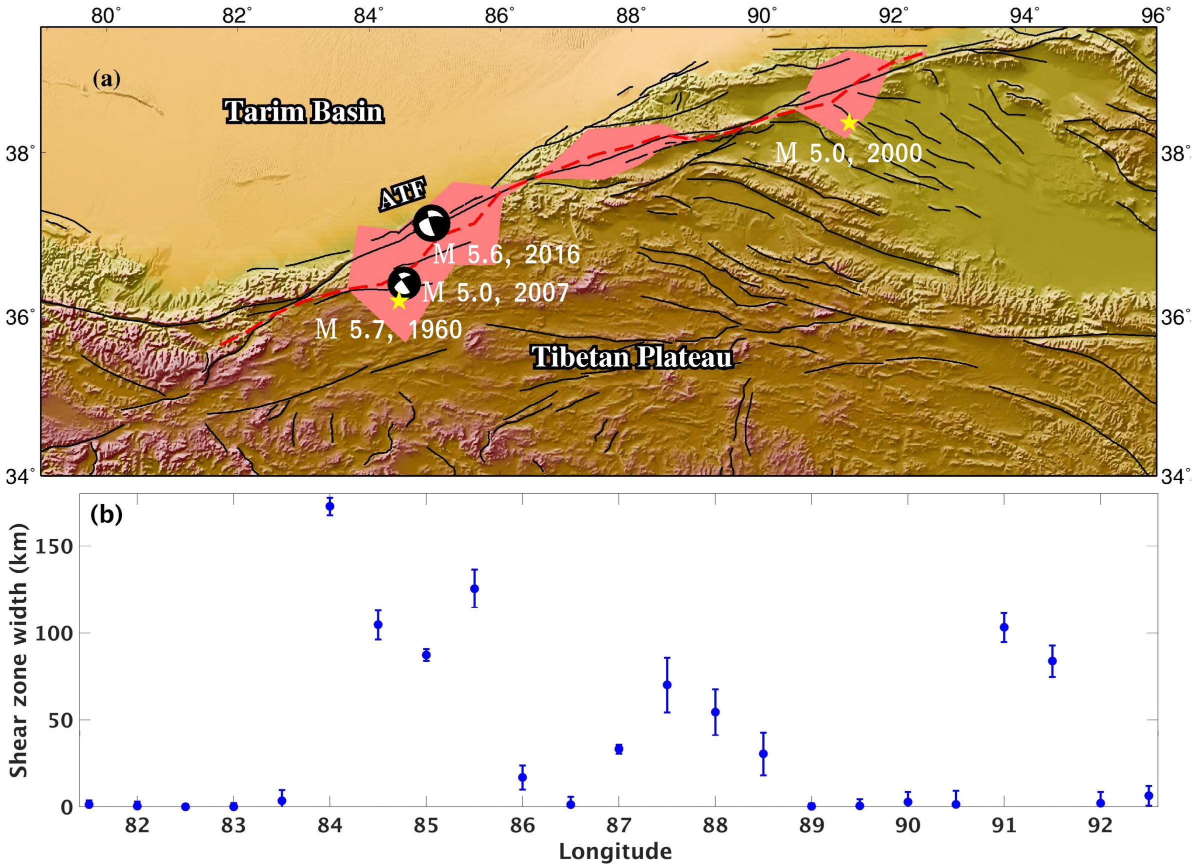

Figure 4.13: Estimated shear zones along the ATF. Light red areas (a) represent the locations of the estimated shear zones along the ATF, and blue points (b) give the estimated width of the shear zones. The red dashed line indicates the locations of the buried dislocations of the ATF estimated from the shear zone model. Yellow stars and focal mechanism solutions represent four earthquakes ($M_w > 5.0$) which have occurred recently in the region that features broad shear zones. The blue errorbars in (b) represent the 68 % confidence bounds on the estimates.

4.5.2 Comparisons to the published slip rates

To investigate any apparent discrepancies, I compare the slip rates estimated in this study to the published slip rates along the ATF (Fig. 4.14).

The western portion from 80.5°E to 84°E is hardly covered by previous studies. At 84°E, I find a total slip rate of 12.0 ± 3.7 mm/yr, which is a sum of the slip rate along the main strand and the slip rate on secondary faults. It is consistent with previous estimates of 7.8–10.2 mm/yr (Xu and Zhu, 2019) and 10–16 mm/yr (Cowgill et al., 2003).

For the central portion from 84.5°E to 85.5°E, I find a total slip rate of 7.0 ± 3.6 mm/yr on average, which is comparable to the published slip rates of 8–12 mm/yr at 85°E (Zhang et al., 2007) and 10.5 mm/yr at 85.5°E (Daout et al., 2018). At 86°E, I obtain slip rate of 6.3 ± 0.6 mm/yr that is consistent with previous estimate of 6–16 mm/yr there (Elliott et al., 2008). The lower slip rates over this region can be explained by the wider shear zones revealed in this study. From 86.5°E to 90°E, the estimated slip rates show a systematic increase and the magnitudes are consistent with most previous modelling of slip rates over this region (e.g., He et al., 2013b; Vernant, 2015).

For the eastern portion from 90.5°E to 92.5°E, Washburn et al. (2003) got slip rate of 10–20 mm/yr at 91.5°E that is consistent with a total slip rate of 12.1 ± 0.4 mm/yr estimated in this study. At 92°E, I find a total slip rate of 11.1 ± 1.6 mm/yr, which is consistent with previous estimate of 7–11 mm/yr in this region (Chen et al., 2000).

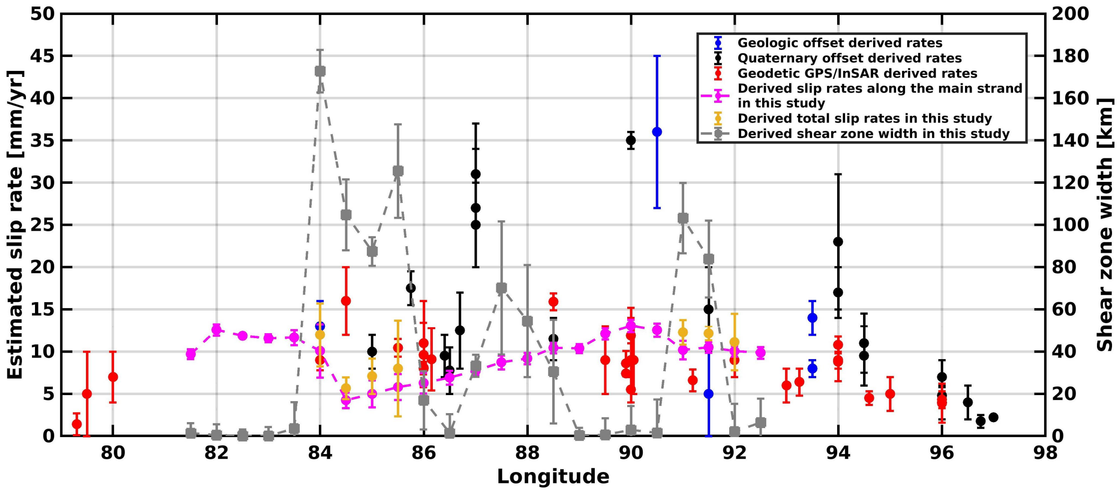

Figure 4.14: Comparisons of slip rates along the ATF between previous measurements (Fig. 4.2) and the estimates derived in this study. The magenta and yellow points show the slip rates derived in this study. The grey squares indicate the shear zone width estimated along the ATF in this study. The magenta, yellow and grey errorbars represent the 95 % confidence bounds on the estimates.

4.5.3 Slip rates on a strike-slip fault in Central Tibet

In Central Tibet, there are a series of conjugate strike-slip fault systems to accommodate east-west extension and north-south contraction there. The systems consist of several right-lateral strike-slip faults in the south, paired with left-lateral faults in the north. Based on the estimated east-west velocity field, I derive four fault-perpendicular profiles along one of the left-lateral strike-slip faults near 84 °E in Central Tibet (Fig. 4.15a), and find slip rates of ∼5 mm/yr over its eastern portion (Fig. 4.15b). The estimates are consistent with previous modelling of slip rates on conjugate strike-slip fault systems in Central Tibet (Taylor and Peltzer, 2006).

Furthermore, profiles that derived from the sub-vertical velocity field in this region reveal a systematic sub-vertical signal of around 4–5 mm/yr that is aligned with the Jinsha suture (Fig. 4.15d). The signal is quite short-wavelength and has a relatively sharp transition. Also, it is "domed" in shape that the signal decreases back down a little south of the suture.

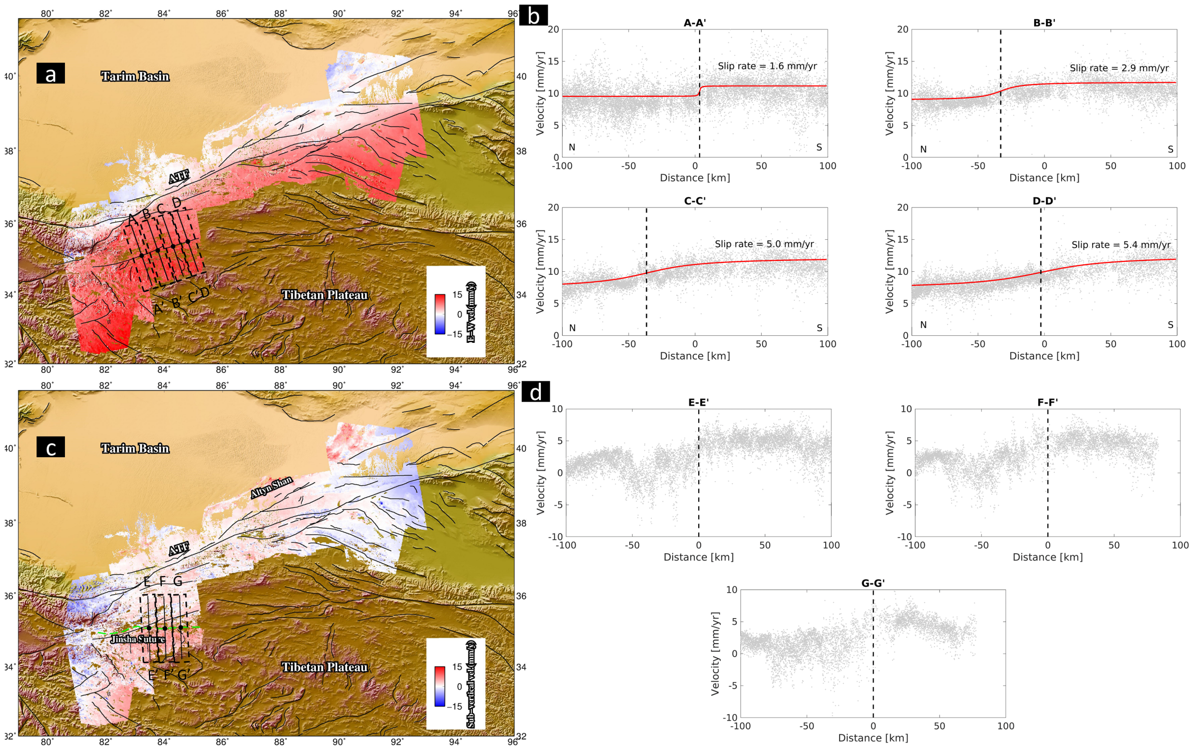

Figure 4.15: Fault-parallel velocity profiles derived from the east-west velocity field (a) along a strike-slip fault (b), and velocity profiles derived from the sub-vertical velocity field (c) along the Jinsha suture (d). Red curves in (b) indicate the optimal solutions of slip rates on the strike-slip fault. Black dashed lines in (b) represent the estimated locations of the buried dislocations. Black dashed lines in (d) represent the location of the Jinsha suture.

4.5.4 High strain rate over the south-western portion

The strain rates estimated from the elastic half-space model reveal higher values along the south-western segment of the ATF, a region that is hardly covered by previous studies (Fig. 4.2). The results show that the clear strain accumulation occurs along the south-western segment, which is structurally linked to another ENE-striking left-lateral strike-slip Longmu-Gozha Co Fault (LGCF) in the west through the Ashikule step-over zone.

This region has been highly active recently on which four major earthquakes ($M_w > 6.3$) have occurred in the year of 2008, 2012, 2014 and 2020, respectively, including the 2008 M_w 7.2 Yutian normal faulting earthquake, which is the largest normal faulting event ever recorded in northern Tibet, the 2012 M_w 6.3 normal faulting earthquake and the 2014 M_w 6.9 Yutian strike-slip earthquake. The estimated slip rate of ~12 mm/yr along the south-western segment of the ATF is much higher than that of the LGCF fault, which is believed to be less than 4 mm/yr (Chevalier et al., 2017; Wang and Wright, 2012). The results suggest that the generation of the SN-trending normal faulting events in the region is ascribed to the EW-trending extensional stress at a step-over between the two left-lateral faults (Elliott et al., 2010; Furuya and Yasuda, 2011; Xu et al., 2013), where the North-South shortening occurs.

To investigate the impact of postseismic deformation following the 2014 M_w 6.9 Yutian strike-slip earthquake, which occurred nine months before the InSAR observations of this study, I calculate the time series of relative LOS displacement between two sites located around 30 km apart, either side of the south-western segment(Fig. 4.16). I calculate the average LOS displacement of points within 2 km distance to each site from the tropospheric corrected single master interferograms, to form a time series of relative LOS displacement between the two sites, and then I fit a linear trend to it. I find a generally consistent rate in the ascending track. For the descending track, however, the displacement in the early time series (673 days before the earthquake occurred) has a systematic bias of being mostly below the estimated linear trend, indicating a higher rate before November 2015 compared to the later time series. I also fit a logarithmic decay trend to the time series as

$$d = a\log(1 + \frac{\triangle t}{T}) \tag{4.10}$$

where d is the relative LOS displacement, a is the amplitude of the transient, T is the Maxwell relaxation time and $\triangle t$ is the time since the earthquake occurred. The best fit model shows that the Maxwell relaxation time is ~1 year for both tracks. However, compared to the linear model, there is no significant improvement when fitting the data with the logarithmic model. This suggests that the postseismic deformation is hard to distinguish from the long term interseismic deformation.

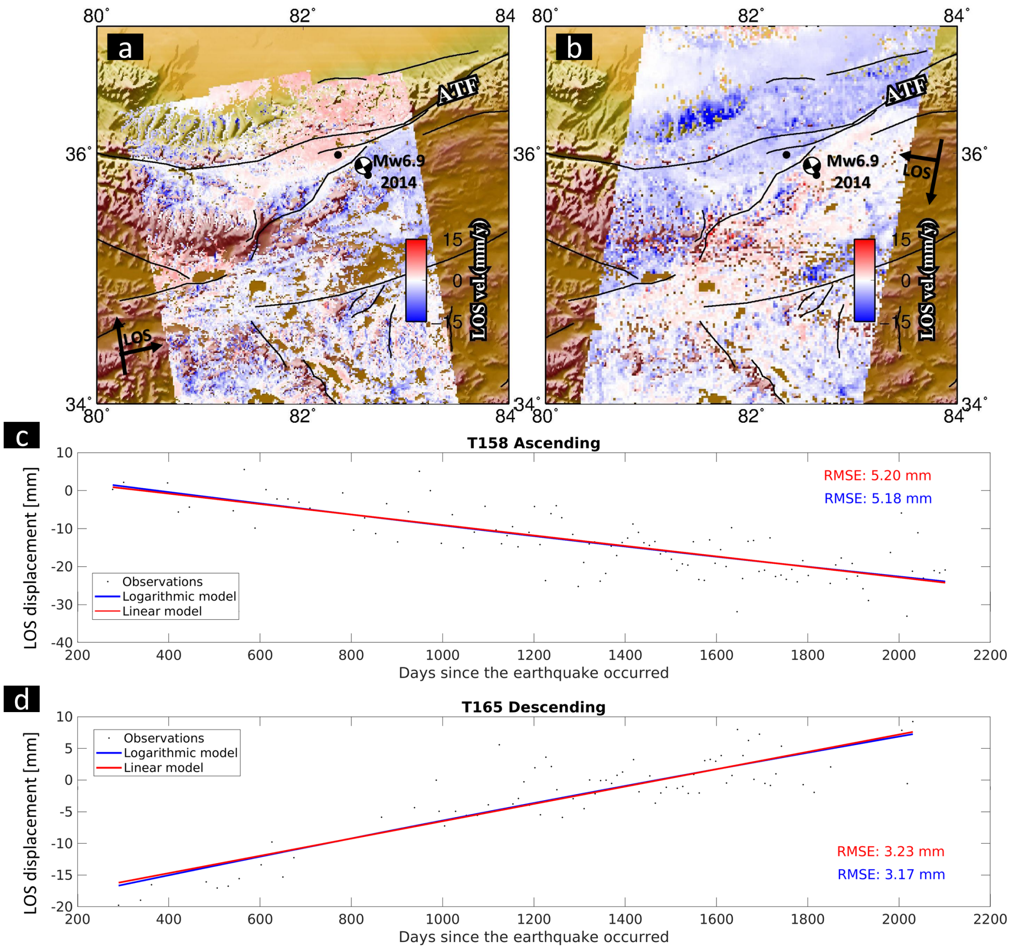

Figure 4.16: Temporal evolution of LOS displacement between two sites on either side of the south-western segment of the ATF. (a) and (b) show the InSAR LOS velocity fields of the ascending track 158 and the descending track 165, respectively. Black points in (a) and (b) represent the locations of two sites. The focal mechanism indicates the 2014 M_w 6.9 Yutian earthquake. Black scatters in (c) and (d) show the time series of the relative LOS displacement between the two sites for the ascending and descending track, respectively. Blue and red lines represent the best fit logarithmic and linear model to the time series, respectively.

Additionally, previous studies show that these recent large earthquakes have significantly increased the stress in this region (e.g., Bie and Ryder, 2014; Li et al., 2020, 2015). Bie and Ryder (2014) calculated the combined stress loading effect of the 2008, 2012 and 2014 earthquakes on the ATF and found that both the 2008 and 2012 normal faulting earthquake exert positive Coulomb stress changes to the 2014 strike-slip earthquake rupture. Li et al. (2015) and Li et al. (2020) found that the 2014 Yutian strike-slip earthquake has further increased the Coulomb failure stress on the south-western segment of the ATF. Therefore, the high strain rate estimated over the south-western portion might be ascribed to the stress loading effects of the recent seismic activities. Although it is not possible to rule out the impact from the postseismic deformation following the 2014 Yutian earthquake, the high strain rate on the south-western segment of the ATF may suggest a relatively greater seismic risk in this region, where another shallow earthquake with magnitude 6.4 occurred on 25th June 2020 most recently.

4.6 Conclusions

This chapter shows the interseismic deformation along the ATF from InSAR measurements, over a large-scale of ~1500 km. I apply the new tropospheric correction method that I describe in Chapter 3 to mitigate the tropospheric effects in the interferograms. I present a new scheme for stitching InSAR LOS velocities estimated from multiple tracks and derive a consistent velocity field over an extensive spatial scale. I find a systemic decrease of the slip rate along the ATF from 12 mm/yr to 8 mm/yr over the western portion to the central portion, whereas it increases again to 10 mm/yr over the eastern portion, using a modified elastic half-space model. This study shows significant strain accumulation along the 1500 km length of the ATF, and that it is fast at about 10 mm/yr and quite localised along the fault. Since no major earthquake ($M_w > 7.0$) has occurred along the ATF since the 1924 events, a slip deficit of ~1 m has been accumulated over the last century. Consequently, the ATF is capable of rupturing along its entire length with the potential for some of the largest earthquakes on the continents. The results also show a high strain rate greater than 0.4 μstrain yr^{-1} along the south-western segment of the fault, implying that there might be a relatively greater earthquake potential in this region compared to other portions.

Chapter 5

Constraints on the 2018 M_W 7.5 Palu earthquake from coseismic surface deformation

This chapter addresses the fourth objectives of my thesis, by presenting a finite fault solution to characterise the coseismic surface deformation field for the 2018 M_w 7.5 Palu earthquake that ruptured approximately 200 km.

5.1 Introduction

The 28 September 2018 M_w 7.5 Palu earthquake ruptured approximately 200 km of the Palu-Koro strike-slip fault in northwestern Sulawesi, Indonesia (USGS, 2018). Large tsunami waves arrived quickly, 2–5 minutes after the earthquake (Takagi et al., 2019; Yalciner et al., 2018) and caused more than 4,000 casualties. The left-lateral strike-slip faulting mechanism with approximately north-south orientation suggested by the centroid moment tensor (USGS, 2018) is consistent with previous tectonic studies in this region (Bellier et al., 2001; Socquet et al., 2006; Walpersdorf et al., 1998; Watkinson and Hall, 2017).

The Palu-Koro fault is a major active tectonic feature, marking the convergence of the India-Australia, Sunda and Pacific-Philippines plates with the Sulawesi block located at the triple junction (Fig. 5.1). This left-lateral strike-slip fault has a NNW-SSE trend and cuts across the island of Sulawesi (Bellier et al., 2006). Geological (Bellier et al., 2006), geomorphological (Bellier et al., 1998, 2001) and geodetic observations (Socquet et al., 2006; Walpersdorf et al., 1998) clearly indicate that the Palu-Koro fault is a very active fault system. By accommodating the left-lateral relative plate motion, the current slip rate along the Palu-Koro fault is estimated to be approximately 40 mm/yr (Bellier et al., 2001; Walpersdorf et al., 1998).

Pelinovsky et al. (1997) and Prasetya et al. (2001) attributed three tsunamis over the last century to earthquakes that occurred on the Palu-Koro zone, although the inferred source mechanisms indicate thrust and normal earthquakes for those events rather than the strike-slip motion that dominated in the 2018 event. The tsunami that devastated the coast of Palu Bay in 2018 is rare as its amplitude is surprisingly large for a strike-slip faulting earthquake, with runup heights over 8 m measured in field surveys (Fritz et al., 2019; Muhari et al., 2018; Omira et al., 2019). Most large tsunamis that exceed runup heights of 10 m have been associated with the vertical motion during tremors or submarine landslides (e.g., Kawamura et al., 2012). However, the magnitudes of tsunamis generated by strike-slip earthquakes are generally much smaller, due to the lack of vertical deformation (e.g., Gusman et al., 2017; Hornbach et al., 2010; Legg et al., 2003).

Although some studies advocate that landslides triggered the tsunami in this event (e.g., Arikawa et al., 2018; Heidarzadeh et al., 2019; Pakoksung et al., 2019; Sassa and Takagawa, 2019; Takagi et al., 2019), the quaternary activity of the Palu-Koro fault shows features of transtensional fault system (Katili, 1970; Watkinson and Hall, 2017), which can induce dip-slip motions in a strike-slip dominated faulting. The fault may then produce significant coseismic vertical deformation beneath the bay when ruptured, which could generate large tsunami amplitudes. Therefore, the coseismic displacement field is crucial to explain the direct cause of the tsunami in this event, which could also shed light on the nature of tsunamis generated from strike-slip earthquakes.

Recent studies have provided insights into possible tsunami genesis through coseismic deformation (e.g., Aránguiz et al., 2020; Jamelot et al., 2019; Socquet et al., 2019; Ulrich et al., 2019; Williamson et al., 2020). For instance, Song et al. (2019) and Ulrich et al. (2019) advocated for a tsunami generated purely through coseismic deformation based on InSAR observations and a teleseismically validated dynamic rupture scenario respectively. Alternatively, Williamson et al. (2020) and Aránguiz et al. (2020) argued for a contribution of both coseismic deformation and landslides to the large tsunami near Palu city. However, datasets used for the inversion of fault slip solutions in some of the studies are not comprehensive enough (e.g., Socquet et al., 2019; Williamson et al., 2020), which could lead to ambiguous conclusions. Furthermore, although the onshore parts of the rupture have been characterised well, the fault strand under the Palu bay, where the rupture has the key tsunami potential, was poorly constrained in previous research (e.g., Aránguiz et al., 2020; Bacques et al., 2020; Fang et al., 2019; He et al., 2019; Socquet et al., 2019; Ulrich et al., 2019).

In this chapter, I present a finite fault solution in a Bayesian inversion framework to estimate a high-resolution 3-D coseismic surface deformation field. To constrain the surface deformation in the coseismic modelling, I use a more complete geodetic dataset, including both continuous and campaign coseismic GPS displacement fields combined with multiple kinds of SAR-derived coseismic displacement fields. Previous geodetic studies were based on satellite observations only (Socquet et al., 2019; Williamson et al., 2020). I investigate possible seismic slip scenarios and fault orientation along the rupture. As parts of the fault strand run below Palu bay, there are no surface observations that precisely locate the course of the rupture. In this study, I test four different scenarios that cover possible fault geometries over the bay, to provide better constraints on surface displacement in this region, compared to previous models based on a fixed geometry over the bay (Aránguiz et al., 2020; Bacques et al., 2020; Fang et al., 2019; He et al., 2019; Socquet et al., 2019; Ulrich et al., 2019).

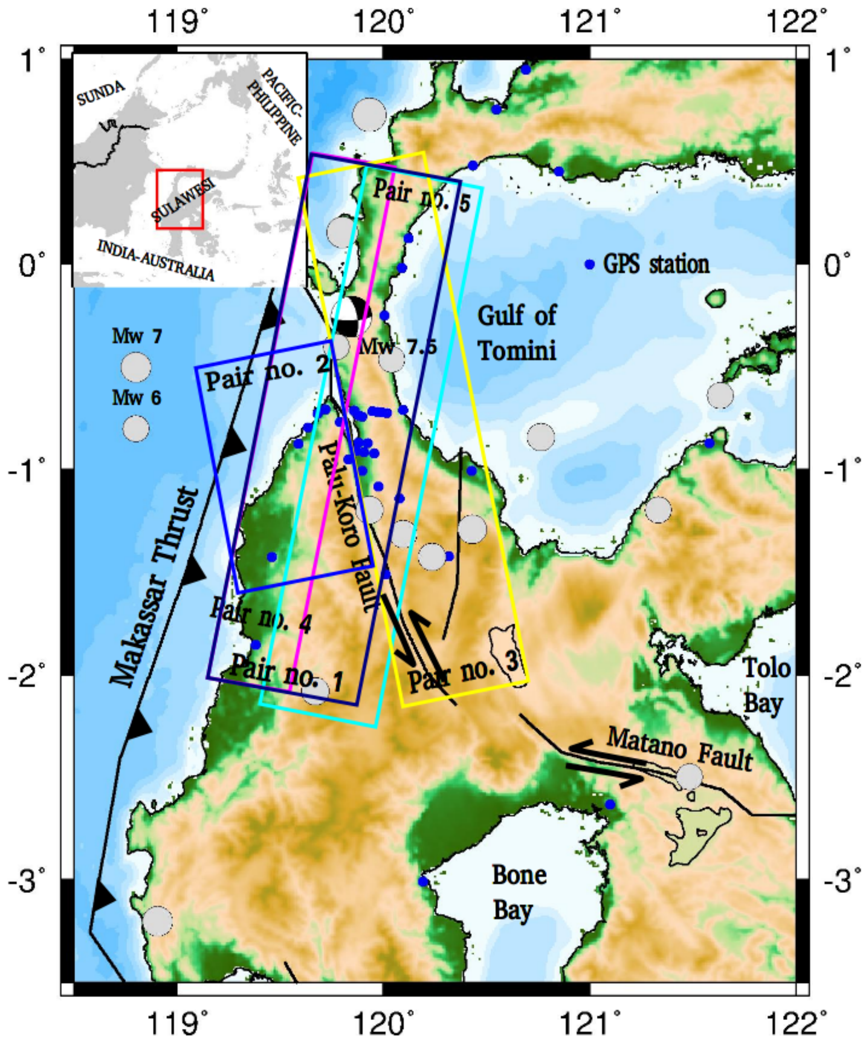

Figure 5.1: Tectonic setting of Sulawesi island. Focal mechanism solution represents the 2018 M_w 7.5 earthquake. Grey points represent major earthquakes ($M_w > 6.0$) with a shallow depth (< 25 km) have occurred in this region since 1900. Colourful polygons indicate the extent of SAR-derived data and blue points are the GPS sites. The background shows the elevation of the study region derived from the Shuttle Radar Topography Mission (SRTM) 3-arc seconds data (Farr et al., 2007), which is also applied to the subsequent figures.

5.2 Geodetic data acquisitions

5.2.1 SAR-derived dataset

As I summarise in Chapter 1, the pixel-offset tracking and the Multiple Aperture Interferometry (MAI) are complementary to InSAR measurements when deriving 3-D surface displacement field for the north-south striking strike-slip faults (Bechor and Zebker, 2006). Since the Palu-Koro has a NNW-SSE trend that is nearly parallel to the azimuth direction of the satellite, InSAR is not sensitive to the north-south strike-slip motion, which dominated in this event. To characterise the coseismic displacement field in three dimensions, I use multiple kinds of SAR-derived dataset from the L-band ALOS-2 sensor, which has better coherence in vegetated regions like Sulawesi island compared to SAR sensors in C-band. The SAR-derived dataset that I incorporate in the coseismic modelling is constructed from a pair of Scanning Synthetic Aperture Radar (ScanSAR) data and four pairs of Stripmap data (Simons et al., 2021), which cover the whole deformation area in both ascending and descending direction (Table 5.1). In contrast to stripmap mode data, which has an approximately constant incidence angle, the antenna beam of ScanSAR mode data switches periodically in the range direction during the operation and so can achieve a much wider swath coverage (Liang and Fielding, 2017). ALOS-2 stripmap mode acquires data with an 70 km swath at 10 m by 10 m spatial resolution, whereas ALOS-2 ScanSAR mode obtains data with an 350 km swath at 100 m by 100 m spatial resolution. The dataset includes three interferograms for measuring the deformation in the line-of-sight (LOS) direction with high precision, two estimates derived from the MAI for the along-track displacements, and six estimates derived from pixel-offset tracking in both azimuth and range directions (Fig. 5.2).

Table 5.1: SAR-derived dataset from the ALOS-2 used in this study.

Pair no.	Date (yyyy.mm.dd)	Mode	Azimuth direction	Data used in coseismic modelling
1	2018.08.21 2018.10.02	ScanSAR	Desc.	InSAR
2	2018.08.08 2018.10.03	Stripmap	Asc.	InSAR, Azimuth offset, Range offset, MAI
3	2018.08.17 2018.10.12	Stripmap	Asc.	InSAR, Azimuth offset, Range offset, MAI
4	2018.04.17 2018.10.16	Stripmap	Desc.	Range offset
5	2018.03.01 2018.10.25	Stripmap	Desc.	Range offset

5.2.2 GPS dataset

Besides the SAR-derived dataset, I also incorporate the coseismic displacement field measured by 51 GPS stations in the coseismic modelling, including five continuous stations and 30 campaign sites in and around Palu, plus another 16 sites in the far-field (Fig. 5.2). The GPS network was developed by the Delft University of Technology and École normale supérieure, in cooperation with the Geospatial Information Agency and Bandung Institute of Technology (Simons et al., 2021). Combining multiple types of SAR-derived dataset with the GPS dataset, I provide more comprehensive datasets for the surface deformation field to constrain a finite fault, compared to previous studies based on satellite observations only (Socquet et al., 2019; Williamson et al., 2020).

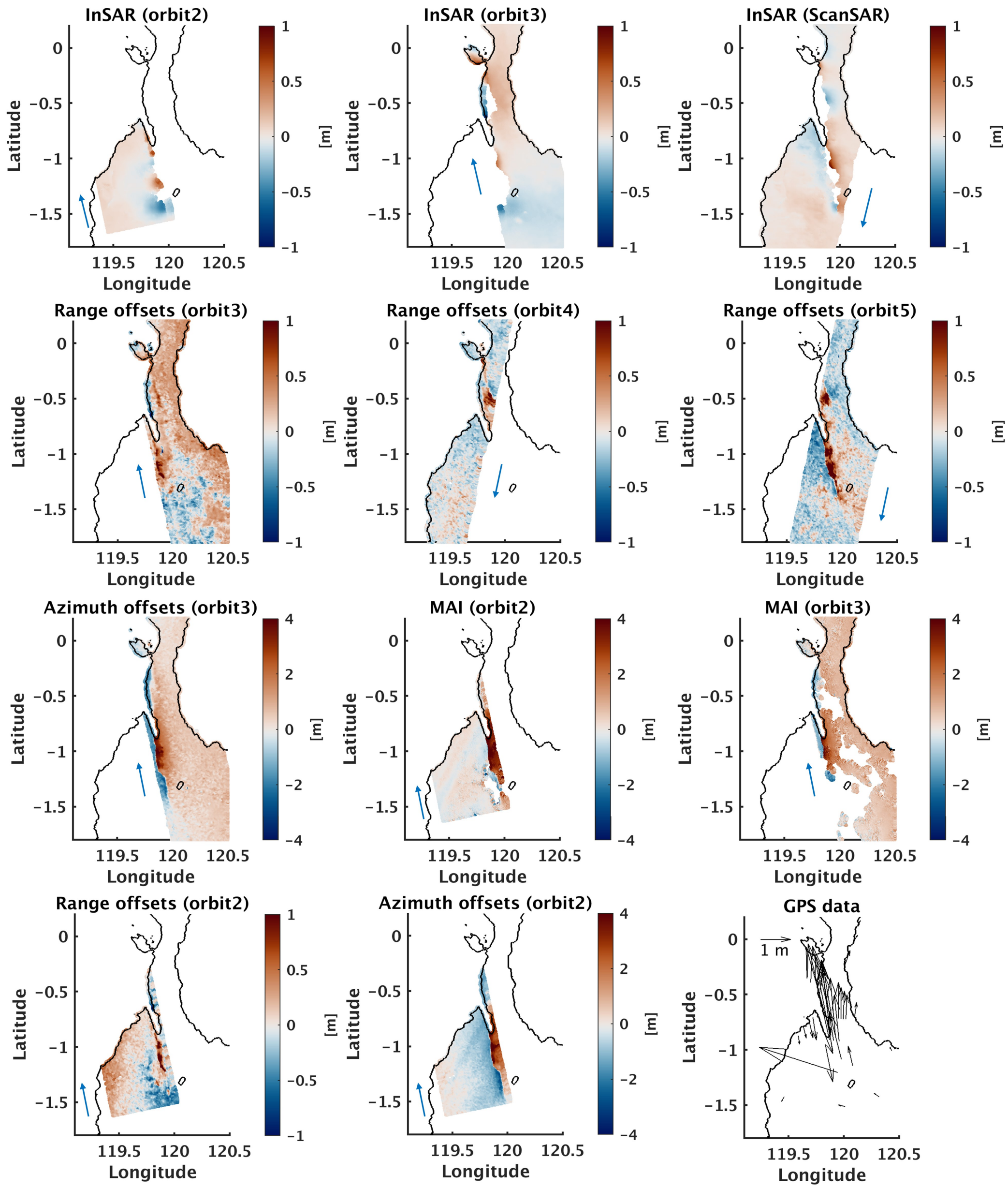

Figure 5.2: The SAR-derived data and the GPS data used in the coseismic modelling. Blue arrows represent satellite flight directions. Positive values in InSAR and Range offsets indicate the motion away from the satellite, whereas negative values show the motion towards the satellite. Positive values in Azimuth offsets and MAI indicate the motion toward the satellite flight direction, whereas negative values show the motion away from the satellite flight direction. Black arrows represent GPS observations. The GPS data is in the latest global reference frame solution IGS14 (Rebischung and Schmid, 2016), based on the International Terrestrial Reference Frame 2014 (ITRF2014) (Altamimi et al., 2016). I also show several datasets at page size (Fig. C.1) to indicate the quality of the SAR-derived data.

5.3 Data reduction and errors

I downsample each SAR-derived dataset in Fig. 5.2 to reduce the number of observation points using an adaptive quadtree sampling algorithm (Decriem et al., 2010). The algorithm divides the data into sets of four polygons until the variance of points within a polygon is lower than a given threshold. Data gaps are accounted for by applying a convex hull to the data points, which means that the polygons can be irregularly shaped. I adjust the variance threshold for each SAR-derived data set iteratively until the deformation field is well represented by the polygons. The final subsampled field of each SAR-derived data set is shown in Fig. 5.3.

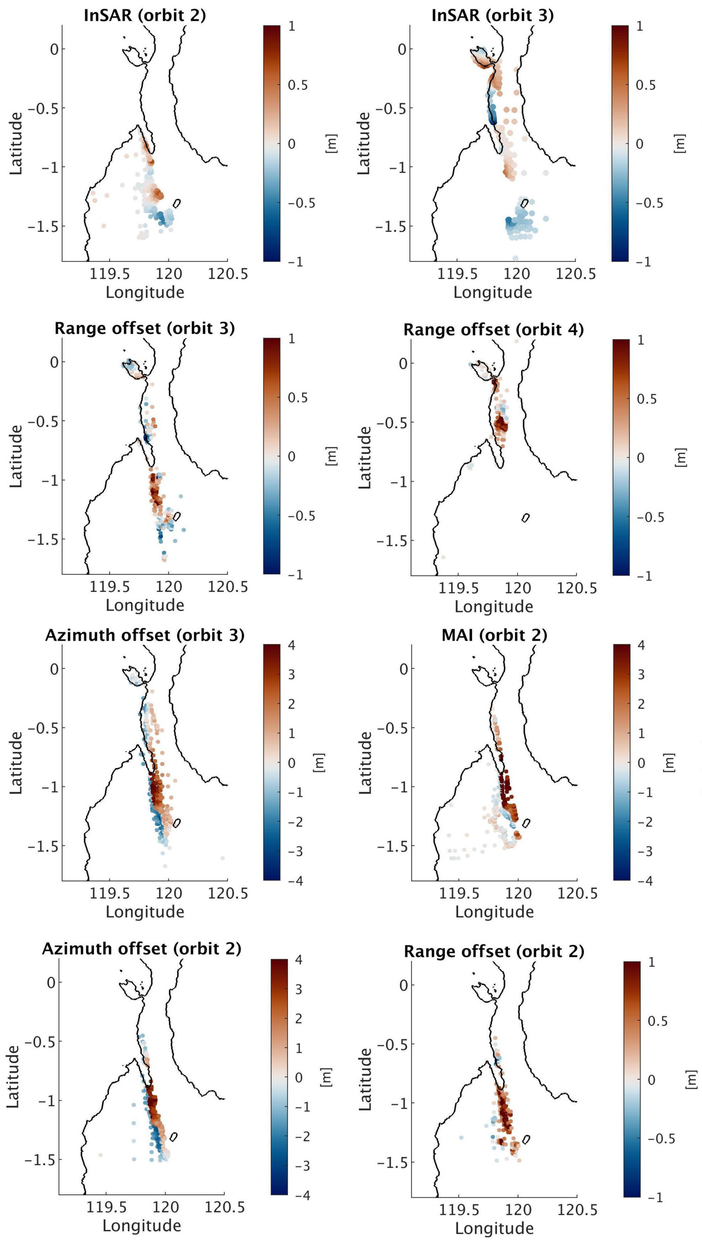

Figure 5.3: Subsampled SAR-derived datasets from an adaptive quadtree sampling algorithm (Decriem et al., 2010). The subsampled points cover the whole deformation field, and the density of these points is much higher in the near-field areas due to the high displacement gradients there.

I calculate data errors by estimating the variance-covariance matrix for each data set. The diagonal elements of the variance-covariance matrix for the GPS are variances of GPS displacements in each component (east, north and vertical) at each station. Assuming the displacements of the three components at each station are independent, I set all off-diagonal elements of the variance-covariance matrix for the GPS data to zero. I estimate the variance-covariance matrix for the SAR-derived data by computing a 1-D experimental semivariogram $\hat{\gamma}(h)$ over the non-deforming region using the deramped displacements d for each data set (Bagnardi and Hooper, 2018; Jolivet et al., 2012; Sudhaus and Jónsson, 2009).

$$\hat{\gamma}(h) = \frac{1}{2N}\sum_{i=1}^{N}(d(\mathbf{r}_i) - d(\mathbf{s}_i))^2 \tag{5.1}$$

Here h is the lag distance, N number of data points in each distance bin, and the distance between sample points $\mathbf{r}_i$ and $\mathbf{s}_i$ falls in bin h. I fit an exponential function $\gamma(h)$ to the experimental semivariogram. Variance and covariance $\Sigma(0)$ and $\Sigma(h)$ are related to the semivariogram by:

$$\gamma(h) = \Sigma(0) - \Sigma(h) \tag{5.2}$$

The SAR covariance as a function of distance h then reads (Bagnardi and Hooper (2018)):

$$\Sigma(h) = \begin{cases} s & \text{if } h = 0 \\ (s - s_0)e^{(\frac{-h}{r})} & \text{if } h > 0 \end{cases} \tag{5.3}$$

with s, sill variance, s_0, nugget variance and r, range. The nugget is spatially independent noise, sill is the maximum of semivariance and range is the distance over which points are spatial correlated. The estimates of the sill, nugget and range are consistent with previous studies (Amey et al., 2018; Bagnardi and Hooper, 2018; Morishita et al., 2016), where pixel-offset tracking and MAI have lower precision and accuracy compared to InSAR (Table 5.2).

Table 5.2: Estimates of the semivariogram for SAR-derive data.

	Sill (cm^2)	**Nugget (cm^2)**	**Range (km)**
InSAR (orbit 2)	4	0.016	9.7
InSAR (orbit 3)	2.4	0.024	9.5
InSAR (ScanSAR)	4.3	0.15	19
Range offsets (orbit 2)	85	9.2	2.2
Range offsets (orbit 3)	320	70	8.4
Range offsets (orbit 4)	180	62	3.2
Range offsets (orbit 5)	210	70	2.4
Azimuth offsets (orbit 2)	240	15	2.5
Azimuth offsets (orbit 3)	350	240	34
MAI (orbit 2)	430	400	0.15
MAI (orbit 3)	1300	990	1.5

5.4 Derivation of the fault model

To set up the fault model, I have to deal with the following conditions: i) the ruptured fault has an extensive spatial scale; ii) I do not have direct observations of the course of the ruptured fault below the Palu bay, and iii) I lack information about the dip orientation of the ruptured fault.

5.4.1 Fault trace

The main strike-slip rupture is clearly visible in SAR pixel-offset tracking and optical data (Valkaniotis et al., 2018) for the onshore part, especially south of the Palu bay. The fault trace manifests itself as a smooth transition from southward to northward motion north of the bay, and a sharp transition south of the bay. The ruptured trace south of the bay generally represents the shape of the Palu-Koro fault (Fig. 5.5). It propagates to ∼1.18°S with an average strike of ∼N350° and jogs eastward to ∼1.23°S and continues for another ∼30 km further south before disappearing at ∼1.48°S. The rupture north of the bay, however, is diverted from the offshore region where the Palu-Koro fault is situated, which bends at

~0.64°S in a strike of ~N15° to the north-east for ~6 km and extends towards the north-west before turning to the peninsula at ~0.07°S.

I assume that the rupture is continuous below the bay (Oglesby, 2005), while I treat the orientation of the connecting fault below the bay as a free parameter.

Distinct from the main strike-slip rupture, the displacement fields derived from the pixel-offset tracking measurements show notable subsidence and horizontal motions in the east of the main fault in the Sulawesi Neck and north-west of the main fault in the Balaesang peninsula (Fig. 5.4). I interpret these characteristics as slip on normal faults in the two areas, with one striking ~N160° extending from ~0.34°S to 0.58°S in the Sulawesi Neck and the other striking ~N90° across the Balaesang peninsula. In addition, as figure 5.4 shows that significant vertical motion is observed onshore, it is not surprising if the sea floor has experienced comparable motion in some places, suggesting that the cosesimic displacements could explain the occurrence of tsunami source in this event.

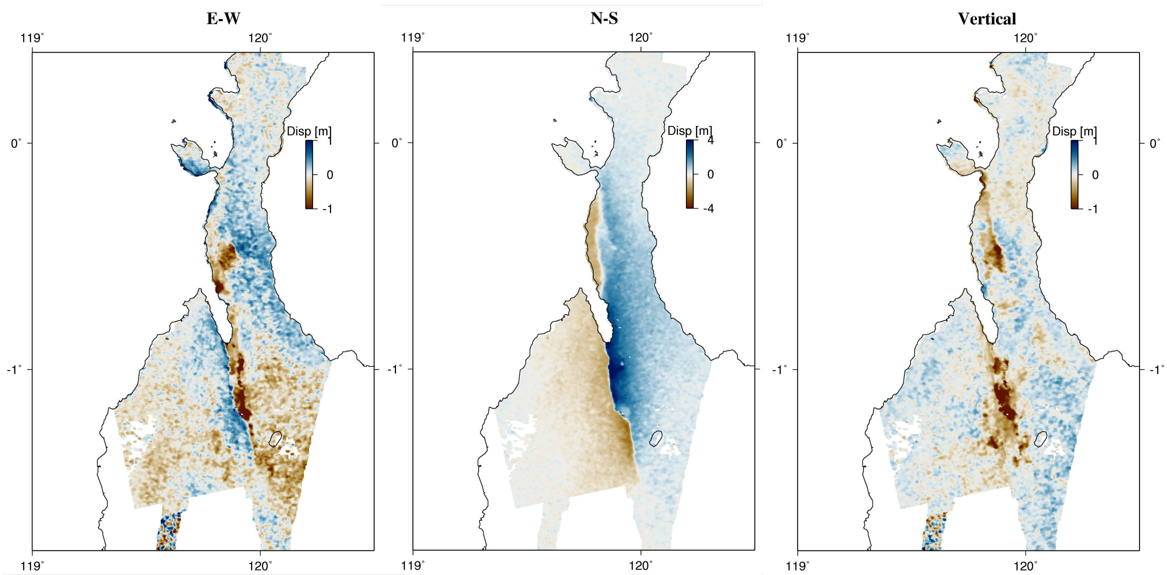

Figure 5.4: 3-D displacement fields derived from the pixel-offset tracking data. Positive values in each panel indicate eastward motion, northward motion and uplift, respectively.

5.4.2 Fault segmentation and discretization

I use 16 fault segments to characterise the complicated fault geometry, of which 13 segments belong to the main fault: segment A to M from the south to north, including four bends (segments B, G, I and K) that differ in strike from the dominant north-south strike (Fig. 5.5). The bends link to the dip-slip motion on the main fault, which left bends producing extension and right bends producing compression (Oglesby, 2005). Segments F, G and H comprise the connection through Palu bay, where segments F and H are the extensions of segments E and I onshore, respectively. Segment O represents the normal fault parallel to the main rupture; the fault in the Belaesang peninsula I model by segment N. Watkinson and Hall (2017) argued that at depth the Palu-Koro fault exists as a straight cross-basin fault, hence I assume a single deep fault that loosely connects to the shallow fault segments. This avoids a negative flower structure at depth caused by varying dip angles of fault segments. The deep cross-basin fault I model by segment P and it is in the average strike of the main fault.

I subdivide the shallow segments (0–7 km depth) in multiple patches that increase in size with depth to impose increasing smoothness with depth. The patch size increases from 1 km by 1 km (0–1 km depth) to 2 km by 2 km (1 km to 7 km depth). The cross-basin fault ranges from 7 to 22 km in depth. As the surface observations are relatively less sensitive to the deep fault motion, I subdivide the deep segment into multiple patches in a size of 5 km by 5 km. As there are no surface observations that precisely locate the course of the fault strand run below Palu bay, I subdivide the three bay segments (segments F, G and H) into multiple patches with a slightly larger size, which is ∼2.5 km by 2.5 km.

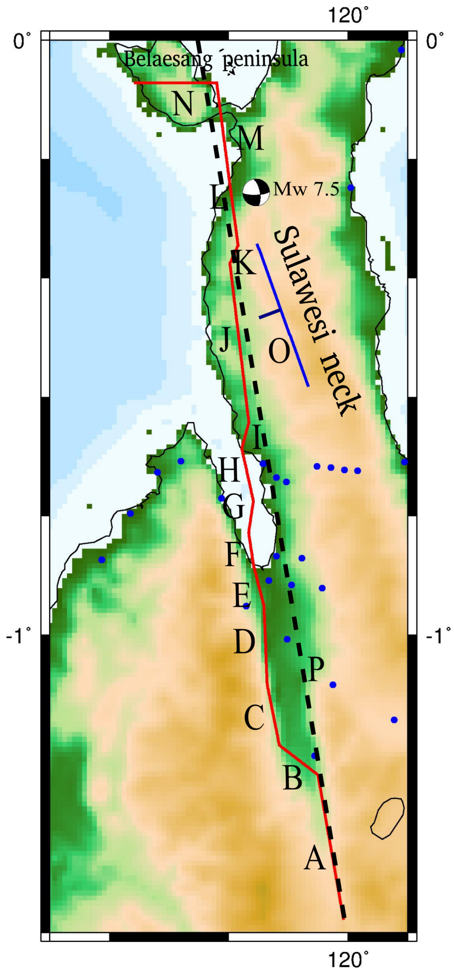

Figure 5.5: Derived fault trace and its segmentation in the map zoomed in from Fig. 5.1. The red line indicates the derived main rupture and the blue line features the parallel normal fault. The black dashed line represents the deep cross-basin fault in the model.

5.5 Bayesian inversion

I apply a Bayesian approach that I describe in Chapter 2 to solve for the optimal value of each model parameter. I assess the model uncertainties from the posterior PDF.

5.5.1 Determining 3-D displacement

For a pixel with 3-D displacement u $= [u_e,\ u_n,\ u_{up}]$, its displacement in the subsampled field of SAR-derived data can be expressed as

$$
\begin{aligned}
D_{InSAR} &= \begin{bmatrix}\sin\theta\cos\phi, & -\sin\theta\sin\phi, & -\cos\theta\end{bmatrix}\begin{bmatrix}u_e\\ u_n\\ u_{up}\end{bmatrix}\\
D_{az.offsets} &= \begin{bmatrix}-\cos\left(\phi-\frac{3\pi}{2}\right), & \sin\left(\phi-\frac{3\pi}{2}\right)\end{bmatrix}\begin{bmatrix}u_e\\ u_n\end{bmatrix}\\
D_{rg.offsets} &= \begin{bmatrix}\sin\theta\cos\phi, & -\sin\theta\sin\phi, & -\cos\theta\end{bmatrix}\begin{bmatrix}u_e\\ u_n\\ u_{up}\end{bmatrix}\\
D_{MAI} &= \begin{bmatrix}-\cos\left(\phi-\frac{3\pi}{2}\right), & \sin\left(\phi-\frac{3\pi}{2}\right)\end{bmatrix}\begin{bmatrix}u_e\\ u_n\end{bmatrix}
\end{aligned}
\tag{5.4}
$$

where D_{InSAR}, $D_{az.offsets}$, $D_{rg.offsets}$ and D_{MAI} are the displacement in the data derived by InSAR, azimuth offsets, range offsets and MAI, respectively; θ is the incidence angle, and ϕ is the azimuth direction of the satellite positive clockwise from the north. The source parameters then can be inverted by iteratively calculating a forward model of the surface displacements, and using the MCMC scheme that I describe in Chapter 2 to arrive at a converged model that fits the data well.

5.5.2 Model parameter priors

Prior constraints in the MCMC sampler for slip magnitude is from 0 to 10 m, assuming a uniform probability distribution over the range. Constraints in the rake are needed to avoid alternating slip directions from patch to patch. The strike-slip segments have rake constrains of -20° to 20° as I expect the rupture to be dominated by the left-lateral strike-slip. The right bends (segments I and K) have rake constraints of 0° to 90°, while the left bends (segments B and N) and the parallel normal fault (segment O) have a -90° to 0° rake constraint, to reflect the expected compression and extension, respectively, for a left-lateral fault system. For the three segments that fully below the bay, segments F and H have rake constraints of -20° to 20°, whereas the central fault bend (segment G) has rake constraints of 0° to 90°.

To test the geodetic constraints on the dip orientation of the ruptured fault, I solve for the dip angle of each segment. The asymmetry of the displacements suggests east-dipping faults, except for the most southern segment A (Fig. 5.6). As the finite fault model of the USGS solution has a dip angle of 66 degrees (USGS, 2018), I constrain dip angles of strike-slip segments between 40° to 90°. I allow shallower dip angles for other segments, between 30° to 90°, to accommodate with dip-slip motions.

I solve for the northern endpoint of segment F and the southern endpoint of segment H below the bay, such that segment G has a free length and orientation.

Simultaneously I estimate a plane for the SAR-derived data to solve for reference errors.

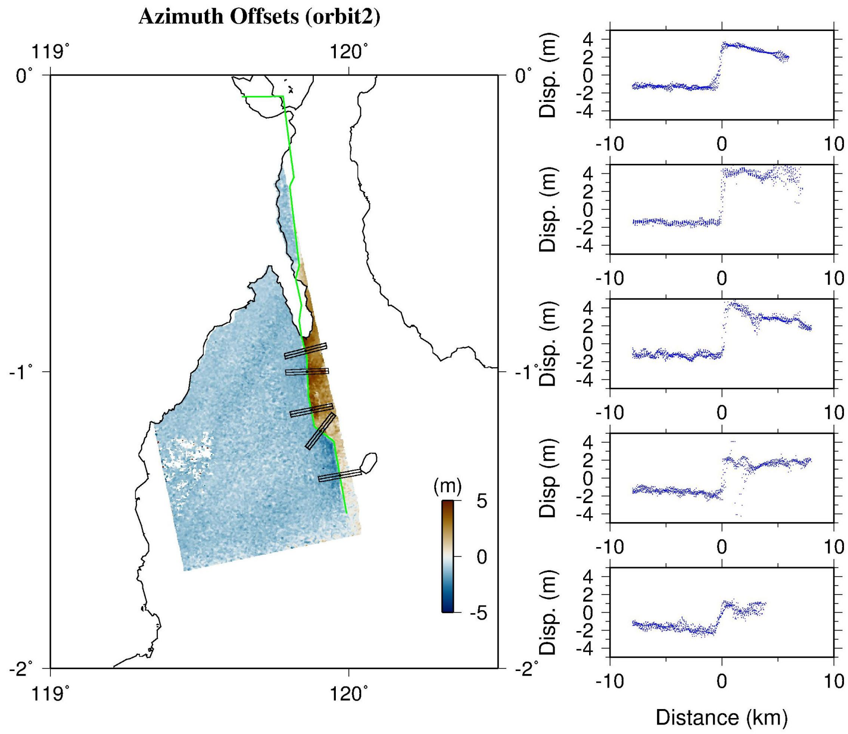

Figure 5.6: Azimuth offsets profiles perpendicular to the fault south of the Palu bay. Blue points show the azimuth displacement of data points projected from within a 2 km perpendicular distance (black rectangles) onto each profile (black lines). The green line is the derived fault trace.

5.5.3 Moment regularisation

As the slip magnitudes of deep patches are usually poorly constrained by the surface observations, changes in the slip magnitudes of the deep patches may not cause a large change to the likelihood. Therefore, I apply a prior on the seismological moment during the inversion to decrease the probability of the solution that has an unreasonable seismological moment. I calculate the probability for each new trial from a Gaussian distribution with a mean and standard deviation defined by the USGS seismological moment 2.497e20 N·m^{-1} (USGS, 2018).

5.5.4 Inversion efficiency

As the number of model parameters I solve for is quite large, recalculating the Green's functions at every iteration for a new dip angle is time-consuming. In order to speed up the inversion, I calculate the Green's functions in advance at a 1° dip angle interval for each patch. During the inversion, I apply a linear interpolation to derive the Green's functions at the dip angle of interest. Exempt from this interpolation are the three bay segments (segments F, G and H) whose length and orientation (segment G) are variable during the inversion.

To find out a reasonable initial solution efficiently, I apply a simulated annealing approach (Van Laarhoven and Aarts, 1987) to search model parameters in a large space. I then use the optimal solution derived from the simulated annealing as the initial solution of the Bayesian inversion.

Meanwhile, I incorporate an automatic step size selection for each model parameter in the inversion to maximise the efficiency of the search for the model parameter (e.g., Amey et al., 2018; Bagnardi and Hooper, 2018; Hooper et al., 2012).

5.6 Finite fault model

Figure 5.7 and 5.8 show the maximum a posterior (MAP) model for the fault slip distribution that reproduces the observations within their uncertainties. I also show the posterior mean model and the posterior median model for the slip distribution in figures 5.9 and 5.10. Predictions of the MAP model for the geodetic data and residuals are given in Fig. 5.11. All three solutions demonstrate a dominance of shallow strike-slip for most of the rupture, mostly limited to the upper 10 km. The large slip (> 5 m) on the segments south of the bay continues up to the surface, whereas the segments north of the bay feature no, or minor, slip on the upper segments, implying that the rupture doesn't reach the surface there. The magnitude of the dip-slip component is generally small on the north-south striking segments, whereas I find significant dip-slip at the bends. Specifically, I find a large normal component on segment B south of Palu, clearly connected to the large subsidence observed by the GPS and SAR-derived data (Fig. 5.11). The observed subsidence provides a direct observation that the bends accommodate significant dip-slip motion (Socquet et al., 2019) deviating from the dominant strike-slip motion. The notable normal components on the normal faulting segments O and N explain the subsidence and horizontal motions observed in the Sulawesi Neck and the Balaesang peninsula. The 2σ uncertainties of slip estimated from the posterior solutions show that the slip on the near-surface patches is well-constrained, whereas the larger uncertainties on the deeper patches indicate they are less sensitive to the surface displacement (Figure 5.12). The slip uncertainties are lower on the bay segments and on the segments south of the Palu bay. It might be ascribed to the constraints of the GPS data, which most of them are located around/south of the Palu bay.

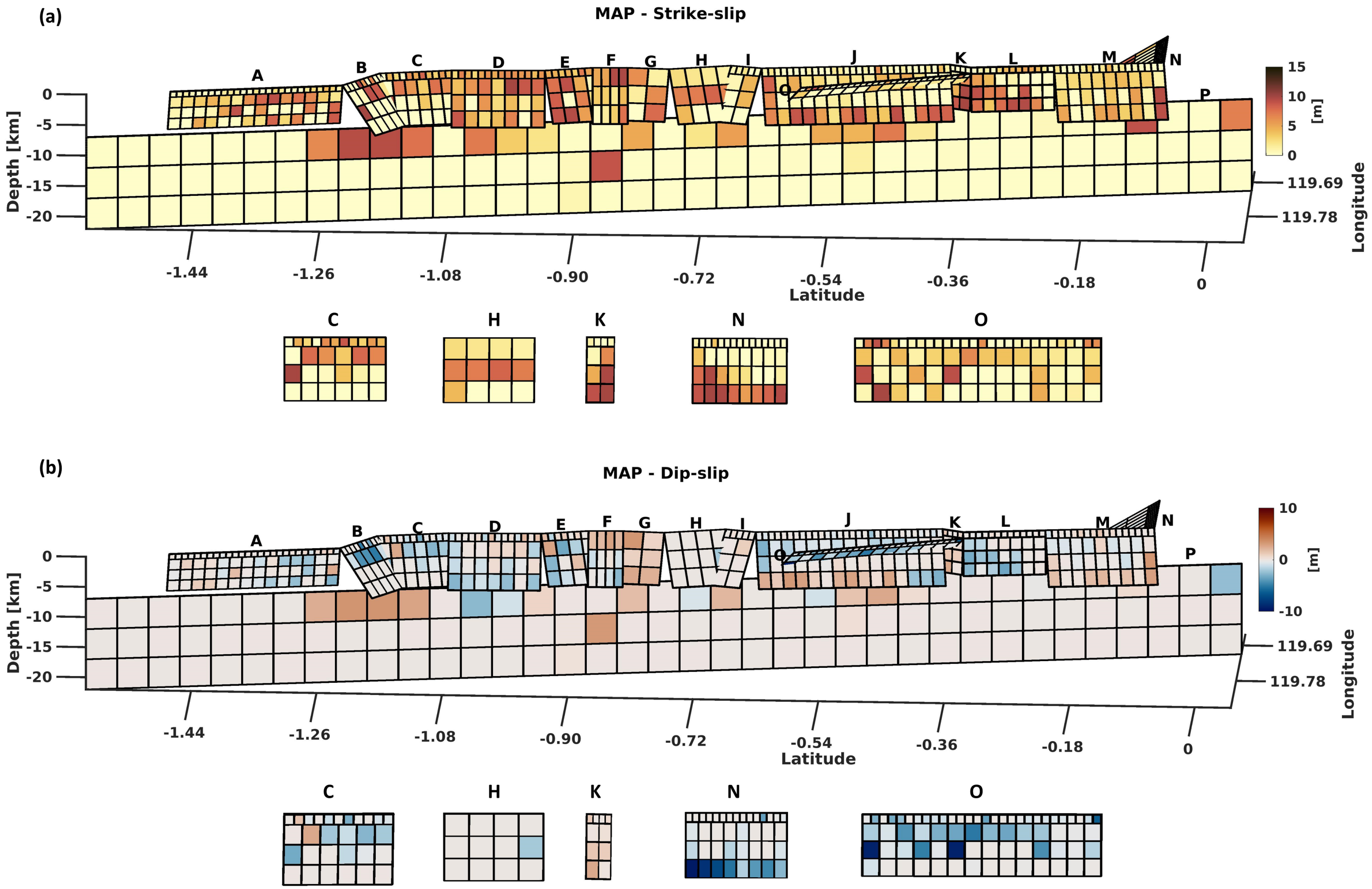

Figure 5.7: Estimated maximum a posterior (MAP) model of strike-slip (a) and dip-slip (b).

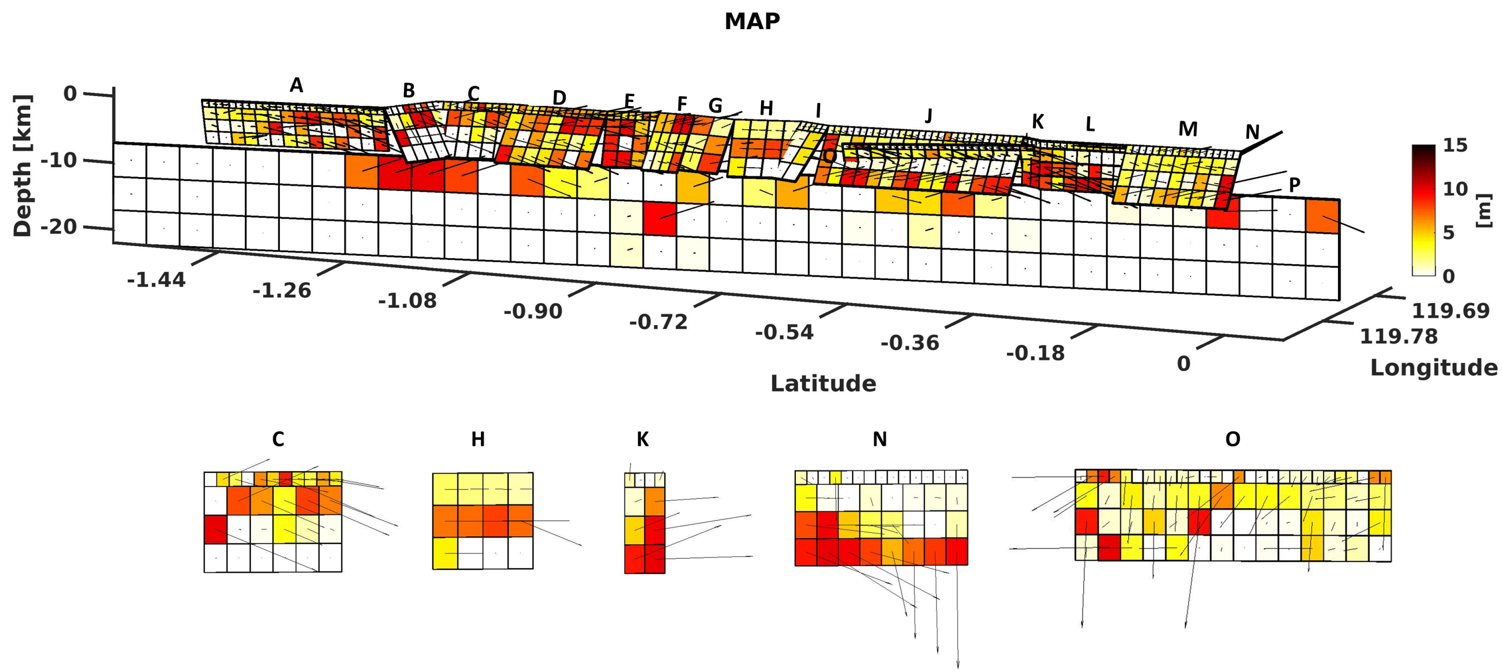

Figure 5.8: Estimated maximum a posterior (MAP) model of fault slip. Black arrows indicate slip rake angle and amplitude.

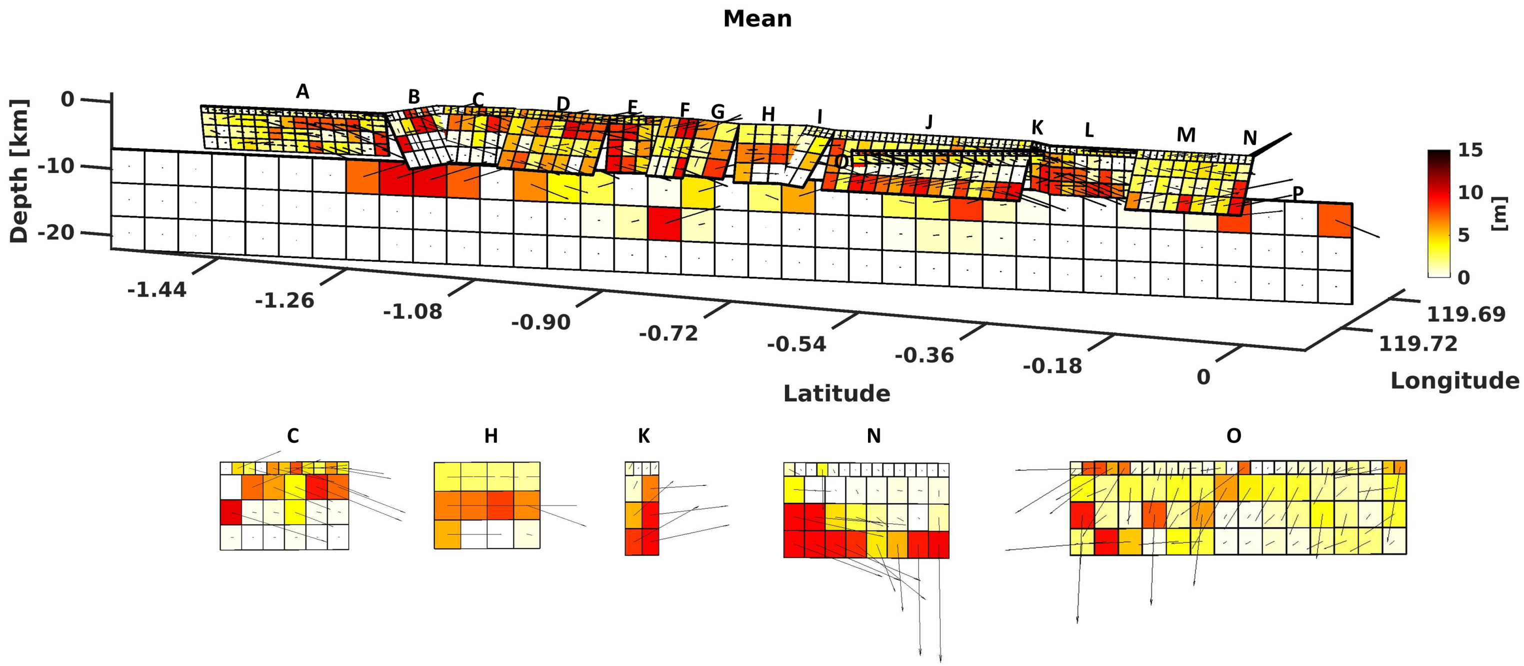

Figure 5.9: Estimated posterior mean model of fault slip. Black arrows indicate slip rake angle and amplitude.

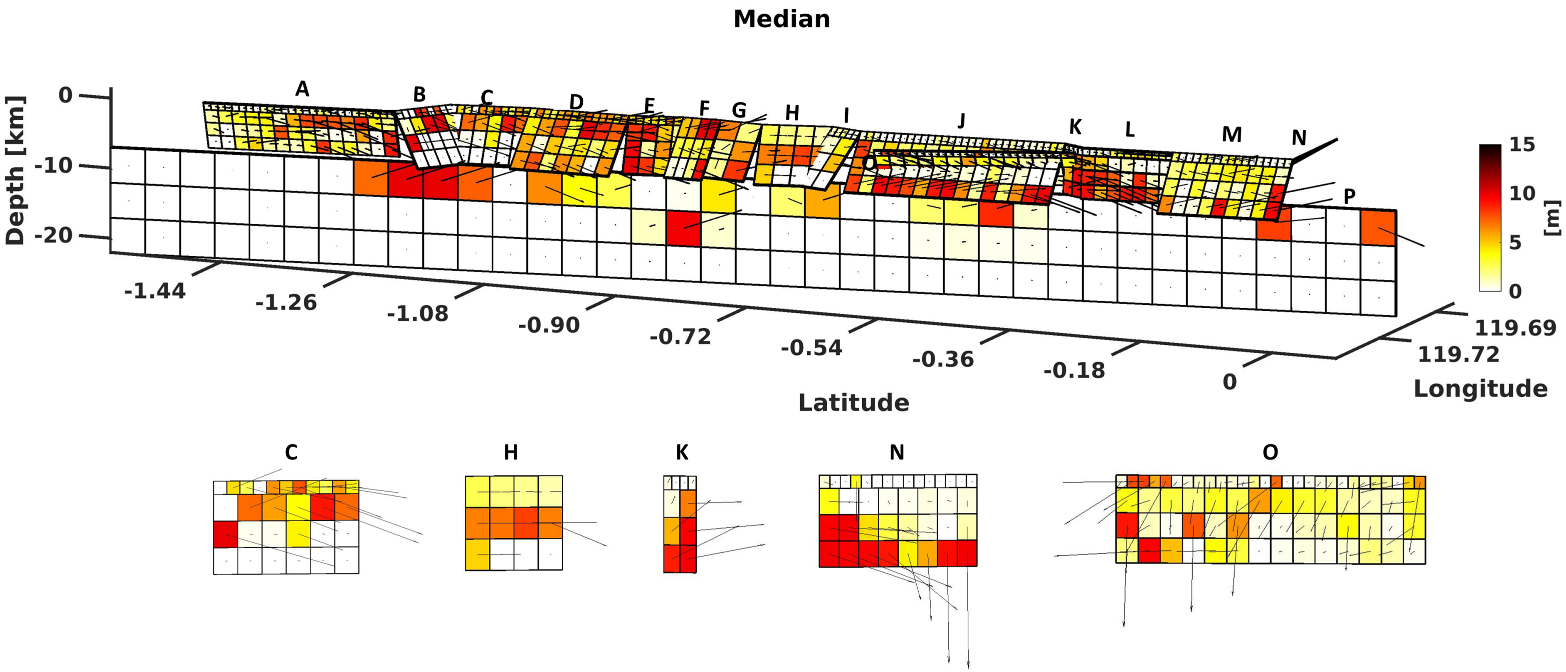

Figure 5.10: Estimated posterior median model of fault slip. Black arrows indicate slip rake angle and amplitude.

Figure 5.11: Fit of the MAP model to geodetic surface observations. The green line is the derived fault trace. Black arrows in (l) represent GPS observations, while red arrows indicate predictions from the MAP solution (noted that black arrows are hidden beneath red ones). The background colour in (l) shows the vertical displacement field from the MAP model. Black circles in (l) are coloured by the vertical observations of GPS sites.

(a)

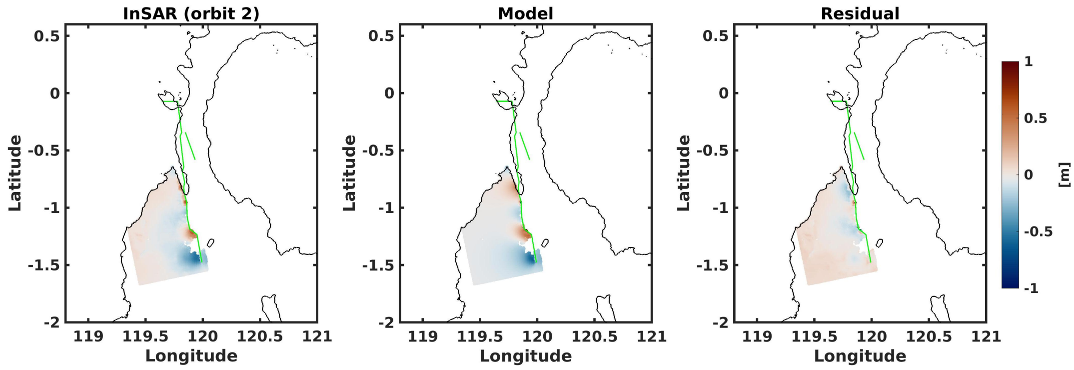

(b)

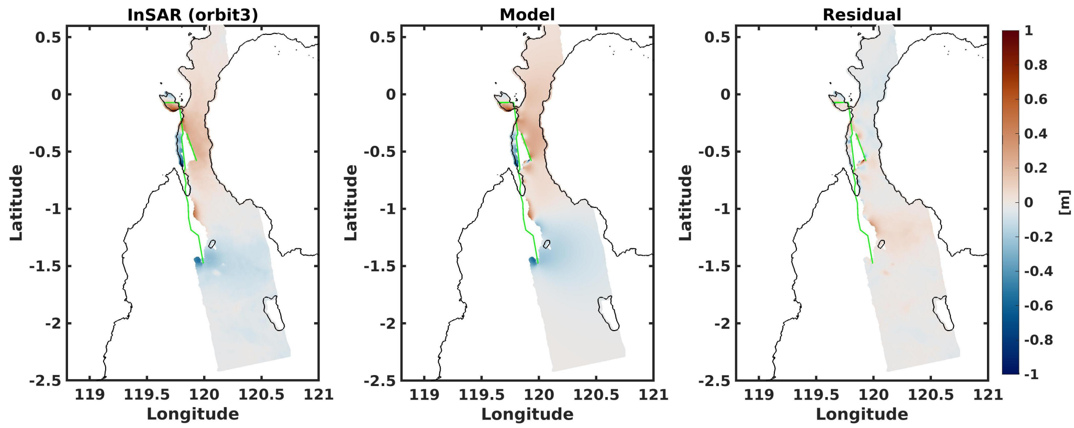

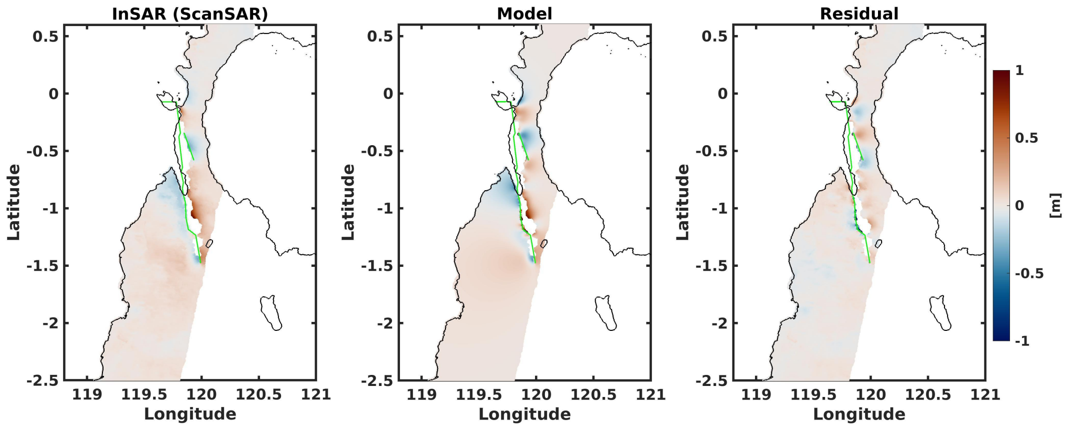
InSAR (ScanSAR)
Model
Residual
Latitude
Longitude
[m]

(c)

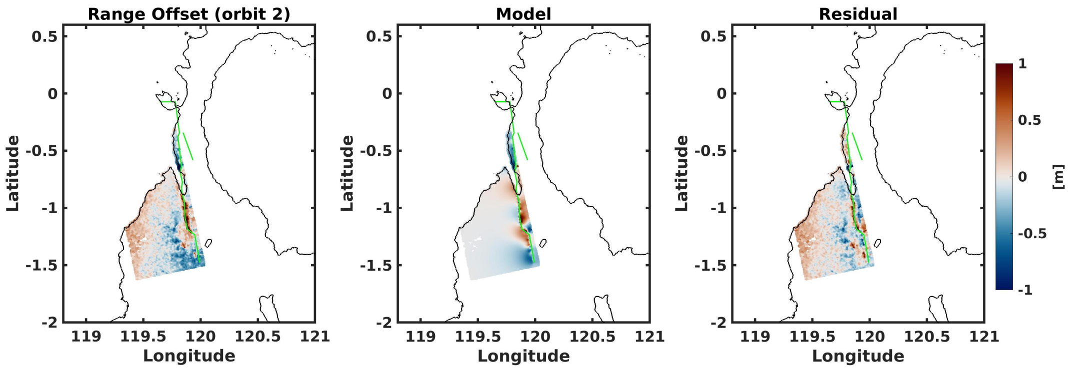
Range Offset (orbit 2)
Model
Residual
Latitude
Longitude
[m]

(d)

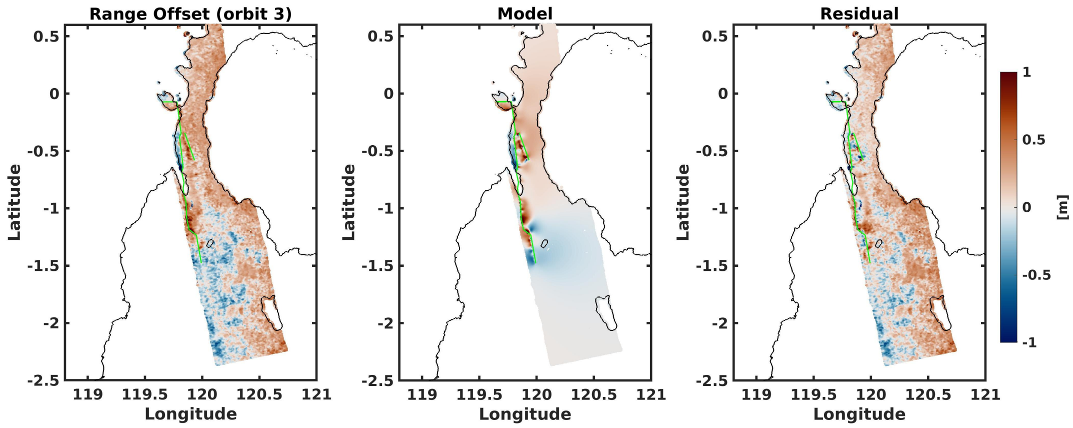
Range Offset (orbit 3)
Model
Residual
Latitude
Longitude
[m]

(e)

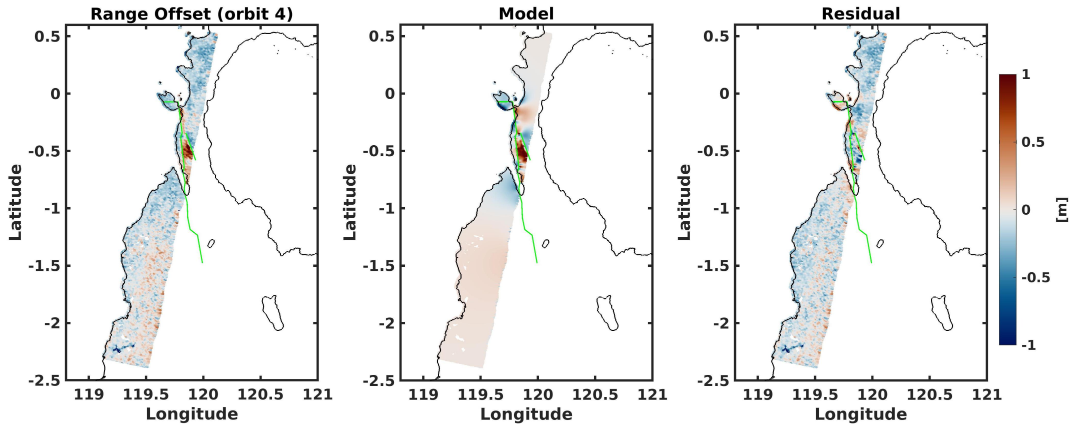
Range Offset (orbit 4)
Model
Residual
Latitude
Longitude
[m]

(f)

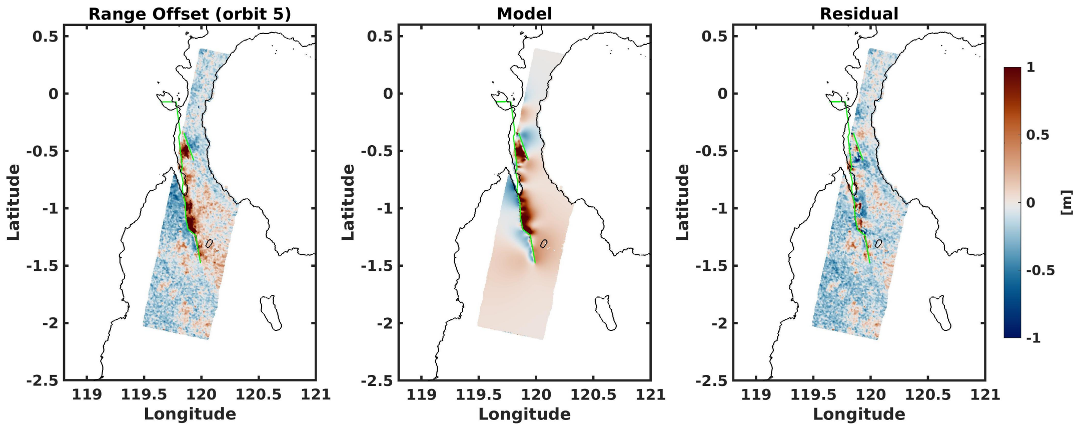
Range Offset (orbit 5)
Model
Residual
Latitude
Longitude
[m]

(g)

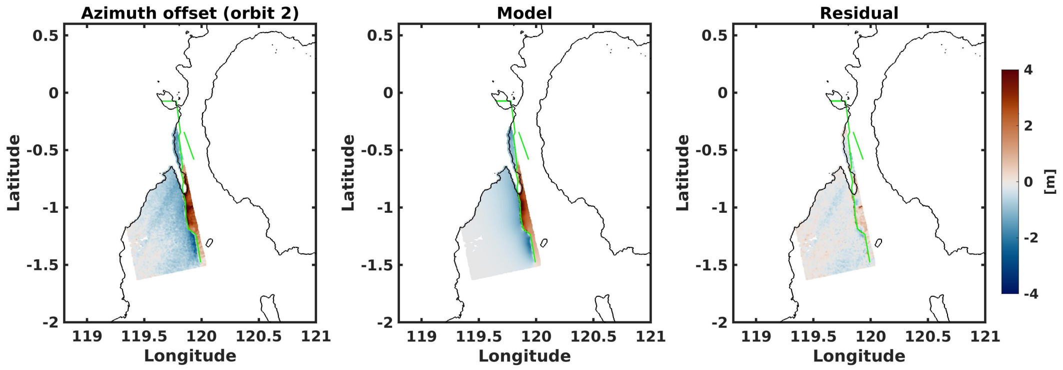
Azimuth offset (orbit 2)
Model
Residual
Latitude
Longitude
[m]

(h)

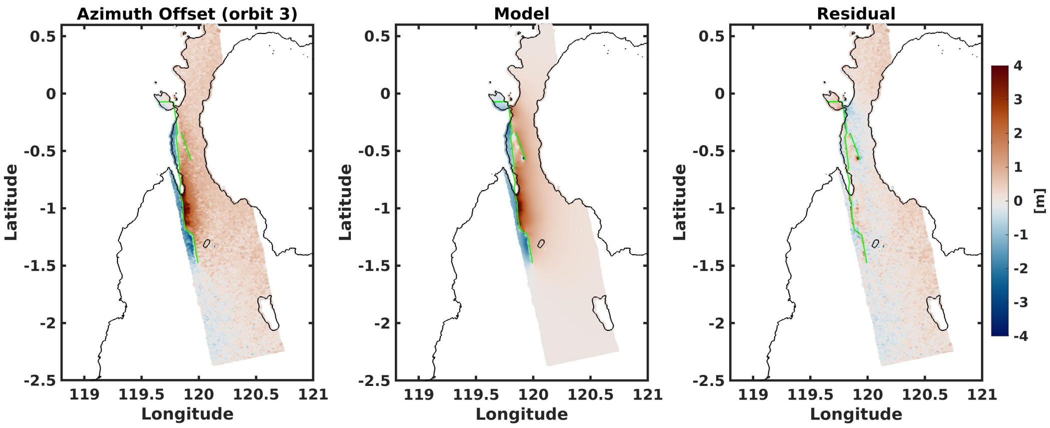
Azimuth Offset (orbit 3)
Model
Residual
Latitude
Longitude
0.5
0
-0.5
-1
-1.5
-2
-2.5
119
119.5
120
120.5
121
[m]
4
3
2
1
0
-1
-2
-3
-4

(i)

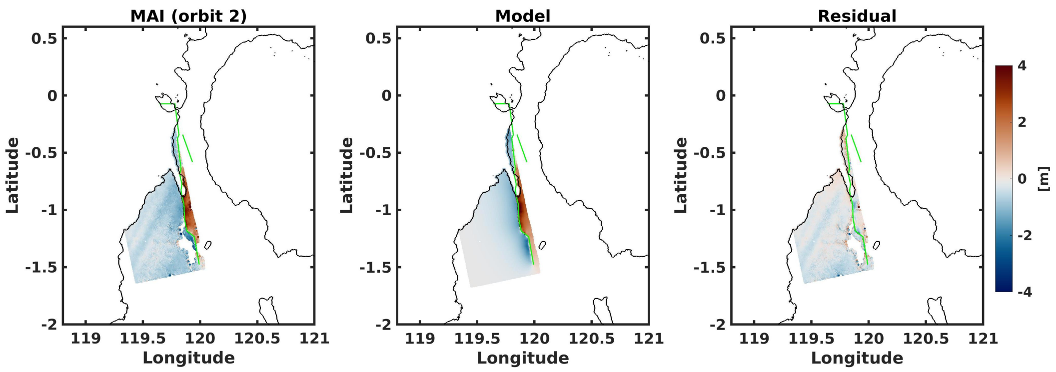
MAI (orbit 2)
Model
Residual
Latitude
Longitude
0.5
0
-0.5
-1
-1.5
-2
119
119.5
120
120.5
121
[m]
4
2
0
-2
-4

(j)

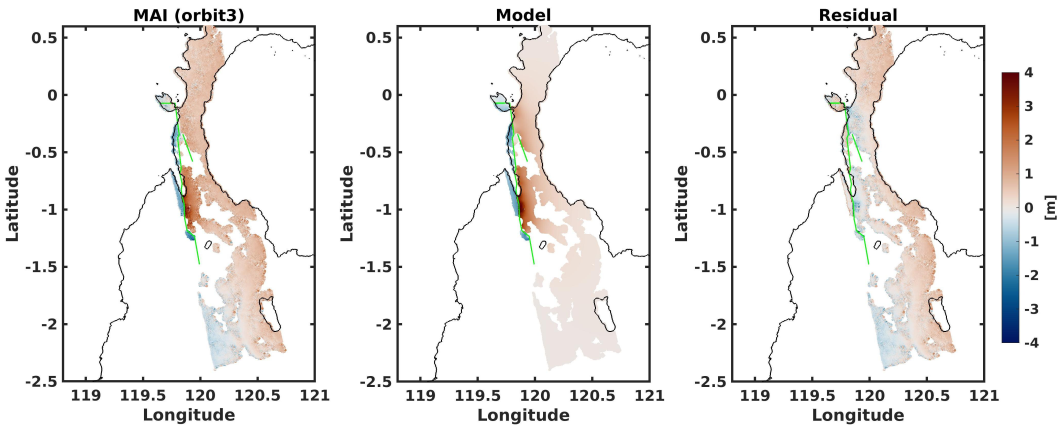
MAI (orbit3)
Model
Residual
Latitude
Longitude
[m]

(k)

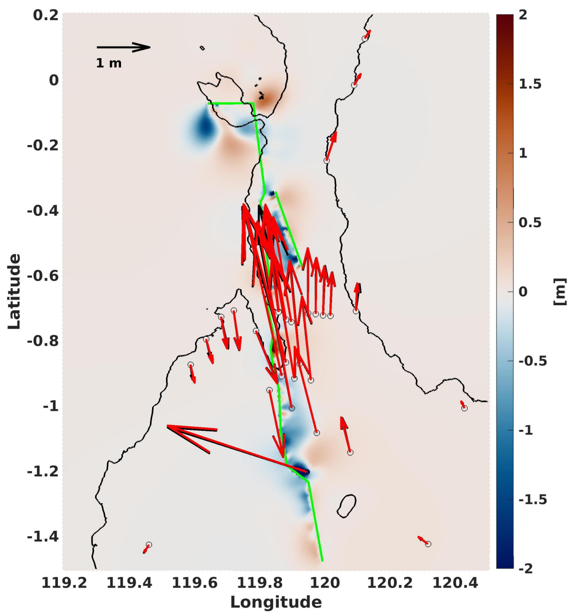
1 m
Latitude
Longitude
[m]

(l)

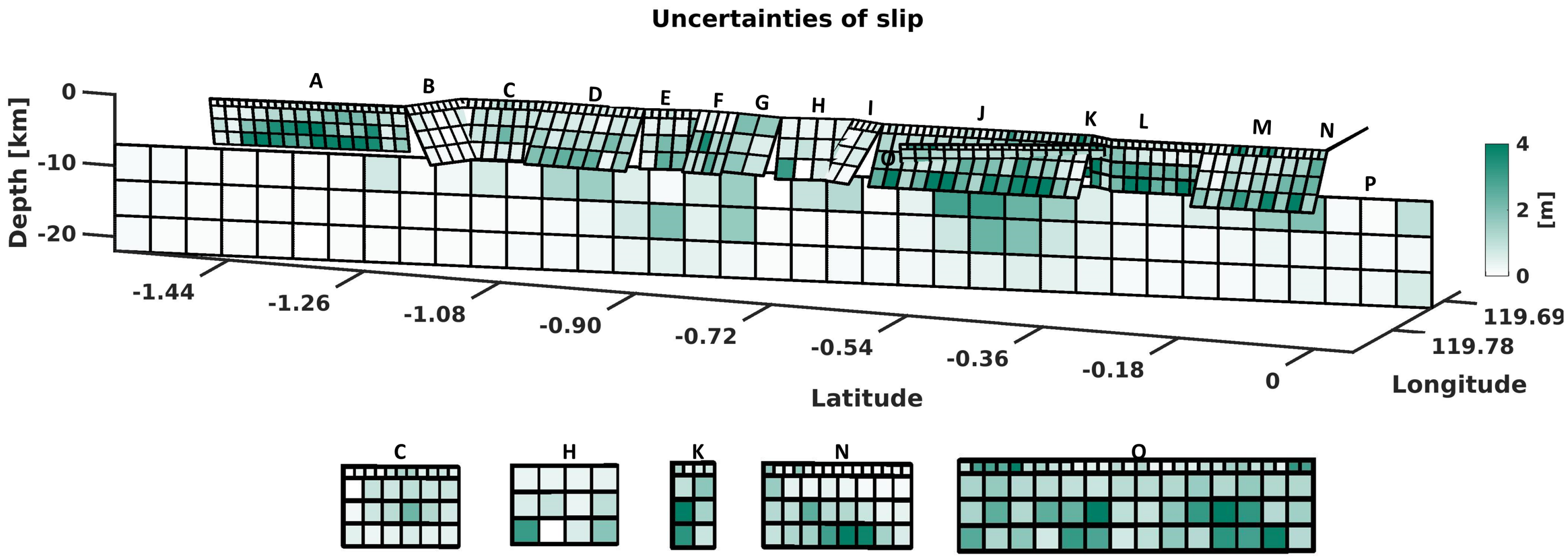

Figure 5.12: Estimated 2σ uncertainties of slip from the posterior solutions.

The estimated dip angles show a preference for 40–50 degrees, except for the fault bends and normal fault, where shallower dip angles are needed to accommodate the dip-slip motion (Fig. 5.13). Also, there is an approximate continuation from the shallow segments to the vertical deep fault segment.

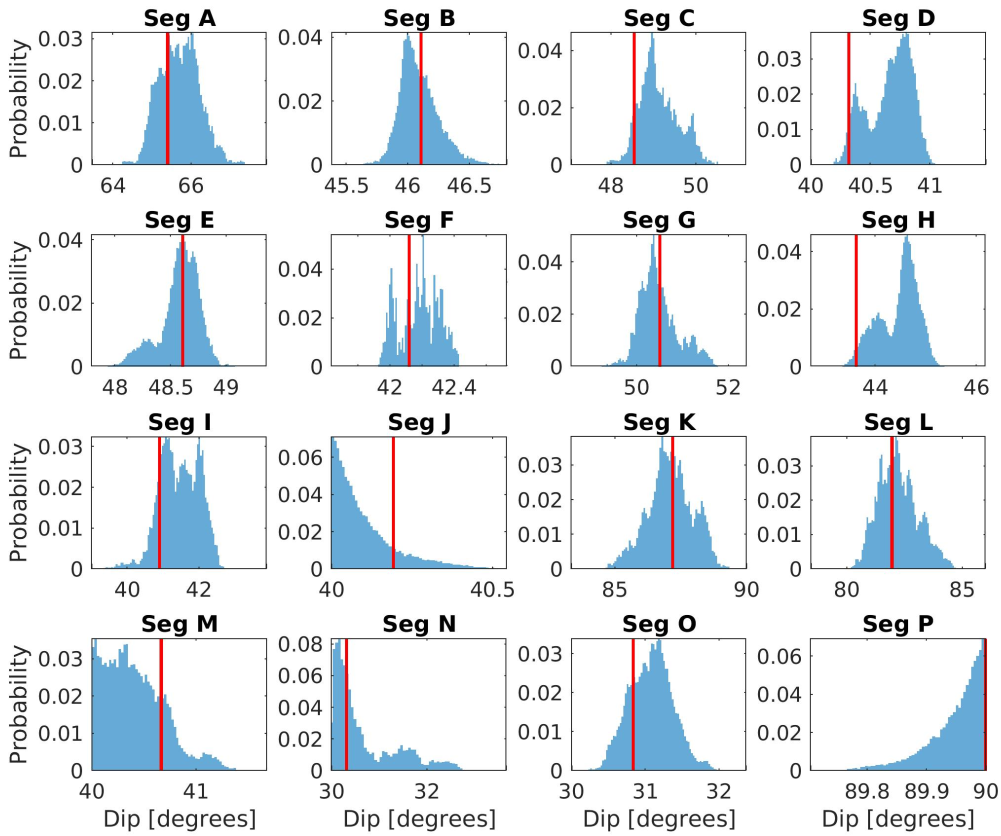

Figure 5.13: Posterior PDF for the dip angle of each segment. Red lines indicate the MAP solution.

I uniformly select 100 samples from all 5 million posterior solutions, which the 100 samples are expected to have the same probability distribution as the original population. I then calculate 3D displacement fields of each selected sample. Figure 5.14 shows the mean of 3D displacements estimated from the samples. The estimated vertical displacement shows that to explain the displacements observed by the GPS data around the bay, the model requires dip-slip on the fault strand below the bay. Most dip-slip motion in this region is produced by the central right bend (segment G) (Fig. C.3).

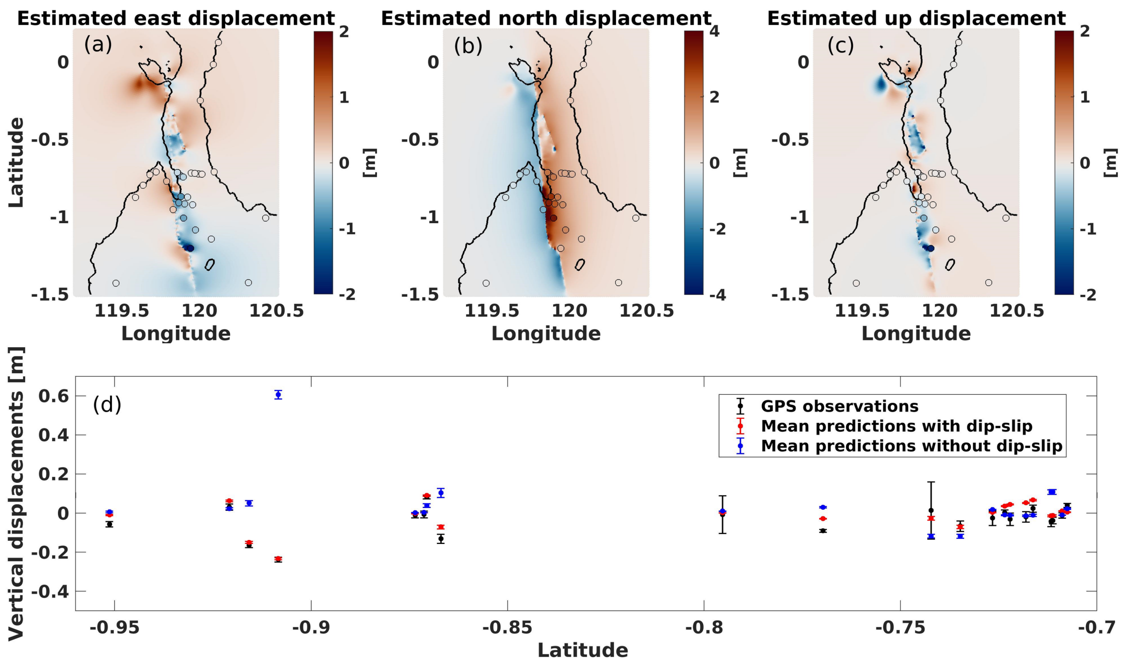

Figure 5.14: The mean of 3D displacements estimated from a sample of all posterior solutions. a) East-west displacement. b) North-south displacement. c) Vertical displacement. Colour in the black circles indicates the GPS measurements in each component. d) Comparisons between the mean GPS predictions inverted from the sample of all posterior solutions (including dip-slip (red dots) or removing dip-slip (blue dots)) and the GPS observations (black dots) around the Palu bay. Error bars represent 2σ uncertainties.

There are some significant residuals in the south of the bay for the range offset, which the RMSE is ~0.5 m. They are mainly caused by local deformation (e.g., landslides (Watkinson and Hall, 2019)) that would not be reproduced by the fault structure. Besides the MAP model, I also show more details including the posterior PDF of solved parameters over the bay in Fig. C.2, Fig. C.3 and Fig. C.4.

To characterise the uncertainties of the estimated vertical displacement over the bay, I pick up models termed as "extremes" from 5 million posterior samples. I calculate the probability of total uplifted volume over the bay and that of the average differences between the vertical displacement of each sample and the mean displacement. I then select 9 extremes at 95% confidence limits of the estimated probability distributions (Fig. 5.15). The vertical displacement estimated from these extremes (Fig. 5.16) can help to yield improved constraints on vertical surface motions in the tsunami modelling.

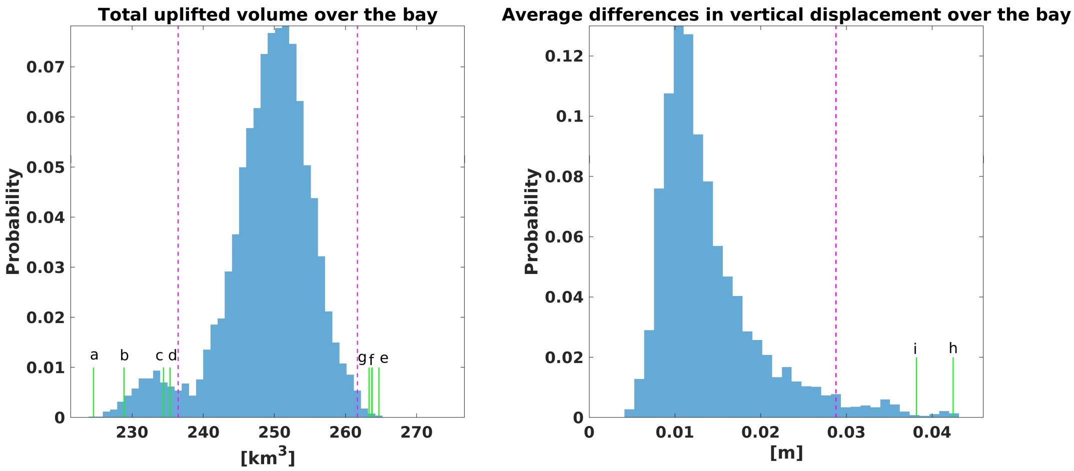

Figure 5.15: Probability distributions of the estimated vertical displacement over the bay. The left panel shows the probability of total uplifted volume over the bay. Magenta dashed lines indicate a 95% confidence level. Green lines represent the total uplifted volume of seven selected model extremes in this scenario (a to g). The right panel shows the probability of the average differences in displacement over the bay between each posterior sample and the mean solution. Green lines represent the average differences in displacement for two selected model extremes (h and i).

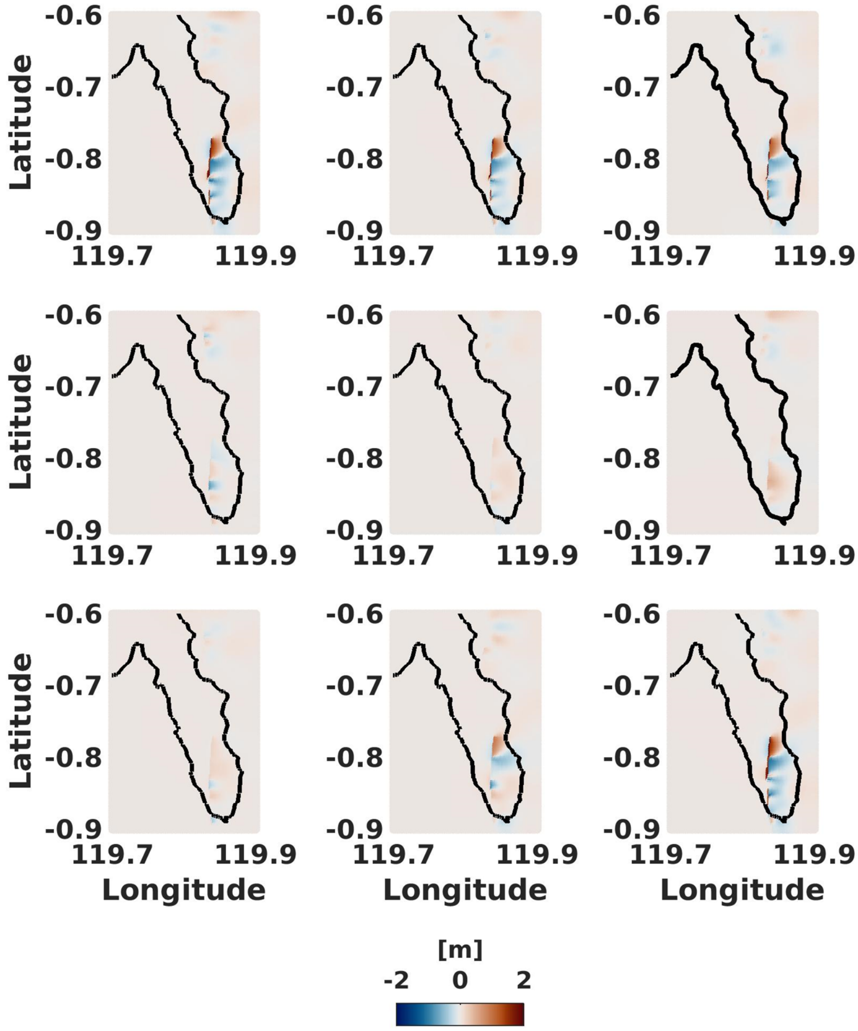

Figure 5.16: Differences of the derived vertical displacement between the selected extremes and the MAP solution.

5.7 Discussion

5.7.1 Comparisons to published results

The inverted fault slip solution shows a dominance of shallow strike-slip for most of the main rupture. For the segments south of the Palu bay, the derived model indicates large slip (> 5 m) continues up to the surface, which is consistent with previous solutions (e.g., He et al., 2019; Socquet et al., 2019; USGS, 2018; Williamson et al., 2020). The model shows significant subsidence on a left bend (segment B), which is also revealed by Socquet et al. (2019), He et al. (2019), Song et al. (2019) and Williamson et al. (2020).

Several previous models which characterise the main rupture only show significant normal slip on the segment in the Sulawesi Neck (e.g., Fang et al., 2019; He et al., 2019; Socquet et al., 2019). By contrast, I find substantial dip-slip motions on a combined north-south trending normal fault (segment O), whereas the parallel main rupture (segment J) shows little normal components. The inverted dip-slip motions on segment O ($\sim$4 m) nearly reach the surface, which shows good agreements with He et al. (2019). The results suggest that the main rupture combined with the normal faulting could allow a more detailed interpretation to the surface motion in the Sulawesi Neck.

The model indicates $\sim$10 m of left-lateral strike-slip with $\sim$8 m of normal slip between 5 to 7 km in depth in the Balaesang peninsula, which is also suggested in the model of Song et al. (2019). Furthermore, the moment magnitude calculated from the model in this study (M_w 7.54) is consistent with the USGS solution (USGS, 2018), which is expected as I apply the moment regularisation to the inversion.

5.7.2 Fault geometries over the Palu bay

Because there are no surface observations that precisely locate the course of the rupture below the bay, I test four different scenarios with variable slip constraints and/or fault orientation for the bay segments (segments F, G and H) (Fig. 5.17). In Model 1, I consider segment H to be the right bend, implying dominant thrusting; segments F and G are forced to be strike-slip segments. Alternatively, to allow for a gradual strike change of the bends, in Model 2, I consider both segments H and G to be right bends, and only segment F is considered strike-slip. Model 3 explores the possibility that all bay segments are dominantly strike-slip. In these three models, I treat the orientation of segment G as a free parameter, while strike angles of segments F and H are fixed based on their onshore parts segments E and I, respectively. Lastly, as videos indicate that the arrival of the tsunami at

Pantoloan is 170 s after the earthquake (Carvajal et al., 2019), I force the location of significant uplifts in the southern part of the Bay in Model 4. To do so, I set the central bay segment G as the fault bend, while I set the northern and southern segments F and H as strike-slip. I fix the length of northern bay segment H at 10 km, such that segment G situates at the 170 s travel time contour from Carvajal et al. (2019). In this scenario, I treat the orientations of segments G and H as free parameters, while the strike angle of segment F is fixed based on its onshore part segment E. Figure 5.17 shows the maximum a posterior (MAP) solutions of the three bay segments for each model. All models have a good fit to the geodetic data (Fig. 5.18).

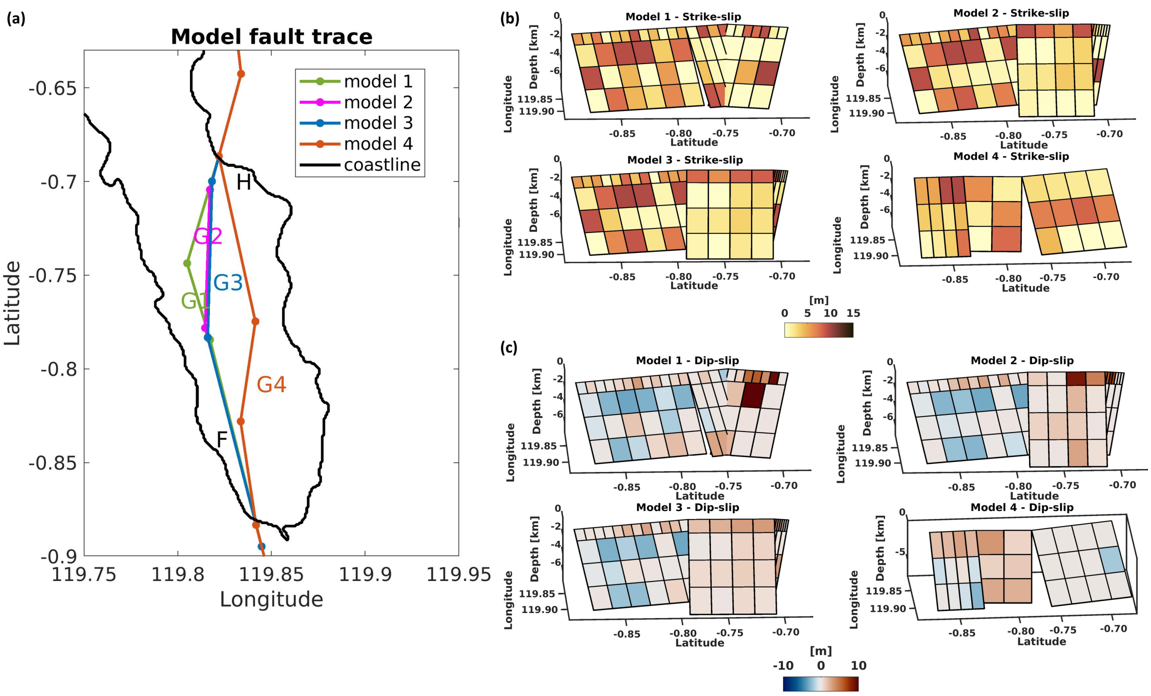

Figure 5.17: Estimated maximum a posterior (MAP) solutions of strike-slip (b) and dip-slip (c) for the fault strand under the bay in four models (a).

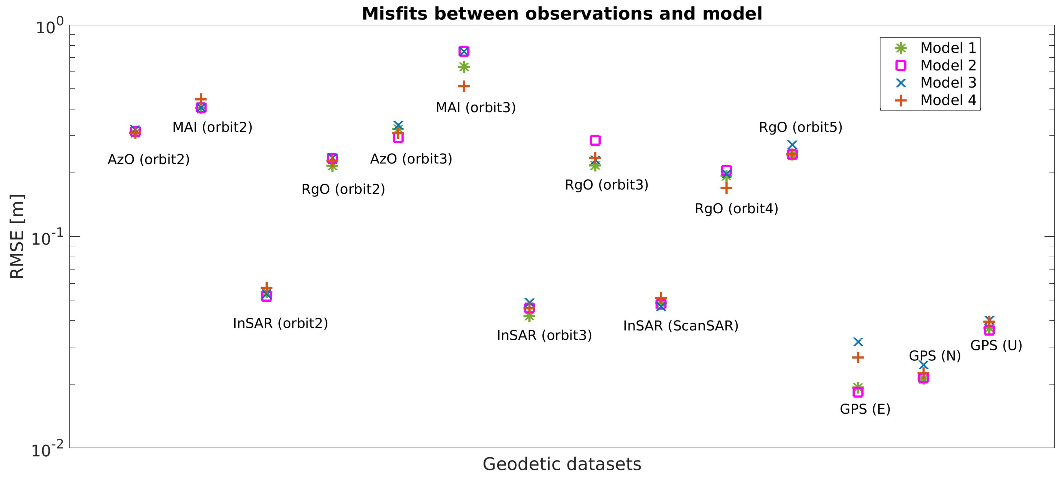

Figure 5.18: RMSE comparisons of four models between geodetic observations and the model predictions.

5.7.3 Tsunami modelling

The numerical simulation of the tsunami propagation and inundation is based on an unstructured finite-volume model, H2Ocean (Cui et al., 2010). H2Ocean is capable of preserving mass and momentum in local cells as well as maintaining the positivity of the water depth in the case of wetting and drying. The tsunami modelling results (Fig. 5.19) show that all four models predict a runup height of tsunami in the southeastern part of the bay that is generally consistent with the field survey (Simons et al., 2021). Furthermore, the arrival times of the leading waves derived from all models show good agreement with the video waveforms in the southeastern bay coast (surveyed sites Talise and KN hotel) (Carvajal et al., 2019). All models provide significant uplift below the bay that can explain runup heights on the order of 2 to 8 m. Therefore, in contrast to the previous arguments that the coseismic deformation is not the dominate cause to generate the tsunami (Carvajal et al., 2019; Socquet et al., 2019), results in this study suggest that the coseismic displacements of the seafloor explain the tsunami in and around Palu.

For the sites south of the bay (sites Palu City, Talise, Dupa and KN hotel), all models perform similarly in explaining the runup heights and the arrival times of tsunami observed by the field surveys at Palu City and Dupa, and model 4 performs better at KN hotel and Talise. For the sites north of the bay (sites Pantoloan and Wani), the runup heights derived from model 4 are more consistent with surveys compared to model 1, 2 and 3. Therefore, model 4 has the best performance compared to the other three models.

Figure 5.19: Comparisons of runup between models and observations from surveys along the Palu bay (adapted from Simons et al. (2021)). Survey data includes Mikami et al. (2019); Omira et al. (2019); Putra et al. (2019). To visualise the spatially high frequent runup in a comprehensible manner, a spatially moving median and 1-99 percentile filter has been applied, which provides a view on the general characteristic and the bandwidth of model results.

(a) model 1

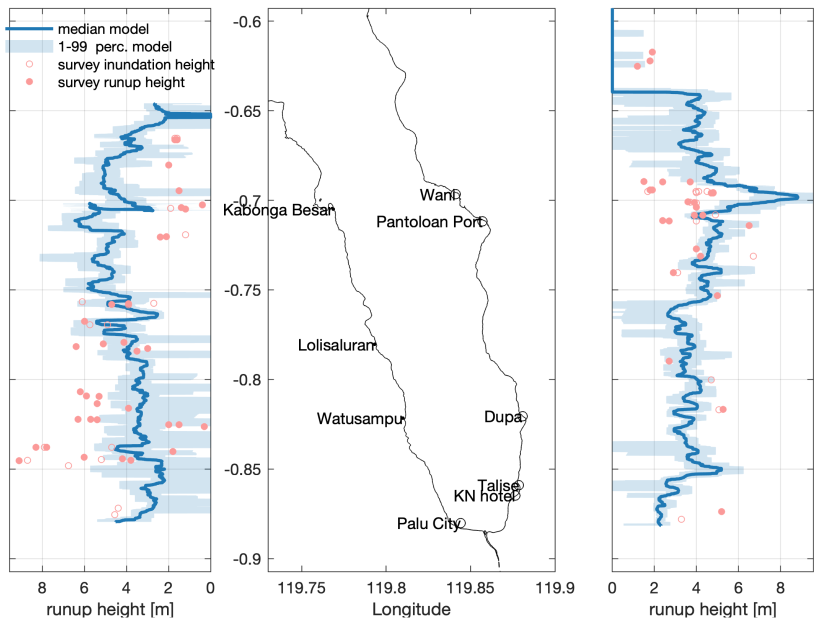

(b) model 2

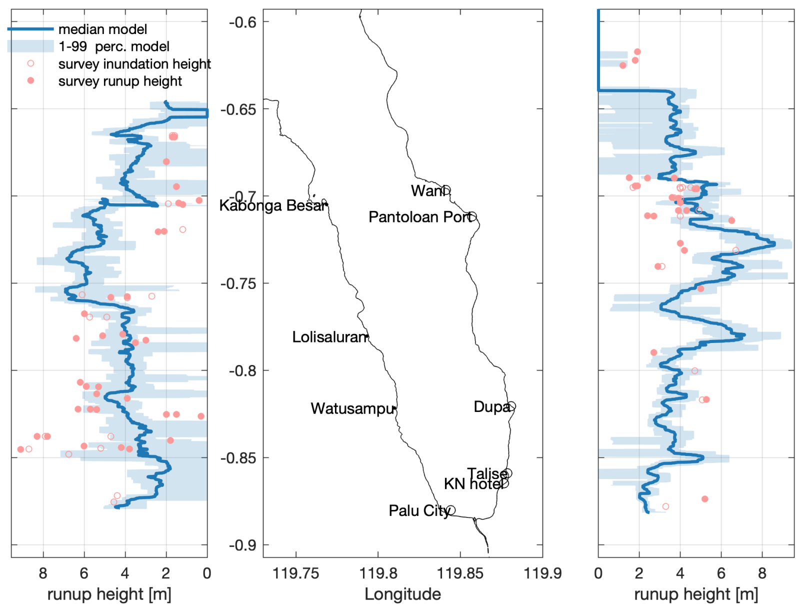

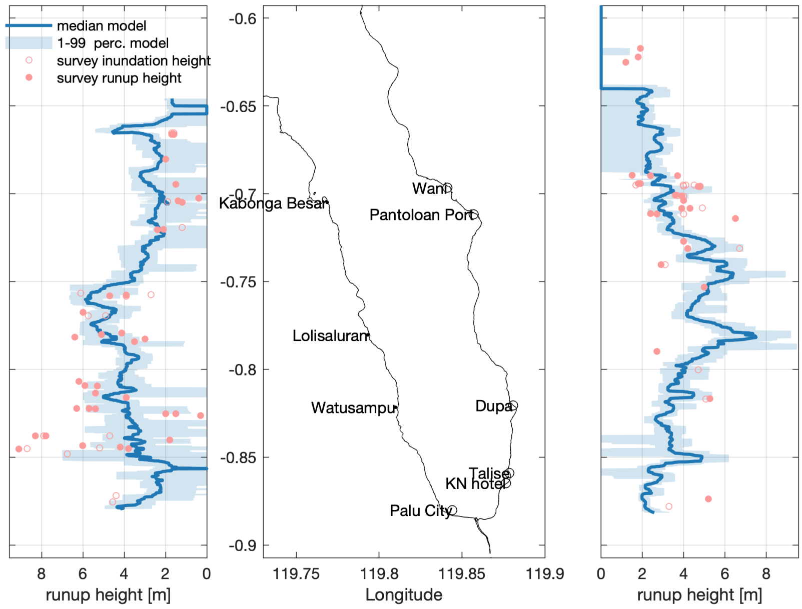

(c) model 3

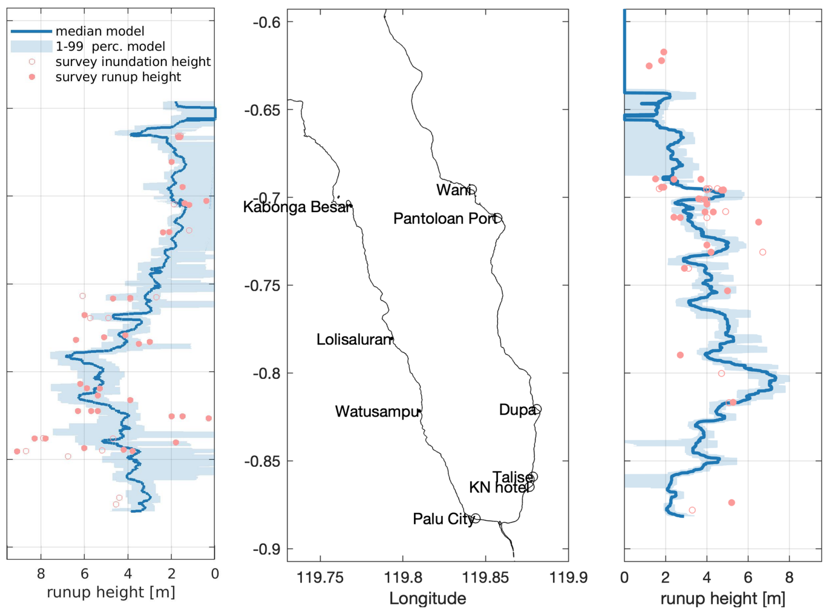

(d) model 4

However, there are still some features in the field survey that are not explained by the models: i) none of the models explain the high runup of ∼8 m and considerable inundation distance of ∼150 m around 0.85°S at the west coast (site Watusampu). ii) for the site Pantoloan that has the late arrival (3 minutes from video waveform) of ∼2 m tsunami waves, model 1 and 2 predict an earlier arrival (∼1–2 minutes) of ∼2 m waves, while model 3 and 4 predict waves in lower amplitude (∼1 m). iii) although the peaks in inundation distance are consistent between surveys and the model predictions, the models underestimate the inundation length in the southern part of the bay. This may be due to the DEM used in the tsunami modelling containing buildings and vegetation. These features suggest that additional landslides have occurred in this event, for instance, landslides at the west side of the Palu bay (Takagi et al., 2019) could explain the high runup at site Watusampu.

In addition, Gusman et al. (2019) found 1 m subsidence along the coast of Palu City based on pixel-offset tracking and argues that the ground subsidence increases the impact of the tsunami potential in this region. However, the precision of data used may not be capable of constraining vertical displacements at the ∼1 m level. Furthermore, the vertical displacement inverted from the finite model fault shows small magnitude along the main rupture south of the bay (Fig. 5.14c), except for the bend (segment B) that accommodating with the significant local subsidence there.

5.8 Conclusions

In this chapter, I present a finite fault solution to characterise the coseismic surface deformation field for the 2018 M_w 7.5 Palu earthquake. I incorporate a more complete geodetic dataset, including the coseismic GPS displacement fields and multiple types of SAR-derived displacement fields to constrain a coseismic model through a Bayesian inversion framework. The estimated fault slip solution shows a dominance of shallow strike-slip for most of the rupture. At the Palu bay, the fault bends, Sulawesi Neck and the Balaesang peninsula, I find significant dip-slip motions. To provide better constraints on surface displacement over the Palu bay, I test four different scenarios that cover possible fault geometries in the region. All four models reproduce displacements observed by the surrounding GPS sites well, and reveal that dip-slip motions below the Palu bay are required to characterise the displacements observed by the GPS data around the bay. The models generally predict consistent runup heights and arrival times of the leading waves compared with the observed field surveys. The results support that the coseismic displacements are the leading cause of major tsunami source in and around Palu. On the other hand, the misfits between the model predictions and the field surveys suggest contributions of other phenomena in this event, such as landslides. In future work, better constraints on the fault strand over the bay can be provided by applying a joint inversion of geodetic dataset and tsunami observations.

Chapter 6

Conclusions

In this chapter, I summarise the key findings of this thesis and provide suggestions for future work.

6.1 Chapter 3

Variation in tropospheric delays is a major limiting factor on the accuracy of InSAR measurements. This is particularly the case when deformation and topography are correlated. To address limitations of previous InSAR tropospheric correction methods, in Chapter 3, I present a new approach for reducing tropospheric effects that combines the use of both external weather model data and the interferometric phase.

Global weather models have the benefits of complete spatial coverage and data availability, and can also account for both the hydrostatic and wet delay. The latest HRES-ECMWF analysis products have a much higher spatial resolution when compared with previous global weather models, which could be beneficial for describing smaller-scale variation in tropospheric delays. In the novel method, I assume that vertical refractivity profiles calculated from the HRES-ECMWF data can generally describe the form of the relationship between tropospheric delay and height but that the magnitude can be incorrect. I estimate a magnitude correction by scaling the original delays to best match the interferometric phase.

I validate the new method using simulated data. In the coseismic simulating case, the results show a greater reduction of the RMSE after the correction using the scaled tropospheric delays. The results demonstrate that the scaling estimation process does not result in an obvious reduction of the deformation signal. In the interseismic simulating case, the low-amplitude long-wavelength deformation can be separated from strong tropospheric delays, and there is a marked improvement over the unscaled case.

I apply the new algorithm to the central portion of the Altyn Tagh Fault in northern Tibet, where deformation correlates strongly with topographic relief of 6,000 m. The derived velocity map from the interferograms after correction using the scaled tropospheric delays is clearly more consistent with left-lateral strike-slip deformation than that corrected using the original tropospheric delays, and the mean standard deviation of velocities drops from 2.9 mm/yr to 2.6 mm/yr. With application of the additional scaling correction, the RMSE drops from 3.0 mm/yr to 1.9 mm/yr compared to the independent GPS measurements. In addition, the results for Taal Volcano in the Philippines demonstrate that the method can be applied to volcanic activities, for which deformation signals are sometimes correlated with topography.

These results suggest that the extra scaling step should be applied wherever weather model data are being used to correct the tropospheric delay in interferograms.

6.2 Chapter 4

The 1600 km-long ATF is a major intra-continental strike-slip fault in the Northern Tibetan Plateau, the slip rate of which has significant implications for our understanding of the tectonic processes of the Tibetan Plateau region. Previous studies of interseismic deformation from geodetic measurements over the ATF have only focused on specific portions and may not provide an overall picture of the variation of localised strain accumulation along the fault.

In Chapter 4, I present an InSAR velocity field over around 1500 km of the ATF, which is the first time such a large-scale analysis of the fault has been carried out with InSAR. To improve the retrieval of long wavelength signals that are strongly masked by tropospheric delay variation across the 6 km topographic relief, I use the correction method that I present in Chapter 3 to mitigate the tropospheric effects in the interferograms. I present a new scheme to remove long wavelength trends from the InSAR velocity field using GPS observations, and derive mosaicked LOS velocities along the fault that are consistent in the overlapping region between adjacent tracks.

Based on the estimated east-west velocity field, the derived 1-D fault-perpendicular profiles at intervals of 0.5° along the fault show visible strain accumulation on the ATF. The asymmetric pattern of interseismic velocities shown in the profiles suggests a decrease in rigidity from the Tarim basin to the Tibetan Plateau. The interseismic modelling results using a modified elastic half-space model reveal a systemic decrease of the slip rate along the ATF from 12 mm/yr to 8 mm/yr over the western portion to the central portion, whereas it increases again to 10 mm/yr over the eastern portion.

The inverted width of shear zones along the fault reveals two sections with broad shear zone along the fault: ~122 km between 84°E to 85.5°E, and ~94 km between 91°E to 91.5°E. Over these areas, the results suggest that the strain is distributed over multiple strands rather than concentrating on a single narrow strand. The wide shear zones also explain the seismic activities on the strands away from the ATF in these areas, on which four earthquakes ($M_w > 5.0$) have occurred recently. The modelling results also show a relatively wider shear zone of ~62 km between 87.5°E to 88°E in the location where the ATF breaks into three parallel strands.

This study shows significant strain accumulation along the 1500 km length of the ATF, and that it is fast at about 10 mm/yr and quite localised along the fault. Since no major earthquake ($M_w > 7.0$) has occurred along the ATF since the 1924 events, a slip deficit of ~1 m has been accumulated over the last century. Consequently, the ATF is capable of rupturing along its entire length, with the potential for some of the largest earthquakes on the continents. The results also show a high strain rate greater than 0.4 μstrain yr^{-1} along the south-western segment of the fault to the west of 83 °E, and it could be ascribed to the stress loading effects of the recent seismic activities in this region. While it is not possible to rule out the impact from the postseismic deformation of the 2014 Yutian earthquake, the high strain rate estimated on the south-western segment of the ATF may imply a relatively greater earthquake potential in this region compared to other portions. Furthermore, the estimated high slip rate of ~12 mm/yr along the south-western segment of the ATF also demonstrates that the generation of the NS-trending normal faulting events in this region, such as the 2008 M_w 7.2 Yutian earthquake, is ascribed to the EW-trending extensional stress at a step-over between the two left-lateral faults.

6.3 Chapter 5

The 2018 M_w 7.5 Palu earthquake caused tsunami waves of surprisingly large magnitudes for a strike-slip faulting earthquake. The coseismic displacement field is instrumental in explaining the direct cause of the tsunami in this event and can shed light on the tsunami potential generated from strike-slip earthquakes.

In Chapter 5, I invert for a finite fault solution constrained from coseismic GPS displacement fields and a suite of SAR-derived coseismic displacement fields including InSAR, MAI and pixel-offset tracking. I find notable dip-slip motions in the east of the main fault in the Sulawesi Neck and north-west of the main fault in the Balaesang peninsula based on the surface observations. I interpret these characteristics as slip on normal faults in the two areas and incorporate them to the model.

I apply a Bayesian approach to solve for the optimal value of source parameters, and the finite fault solution reveals a dominance of shallow strike-slip motion for most of the rupture, mostly limited to the upper 10 km. The results show that the large slip (> 5 m) on the segments south of the bay continues up to the surface, whereas the segments north of the bay feature no, or minor slip, on the upper segments, implying that the rupture doesn't reach the surface there. Besides the two normal faults, the results show significant dip-slip motions at the fault bends of the main rupture.

To provide better constraints on surface displacement over the Palu bay, I investigate four different scenarios that cover possible fault geometries in the region. All four models reproduce displacements observed by the surrounding GPS sites well, and reveal that dip-slip motions below the Palu bay are required to characterise the displacements observed by the GPS data around the bay. The models generally predict consistent runup heights and arrival times of the leading waves compared with the observed field surveys.

The results suggest that displacements due to coseismic slip are the leading cause of the major tsunami source in and around Palu. However, the misfits between the model predictions and the field surveys suggest contributions of other phenomena in this event, such as landslides.

6.4 Future work

6.4.1 Enhancing the scaling tropospheric correction method

The scaling tropospheric correction method could potentially be enhanced in two ways: i) using an upgraded weather model product with a higher spatial and/or temporal resolution; ii) estimating a model for deformation while estimating the scaling parameter.

6.4.2 Improved seismic hazard evaluation for both the Altyn Tagh fault and other faults within Tibet

A two-dimensional strain rate map in a high resolution might be more informative in terms of seismic hazard evaluation. In future work, it may be possible to apply a VELMAP approach (Wang and Wright, 2012) or a spherical wavelet-based multiscale approach (Tape et al., 2009) to invert for a strain rate map over the ATF and other faults within Tibet, based on the InSAR LOS velocity field derived in this thesis. In addition, it may be possible to apply some more advanced tools, such as Blocks (Meade and Loveless, 2009), to characterise the internal deformation of Tibet.

6.4.3 Applying a joint inversion of geodetic dataset and tsunami observations to the 2018 M_w 7.5 Palu earthquake

For the 2018 M_w 7.5 Palu earthquake, it may be possible to perform a joint inversion using geodetic dataset and tsunami waveforms in future work, to provide better constraints on the fault strand over the Palu bay.

6.5 Concluding remarks

The work in this thesis is concerned with characterising seismic hazard by determining short-term seismic deformation and long-term crustal displacement. I highlighted two case studies over large length scales, one showing the interseismic strain accumulation along the Altyn Tagh Fault over a spatial scale of approximately 1500 km, and the other providing the finite fault solution to characterise the coseismic surface deformation field for the 2018 M_w 7.5 Palu earthquake that ruptured around 200 km.

The fast and localised interseismic strain accumulation along the Altyn Tagh Fault suggests that the fault is capable of rupturing along its entire length, with the potential for some of the largest earthquakes on the continents.

The finite fault solution of the 2018 M_w 7.5 Palu earthquake constrained from geodetic datasets shows that displacements due to coseismic slip are the leading cause of the major tsunami source in and around Palu.

Additionally, I demonstrated that applying the scaling step to the tropospheric delays estimated from the HRES-ECMWF can improve the retrieval of deformation signals from InSAR in different aspects of seismic hazard.

Appendix A

Supplementary materials for Chapter 3

A.1 Figures

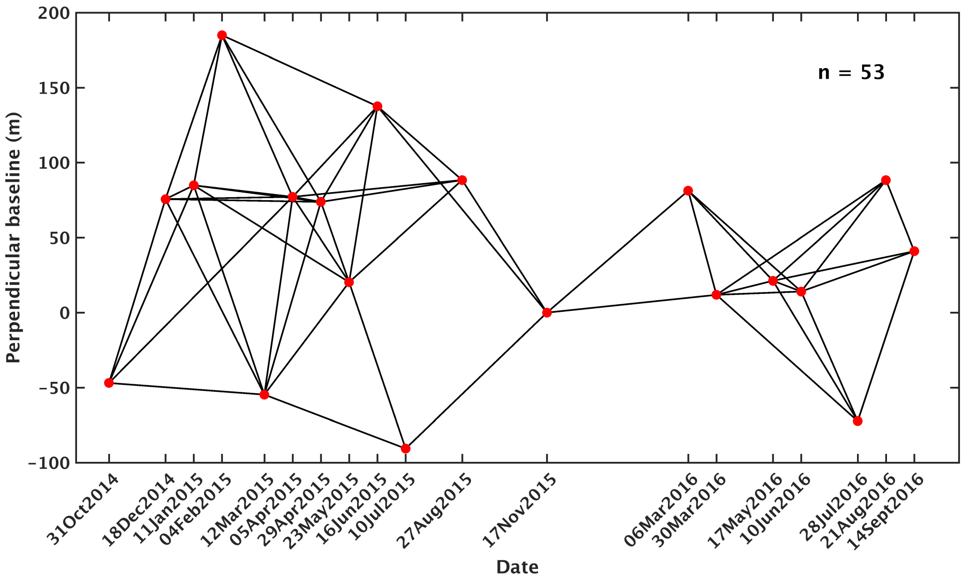

Figure A.1: Small baseline subset network of interferograms. I make 53 interferograms for which the temporal baseline is shorter than 120 days and the perpendicular baseline is less than 150 m. The red points represent the 19 epochs and the black lines indicates the small baseline interferograms

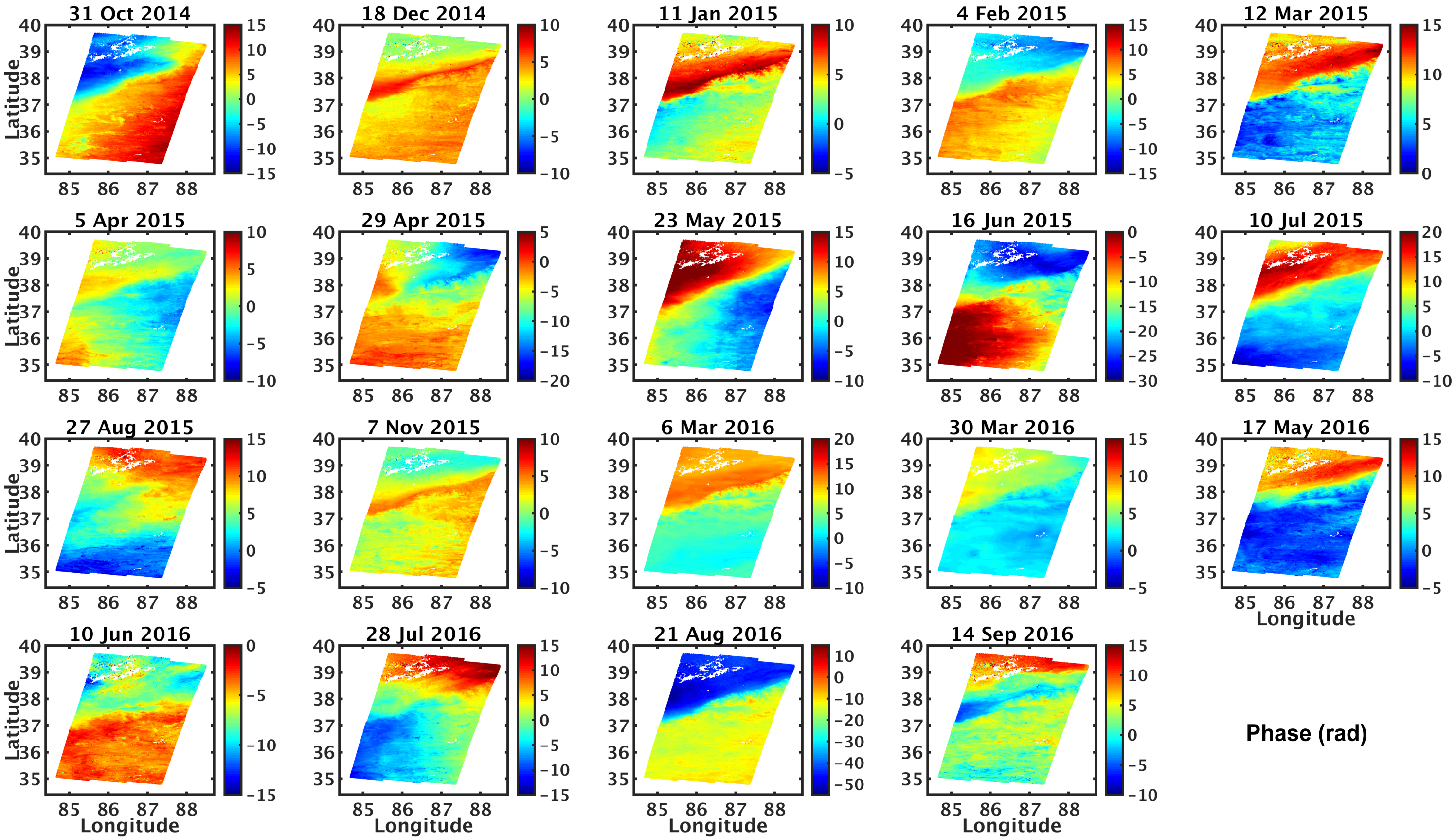

Figure A.2: InSAR phase delay anomalies for all 19 epochs estimated from the small baseline interferograms with a minimum norm constraint.

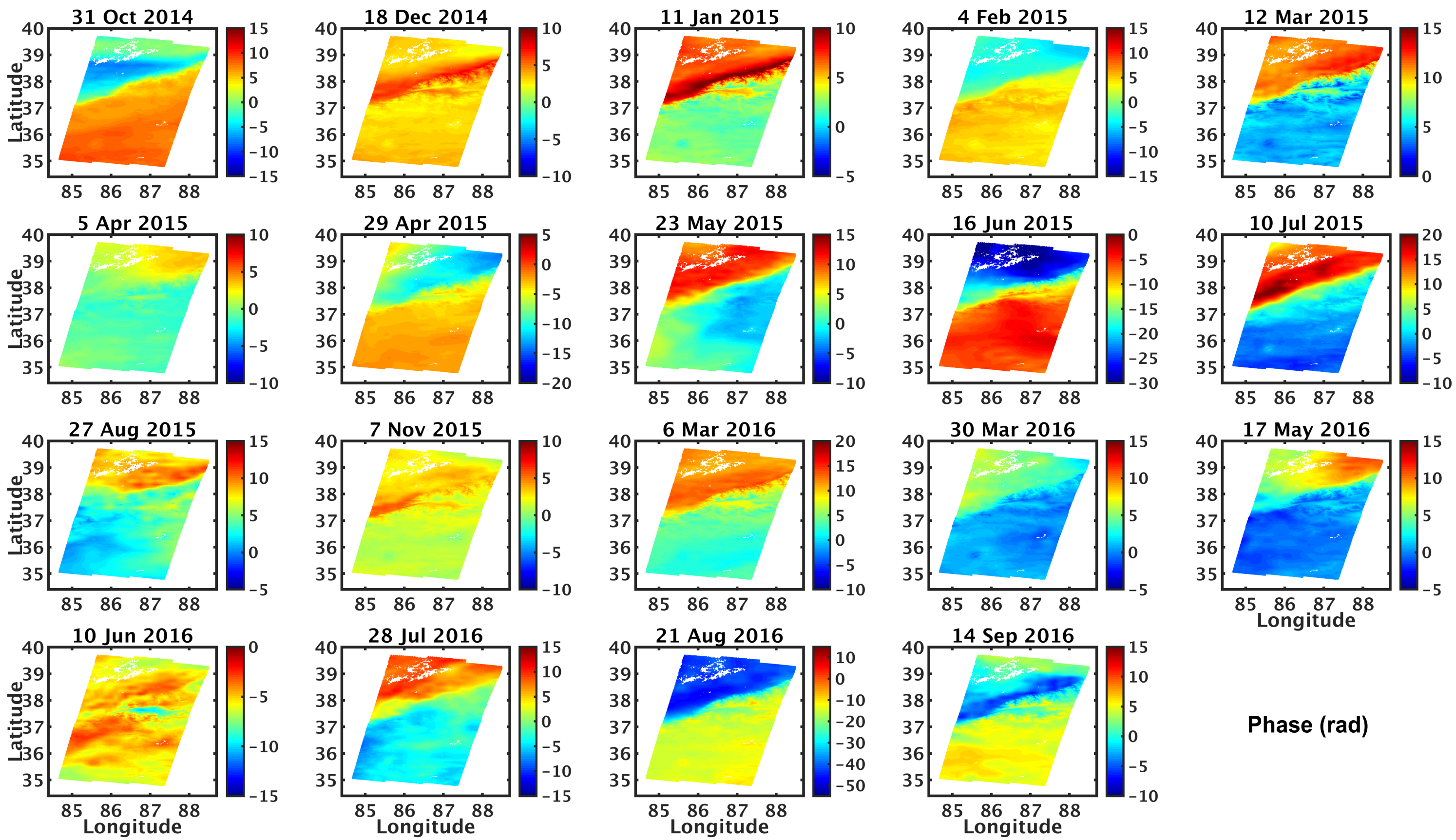

Figure A.3: Tropospheric phase delay anomalies for all 19 epochs estimated from the HRES-ECMWF using the minimum norm solution. The value in each epoch is referenced to the InSAR phase delay anomaly of the corresponding epoch for the comparison.

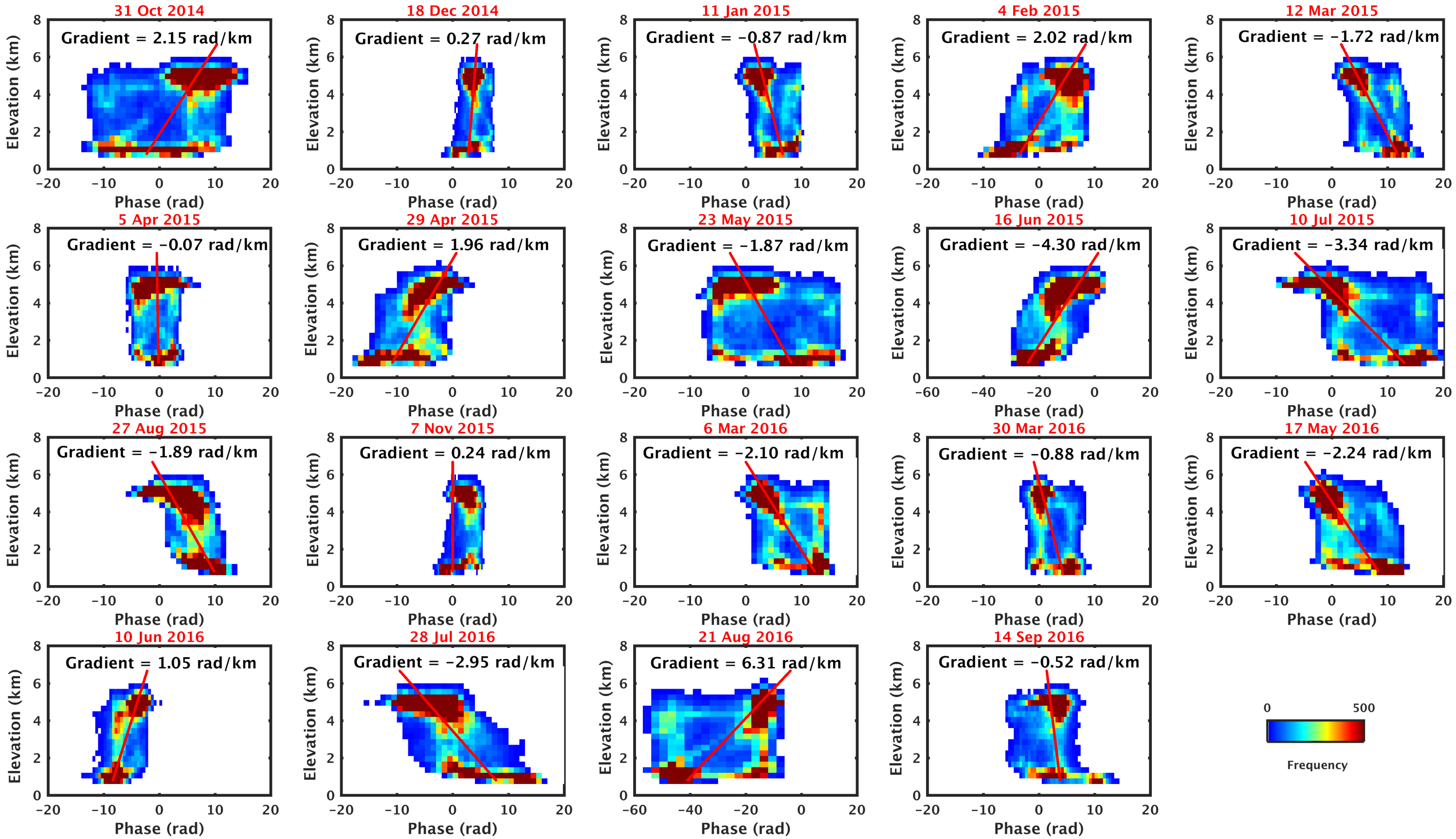

Figure A.4: Histograms of the InSAR phase delay anomalies versus topography for all 19 epochs before tropospheric corrections. The red lines are the best fitting linear function, shown for reference.

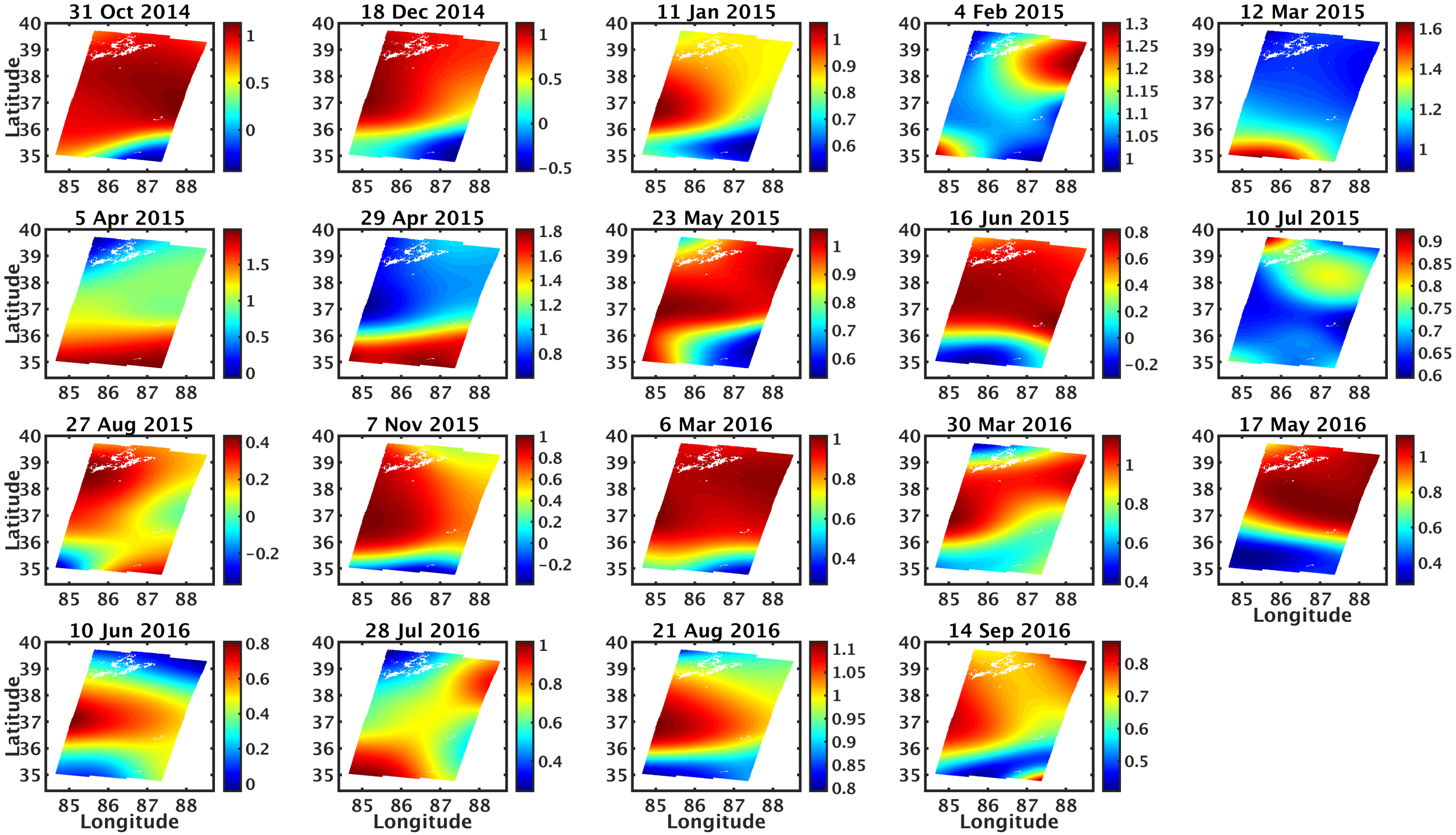

Figure A.5: Spatial distributions of the smoothed scaling factor (K) applied to the HRES-ECMWF correction for all 19 epochs.

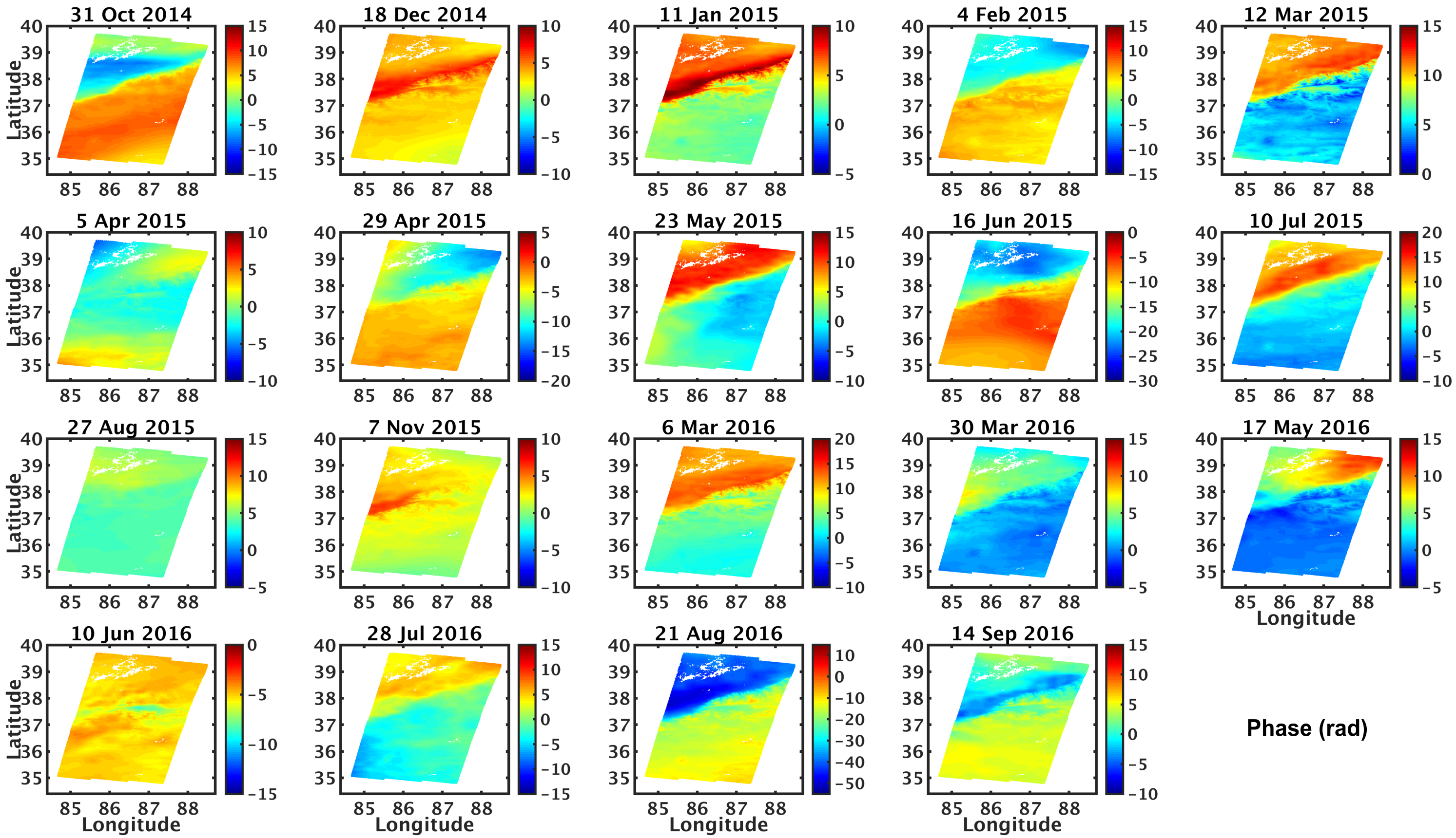

Figure A.6: Scaled tropospheric phase delay anomalies for all 19 epochs. The value in each epoch is referenced to the InSAR phase delay anomaly of the corresponding epoch for the comparison.

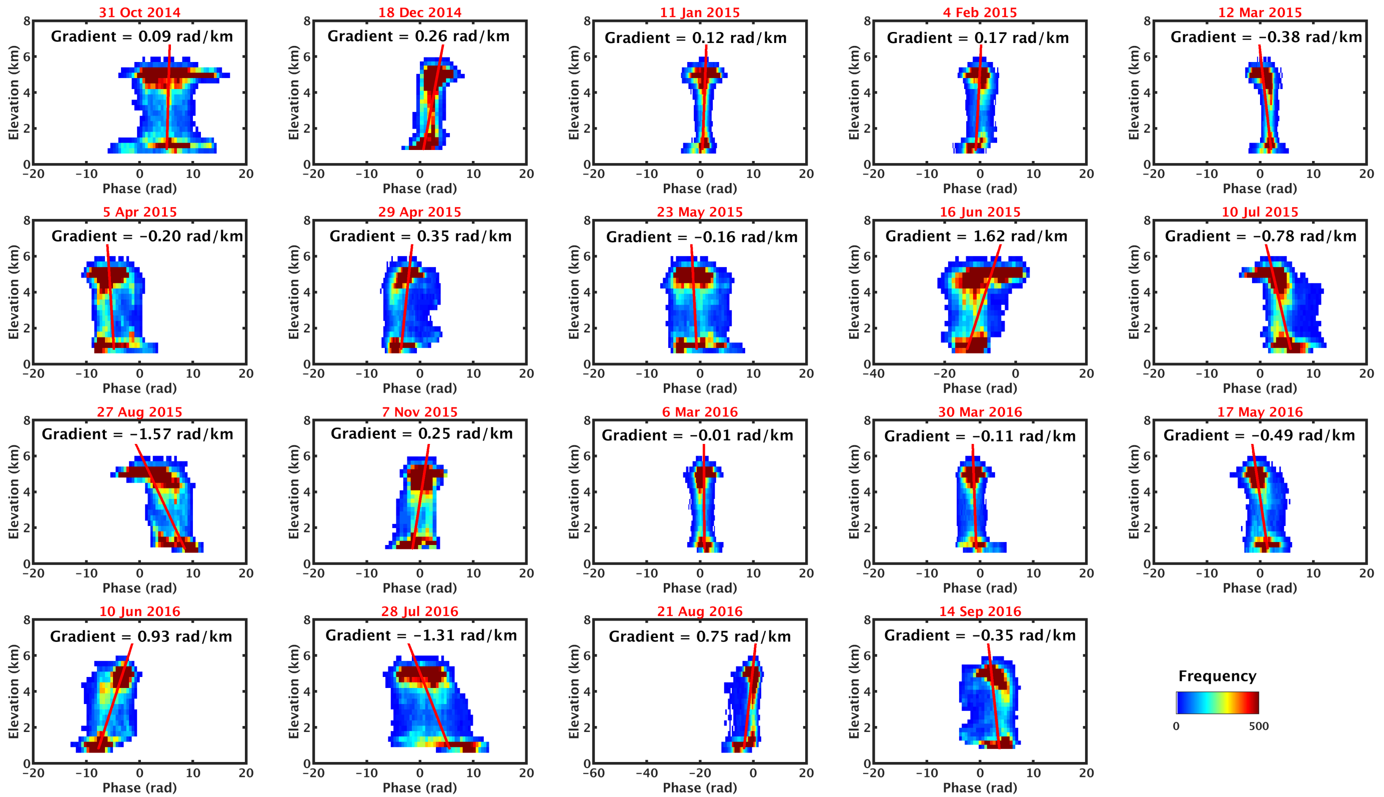

Figure A.7: Histograms of the InSAR phase delay anomalies after correction using the scaled weather model anomalies versus topography for all 19 epochs. The red lines are the best fitting linear function, shown for reference.

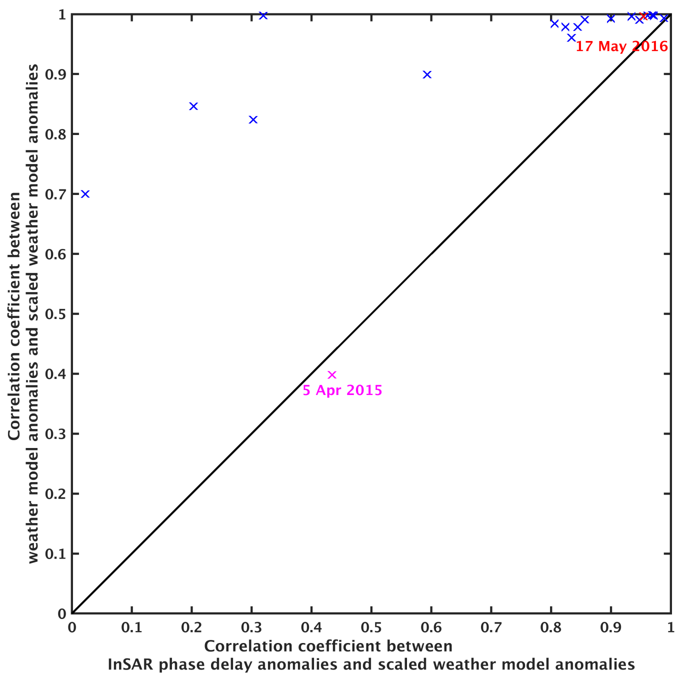

Figure A.8: Comparison for the correlation coefficient between the InSAR phase delay anomalies and scaled weather model anomalies to the value between the original weather model anomalies and scaled weather model anomalies for all 19 epochs. The red cross represents the epoch I selected as an example to show in Fig. 3.1 and 3.2. The magenta cross shows the epoch for which the scaled weather model anomalies are more correlated with the InSAR phase delay anomalies.

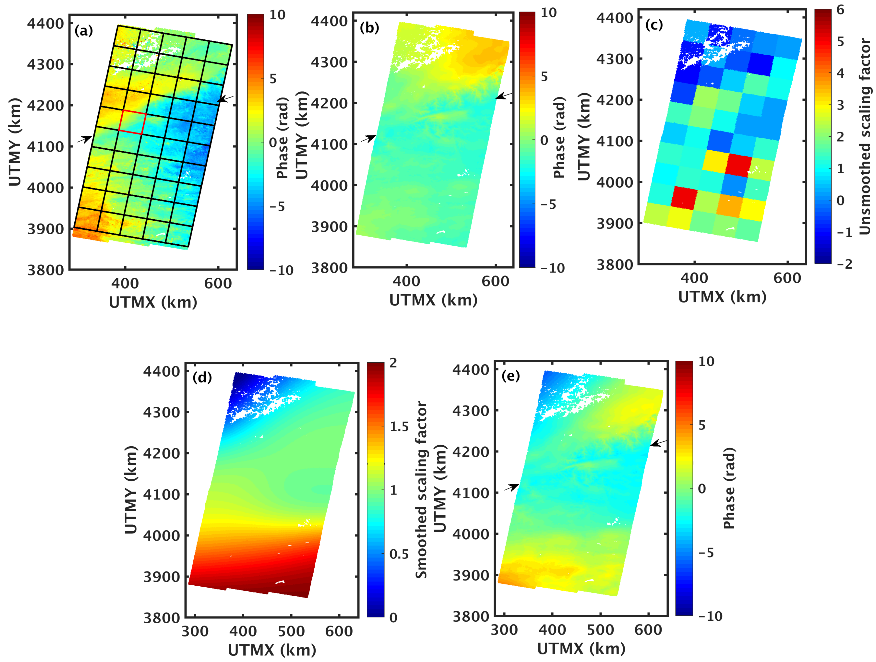

Figure A.9: Scaling results for an atypical epoch 5 April 2015. (a) and (b) are the InSAR phase delay anomalies and the tropospheric phase delay anomalies estimated from the weather model respectively, estimated using the minimum norm approach. The black arrows indicate the fault orientation. The overlapped grid in (a) is rotated to the heading direction of the satellite, and each patch is completely within the SAR area so as to make sure the number of points in each patch is similar. (c) shows the scaling factors of all patches. (d) shows the spatial pattern of the spatially-varying smoothed scaling factors. (e) shows the scaled tropospheric phase delay anomalies.

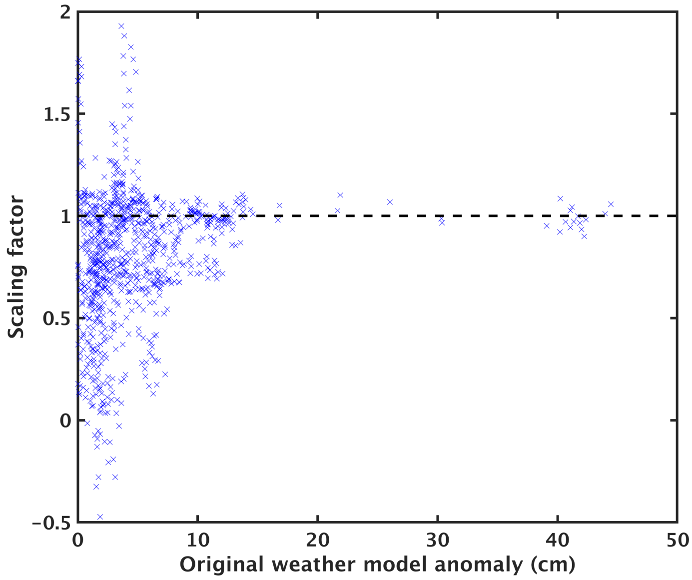

Figure A.10: Original weather model anomaly against scaling factor. Blue crosses represent all 50 patches of all 19 epochs.

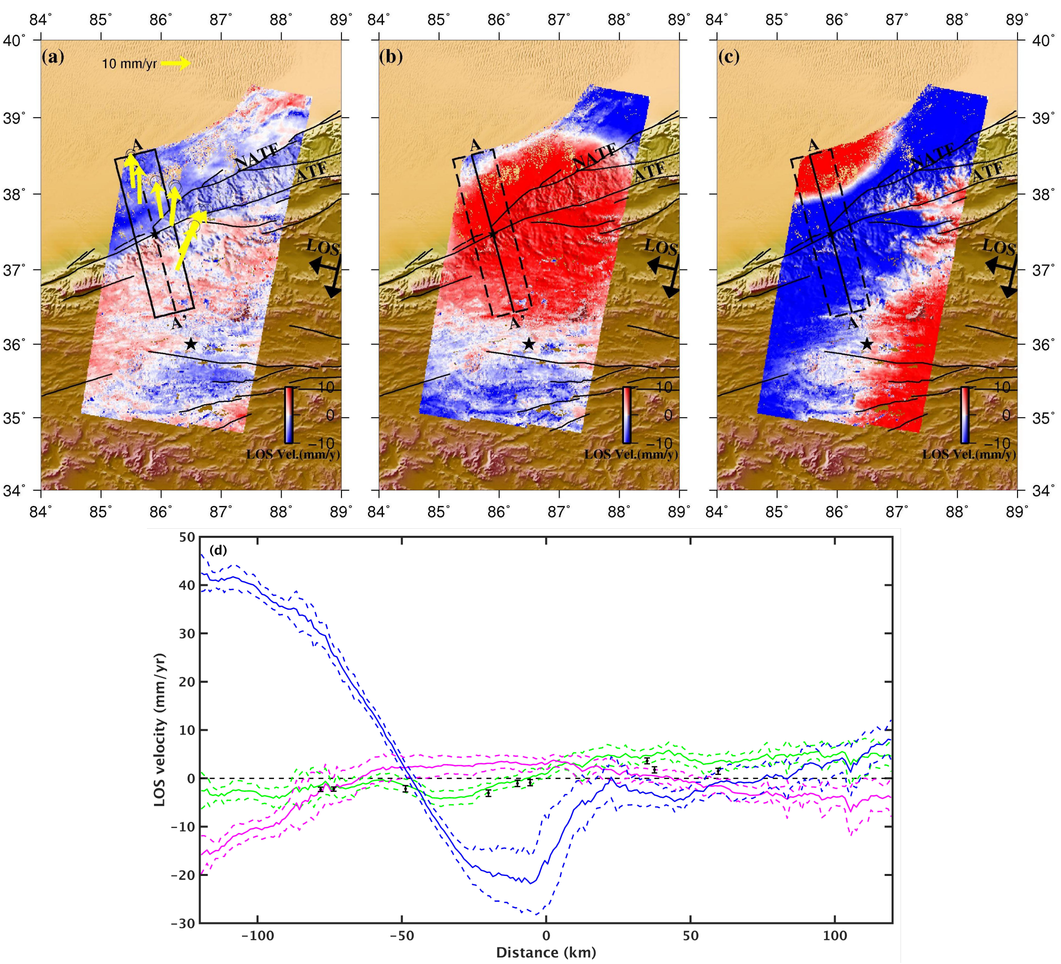
(a)
(b)
(c)
(d)
10 mm/yr
A
A'
NATF
ATF
LOS
LOS Vel.(mm/y)
84°
85°
86°
87°
88°
89°
34°
35°
36°
37°
38°
39°
40°
10
0
−10
LOS velocity (mm/yr)
Distance (km)
-100
-50
0
50
100
50
40
30
20
10
0
-10
-20
-30

Figure A.11: LOS annual velocity maps derived from the deramped single master interferograms corrected with a, the scaled tropospheric delays in the correct order; b, the scaled tropospheric delays in the randomized order A (Table A.2) and c, the scaled tropospheric delays in the randomized order B. Incoherent scatterers in the northern sandy area were masked out. For each panel, positive values indicate motion towards the satellite, and negative values indicate motion away from the satellite relative to the reference region (black star). Black lines A-A' represents profiles which are perpendicular to the strike of the Altyn Tagh Fault with the centre of 85.9°E, 37.5°N and a 120 km extension of each side of the fault. The black dash line indicates the extent of the velocity projection (swath wides 30 km). Yellow arrows show velocities of available campaign GPS stations near the fault within the InSAR area, which are in a Eurasia reference frame with uncertainties plotted at 95% confidence level. (d) shows the LOS velocity comparison between the InSAR profile A-A' in a (green), b (magenta) and c (blue) and surrounding campaign GPS measurements (black errorbars). The full line and dashed line represent the average values and the $\pm 1\sigma$ of the profile, respectively, calculated from 5 km long bins. The InSAR profiles have been referenced the same reference frame as the GPS data.

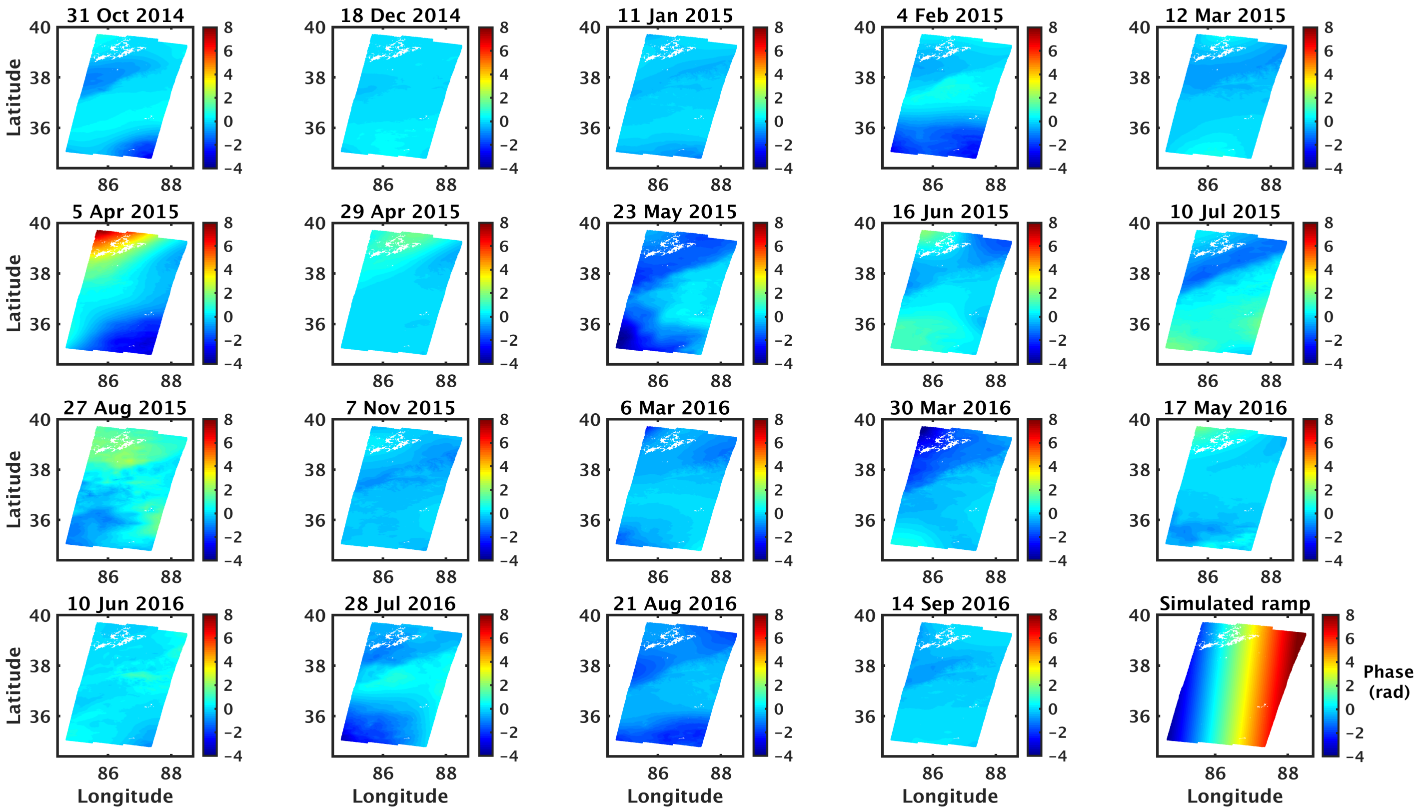

Figure A.12: Changes in tropospheric phase delay anomalies.

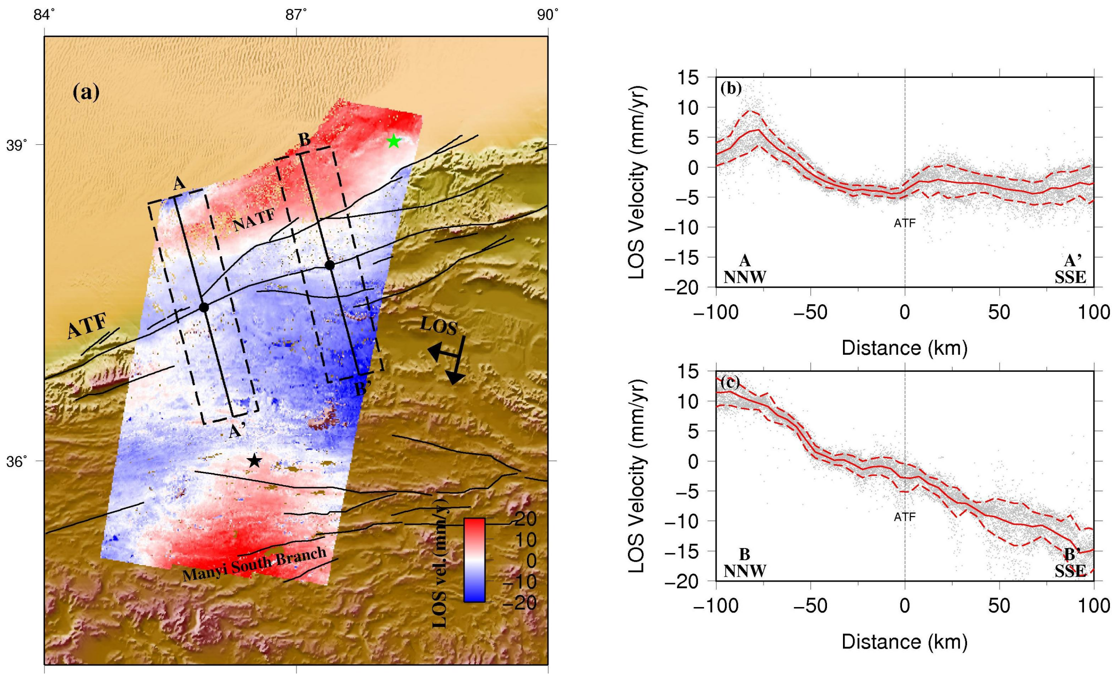

Figure A.13: (a) LOS annual velocity maps derived from the deramped single master interferograms corrected using the power law method (Bekaert et al., 2015a). Incoherent scatterers in the northern sandy area were masked out. Positive values indicate motion towards the satellite, and negative values indicate motion away from the satellite relative to the reference region (black star). The green star shows the location the sounding station 51777. (b) and (c) show LOS velocities for profiles A-A' and B-B'. The full line and the dashed line represent the average values and the $\pm 1\sigma$ of the profiles, respectively, calculated from 5 km long bins.

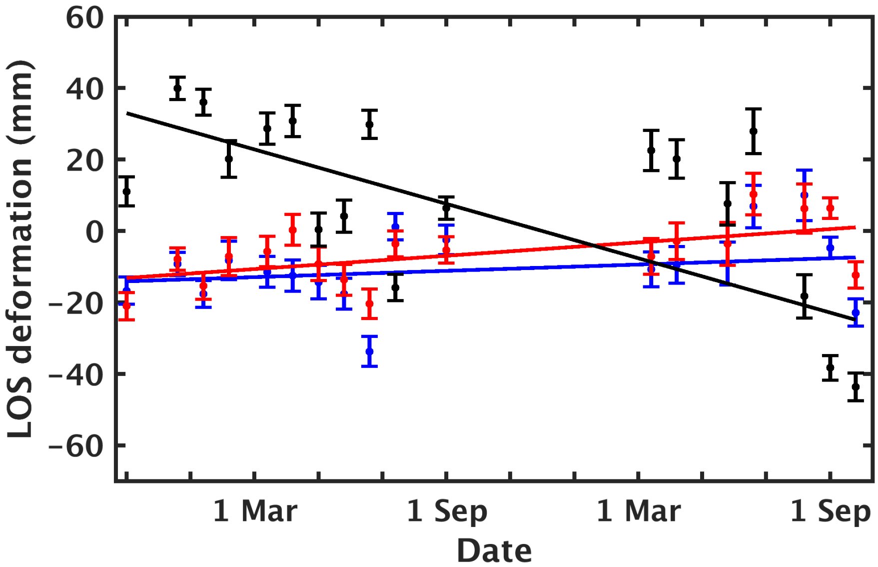

Figure A.14: Temporal evolution of deformation between two distant points (green points along the profile B-B' in Fig. 3.10a and 3.10b) derived using the interferograms after correction with the original HRES-ECMWF (blue), the scaled HRES-ECMWF (red) and the power law method (black). Error bars represent the $\pm 1\sigma$ spread. The full lines represent the corresponding best-fitting linear function.

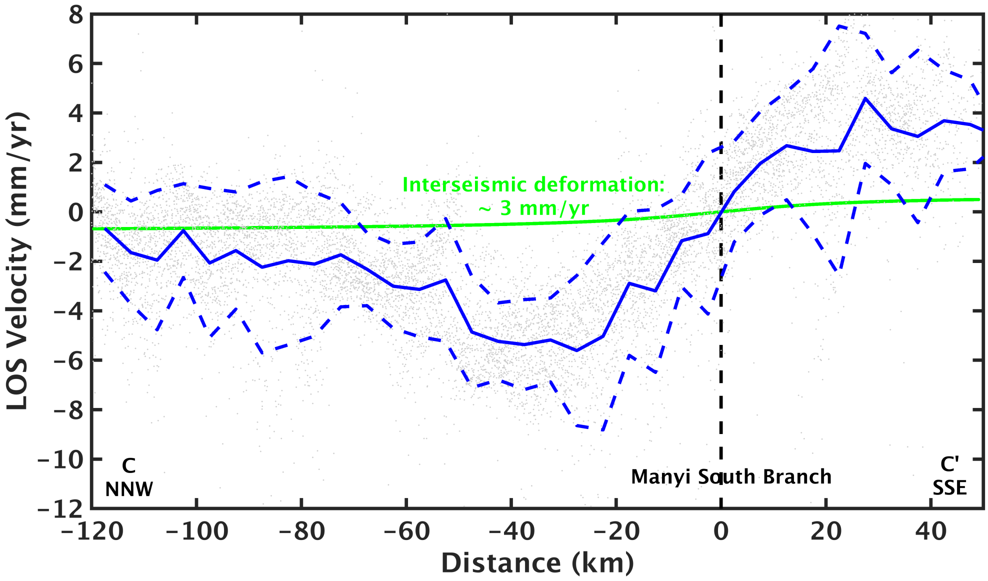

Figure A.15: Comparison between InSAR LOS velocities for the profile C-C' (grey dots) and previous interseismic deformation measurement (green line) (Bell et al., 2011) across the Manyi south branch. The blue full line and blue dashed line represent the average values and the $\pm 1\sigma$ of the grey dots, calculated from 5 km long bins.

A.2 Tables

Table A.1: Tropospheric phase delay anomalies for each epoch in the LOS direction estimated from continuous GPS data.

Date	Delay (cm)	
	XJQM	XJRQ
31 Oct 2014	3.58	0.65
18 Dec 2014	-2.45	-1.65
11 Jan 2015	-5.57	-3.88
4 Feb 2015	-0.76	0.66
12 Mar 2015	-6.44	-5.91
5 Apr 2015	-3.92	-4.41
29 Apr 2015	-0.51	5.00
23 May 2015	-5.22	-3.46
16 Jun 2015	-6.11	— [a]
10 Jul 2015	-2.66	-1.39
27 Aug 2015	1.28	-0.72
17 Nov 2015	-3.21	-0.49
6 Mar 2016	-7.38	-6.52
30 Mar 2016	-5.45	-2.53
17 May 2016	-2.01	-3.99
10 Jun 2016	4.10	4.36
28 July 2016	2.30	-0.85
21 Aug 2016	23.70	21.62
14 Sept 2016	4.50	3.51

[a] The original data is unavailable.

Table A.2: Randomized weather model.

	Epoch																		
Group A	3	5	13	15	7	10	19	12	14	1	4	6	18	17	2	11	8	16	9
Group B	13	15	3	5	17	1	9	2	4	11	14	16	8	7	12	10	18	6	19

Table A.3: Parameters of the power law method used.

Parameter	Value
Number of patches	70
Patch overlap (%)	30
Powerlaw_h0 (km)	7.7 [a]
Powerlaw_alpha	1.3 [a]
Powerlaw_xy_res (m)	[1000 1000]
Spatial filter band (m)	[2000 4000 4000 8000 8000 16000 16000 32000]

[a] I estimated the Powerlaw_h0 and the Powerlaw_alpha from the balloon sounding data of the station 51777 between October 2014 and October 2016, which the data was downloaded from http://weather.uwyo.edu/upperair/sounding.html.

A.3 Package for A Spatially Varying Scaling (ASVS) Method

A.3.1 Introduction

A spatially varying scaling (ASVS) method for InSAR tropospheric corrections is developed to address a major limiting factor in InSAR measurements, that of variable delay through the troposphere. This approach combines the use of both external weather model data and the interferometric phase, which has overcome the limitations of using either approach individually. The distributed ASVS package consists of Matlab scripts only and is compatible with the StaMPS software and the TRAIN.

A.3.2 Configuration

The ASVS package has been developed based on Matlab 2018, whereas it is expected to run without large problems with older versions.

The ASVS package is compatible with the StaMPS software version 4.0 and could recognize the StaMPS structure to extract required parameters of interferograms.

The ASVS package is integrated with the TRAIN version 1beta and could extract tropospheric delays computed from the external weather model data using the TRAIN automatically.

A.3.3 Data preparation

As the ASVS package is independent of any processor of InSAR and InSAR tropospheric correction, interferometric phase and tropospheric delay phase estimated from the external weather model data should be provided in advance. A DEM file, a Lon-Lat coordinates file, and other required parameters should be prepared by users as well. If users process the InSAR with the StaMPS software and use the TRAIN to compute tropospheric delays from the external weather model data, most of the required processing parameters can be automatically extracted based on the files of the StaMPS and the TRAIN. All required parameters are stored in a Matlab matrix named as parms_ASVS.mat. Table A.4 shows the detailed information of each processing parameter.

Table A.4: Processing parameters used in the package.

<table>
<tr><th rowspan="2">Parameter</th><th rowspan="2">Description</th><th colspan="2">Interferograms</th><th colspan="2">Tropospheric delays</th></tr>
<tr><th>StaMPS structure</th><th>Non-StaMPS structure</th><th>TRAIN structure</th><th>Non-TRAIN structure</th></tr>
<tr><td>stamps_processed</td><td>StaMPS structure</td><td>‘y’</td><td>‘n’</td><td>-</td><td>-</td></tr>
<tr><td>train_processed</td><td>TRAIN structure</td><td>-</td><td>-</td><td>‘y’</td><td>‘n’</td></tr>
<tr><td>phuw_file</td><td>Full file path of unwrapped interferograms stored as a matrix of size [n_points n_ifgs] in radian units, variable ‘ph_uw’</td><td>Automatically loading from the StaMPS processed phuw_sb2.mat</td><td>Loading the file path given by users</td><td>-</td><td>-</td></tr>
<tr><td>ph_tropo_era_file</td><td>Full file path of tropospheric delays stored as a matrix of size [n_points n_ifgs] in radian units, variable ‘ph_tropo_era’</td><td>-</td><td>-</td><td>Automatically loading from the TRAIN processed tca_sb2.mat</td><td>Loading the file path given by users</td></tr>
<tr><td>hgt_file</td><td>Full file path of the topography stored as a matrix of size [n_points,1] in meter units, variable ‘hgt’</td><td>Automatically loading from the StaMPS processed hgt2.mat</td><td>Loading the file path given by users</td><td>-</td><td>-</td></tr>
<tr><td>ll_file</td><td>Full file path of the Lon-Lat geo-coordinates, stored as a matrix of size [n_points, 2] in the longitude and latitude, variable ‘lonlat’</td><td>Automatically loading from the StaMPS processed ps2.mat</td><td>Loading the file path given by users</td><td>-</td><td>-</td></tr>
<tr><td>utm_zone</td><td>The utm zone of the ROI</td><td colspan="4" rowspan="7">From users</td></tr>
<tr><td>heading_InSAR</td><td>The azimuth direction of the satellite in degree units</td></tr>
<tr><td>win_size</td><td>The grid size in kilometer units</td></tr>
<tr><td>x_min</td><td rowspan="4">The grid corners in kilometer units</td></tr>
<tr><td>x_max</td></tr>
<tr><td>y_min</td></tr>
<tr><td>y_max</td></tr>
<tr><td>sm_std</td><td>The Gaussian smoothing width in kilometer units</td><td colspan="4">Default value is 71 km</td></tr>
<tr><td>n_ifg</td><td>The number of interferograms</td><td rowspan="3">Automatically loading from the StaMPS processed ps2.mat</td><td rowspan="3">From users</td><td rowspan="3">-</td><td rowspan="3">-</td></tr>
<tr><td>n_image</td><td>The number of images</td></tr>
<tr><td>ifgday_ix_file</td><td>Full path of the design matrix relating the relevant observation epochs for each interferogram, stored with name ‘ifgday_ix’</td></tr>
</table>

A.3.4 Programs

After unzipping the zip file of the ASVS package at YOURPATH, to source functions in the sub-folder named 'functions' , users should be able to run the following command in Matlab: addpath('YOURPATH/ASVS/functions').

A.3.4.1 Step 1: Getting a grid overlapped with the Region of Interest (ROI)

A grid overlapped with the ROI is generated in step 1. Users may need to run this step for multiple times to adjust the geometry of the grid until it is well-overlapped with the ROI. Results of this step are saved in a Matlab matrix named as scaling_grid.mat that then will be used in step 2.

A.3.4.2 Step 2: Estimating spatially varying scaling factors

Spatially varying scaling factors are derived in step 2. Outputs of this step are the scaled tropospheric phase delay anomaly of every single epoch and the estimated smoothed spatially varying scaling factors of every point in the ROI. These final results are saved in a Matlab matrix as ASVS_results.mat. Users then could compute the scaled interferometric tropospheric delays and subtract them from the interferometric phase to derive tropospheric corrected interferograms.

Appendix B

Supplementary materials for Chapter 4

B.1 Figures

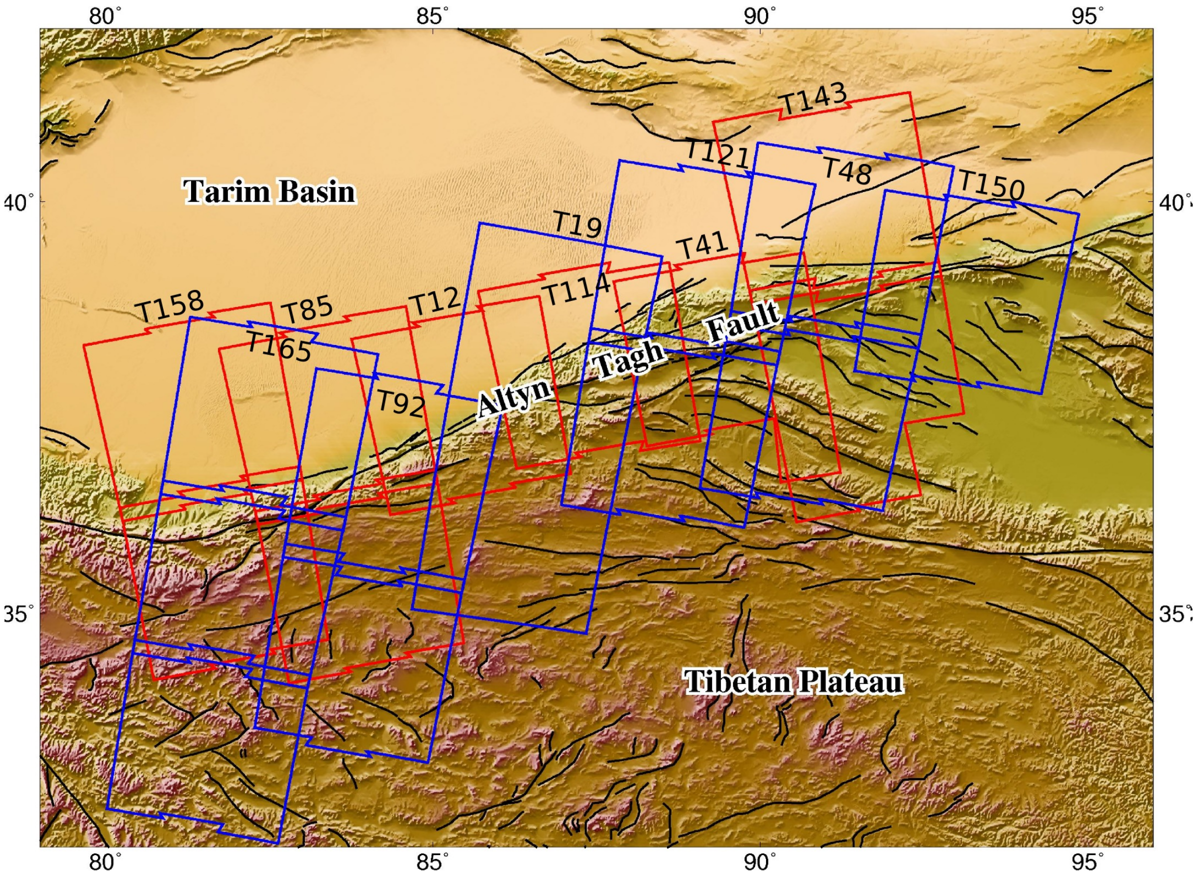

Figure B.1: Sentinel-1 data frames across the ATF, including 6 tracks in ascending (red polygons) and 6 tracks in descending (blue polygons).

Figure B.2: Small baseline subset networks of the individual tracks. The red circles represent the epochs of SAR acquisitions and the black lines indicate the generated small temporal baseline interferograms.

(a)

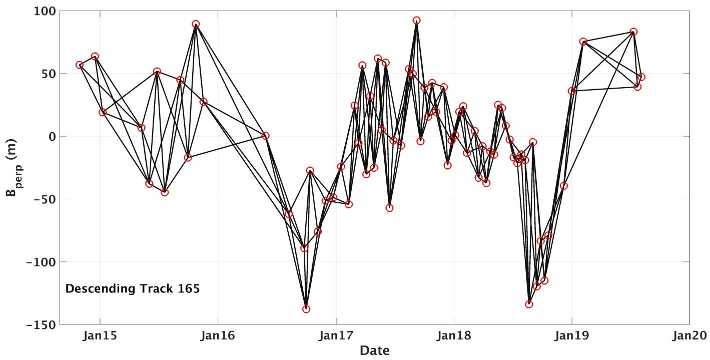

(b)

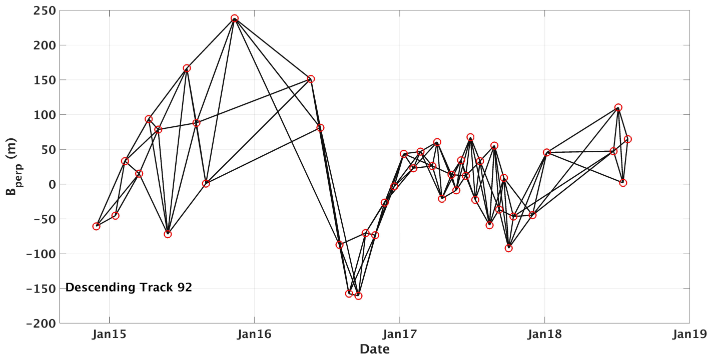

(c)

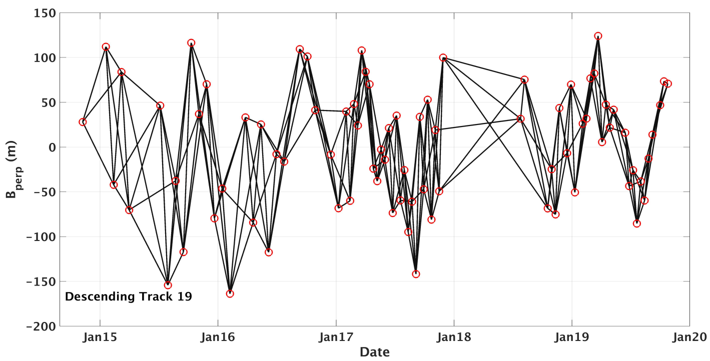

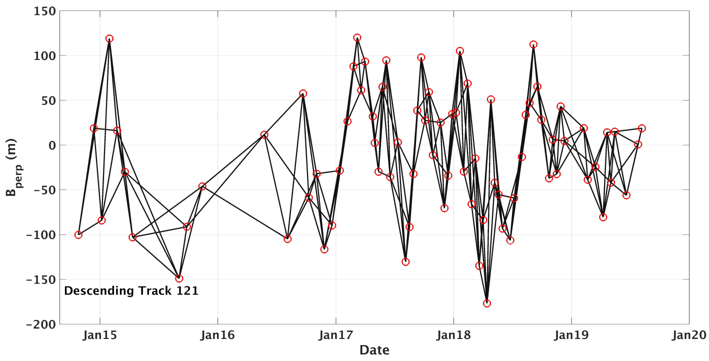

Descending Track 121
Bperp (m)
Date
150
100
50
0
−50
−100
−150
−200
Jan15
Jan16
Jan17
Jan18
Jan19
Jan20

(d)

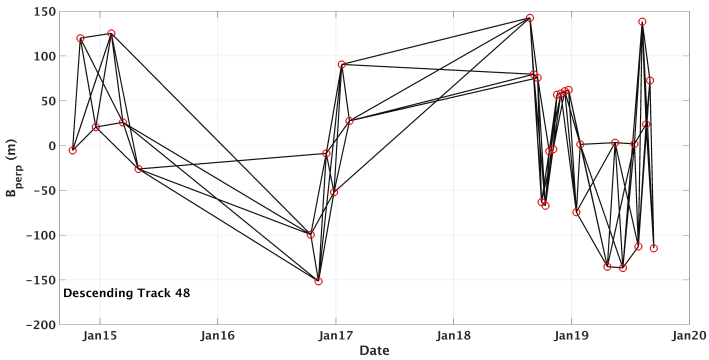

Descending Track 48
Bperp (m)
Date
150
100
50
0
−50
−100
−150
−200
Jan15
Jan16
Jan17
Jan18
Jan19
Jan20

(e)

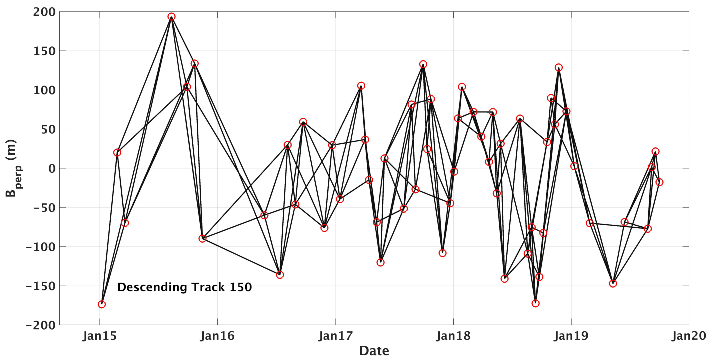

Descending Track 150
Bperp (m)
Date
200
150
100
50
0
−50
−100
−150
−200
Jan15
Jan16
Jan17
Jan18
Jan19
Jan20

(f)

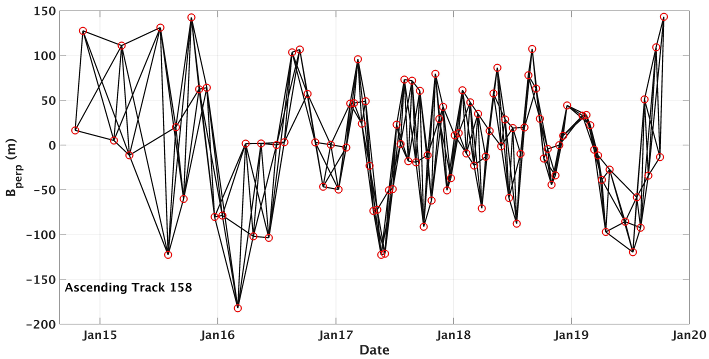
Ascending Track 158
Bperp (m)
Date
150
100
50
0
−50
−100
−150
−200
Jan15
Jan16
Jan17
Jan18
Jan19
Jan20

(g)

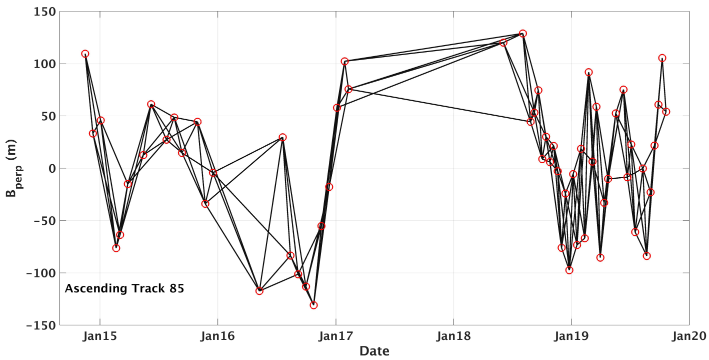
Ascending Track 85
Bperp (m)
Date
150
100
50
0
−50
−100
−150
Jan15
Jan16
Jan17
Jan18
Jan19
Jan20

(h)

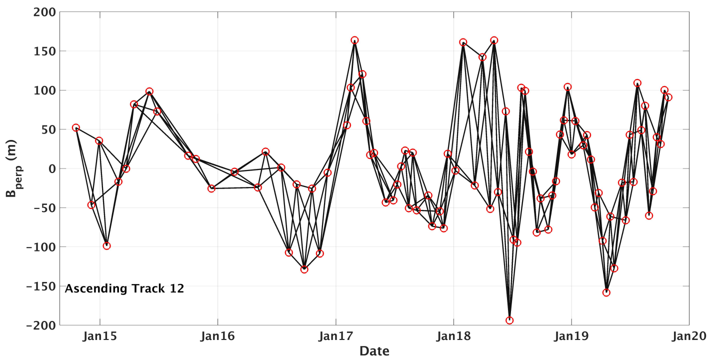
Ascending Track 12
Bperp (m)
Date
200
150
100
50
0
−50
−100
−150
−200
Jan15
Jan16
Jan17
Jan18
Jan19
Jan20

(i)

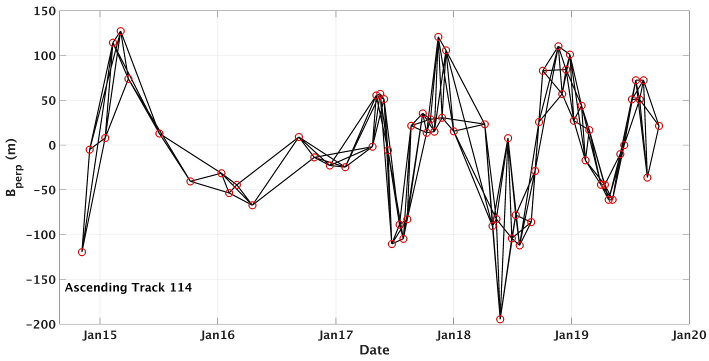
150
100
50
0
−50
−100
−150
−200
B_perp (m)
Ascending Track 114
Jan15
Jan16
Jan17
Jan18
Jan19
Jan20
Date

(j)

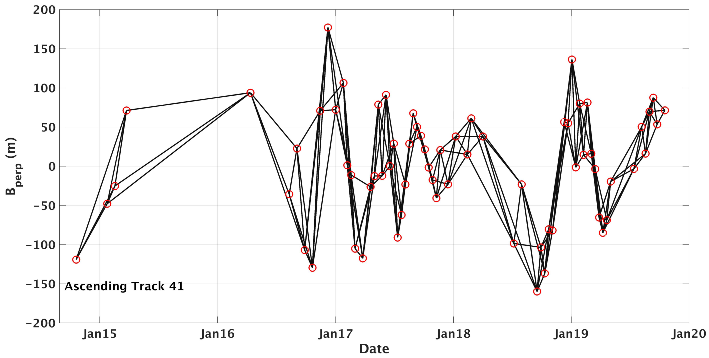
200
150
100
50
0
−50
−100
−150
−200
B_perp (m)
Ascending Track 41
Jan15
Jan16
Jan17
Jan18
Jan19
Jan20
Date

(k)

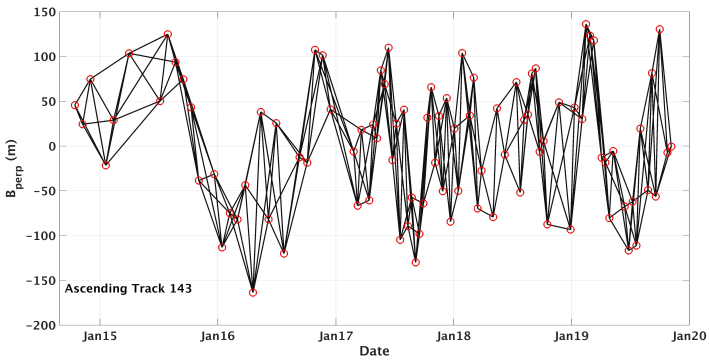
150
100
50
0
−50
−100
−150
−200
B_perp (m)
Ascending Track 143
Jan15
Jan16
Jan17
Jan18
Jan19
Jan20
Date

(l)

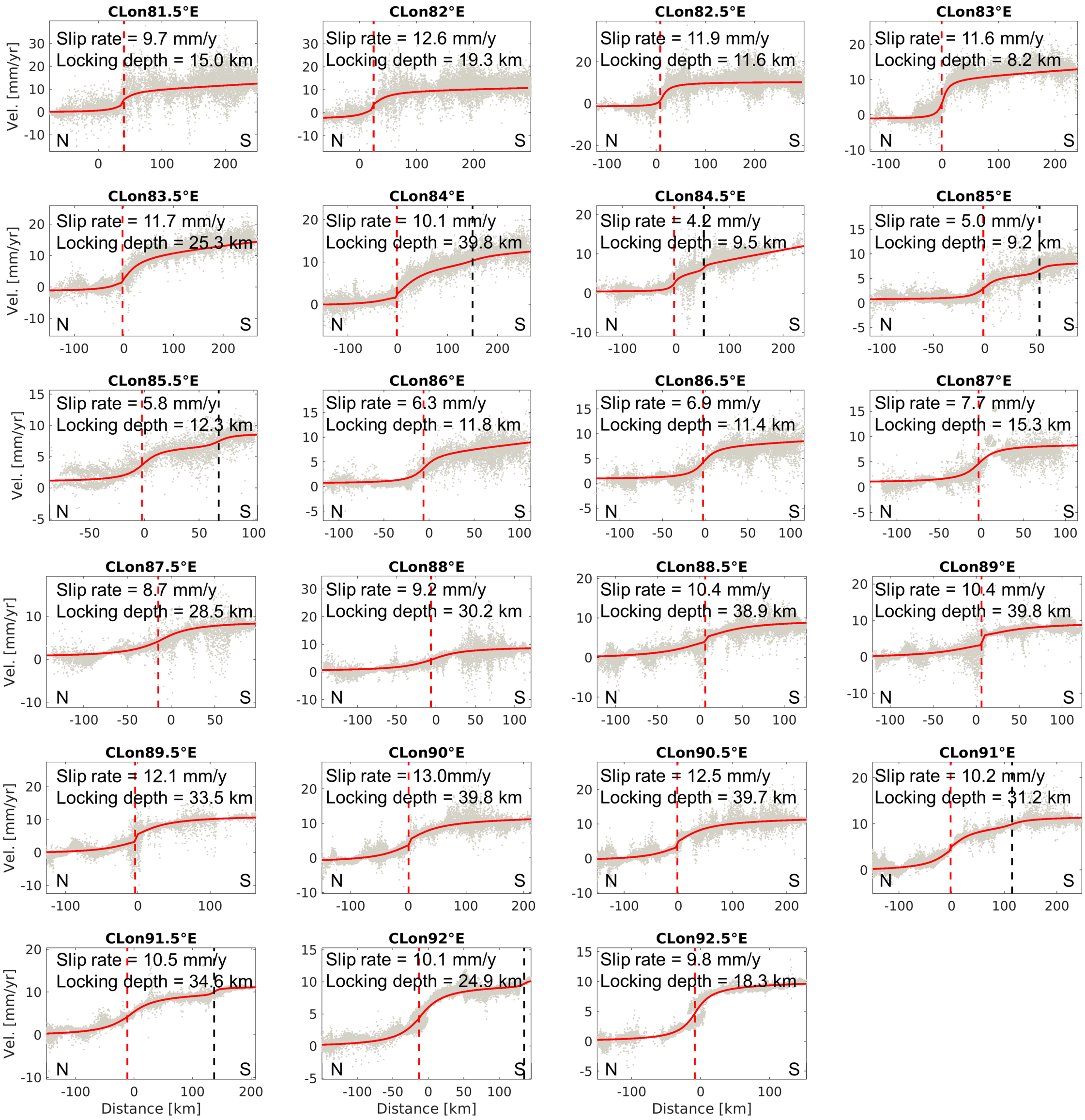

Figure B.3: The MAP solution for each fault-perpendicular profile (red curves). Red dashed lines represent the estimated locations of the buried dislocations along the ATF. Black dashed lines show the estimated locations of the buried dislocation of the additional strain on these profiles.

Figure B.4: Marginal probability distributions of each profile. Abbreviations of labels include 'S rate (Slip rate)', 'L depth (Locking depth)', 'H shifts (Horizontal shifts)', 'S offset (Static offset)', 'R ratio (Rigidity ratio)', 'C L depth (Creeping depth)', 'C rate (Creep rate)', 'R rate (Rotation rate)', 'A L depth (Additional locking depth)','A S rate (Additional slip rate)' and 'A H shifts (Additional horizontal shifts)'.

(a) At 81.5 °E.

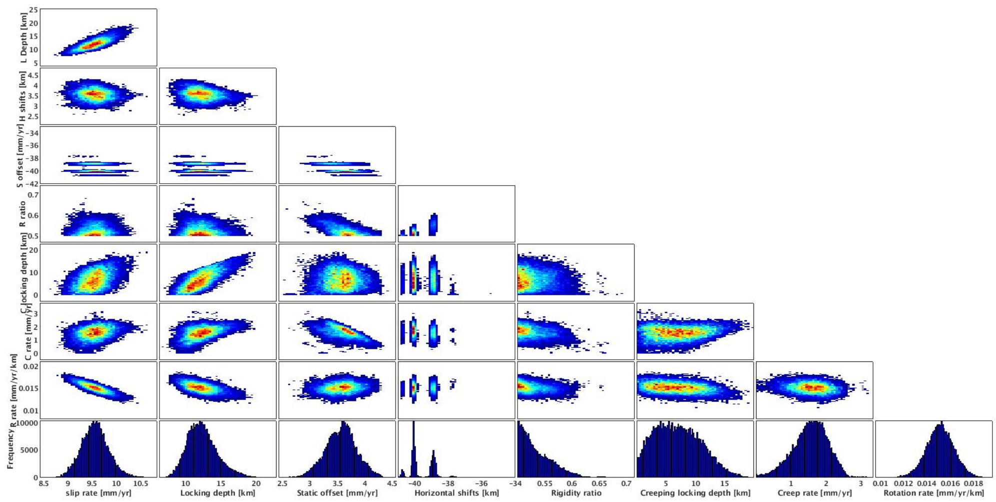

(b) At 82 °E.

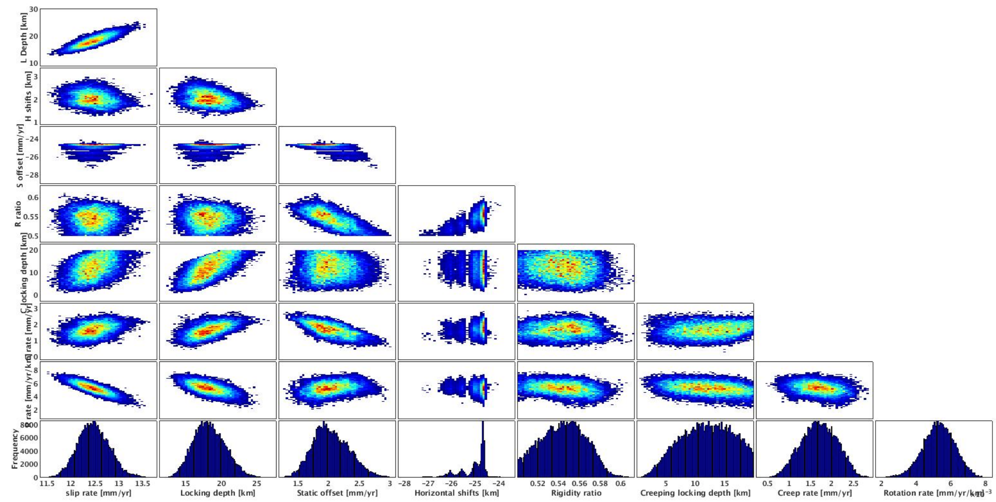

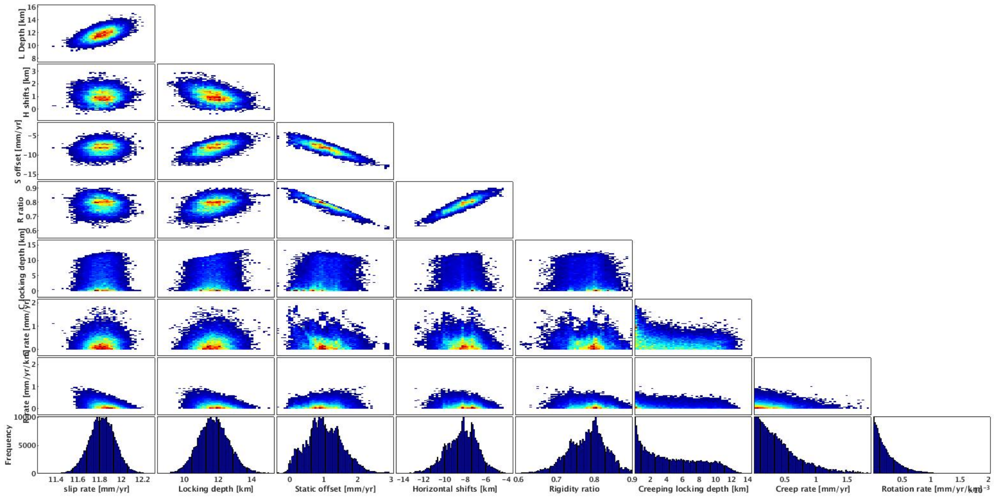

(c) At 82.5 °E.

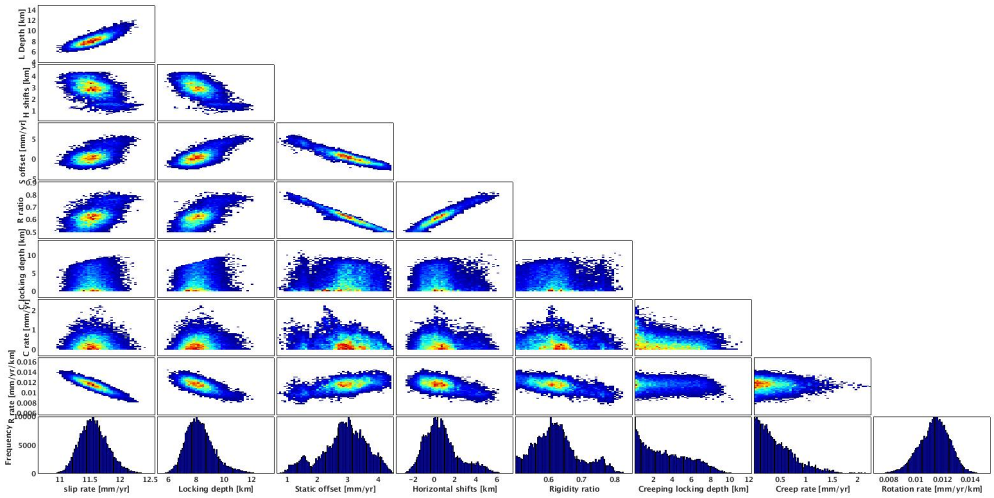

(d) At 83 °E.

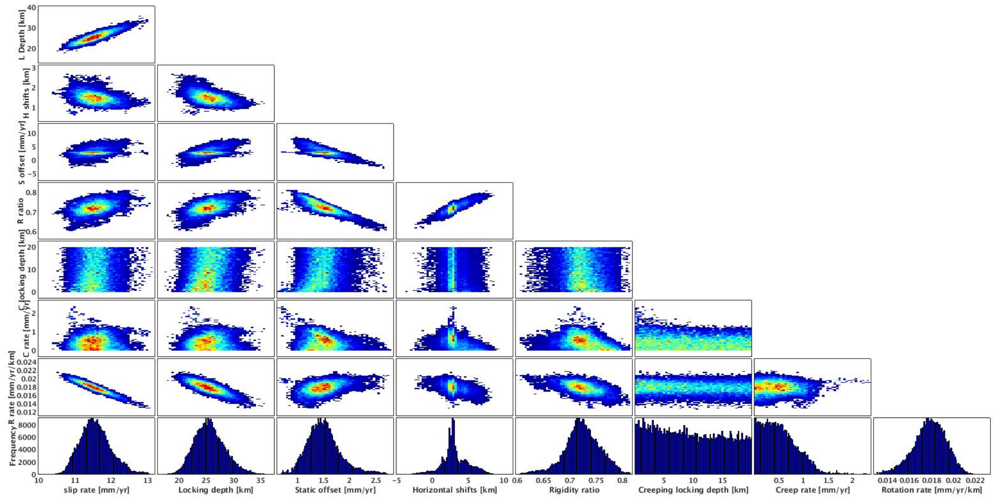

(e) At 83.5 °E.

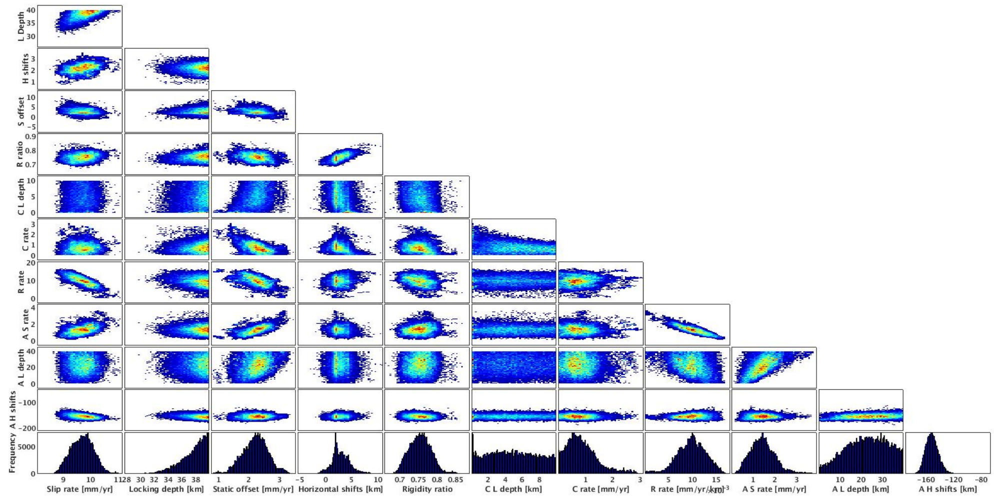

(f) At 84 °E.

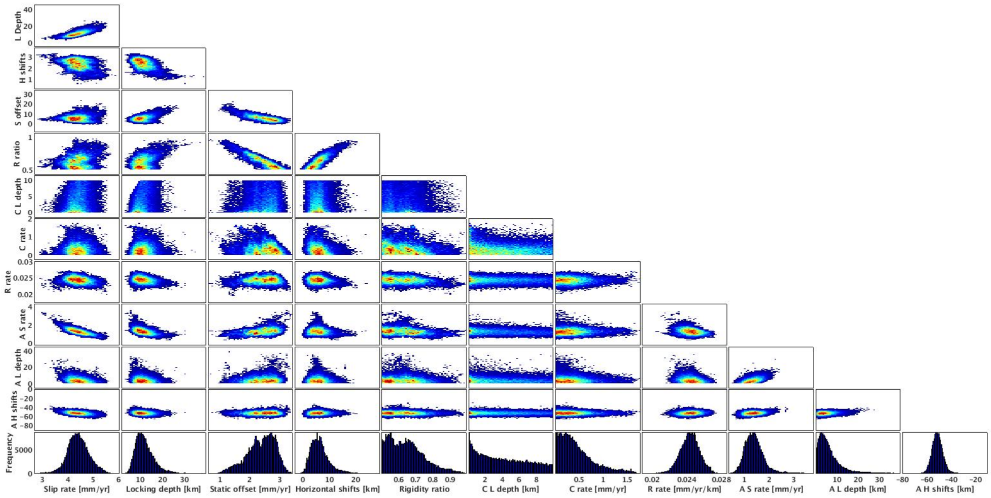

(g) At 84.5 °E.

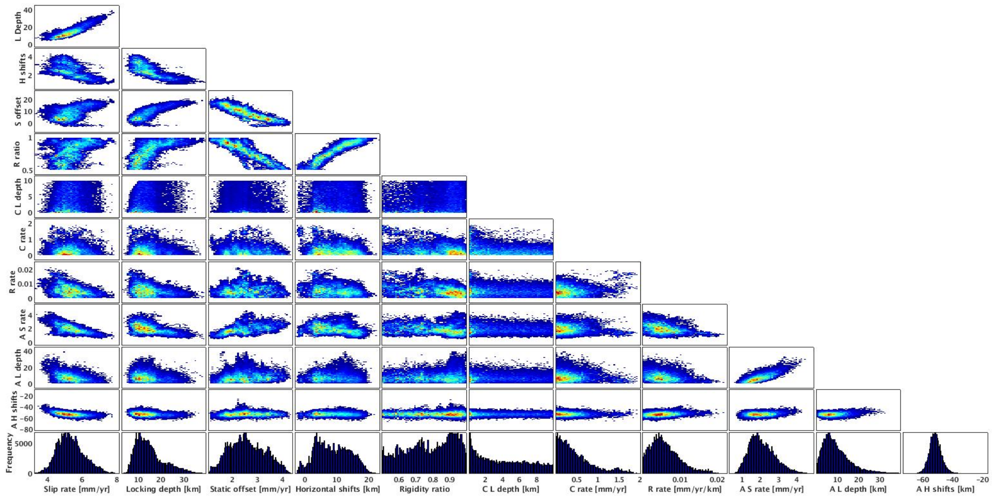

(h) At 85 °E.

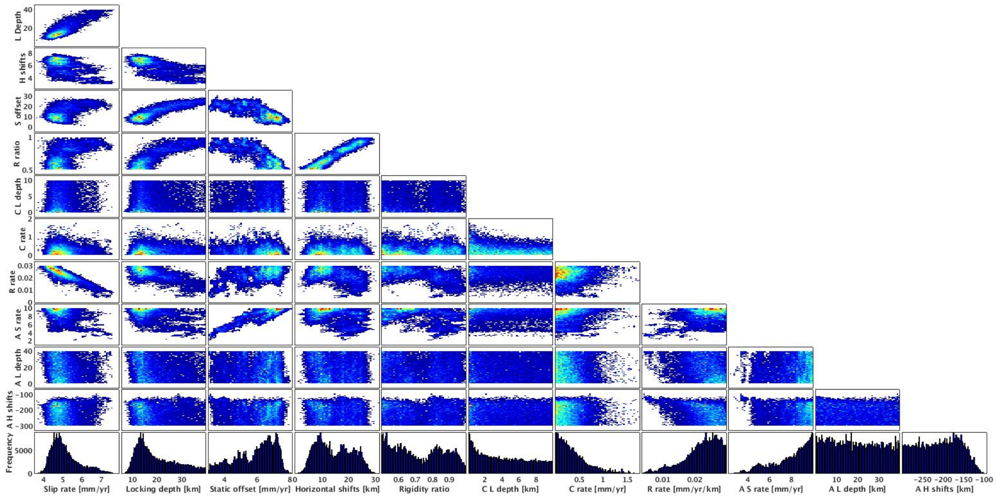

(i) At 85.5 °E.

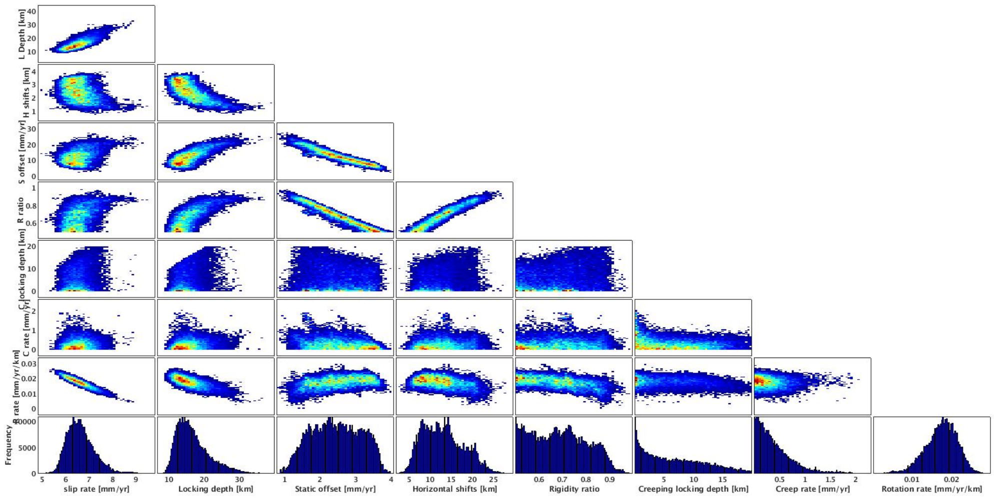

(j) At 86 °E.

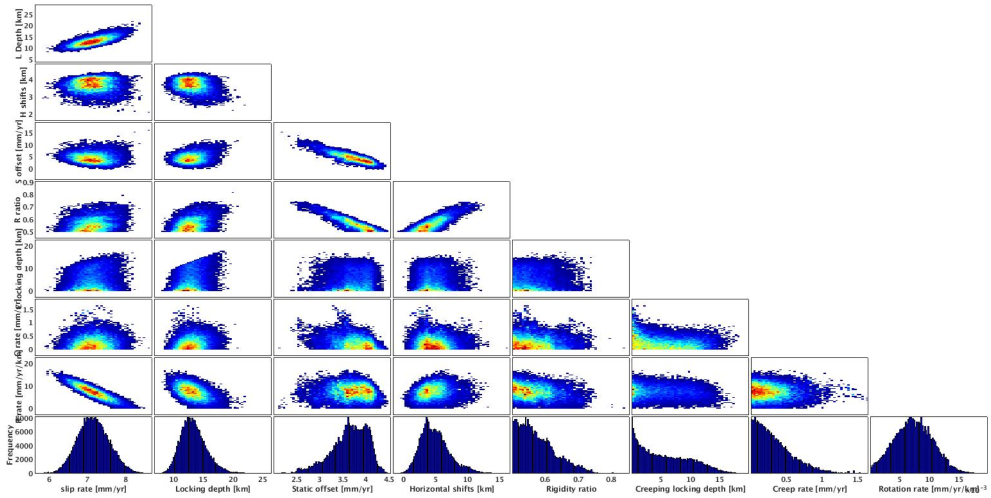

(k) At 86.5 °E.

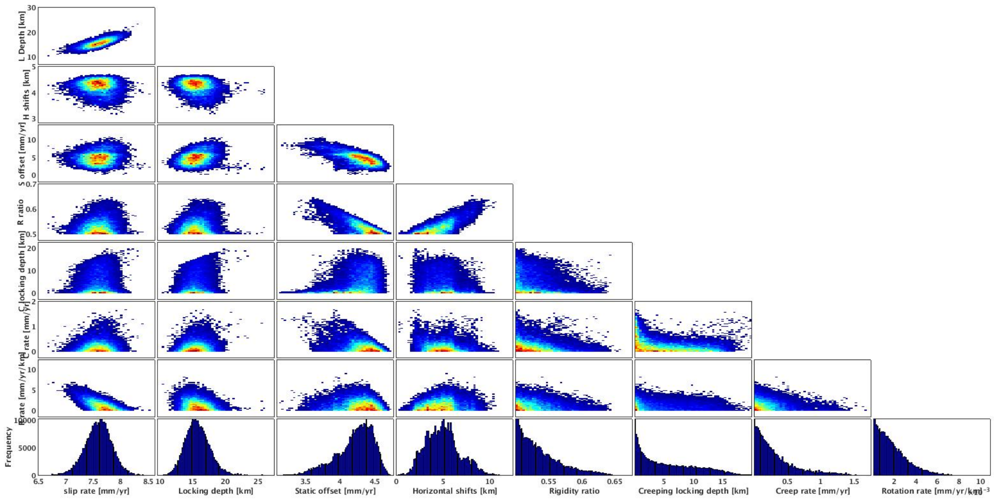

(l) At 87 °E.

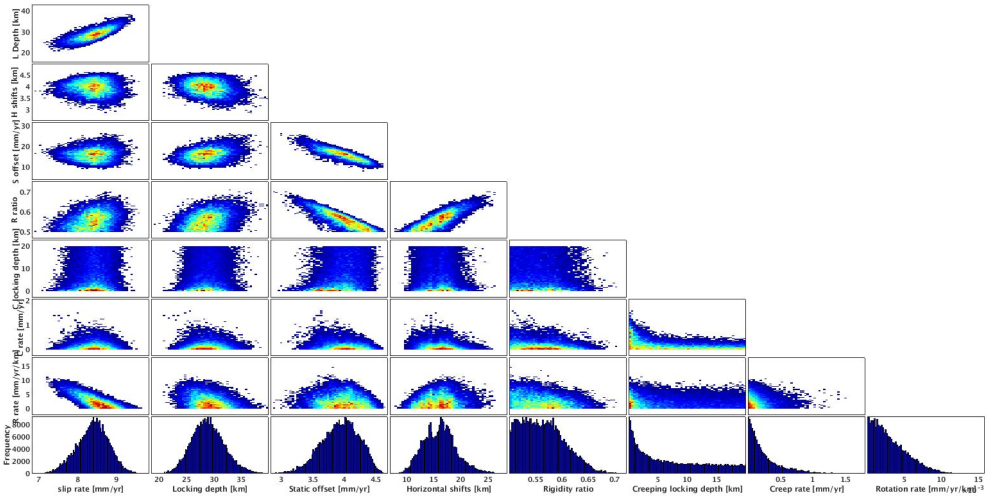

(m) At 87.5 °E.

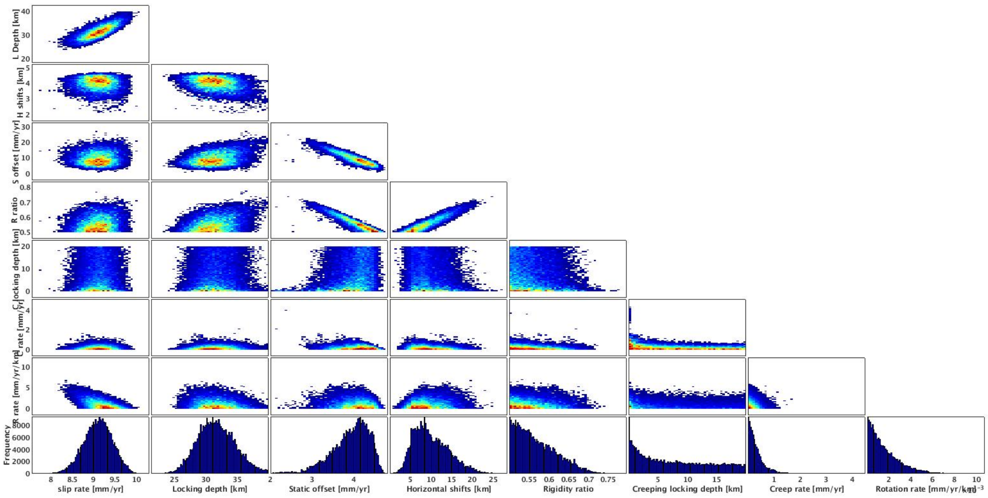

(n) At 88 °E.

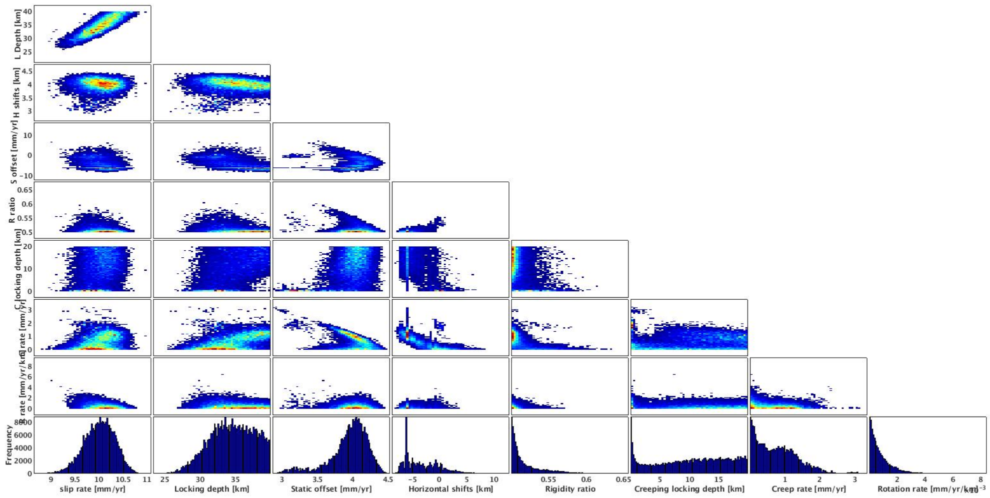

(o) At 88.5 °E.

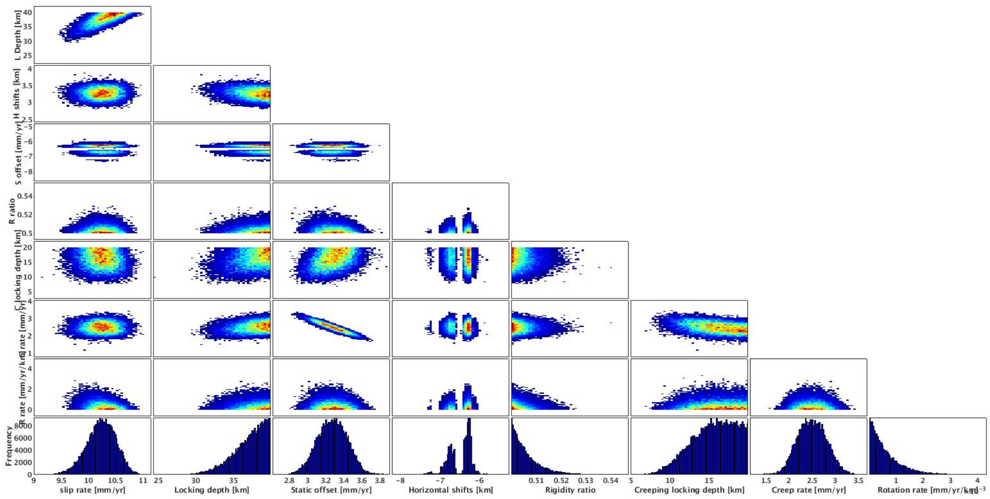

(p) At 89 °E.

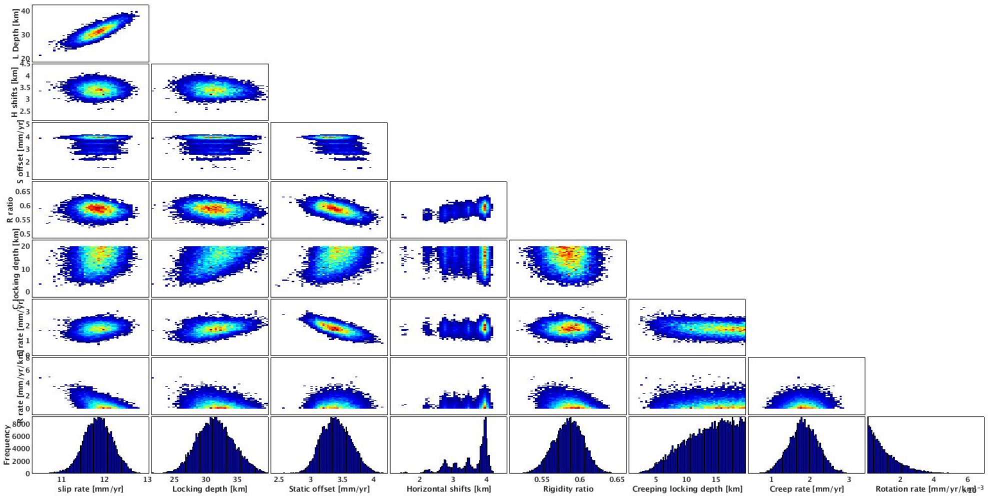

(q) At 89.5 °E.

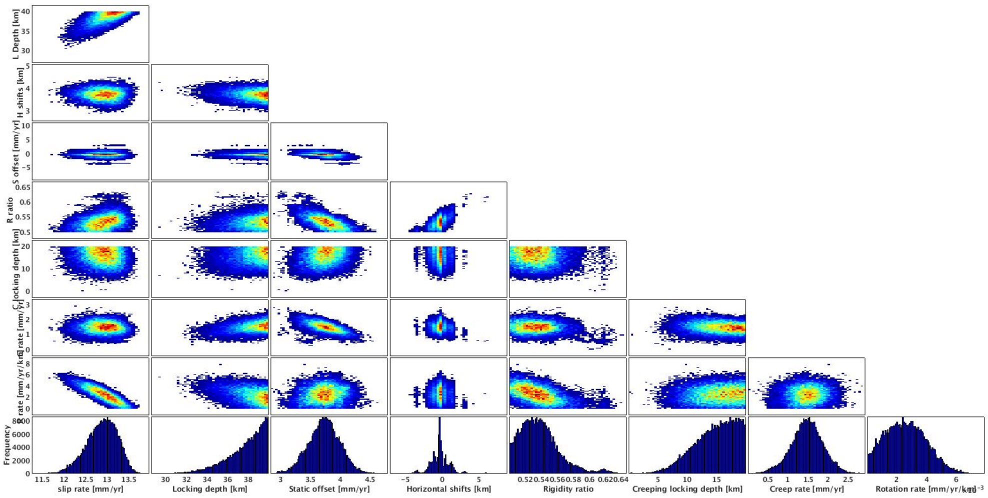

(r) At 90 °E.

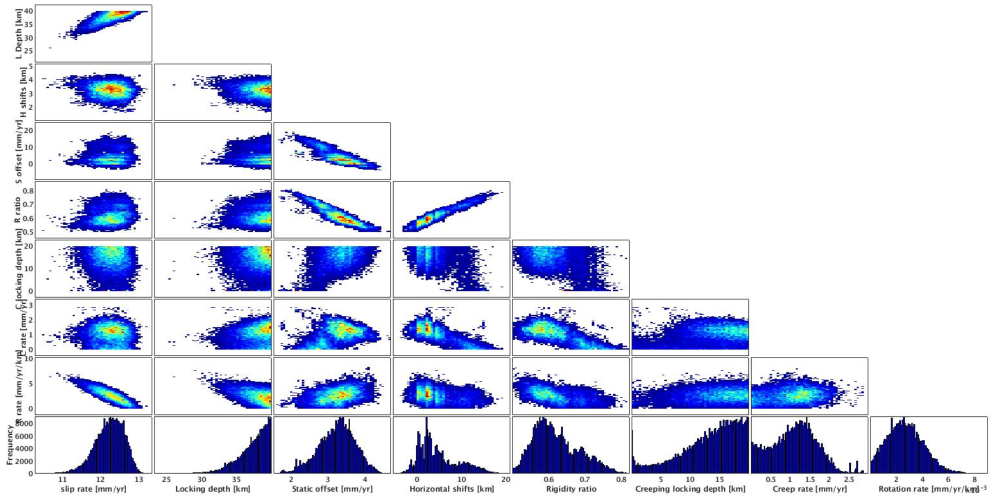

(s) At 90.5 °E.

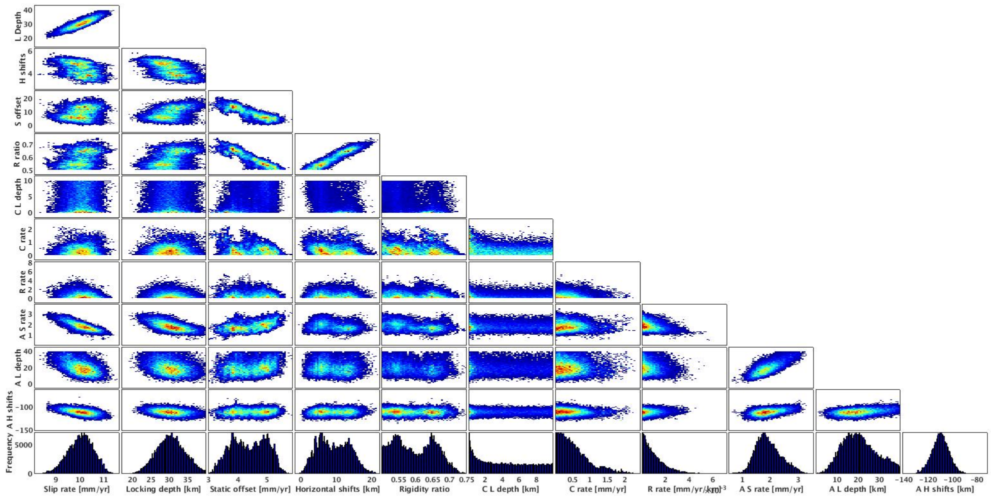

(t) At 91 °E.

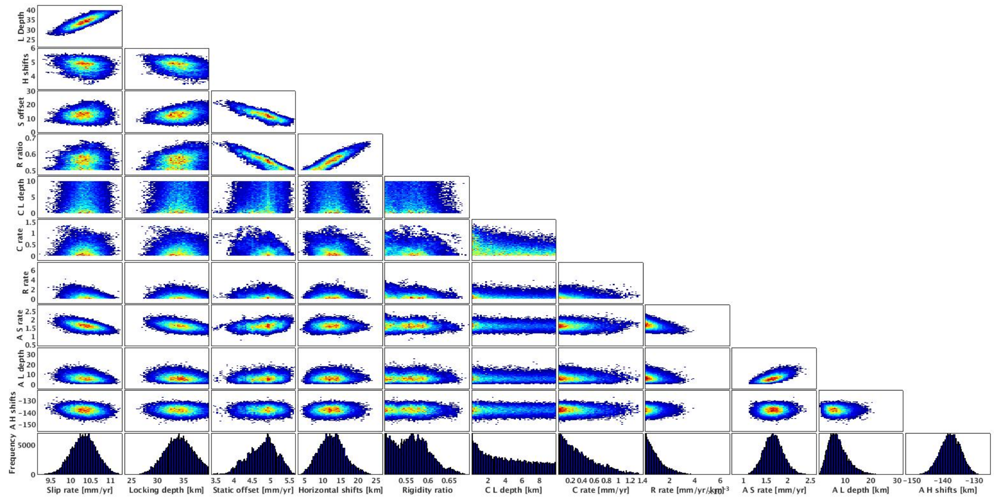

(u) At 91.5 °E.

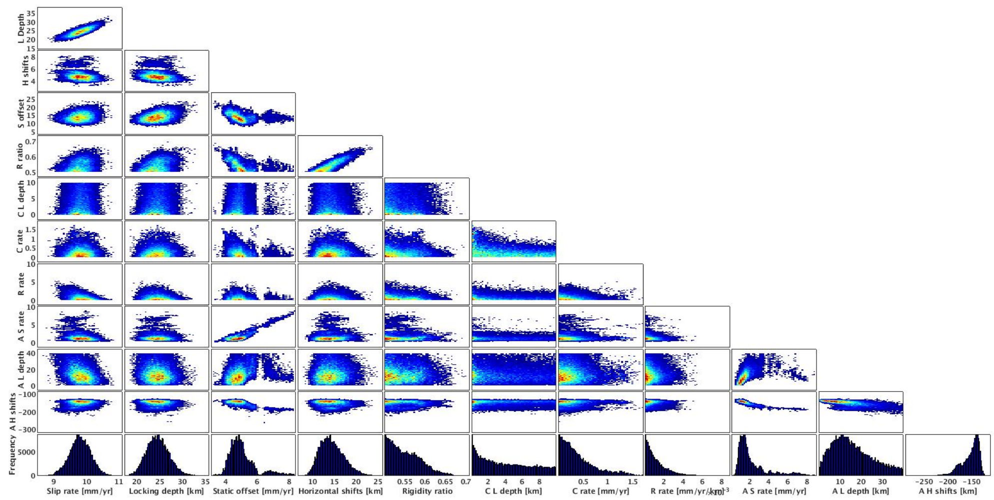

(v) At 92 °E.

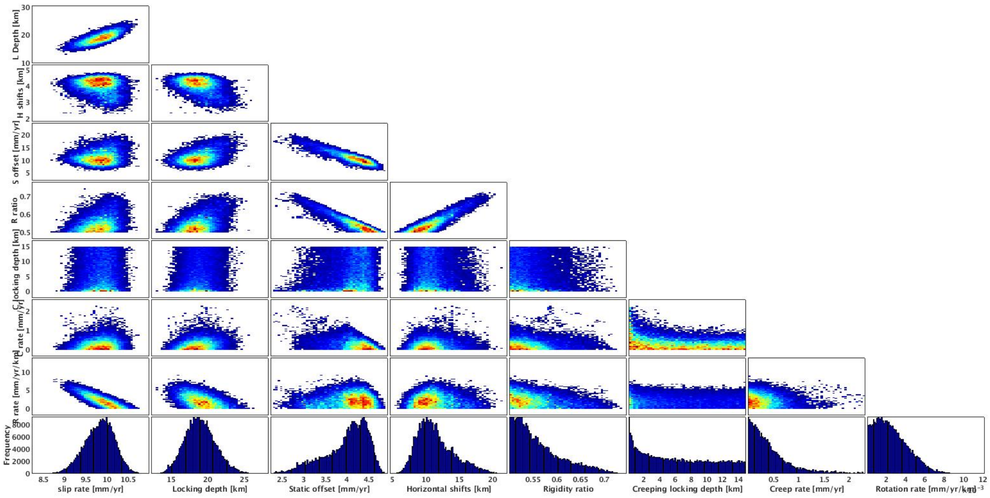
L Depth [km]
H shifts [km]
S offset [mm/yr]
R ratio
C locking depth [km]
C rate [mm/yr]
R rate [mm/yr/km]
Frequency
slip rate [mm/yr]
Locking depth [km]
Static offset [mm/yr]
Horizontal shifts [km]
Rigidity ratio
Creeping locking depth [km]
Creep rate [mm/yr]
Rotation rate [mm/yr/km]
$\times 10^{-3}$

(w) At 92.5 °E.

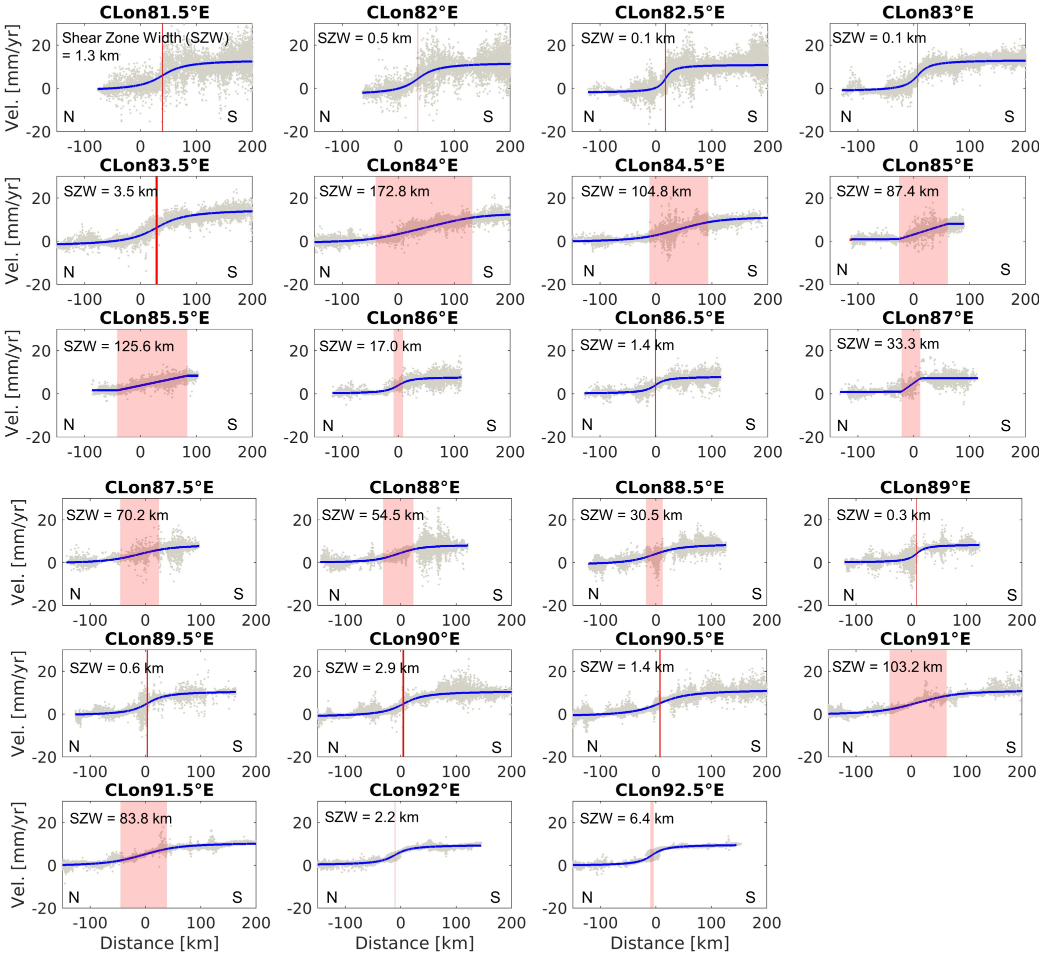

Figure B.5: The MAP solution of the shear zone model for each fault-perpendicular profile (blue curves). Red rectangles represent the estimated locations of the shear zone.

Appendix C

Supplementary materials for Chapter 5

C.1 Figures

Figure C.1: SAR-derived datasets at page size.

(a)

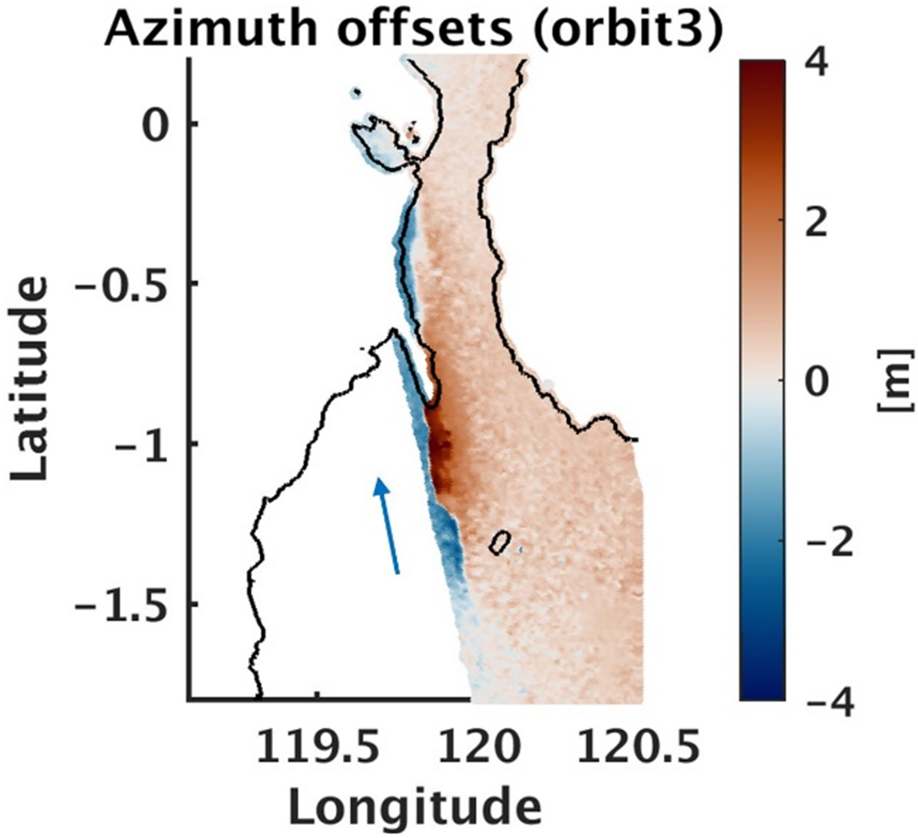

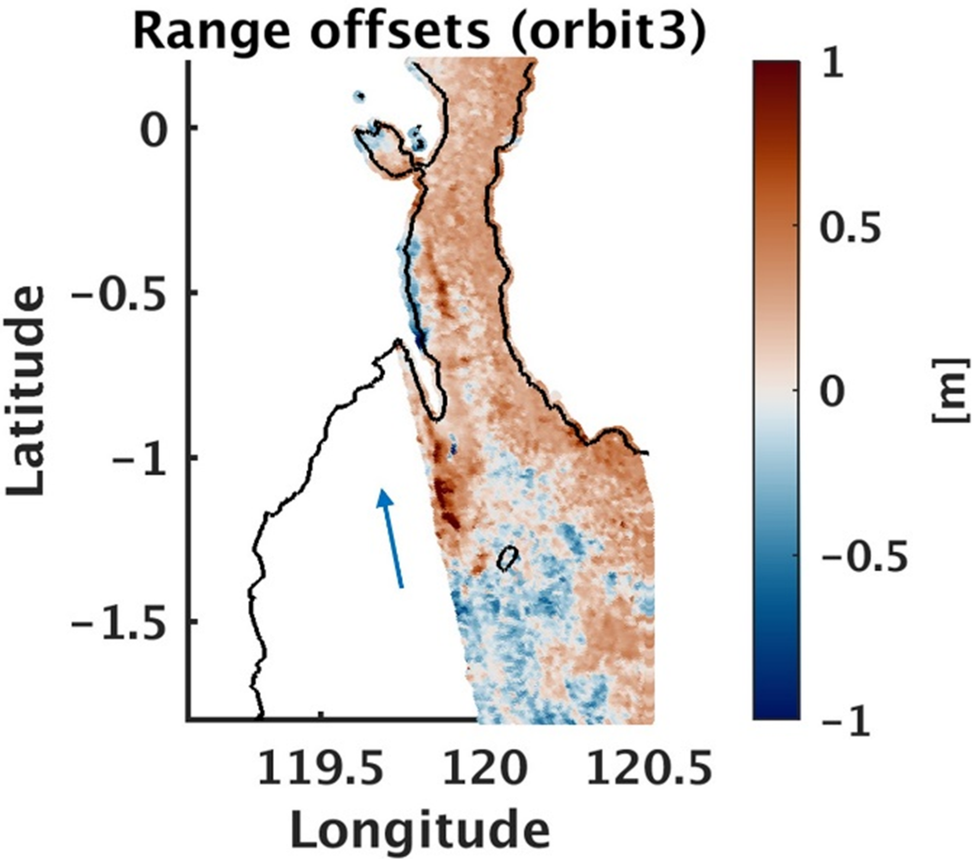
Range offsets (orbit3)
0
−0.5
−1
−1.5
Latitude
119.5
120
120.5
Longitude
1
0.5
0
−0.5
−1
[m]

(b)

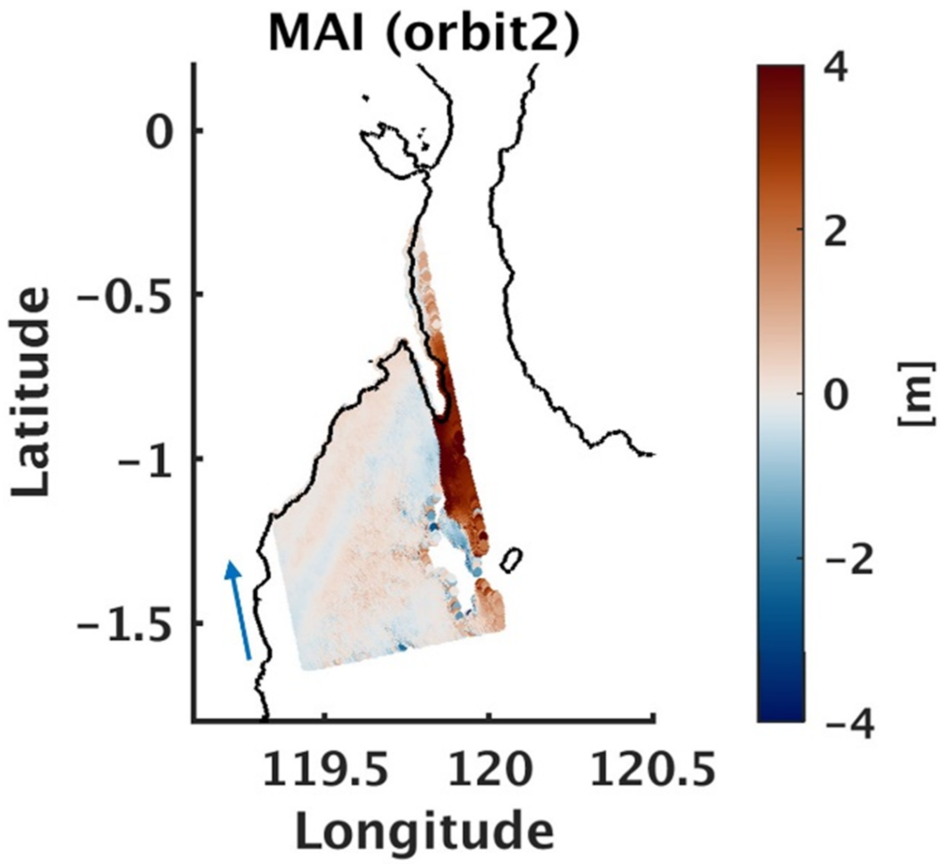

(c)

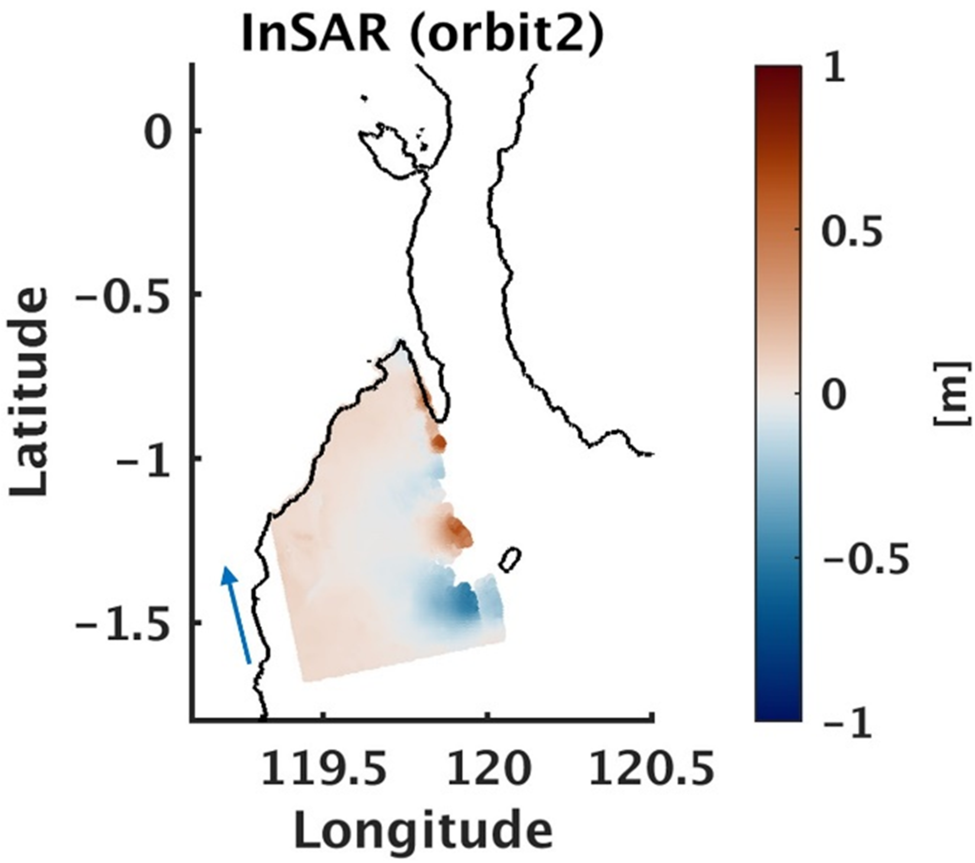
InSAR (orbit2)
Latitude
0
−0.5
−1
−1.5
Longitude
119.5
120
120.5
1
0.5
0
−0.5
−1
[m]

(d)

Figure C.2: Posterior PDF of the strike-slip component for each patch on three segments over the Palu bay. Red lines indicate the MAP solution.

(a) Segment F

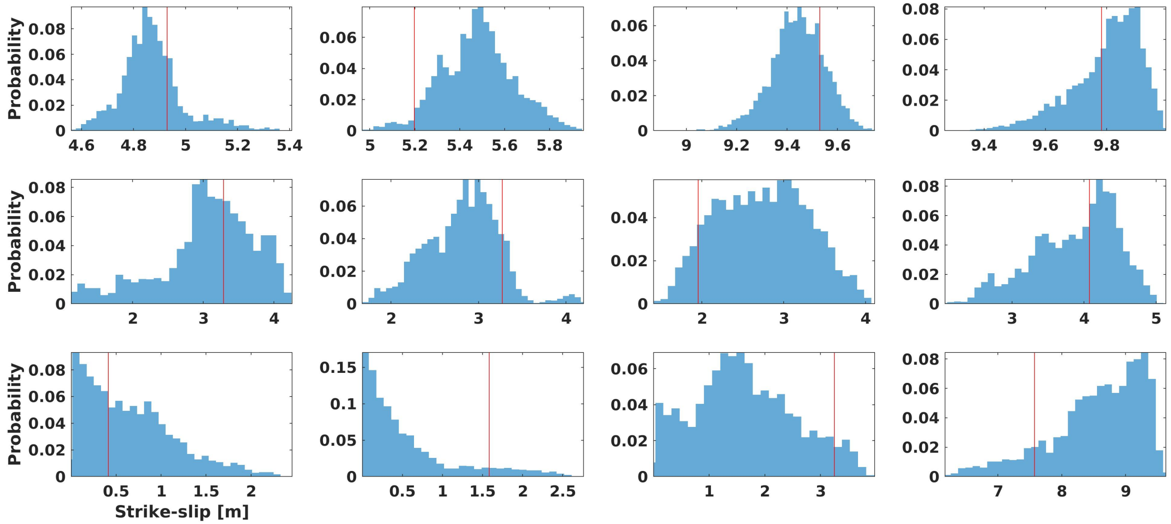

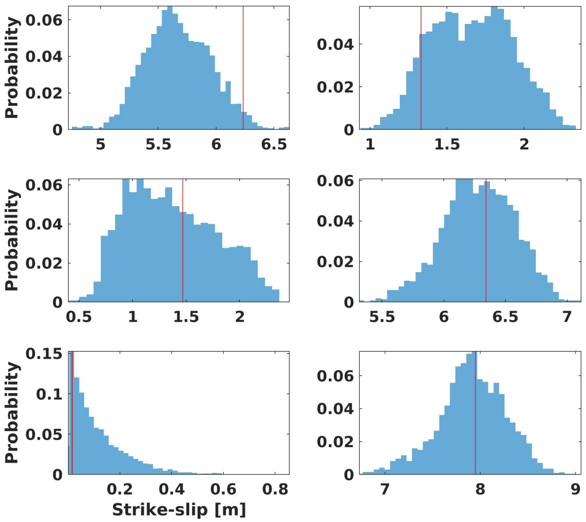

(b) Segment G

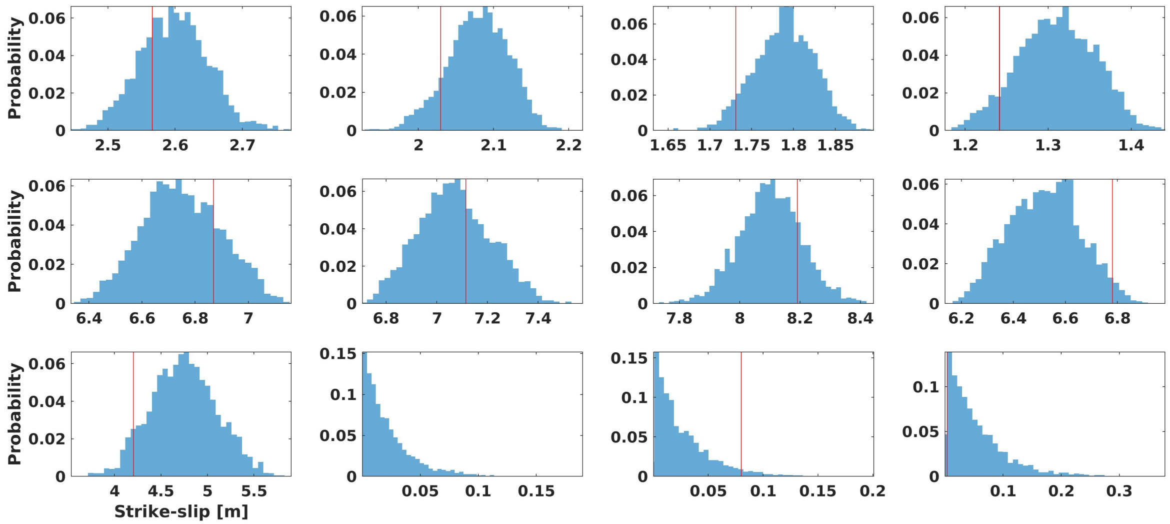
Probability
Probability
Probability
Strike-slip [m]
0.06
0.04
0.02
0
2.5
2.6
2.7
2
2.1
2.2
1.65
1.7
1.75
1.8
1.85
1.2
1.3
1.4
6.4
6.6
6.8
7
7.2
7.4
7.8
8
8.2
8.4
6.2
4
4.5
5
5.5
0.15
0.1
0.05
0.2
0.3

(c) Segment H

Figure C.3: Posterior PDF of the dip-slip component for each patch on three segments over the Palu bay. Red lines indicate the MAP solution.

(a) Segment F

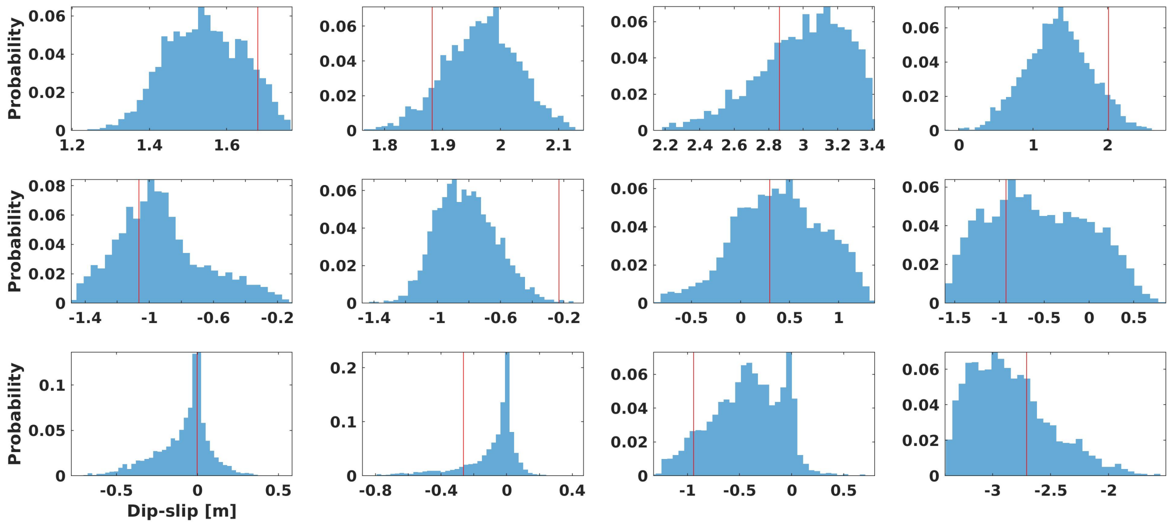

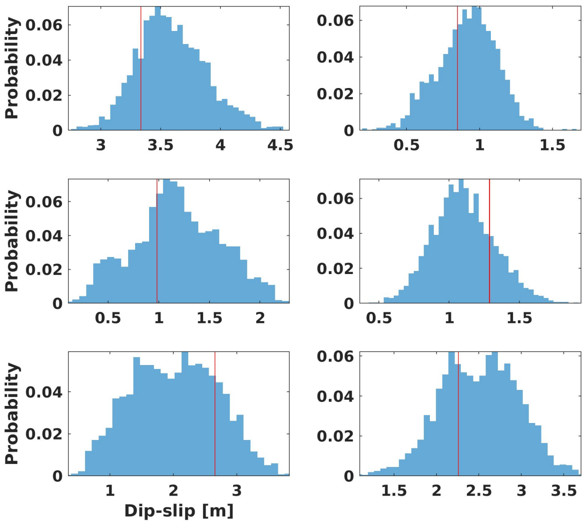

(b) Segment G

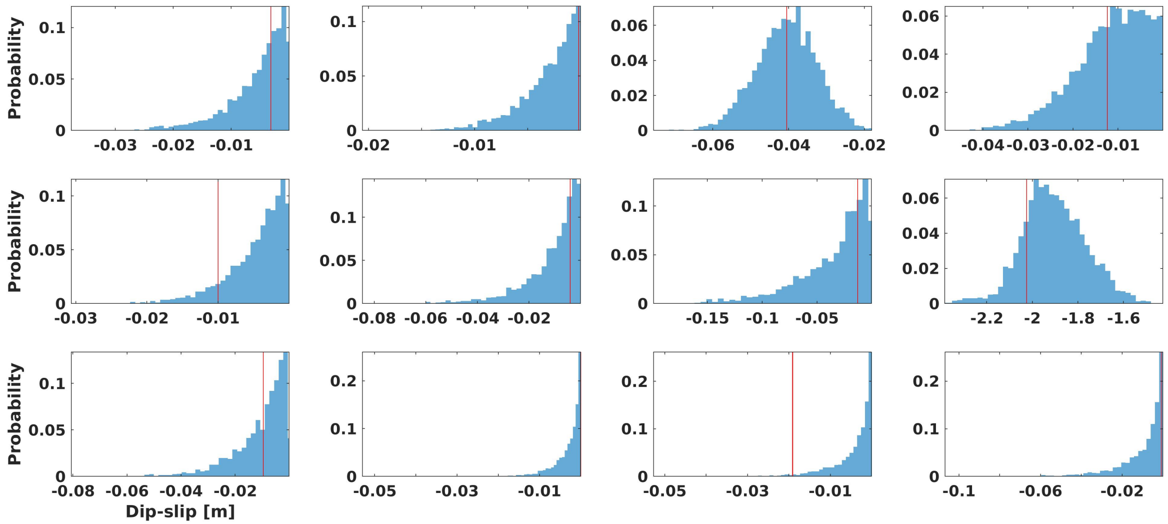
Probability
0.1
0.05
0
-0.03 -0.02 -0.01
-0.02 -0.01
0.06
0.04
0.02
-0.06 -0.04 -0.02
-0.04-0.03-0.02-0.01
-0.03 -0.02 -0.01
-0.08 -0.06 -0.04 -0.02
-0.15 -0.1 -0.05
-2.2 -2 -1.8 -1.6
0.2
-0.05 -0.03 -0.01
-0.1 -0.06 -0.02
Dip-slip [m]

(c) Segment H

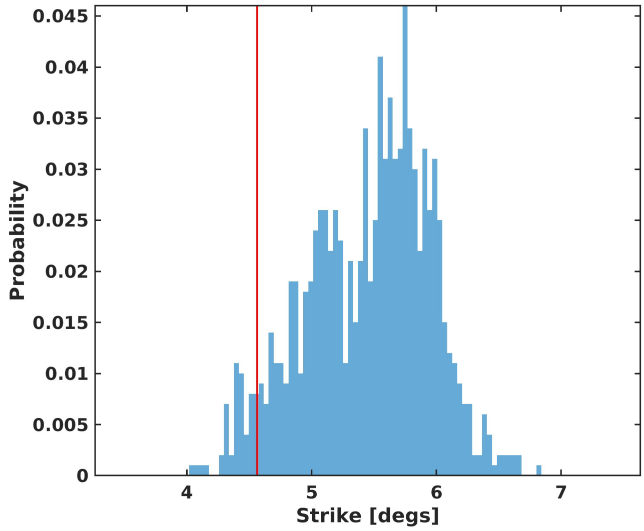

Figure C.4: Posterior PDF of the strike for segment G over the bay. Red lines indicate the MAP solution.

References

Ader, Thomas, Jean-Philippe Avouac, Jing Liu-Zeng, Hélène Lyon-Caen, Laurent Bollinger, John Galetzka, Jeff Genrich, Marion Thomas, Kristel Chanard, Soma Nath Sapkota et al. 2012. Convergence rate across the Nepal Himalaya and interseismic coupling on the Main Himalayan Thrust: Implications for seismic hazard. *Journal of Geophysical Research: Solid Earth.* **117**(B4). 2

Ainscoe, EA, JR Elliott, A Copley, TJ Craig, T Li, BE Parsons and RT Walker. 2017. Blind Thrusting, Surface Folding, and the Development of Geological Structure in the Mw 6.3 2015 Pishan (China) Earthquake. *Journal of Geophysical Research: Solid Earth.* **122**(11), pp. 9359–9382. 29

Altamimi, Zuheir, Paul Rebischung, Laurent Métivier and Xavier Collilieux. 2016. ITRF2014: A new release of the International Terrestrial Reference Frame modeling nonlinear station motions. *Journal of Geophysical Research: Solid Earth.* **121**(8), pp. 6109–6131. 98

Amey, RMJ, A Hooper and RJ Walters. 2018. A Bayesian method for incorporating self-similarity into earthquake slip inversions. *Journal of Geophysical Research: Solid Earth.* **123**(7), pp. 6052–6071. 101, 108

Aránguiz, Rafael, Miguel Esteban, Hiroshi Takagi, Takahito Mikami, Tomoyuki Takabatake, Matías Gómez, Juan González, Tomoya Shibayama, Ryo Okuwaki, Yuji Yagi et al. 2020. The 2018 Sulawesi tsunami in Palu city as a result of several landslides and coseismic tsunamis. *Coastal Engineering Journal.* pp. 1–15. 92, 93

Arikawa, Taro, Abdul Muhari, Yoshihiro Okumura, Yuji Dohi, Bagus Afriyanto, Karina Aprilia Sujatmiko and Fumihiko Imamura. 2018. Coastal subsidence induced several tsunamis during the 2018 Sulawesi earthquake. *Journal of Disaster Research*. **13**, pp. 1–3. 92

Avouac, Jean-Philippe and Paul Tapponnier. 1993. Kinematic model of active deformation in central Asia. *Geophysical Research Letters*. **20**(10), pp. 895–898. 57

Bacques, Guillaume, Marcello de Michele, Michael Foumelis, Daniel Raucoules, Anne Lemoine and Pierre Briole. 2020. Sentinel optical and SAR data highlights multi-segment faulting during the 2018 Palu-Sulawesi earthquake (Mw 7.5). *Scientific Reports*. **10**(1), pp. 1–11. 93

Bagnardi, Marco and Andrew Hooper. 2018. Inversion of surface deformation data for rapid estimates of source parameters and uncertainties: A Bayesian approach. *Geochemistry, Geophysics, Geosystems*. **19**(7), pp. 2194–2211. 28, 101, 108

Barnhart, William D. 2017. Fault creep rates of the Chaman fault (Afghanistan and Pakistan) inferred from InSAR. *Journal of Geophysical Research: Solid Earth*. **122**(1), pp. 372–386. 7

Bechor, Noa BD and Howard A Zebker. 2006. Measuring two-dimensional movements using a single InSAR pair. *Geophysical research letters*. **33**(16). 9, 95

Béjar-Pizarro, Marta, Anne Socquet, Rolando Armijo, Daniel Carrizo, Jeff Genrich and Mark Simons. 2013. Andean structural control on interseismic coupling in the North Chile subduction zone. *Nature Geoscience*. **6**(6), pp. 462–467. 6

Bekaert, DPS, A Hooper and TJ Wright. 2015a. A spatially variable power law tropospheric correction technique for InSAR data. *Journal of Geophysical Research: Solid Earth*. **120**(2), pp. 1345–1356. 13, 14, 52, 153

Bekaert, DPS, RJ Walters, TJ Wright, AJ Hooper and DJ Parker. 2015b. Statistical comparison of InSAR tropospheric correction techniques. *Remote Sensing of Environment*. **170**, pp. 40–47. 10, 12, 39

Bell, MA, JR Elliott and BE Parsons. 2011. Interseismic strain accumulation across the Manyi fault (Tibet) prior to the 1997 Mw 7.6 earthquake. *Geophysical Research Letters*. **38**(24). 23, 53, 155

Bellier, O, Th Beaudouin, M Sebrier, M Villeneuve, I Bahar, E Putranto, I Pratomo, M Massault and D Seward. 1998. Active faulting in central Sulawesi (eastern Indonesia). *The Geodynamics of S and SE Asia (GEODYSSEA project)*. pp. 276–312. 17, 92

Bellier, Olivier, Michel Sébrier, Diane Seward, Thierry Beaudouin, Michel Villeneuve and Eka Putranto. 2006. Fission track and fault kinematics analyses for new insight into the Late Cenozoic tectonic regime changes in West-Central Sulawesi (Indonesia). *Tectonophysics*. **413**(3-4), pp. 201–220. 16, 17, 92

Bellier, Olivier, Michel Sébrier, Thierry Beaudouin, Michel Villeneuve, Regis Braucher, Didier Bourles, Lionel Siame, Eka Putranto and Indyo Pratomo. 2001. High slip rate for a low seismicity along the Palu-Koro active fault in central Sulawesi (Indonesia). *Terra Nova*. **13**(6), pp. 463–470. 17, 91, 92

Bendick, Rebecca, Roger Bilham, Jeffrey Freymueller, Kristine Larson and Guanghua Yin. 2000. Geodetic evidence for a low slip rate in the Altyn Tagh fault system. *Nature*. **404**(6773), pp. 69–72. 60, 62

Berardino, Paolo, Gianfranco Fornaro, Riccardo Lanari and Eugenio Sansosti. 2002. A new algorithm for surface deformation monitoring based on small baseline differential SAR interferograms. *IEEE Transactions on geoscience and remote sensing*. **40**(11), pp. 2375–2383. 21

Berrada Baby, H, P Gole and J Lavergnat. 1988. A model for the tropospheric excess path length of radio waves from surface meteorological measurements. *Radio science*. **23**(6), pp. 1023–1038. 24

Bettinelli, Pierre, Jean-Philippe Avouac, Mireille Flouzat, François Jouanne, Laurent Bollinger, Pascal Willis and Gyani Raja Chitrakar. 2006. Plate motion of India and interseismic strain in the Nepal Himalaya from GPS and DORIS measurements. *Journal of Geodesy*. **80**(8-11), pp. 567–589. 4

Bie, Lidong and Isabelle Ryder. 2014. Recent seismic and aseismic activity in the Ashikule stepover zone, NW Tibet. *Geophysical Journal International*. **198**(3), pp. 1632–1643. 16, 89

Bie, Lidong, Pablo J González and Andreas Rietbrock. 2017. Slip distribution of the 2015 Lefkada earthquake and its implications for fault segmentation. *Geophysical Journal International*. **210**(1), pp. 420–427. 8

Biggs, Juliet and Tim J Wright. 2020. How satellite InSAR has grown from opportunistic science to routine monitoring over the last decade. *Nature Communications*. **11**(1), pp. 1–4. 2

Bird, Peter and Corné Kreemer. 2015. Revised tectonic forecast of global shallow seismicity based on version 2.1 of the Global Strain Rate Map. *Bulletin of the Seismological Society of America*. **105**(1), pp. 152–166. 2

Bourne, SJ, PC England and B Parsons. 1998. The motion of crustal blocks driven by flow of the lower lithosphere and implications for slip rates of continental strike-slip faults. *Nature*. **391**(6668), pp. 655–659. 15

Burford, Robert O. 1988. Retardations in fault creep rates before local moderate earthquakes along the San Andreas fault system, central California. *Pure and Applied Geophysics*. **126**(2-4), pp. 499–529. 7

Cakir, Ziyadin, Ahmet M Akoglu, Samir Belabbes, Semih Ergintav and Mustapha Meghraoui. 2005. Creeping along the Ismetpasa section of the North Anatolian fault (Western Turkey): Rate and extent from InSAR. *Earth and Planetary Science Letters*. **238**(1-2), pp. 225–234. 7

Carvajal, Matías, Cristian Araya-Cornejo, Ignacio Sepúlveda, Daniel Melnick and Jennifer S Haase. 2019. Nearly instantaneous tsunamis following the Mw 7.5

2018 Palu earthquake. *Geophysical Research Letters*. **46**(10), pp. 5117–5126. 126, 127

Cavalié, O, Cécile Lasserre, M-P Doin, G Peltzer, J Sun, X Xu and Z-K Shen. 2008. Measurement of interseismic strain across the Haiyuan fault (Gansu, China), by InSAR. *Earth and Planetary Science Letters*. **275**(3-4), pp. 246–257. 3, 6

Cavalié, Olivier and Sigurjón Jónsson. 2014. Block-like plate movements in eastern Anatolia observed by InSAR. *Geophysical Research Letters*. **41**(1), pp. 26–31. 14

Cervelli, Peter. 2000. USGS staff profile: Peter Cervelli [Online]. *Available from: https://www.usgs.gov/staff-profiles/peter-cervelli.* . 27

Champenois, J, Bénédicte Fruneau, E Pathier, B Deffontaines, K-C Lin and J-C Hu. 2012. Monitoring of active tectonic deformations in the Longitudinal Valley (Eastern Taiwan) using Persistent Scatterer InSAR method with ALOS PALSAR data. *Earth and Planetary Science Letters*. **337**, pp. 144–155. 7

Chaussard, Estelle, Shimon Wdowinski, Enrique Cabral-Cano and Falk Amelung. 2014. Land subsidence in central Mexico detected by ALOS InSAR time-series. *Remote sensing of environment*. **140**, pp. 94–106. 10, 30

Chen, Lin, Fabio A Capitanio, Lijun Liu and Taras V Gerya. 2017. Crustal rheology controls on the Tibetan plateau formation during India-Asia convergence. *Nature communications*. **8**(1), pp. 1–8. 56

Chen, Yan, Stuart Gilder, Nadir Halim, Jean Pascal Cogné and Vincent Courtillot. 2002. New paleomagnetic constraints on central Asian kinematics: Displacement along the Altyn Tagh fault and rotation of the Qaidam Basin. *Tectonics*. **21**(5), pp. 6–1. 62

Chen, ZH, BC Burchfiel, Y Liu, RW King, LH Royden, W Tang, E Wang, J Zhao and X Zhang. 2000. Global Positioning System measurements from eastern Tibet and their implications for India/Eurasia intercontinental deformation. *Journal of Geophysical Research: Solid Earth*. **105**(B7), pp. 16215–16227. 62, 85

Chevalier, Marie-Luce, Jiawei Pan, Haibing Li, Zhiming Sun, Dongliang Liu, Junling Pei, Wei Xu and Chan Wu. 2017. First tectonic-geomorphology study along the Longmu–Gozha Co fault system, Western Tibet. *Gondwana Research*. **41**, pp. 411–424. 88

Chinnery, MA. 1961. The deformation of the ground around surface faults. *Bulletin of the Seismological Society of America*. **51**(3), pp. 355–372. 26

Cimini, D, N Pierdicca, E Pichelli, R Ferretti, V Mattioli, S Bonafoni, M Montopoli and D Perissin. 2012. On the accuracy of integrated water vapor observations and the potential for mitigating electromagnetic path delay error in InSAR. *Atmospheric Measurement Techniques*. **5**(5), p. 1015. 12

Cowgill, E. 2007. Cenozoic Right-slip Faulting Along the East Flank of the Pamirs, NW China: Implications for the Kinematic Evolution of a Major Salient in the Northern Margin of the Himalayan-Tibetan Orogen. In *AGU Fall Meeting 2007*. 60, 62

Cowgill, Eric, An Yin, T Mark Harrison and Wang Xiao-Feng. 2003. Reconstruction of the Altyn Tagh fault based on U-Pb geochronology: Role of back thrusts, mantle sutures, and heterogeneous crustal strength in forming the Tibetan Plateau. *Journal of Geophysical Research: Solid Earth*. **108**(B7). 62, 85

Cowgill, Eric, Ryan D Gold, Chen Xuanhua, Wang Xiao-Feng, J Ramón Arrowsmith and John Southon. 2009. Low Quaternary slip rate reconciles geodetic and geologic rates along the Altyn Tagh fault, northwestern Tibet. *Geology*. **37**(7), pp. 647–650. 60, 62, 82

Cui, Haiyang, JD Pietrzak and GS Stelling. 2010. A finite volume analogue of the P1NC-P1 finite element: With accurate flooding and drying. *Ocean Modelling*. **35**(1-2), pp. 16–30. 127

Cummins, Phil R. 2017. Geohazards in Indonesia: Earth science for disaster risk reduction–introduction. *Geological Society, London, Special Publications*. **441**(1), pp. 1–7. 16

Curlander, John C and Robert N McDonough. 1991. *Synthetic aperture radar*. Vol. 11 Wiley, New York. 19

Daout, Simon, Marie-Pierre Doin, Gilles Peltzer, Anne Socquet and Cécile Lasserre. 2017. Large-scale InSAR monitoring of permafrost freeze-thaw cycles on the Tibetan Plateau. *Geophysical Research Letters*. **44**(2), pp. 901–909. 53, 65

Daout, Simon, Marie-Pierre Doin, Gilles Peltzer, Cécile Lasserre, Anne Socquet, Matthieu Volat and Henriette Sudhaus. 2018. Strain partitioning and present-day fault kinematics in NW Tibet from Envisat SAR interferometry. *Journal of Geophysical Research: Solid Earth*. **123**(3), pp. 2462–2483. 10, 60, 62, 73, 75, 85

Decriem, J, Th Árnadóttir, A Hooper, H Geirsson, F Sigmundsson, M Keiding, BG Ófeigsson, S Hreinsdóttir, P Einarsson, P LaFemina et al. 2010. The 2008 May 29 earthquake doublet in SW Iceland. *Geophysical Journal International*. **181**(2), pp. 1128–1146. 99, 100

Dee, D, J Fasullo, D Shea, J Walsh and Staff NCAR. 2016. The climate data guide: atmospheric reanalysis: overview & comparison tables [Online]. *Available from: https://climatedataguide.ucar.edu/climate-data/atmospheric-reanalysis-overview-comparison-tables*. **1**, p. 2017. 12

Dee, Dick P, SM Uppala, AJ Simmons, Paul Berrisford, P Poli, S Kobayashi, U Andrae, MA Balmaseda, G Balsamo, P Bauer et al. 2011. The ERA-Interim reanalysis: Configuration and performance of the data assimilation system. *Quarterly Journal of the royal meteorological society*. **137**(656), pp. 553–597. 12

Delacourt, C, P Briole and JA Achache. 1998. Tropospheric corrections of SAR interferograms with strong topography. Application to Etna. *Geophysical Research Letters*. **25**(15), pp. 2849–2852. 11

Delouis, B, D Giardini, P Lundgren and J Salichon. 2002. Joint inversion of InSAR, GPS, teleseismic, and strong-motion data for the spatial and temporal distribution of earthquake slip: Application to the 1999 Izmit mainshock. *Bulletin of the Seismological Society of America*. **92**(1), pp. 278–299. 9

Delouis, Bertrand, Jean-Mathieu Nocquet and Martin Vallée. 2010. Slip distribution of the February 27, 2010 Mw= 8.8 Maule earthquake, central Chile, from static and high-rate GPS, InSAR, and broadband teleseismic data. *Geophysical Research Letters*. **37**(17). 29

Ding, Xiao-li, Zhi-wei Li, Jian-jun Zhu, Guang-cai Feng and Jiang-ping Long. 2008. Atmospheric effects on InSAR measurements and their mitigation. *Sensors*. **8**(9), pp. 5426–5448. 24

Doin, M-P, Cécile Lasserre, Gilles Peltzer, Olivier Cavalié and Cécile Doubre. 2009. Corrections of stratified tropospheric delays in SAR interferometry: Validation with global atmospheric models. *Journal of Applied Geophysics*. **69**(1), pp. 35–50. 11, 14, 24

Dreger, Douglas S, Mong-Han Huang, Arthur Rodgers, TakaâĂŹaki Taira and Kathryn Wooddell. 2015. Kinematic finite-source model for the 24 August 2014 South Napa, California, earthquake from joint inversion of seismic, GPS, and InSAR data. *Seismological Research Letters*. **86**(2A), pp. 327–334. 9

Duquesnoy, Th, E Barrier, M Kasser, M Aurelio, R Gaulon, RS Punongbayan and C Rangin. 1994. Detection of creep along the Philippine fault: First results of geodetic measurements on Leyte island, central Philippine. *Geophysical Research Letters*. **21**(11), pp. 975–978. 7

ECMWF. 2016. HRES-ECMWF dataset [Online]. *Available from: https://www.ecmwf.int/en/forecasts/datasets/set-i*. . 12, 24

Efron, Bradley and Robert J Tibshirani. 1994. *An introduction to the bootstrap*. CRC press. 49, 50, 65, 66

Elliott, AJ, ME Oskin, J Liu-Zeng and Y-X Shao. 2018. Persistent rupture terminations at a restraining bend from slip rates on the eastern Altyn Tagh fault. *Tectonophysics*. **733**, pp. 57–72. 59, 78

Elliott, Austin J, Michael E Oskin, Jing Liu-Zeng and Yanxiu Shao. 2015. Rupture termination at restraining bends: The last great earthquake on the Altyn Tagh fault. *Geophysical Research Letters*. **42**(7), pp. 2164–2170. 59, 78

Elliott, JR. 2020. Earth Observation for the assessment of earthquake hazard, risk and disaster management. *Surveys in Geophysics*. pp. 1–32. 1, 2, 3

Elliott, JR, J Biggs, B Parsons and TJ Wright. 2008. InSAR slip rate determination on the Altyn Tagh Fault, northern Tibet, in the presence of topographically correlated atmospheric delays. *Geophysical Research Letters*. **35**(12). 13, 23, 24, 38, 60, 61, 62, 85

Elliott, JR, RJ Walters, PC England, JA Jackson, Z Li and B Parsons. 2010. Extension on the Tibetan plateau: recent normal faulting measured by InSAR and body wave seismology. *Geophysical Journal International*. **183**(2), pp. 503–535. 3, 88

Elliott, JR, RJ Walters and TJ Wright. 2016. The role of space-based observation in understanding and responding to active tectonics and earthquakes. *Nature communications*. **7**, p. 13844. 6, 7, 10, 30

England, Philip and Dan McKenzie. 1982. A thin viscous sheet model for continental deformation. *Geophysical Journal International*. **70**(2), pp. 295–321. 57

England, Philip and Peter Molnar. 1990. Surface uplift, uplift of rocks, and exhumation of rocks. *Geology*. **18**(12), pp. 1173–1177. 57

England, Philip and Peter Molnar. 1997. Active deformation of Asia: From kinematics to dynamics. *Science*. **278**(5338), pp. 647–650. 57

England, Philip and Peter Molnar. 2005. Late Quaternary to decadal velocity fields in Asia. *Journal of Geophysical Research: Solid Earth*. **110**(B12). 56

Fang, Jin, Caijun Xu, Yangmao Wen, Shuai Wang, Guangyu Xu, Yingwen Zhao and Lei Yi. 2019. The 2018 Mw 7.5 Palu earthquake: A supershear rupture event constrained by InSAR and broadband regional seismograms. *Remote Sensing*. **11**(11), p. 1330. 93, 125

Farr, Tom G, Paul A Rosen, Edward Caro, Robert Crippen, Riley Duren, Scott Hensley, Michael Kobrick, Mimi Paller, Ernesto Rodriguez, Ladislav Roth et al. 2007. The shuttle radar topography mission. *Reviews of geophysics*. **45**(2). 23, 37, 59, 94

Ferretti, Alessandro, Alfio Fumagalli, Fabrizio Novali, Claudio Prati, Fabio Rocca and Alessio Rucci. 2011. A new algorithm for processing interferometric data-stacks: SqueeSAR. *IEEE transactions on geoscience and remote sensing*. **49**(9), pp. 3460–3470. 14

Ferretti, Alessandro, Claudio Prati and Fabio Rocca. 2001. Permanent scatterers in SAR interferometry. *IEEE Transactions on geoscience and remote sensing*. **39**(1), pp. 8–20. 14, 20, 21

Fialko, Yuri. 2006. Interseismic strain accumulation and the earthquake potential on the southern San Andreas fault system. *Nature*. **441**(7096), pp. 968–971. 6, 10, 29

Foster, James, John Kealy, Tiziana Cherubini, Steven Businger, Zhong Lu and Michael Murphy. 2013. The utility of atmospheric analyses for the mitigation of artifacts in InSAR. *Journal of Geophysical Research: Solid Earth*. **118**(2), pp. 748–758. 12

Fournier, Thomas, Matthew E Pritchard and Noah Finnegan. 2011. Accounting for atmospheric delays in InSAR data in a search for long-wavelength deformation in South America. *IEEE Transactions on Geoscience and Remote Sensing*. **49**(10), pp. 3856–3867. 10

Fritz, Hermann M, Costas E Synolakis, Nikos Kalligeris, Vassilis Skanavis, Fajar J Santoso, Mohammad Rizal, Gegar Prasetya, Yibin Liu and Philip LF Liu. 2019. The 2018 Sulawesi tsunami: Field survey and eyewitness video analysis using LiDAR. In *Geophysical Research Abstracts*. 92

Funnel. 2006. Fault Creep Monitoring Project [Online]. *Available from: http://funnel.sfsu.edu/creep/WhatsCreepPage.html.* . 5

Funning, Gareth J, Barry Parsons and Tim J Wright. 2007. Fault slip in the 1997 Manyi, Tibet earthquake from linear elastic modelling of InSAR displacements. *Geophysical Journal International*. **169**(3), pp. 988–1008. 53

Furuya, Masato and Takatoshi Yasuda. 2011. The 2008 Yutian normal faulting earthquake (Mw 7.1), NW Tibet: Non-planar fault modeling and implications for the Karakax Fault. *Tectonophysics*. **511**(3-4), pp. 125–133. 88

Gan, Weijun, Peizhen Zhang, Zheng-Kang Shen, Zhijun Niu, Min Wang, Yongge Wan, Demin Zhou and Jia Cheng. 2007. Present-day crustal motion within the Tibetan Plateau inferred from GPS measurements. *Journal of Geophysical Research: Solid Earth*. **112**(B8). 60, 62

Gold, Ryan D, Eric Cowgill, J Ramón Arrowsmith, Xuanhua Chen, Warren D Sharp, Kari M Cooper and Xiao-Feng Wang. 2011. Faulted terrace risers place new constraints on the late Quaternary slip rate for the central Altyn Tagh fault, northwest Tibet. *Bulletin*. **123**(5-6), pp. 958–978. 60, 62

Gong, Wenyu, Franz J Meyer, Shizhuo Liu and Ramon F Hanssen. 2015. Temporal filtering of InSAR data using statistical parameters from NWP models. *IEEE Transactions on geoscience and remote sensing*. **53**(7), pp. 4033–4044. 12

Gonzalez, Pablo J, Richard J Walters, Emma L Hatton, Karsten Spaans, Andrew J Hooper and Tim J Wright. 2016. LiCSAR: Tools for automated generation of Sentinel-1 frame interferograms. In *2016 AGU Fall Meeting*. AGU. 23, 63

Grandin, Raphaël, Marie-Pierre Doin, Laurent Bollinger, Béatrice Pinel-Puysségur, Gabriel Ducret, Romain Jolivet and Soma Nath Sapkota. 2012. Long-term growth of the Himalaya inferred from interseismic InSAR measurement. *Geology*. **40**(12), pp. 1059–1062. 6

Gray, A Laurence, Karim E Mattar and George Sofko. 2000. Influence of ionospheric electron density fluctuations on satellite radar interferometry. *Geophysical Research Letters*. **27**(10), pp. 1451–1454. 10

Gusman, Aditya Riadi, Kenji Satake, Masanao Shinohara, ShinâĂŹichi Sakai and Yuichiro Tanioka. 2017. Fault slip distribution of the 2016 Fukushima earthquake estimated from tsunami waveforms. *Pure and Applied Geophysics*. **174**(8), pp. 2925–2943. 92

Gusman, Aditya Riadi, Pepen Supendi, Andri Dian Nugraha, William Power, Hamzah Latief, Haris Sunendar, Sri Widiyantoro, Samsul Hadi Wiyono, Aradea Hakim, Abdul Muhari et al. 2019. Source model for the tsunami inside Palu Bay following the 2018 Palu earthquake, Indonesia. *Geophysical Research Letters*. **46**(15), pp. 8721–8730. 131

Hall, R and MEJ Wilson. 2000. Neogene sutures in eastern Indonesia. *Journal of Asian Earth Sciences*. **18**(6), pp. 781–808. 16

Hamling, Ian J, Sigrún Hreinsdóttir, Kate Clark, John Elliott, Cunren Liang, Eric Fielding, Nicola Litchfield, Pilar Villamor, Laura Wallace, Tim J Wright et al. 2017. Complex multifault rupture during the 2016 Mw 7.8 Kaikōura earthquake, New Zealand. *Science*. **356**(6334). 1, 3, 8, 29

Hanssen, Ramon F. 2001. *Radar interferometry: data interpretation and error analysis*. Springer Science & Business Media. 13, 24

Hanssen, Raymond Franciscus. 1998. *Atmospheric heterogeneities in ERS tandem SAR interferometry*. Delft University Press. 24

Hastings, W Keith. 1970. Monte Carlo sampling methods using Markov chains and their applications. *Biometrika*. **57**(1), pp. 97–109. 28

He, Jiankun, Philippe Vernant, Jean Chéry, Weimin Wang, Shuangjiang Lu, Wenfei Ku, Wenhai Xia and Roger Bilham. 2013b. Nailing down the slip rate of the Altyn Tagh fault. *Geophysical Research Letters*. **40**(20), pp. 5382–5386. 49, 60, 62, 85

He, Jiankun, Shuangjiang Lu and Weimin Wang. 2013a. Three-dimensional mechanical modeling of the GPS velocity field around the northeastern Tibetan plateau and surrounding regions. *Tectonophysics*. **584**, pp. 257–266. 37, 38, 49, 50

He, Lijia, Guangcai Feng, Zhiwei Li, Zhixiong Feng, Hua Gao and Xiongxiao Wu. 2019. Source parameters and slip distribution of the 2018 Mw 7.5 Palu, Indonesia earthquake estimated from space-based geodesy. *Tectonophysics*. **772**, p. 228216. 93, 125

Heidarzadeh, Mohammad, Abdul Muhari and Antonius B Wijanarto. 2019. Insights on the source of the 28 September 2018 Sulawesi tsunami, Indonesia based on spectral analyses and numerical simulations. *Pure and Applied Geophysics*. **176**(1), pp. 25–43. 92

Heleno, Sandra IN, Corine Frischknecht, Nicolas dâĂŹOreye, JNP Lima, B Faria, R Wall and F Kervyn. 2010. Seasonal tropospheric influence on SAR interferograms near the ITCZ–The case of Fogo Volcano and Mount Cameroon. *Journal of African Earth Sciences*. **58**(5), pp. 833–856. 10

Herring, TA, RW King and SC Mcclusky. 2015. Introduction to GAMIT/GLOBK, Release 10.6. Massachusetts Institute of Technology, 2015. 35

Himematsu, Yuji and Masato Furuya. 2016. Fault source model for the 2016 Kumamoto earthquake sequence based on ALOS-2/PALSAR-2 pixel-offset data: evidence for dynamic slip partitioning. *Earth, Planets and Space*. **68**(1), p. 169. 9

Hooper, Andrew. 2008. A multi-temporal InSAR method incorporating both persistent scatterer and small baseline approaches. *Geophysical Research Letters*. **35**(16). 21, 23

Hooper, Andrew. 2010. A statistical-cost approach to unwrapping the phase of InSAR time series. In *Proceedings of the International Workshop on ERS SAR Interferometry*. pp. 1–6. 23

Hooper, Andrew, David Bekaert, Karsten Spaans and Mahmut Arıkan. 2012. Recent advances in SAR interferometry time series analysis for measuring crustal deformation. *Tectonophysics*. **514**, pp. 1–13. 10, 20, 21, 23, 108

Hooper, Andrew and Howard A Zebker. 2007. Phase unwrapping in three dimensions with application to InSAR time series. *JOSA A*. **24**(9), pp. 2737–2747. 23

Hooper, Andrew, Howard Zebker, Paul Segall and Bert Kampes. 2004. A new method for measuring deformation on volcanoes and other natural terrains using InSAR persistent scatterers. *Geophysical research letters*. **31**(23). 14, 20, 21

Hornbach, Matthew J, Nicole Braudy, Richard W Briggs, Marie-Helene Cormier, Marcy B Davis, John B Diebold, Nicole Dieudonne, Roby Douilly, Cliff Frohlich, Sean PS Gulick et al. 2010. High tsunami frequency as a result of combined strike-slip faulting and coastal landslides. *Nature Geoscience*. **3**(11), pp. 783–788. 92

Houseman, Gregory and Philip England. 1986. Finite strain calculations of continental deformation: 1. Method and general results for convergent zones. *Journal of Geophysical Research: Solid Earth*. **91**(B3), pp. 3651–3663. 57

Houseman, Gregory and Philip England. 1993. Crustal thickening versus lateral expulsion in the Indian-Asian continental collision. *Journal of Geophysical Research: Solid Earth*. **98**(B7), pp. 12233–12249. 57

Hussain, Ekbal, Andrew Hooper, Tim J Wright, Richard J Walters and David PS Bekaert. 2016a. Interseismic strain accumulation across the central North Anatolian Fault from iteratively unwrapped InSAR measurements. *Journal of Geophysical Research: Solid Earth*. **121**(12), pp. 9000–9019. 6, 10, 23, 29, 78

Hussain, Ekbal, Tim J Wright, Richard J Walters, David Bekaert, Andrew Hooper and Gregory A Houseman. 2016b. Geodetic observations of postseismic creep in the decade after the 1999 Izmit earthquake, Turkey: Implications for a shallow slip deficit. *Journal of Geophysical Research: Solid Earth*. **121**(4), pp. 2980–3001. 25

Hussain, Ekbal, Tim J Wright, Richard J Walters, David PS Bekaert, Ryan Lloyd and Andrew Hooper. 2018. Constant strain accumulation rate between major earthquakes on the North Anatolian Fault. *Nature communications*. **9**(1), pp. 1–9. 3, 14, 67, 82

Ingleby, T, TJ Wright, A Hooper, TJ Craig and JR Elliott. 2020. Constraints on the geometry and frictional properties of the Main Himalayan Thrust using coseismic, postseismic, and interseismic deformation in Nepal. *Journal of Geophysical Research: Solid Earth*. **125**(2), p. e2019JB019201. 3

Jamelot, A, A Gailler, Ph Heinrich, A Vallage and J Champenois. 2019. Tsunami simulations of the Sulawesi Mw 7.5 event: Comparison of seismic sources issued from a tsunami warning context versus post-event finite source. *Pure and Applied Geophysics*. **176**(8), pp. 3351–3376. 92

Jena, Ratiranjan, Biswajeet Pradhan, Ghassan Beydoun, Abdullah Al-Amri and Hizir Sofyan. 2020. Seismic hazard and risk assessment: a review of state-of-the-art traditional and GIS models. *Arabian Journal of Geosciences*. **13**(2), p. 50. 1

Jiang, Guoyan, Xiwei Xu, Guihua Chen, Yajing Liu, Yukitoshi Fukahata, Hua Wang, Guihua Yu, Xibin Tan and Caijun Xu. 2015. Geodetic imaging of potential seismogenic asperities on the Xianshuihe-Anninghe-Zemuhe fault system, southwest China, with a new 3-D viscoelastic interseismic coupling model. *Journal of Geophysical Research: Solid Earth*. **120**(3), pp. 1855–1873. 6

Jin, Lizhen and Gareth J Funning. 2017. Testing the inference of creep on the northern Rodgers Creek fault, California, using ascending and descending persistent scatterer InSAR data. *Journal of Geophysical Research: Solid Earth*. **122**(3), pp. 2373–2389. 6

Jo, Min-Jeong, Hyung-Sup Jung, Joong-Sun Won, Michael P Poland, Asta Miklius and Zhong Lu. 2015. Measurement of slow-moving along-track displacement from an efficient multiple-aperture SAR interferometry (MAI) stacking. *Journal of Geodesy*. **89**(5), pp. 411–425. 9

Johanson, IA and R Bürgmann. 2005. Creep and quakes on the northern transition zone of the San Andreas fault from GPS and InSAR data. *Geophysical Research Letters*. **32**(14). 7

Jolivet, Romain, Cécile Lasserre, M-P Doin, G Peltzer, J-P Avouac, Jianbao Sun and R Dailu. 2013. Spatio-temporal evolution of aseismic slip along the Haiyuan fault, China: Implications for fault frictional properties. *Earth and Planetary Science Letters*. **377**, pp. 23–33. 7

Jolivet, Romain, Cécile Lasserre, M-P Doin, Stéphane Guillaso, Gilles Peltzer, R Dailu, Jimin Sun, Z-K Shen and X Xu. 2012. Shallow creep on the Haiyuan fault (Gansu, China) revealed by SAR interferometry. *Journal of Geophysical Research: Solid Earth*. **117**(B6). 101

Jolivet, Romain, Piyush Shanker Agram, Nina Y Lin, Mark Simons, Marie-Pierre Doin, Gilles Peltzer and Zhenhong Li. 2014. Improving InSAR geodesy using global atmospheric models. *Journal of Geophysical Research: Solid Earth*. **119**(3), pp. 2324–2341. 11

Jolivet, Romain, R Cattin, Nicolas Chamot-Rooke, Cécile Lasserre and G Peltzer. 2008. Thin-plate modeling of interseismic deformation and asymmetry across the Altyn Tagh fault zone. *Geophysical Research Letters*. **35**(2). 10, 29, 60, 62, 76, 78

Jung, Hyung-Sup, Joong-Sun Won and Sang-Wan Kim. 2009. An improvement of the performance of multiple-aperture SAR interferometry (MAI). *IEEE Transactions on Geoscience and Remote Sensing*. **47**(8), pp. 2859–2869. 9

Kampes, BM. 2005. Displacement parameter estimation using permanent scatterer interferometry. Ph.D. thesis. *Dutch: Delft University of Technology*. . 20

Kaneko, Y, Y Fialko, David T Sandwell, Xiaopeng Tong and M Furuya. 2013. Interseismic deformation and creep along the central section of the North Anatolian fault (Turkey): InSAR observations and implications for rate-and-state friction properties. *Journal of Geophysical Research: Solid Earth*. **118**(1), pp. 316–331. 6

Karimzadeh, Sadra, Ziyadin Cakir, Batuhan Osmanoğlu, Gina Schmalzle, Masakatsu Miyajima, Reza Amiraslanzadeh and Yahya Djamour. 2013. Interseismic strain accumulation across the North Tabriz Fault (NW Iran) deduced from InSAR time series. *Journal of Geodynamics*. **66**, pp. 53–58. 6

Katili, John A. 1970. Large transcurrent faults in Southeast Asia with special reference to Indonesia. *Geologische Rundschau*. **59**(2), pp. 581–600. 17, 92

Kawamura, Kiichiro, Tomoyuki Sasaki, Toshiya Kanamatsu, Arito Sakaguchi and Yujiro Ogawa. 2012. Large submarine landslides in the Japan Trench: A new scenario for additional tsunami generation. *Geophysical Research Letters*. **39**(5). 92

King, Geoffrey CP, Ross S Stein and Jian Lin. 1994. Static stress changes and the triggering of earthquakes. *Bulletin of the Seismological Society of America*. **84**(3), pp. 935–953. 8

Kong, Xianghong and Peter Bird. 1994. *Neotectonics of Asia: thin-shell finite-element models with faults*. 57

Kreemer, Corné, Geoffrey Blewitt and Elliot C Klein. 2014. A geodetic plate motion and Global Strain Rate Model. *Geochemistry, Geophysics, Geosystems*. **15**(10), pp. 3849–3889. 2

Lanari, Riccardo, Francesco Casu, Mariarosaria Manzo, Giovanni Zeni, Paolo Berardino, Michele Manunta and Antonio Pepe. 2007. An overview of the small baseline subset algorithm: A DInSAR technique for surface deformation analysis. In *Deformation and Gravity Change: Indicators of Isostasy, Tectonics, Volcanism, and Climate Change*. Springer pp. 637–661. 21

Lasserre, Cécile, G Peltzer, F Crampé, Yann Klinger, Jerome Van Der Woerd and Paul Tapponnier. 2005. Coseismic deformation of the 2001 Mw= 7.8 Kokoxili earthquake in Tibet, measured by synthetic aperture radar interferometry. *Journal of Geophysical Research: Solid Earth*. **110**(B12). 80

Lawson, Andrew Cowper. 1908. *The California earthquake of April 18, 1906: Report of the state earthquake investigation commission...* Carnegie institution of Washington. 1

Lazeckỳ, Milan, Karsten Spaans, Pablo J González, Yasser Maghsoudi, Yu Morishita, Fabien Albino, John Elliott, Nicholas Greenall, Emma Hatton, Andrew Hooper et al. 2020. LiCSAR: An automatic InSAR tool for measuring and monitoring tectonic and volcanic activity. *Remote Sensing*. **12**(15), p. 2430. 23, 63

Legg, MR, JC Borrero and CE Synolakis. 2003. Tsunami hazards from strike-slip earthquakes. In *AGU Fall Meeting 2003*. 92

Li, Xing, Wenbin Xu, Sigurjón Jónsson, Yann Klinger and Guohong Zhang. 2020. Source Model of the 2014 M w 6.9 Yutian Earthquake at the Southwestern End of the Altyn Tagh Fault in Tibet Estimated from Satellite Images. *Seismological Society of America*. **91**(6), pp. 3161–3170. 16, 89, 90

Li, Yujiang, Lianwang Chen, Shaofeng Liu, Shuxin Yang, Xingyue Yang and Guangwei Zhang. 2015. Coseismic Coulomb stress changes caused by the Mw6. 9 Yutian earthquake in 2014 and its correlation to the 2008 Mw7. 2 Yutian earthquake. *Journal of Asian Earth Sciences*. **105**, pp. 468–475. 89, 90

Li, Zhenhong, EJ Fielding, P Cross and R Preusker. 2009. Advanced InSAR atmospheric correction: MERIS/MODIS combination and stacked water vapour models. *International Journal of Remote Sensing*. **30**(13), pp. 3343–3363. 11

Li, Zhenhong, Eric J Fielding, Paul Cross and Jan-Peter Muller. 2006. Interferometric synthetic aperture radar atmospheric correction: GPS topography-dependent turbulence model. *Journal of Geophysical Research: Solid Earth*. **111**(B2). 11

Liang, Cunren and Eric J Fielding. 2017. Interferometry with ALOS-2 full-aperture ScanSAR data. *IEEE Transactions on Geoscience and Remote Sensing*. **55**(5), pp. 2739–2750. 95

Liang, Hongyu, Lei Zhang, Xiaoli Ding, Zhong Lu and Xin Li. 2018. Toward mitigating stratified tropospheric delays in multitemporal InSAR: a quadtree aided joint model. *IEEE Transactions on Geoscience and Remote Sensing*. **57**(1), pp. 291–303. 13

Liang, Shiming, Weijun Gan, Chuanzheng Shen, Genru Xiao, Jing Liu, Weitao Chen, Xiaoguang Ding and Deming Zhou. 2013. Three-dimensional velocity field of present-day crustal motion of the Tibetan Plateau derived from GPS measurements. *Journal of geophysical research: solid earth*. **118**(10), pp. 5722–5732. 35, 37, 49, 50

Lienkaemper, James J and Jon S Galehouse. 1997. Revised long-term creep rates on the Hayward fault, Alameda and Contra Costa counties, California. *US Geol. Surv., Open-File Rep. 97*. **690**, p. 18. 7

Lin, YN, Romain Jolivet, Mark Simons, PS Agram, Hilary R Martens, Zhenhong Li and SH Lodi. 2015. High interseismic coupling in the Eastern Makran (Pakistan) subduction zone. *Earth and Planetary Science Letters*. **420**, pp. 116–126. 6

Lin, Yu-nung Nina, Mark Simons, Eric A Hetland, Pablo Muse and Christopher DiCaprio. 2010. A multiscale approach to estimating topographically correlated propagation delays in radar interferograms. *Geochemistry, Geophysics, Geosystems*. **11**(9). 13

Lin, Zhou, Jing Liu-Zeng, Ray J Weldon II, Jing Tian, Chao Ding and Yu Du. 2020. Modeling repeated coseismic slip to identify and characterize individual earthquakes from geomorphic offsets on strike-slip faults. *Earth and Planetary Science Letters*. **545**, p. 116313. 2

Lindsey, Eric O, Ryo Natsuaki, Xiaohua Xu, Masanobu Shimada, Manabu Hashimoto, Diego Melgar and David T Sandwell. 2015. Line-of-sight displacement from ALOS-2 interferometry: Mw 7.8 Gorkha Earthquake and Mw 7.3 aftershock. *Geophysical Research Letters*. **42**(16), pp. 6655–6661. 29

Lindsey, Eric O, Valerie J Sahakian, Yuri Fialko, Yehuda Bock, Sylvain Barbot and Thomas K Rockwell. 2014. Interseismic strain localization in the San Jacinto fault zone. *Pure and Applied Geophysics*. **171**(11), pp. 2937–2954. 6

Liu, Chuanjin, Lingyun Ji, Liangyu Zhu and Chaoying Zhao. 2018. InSAR-constrained interseismic deformation and potential seismogenic asperities on the Altyn Tagh fault at 91.5–95 E, Northern Tibetan Plateau. *Remote Sensing*. **10**(6), p. 943. 60, 61, 62

Lohman, Rowena B and Mark Simons. 2005. Locations of selected small earthquakes in the Zagros mountains. *Geochemistry, Geophysics, Geosystems*. **6**(3). 8

Lohman, Rowena B, Mark Simons and Brian Savage. 2002. Location and mechanism of the Little Skull Mountain earthquake as constrained by satellite radar interferometry and seismic waveform modeling. *Journal of Geophysical Research: Solid Earth*. **107**(B6), pp. ETG–7. 8

Loveless, John P and Brendan J Meade. 2011. Partitioning of localized and diffuse deformation in the Tibetan Plateau from joint inversions of geologic and geodetic observations. *Earth and Planetary Science Letters*. **303**(1-2), pp. 11–24. 58

Martínez-Díaz, José J, Marta Bejar-Pizarro, José A Álvarez-Gómez, Flor de Lis Mancilla, Daniel Stich, Gerardo Herrera and Jose Morales. 2012. Tectonic and seismic implications of an intersegment rupture: The damaging May 11th 2011 Mw 5.2 Lorca, Spain, earthquake. *Tectonophysics*. **546**, pp. 28–37. 8

Massonnet, Didier and Kurt L Feigl. 1998. Radar interferometry and its application to changes in the Earth's surface. *Reviews of geophysics*. **36**(4), pp. 441–500. 20

Massonnet, Didier, Marc Rossi, César Carmona, Frédéric Adragna, Gilles Peltzer, Kurt Feigl and Thierry Rabaute. 1993. The displacement field of the Landers earthquake mapped by radar interferometry. *nature*. **364**(6433), pp. 138–142. 3, 7

Mattar, KE and AL Gray. 2002. Reducing ionospheric electron density errors in satellite radar interferometry applications. *Canadian Journal of Remote Sensing*. **28**(4), pp. 593–600. 10

McCloskey, John, Suleyman S Nalbant and Sandy Steacy. 2005. Earthquake risk from co-seismic stress. *Nature*. **434**(7031), pp. 291–291. 8

Meade, Brendan J and John P Loveless. 2009. Block modeling with connected fault-network geometries and a linear elastic coupling estimator in spherical coordinates. *Bulletin of the Seismological Society of America*. **99**(6), pp. 3124–3139. 137

Mériaux, A-S, FJ Ryerson, P Tapponnier, J Van der Woerd, RC Finkel, Xiwei Xu, Zhiqin Xu and MW Caffee. 2004. Rapid slip along the central Altyn Tagh Fault: morphochronologic evidence from Cherchen He and Sulamu Tagh. *Journal of Geophysical Research: Solid Earth*. **109**(B6). 60, 62

Mériaux, A-S, Jerome Van Der Woerd, Paul Tapponnier, Frederick J Ryerson, Robert C Finkel, Cécile Lasserre and Xiwei Xu. 2012. The Pingding segment of the Altyn Tagh Fault (91 E): Holocene slip-rate determination from cosmogenic radionuclide dating of offset fluvial terraces. *Journal of Geophysical Research: Solid Earth*. **117**(B9). 60

Mériaux, A-S, P Tapponnier, FJ Ryerson, Xu Xiwei, G King, J Van der Woerd, RC Finkel, Li Haibing, MW Caffee, Xu Zhiqin et al. 2005. The Aksay segment of the northern Altyn Tagh fault: Tectonic geomorphology, landscape evolution, and Holocene slip rate. *Journal of Geophysical Research: Solid Earth*. **110**(B4). 60, 62

Merryman Boncori, John Peter and Giuseppe Pezzo. 2015. Measuring the north–south coseismic displacement component with high-resolution multi-aperture InSAR. *Terra nova*. **27**(1), pp. 28–35. 9

Metropolis, Nicholas, Arianna W Rosenbluth, Marshall N Rosenbluth, Augusta H Teller and Edward Teller. 1953. Equation of state calculations by fast computing machines. *The journal of chemical physics*. **21**(6), pp. 1087–1092. 28

Meyer, B, P Tapponnier, Y Gaudemer, G Peltzer, Guo Shunmin and Chen Zhitai. 1996. Rate of left-lateral movement along the easternmost segment of the Altyn Tagh fault, east of 96 E (China). *Geophysical Journal International*. **124**(1), pp. 29–44. 62

Meyer, Franz, Richard Bamler, Norbert Jakowski and Thomas Fritz. 2006. The potential of low-frequency SAR systems for mapping ionospheric TEC distributions. *IEEE Geoscience and Remote Sensing Letters*. **3**(4), pp. 560–564. 10

Michel, Sylvain, Jean-Philippe Avouac, Romain Jolivet and Lifeng Wang. 2018. Seismic and aseismic moment budget and implication for the seismic potential of the Parkfield segment of the San Andreas fault. *Bulletin of the Seismological Society of America*. **108**(1), pp. 19–38. 2

Mikami, Takahito, Tomoya Shibayama, Miguel Esteban, Tomoyuki Takabatake, Ryota Nakamura, Yuta Nishida, Hendra Achiari, Abdul Gafur Marzuki, Muhammad Fadel Hidayat Marzuki, Jacob Stolle et al. 2019. Field survey of the 2018 Sulawesi tsunami: inundation and run-up heights and damage to coastal communities. *Pure and Applied Geophysics*. **176**(8), pp. 3291–3304. 129

Mohadjer, Solmaz, Todd A Ehlers, Rebecca Bendick and Sebastian G Mutz. 2017. Review of GPS and Quaternary fault slip rates in the Himalaya-Tibet orogen. *Earth-Science Reviews*. **174**, pp. 39–52. 60

Molnar, Peter. 1979. Earthquake recurrence intervals and plate tectonics. *Bulletin of the Seismological Society of America*. **69**(1), pp. 115–133. 2

Molnar, Peter and Paul Tapponnier. 1975. Cenozoic tectonics of Asia: effects of a continental collision. *science*. **189**(4201), pp. 419–426. 57

Morishita, Yu, Milan Lazecky, Tim J Wright, Jonathan R Weiss, John R Elliott and Andy Hooper. 2020. LiCSBAS: An Open-Source InSAR Time Series Analysis Package Integrated with the LiCSAR Automated Sentinel-1 InSAR Processor. *Remote Sensing*. **12**(3), p. 424. 65

Morishita, Yu, Tomokazu Kobayashi and Hiroshi Yarai. 2016. Three-dimensional deformation mapping of a dike intrusion event in Sakurajima in 2015 by exploiting the right-and left-looking ALOS-2 InSAR. *Geophysical Research Letters*. **43**(9), pp. 4197–4204. 101

Muhari, Abdul, Fumihiko Imamura, Taro Arikawa, Aradea R Hakim and Bagus Afriyanto. 2018. Solving the puzzle of the September 2018 Palu, Indonesia, tsunami mystery: clues from the tsunami waveform and the initial field survey data. *Journal of Disaster Research*. **13**(Scientific Communication), p. sc20181108. 92

Nocquet, Jean-Mathieu. 2012. Present-day kinematics of the Mediterranean: A comprehensive overview of GPS results. *Tectonophysics*. **579**, pp. 220–242. 78

Oglesby, David D. 2005. The dynamics of strike-slip step-overs with linking dip-slip faults. *Bulletin of the Seismological Society of America*. **95**(5), pp. 1604–1622. 103, 104

Okada, Yoshimitsu. 1985. Surface deformation due to shear and tensile faults in a half-space. *Bulletin of the seismological society of America*. **75**(4), pp. 1135–1154. 27

Okada, Yoshimitsu. 1992. Internal deformation due to shear and tensile faults in a half-space. *Bulletin of the seismological society of America*. **82**(2), pp. 1018–1040. 7, 26, 27

Omira, R, GG Dogan, R Hidayat, S Husrin, G Prasetya, A Annunziato, C Proietti, P Probst, MA Paparo, M Wronna et al. 2019. The September 28th, 2018, tsunami in Palu-Sulawesi, Indonesia: A post-event field survey. *Pure and Applied Geophysics*. **176**(4), pp. 1379–1395. 92, 129

Onn, F and HA Zebker. 2006. Correction for interferometric synthetic aperture radar atmospheric phase artifacts using time series of zenith wet delay observations from a GPS network. *Journal of Geophysical Research: Solid Earth*. **111**(B9). 11

Pakoksung, Kwanchai, Anawat Suppasri, Fumihiko Imamura, Cipta Athanasius, Amalfi Omang and Abdul Muhari. 2019. Simulation of the submarine landslide tsunami on 28 September 2018 in Palu Bay, Sulawesi Island, Indonesia, using a two-layer model. *Pure and Applied Geophysics*. **176**(8), pp. 3323–3350. 92

Parker, Amy L, Juliet Biggs, Richard J Walters, Susanna K Ebmeier and Tim J Wright. 2015. Systematic assessment of atmospheric uncertainties for InSAR data at volcanic arcs using large-scale atmospheric models: Application to the Cascade volcanoes, United States. *Remote Sensing of Environment*. **170**, pp. 102–114. 10, 15, 30

Patria, Adi and Purna Sulastya Putra. 2020. Development of the Palu–Koro Fault in NW Palu Valley, Indonesia. *Geoscience Letters*. **7**(1), pp. 1–11. 16, 17

Pelinovsky, Efim, Dede Yuliadi, Gegar Prasetya and Rahman Hidayat. 1997. The 1996 Sulawesi tsunami. *Natural Hazards*. **16**(1), pp. 29–38. 92

Peltzer, Gilles and Paul Tapponnier. 1988. Formation and evolution of strike-slip faults, rifts, and basins during the India-Asia collision: An experimental approach. *Journal of Geophysical Research: Solid Earth*. **93**(B12), pp. 15085–15117. 57

Peltzer, Gilles, Paul Tapponnier and Rolando Armijo. 1989. Magnitude of late Quaternary left-lateral displacements along the north edge of Tibet. *Science*. **246**(4935), pp. 1285–1289. 60, 62

Pepe, Antonio and Fabiana Calò. 2017. A review of interferometric synthetic aperture RADAR (InSAR) multi-track approaches for the retrieval of Earth's surface displacements. *Applied Sciences*. **7**(12), p. 1264. 19

Perissin, Daniele and Teng Wang. 2011. Time-series InSAR applications over urban areas in China. *IEEE journal of selected topics in applied earth observations and remote sensing*. **4**(1), pp. 92–100. 10, 30

Pinel, Virginie, A Hooper, S De la Cruz-Reyna, G Reyes-Davila, MP Doin and Pascale Bascou. 2011. The challenging retrieval of the displacement field from InSAR data for andesitic stratovolcanoes: Case study of Popocatepetl and Colima Volcano, Mexico. *Journal of Volcanology and Geothermal Research*. **200**(1), pp. 49–61. 11

Prasetya, GS, WP De Lange and TR Healy. 2001. The makassar strait tsunamigenic region, Indonesia. *Natural Hazards*. **24**(3), pp. 295–307. 92

Prescott, William H and Amos Nur. 1981. The accommodation of relative motion at depth on the San Andreas fault system in California. *Journal of Geophysical Research: Solid Earth*. **86**(B2), pp. 999–1004. 83

Puntanen, Simo, George PH Styan and Hans Joachim Werner. 2000. Two matrix-based proofs that the linear estimator Gy is the best linear unbiased estimator. *Journal of statistical planning and inference*. **88**(2), pp. 173–179. 47, 65

Putra, Purna Sulastya, Aswan Aswan, Khoiril Anwar Maryunani, Eko Yulianto and Widjo Kongko. 2019. Field survey of the 2018 Sulawesi tsunami deposits. *Pure and Applied Geophysics*. **176**(6), pp. 2203–2213. 129

Puysségur, Béatrice and Michel, Rémi and Avouac, Jean-Philippe. 2007. Tropospheric phase delay in interferometric synthetic aperture radar estimated from meteorological model and multispectral imagery. *Journal of Geophysical Research: Solid Earth*. **112**(B5). 11

Qiu, Jiangtao, Lei Liu, Chen Wang and Yang Wang. 2019. Present-day tectonic activity along the central section of the Altyn Tagh fault derived from time series InSAR. *Geodesy and Geodynamics*. **10**(4), pp. 307–314. 60, 61, 62

Rebischung, Paul and Ralf Schmid. 2016. IGS14/igs14. atx: a new framework for the IGS products. In *AGU Fall Meeting 2016*. 98

Reid, Harry Fielding, State Earthquake Investigation Commission et al. 1910. *The California earthquake of April 18, 1906: Report of the State Earthquake Investigation Commission. 2. The mechanics of the earthquake*. Carnegie Inst. of Washington. 2

Replumaz, Anne and P Tapponnier. 2003. Reconstruction of the deformed collision zone between India and Asia by backward motion of lithospheric blocks. *Journal of Geophysical Research: Solid Earth*. **108**(B6). 57

Robinson, Delores M, Guillaume Dupont-Nivet, George E Gehrels and Yueqiao Zhang. 2003. The Tula uplift, northwestern China: Evidence for regional tectonism of the northern Tibetan Plateau during late Mesozoic–early Cenozoic time. *Geological Society of America Bulletin*. **115**(1), pp. 35–47. 15

Robinson, DP, S Das and MP Searle. 2010. Earthquake fault superhighways. *Tectonophysics*. **493**(3-4), pp. 236–243. 15, 58

Rollins, Chris and Jean-Philippe Avouac. 2019. A geodesy-and seismicity-based local earthquake likelihood model for central Los Angeles. *Geophysical Research Letters*. **46**(6), pp. 3153–3162. 2

Ryder, Isabelle, Barry Parsons, Tim J Wright and Gareth J Funning. 2007. Post-seismic motion following the 1997 Manyi (Tibet) earthquake: InSAR observations and modelling. *Geophysical Journal International*. **169**(3), pp. 1009–1027. 53

Ryerson, Frederick J, Paul Tapponnier, Robert C Finkel, A Meriaux, Jérôme Van der Woerd, Cécile Lasserre, M Chevalier, Xi-wei Xu, Hai-bing Li and Geoffrey CP King. 2006. Applications of morphochronology to the active tectomics of Tibet. *SPECIAL PAPERS-GEOLOGICAL SOCIETY OF AMERICA*. **415**, p. 61. 57

Sassa, Shinji and Tomohiro Takagawa. 2019. Liquefied gravity flow-induced tsunami: first evidence and comparison from the 2018 Indonesia Sulawesi earthquake and tsunami disasters. *Landslides*. **16**(1), pp. 195–200. 92

Savage, James C. 1983. A dislocation model of strain accumulation and release at a subduction zone. *Journal of Geophysical Research: Solid Earth*. **88**(B6), pp. 4984–4996. 25

Savage, James C, WH Prescott, Michael Lisowski and N King. 1979b. Deformation across the Salton trough, California, 1973–1977. *Journal of Geophysical Research: Solid Earth*. **84**(B6), pp. 3069–3079. 4

Savage, JC and M Lisowski. 1993. Inferred depth of creep on the Hayward fault, central California. *Journal of Geophysical Research: Solid Earth*. **98**(B1), pp. 787–793. 7

Savage, JC and RO Burford. 1973. Geodetic determination of relative plate motion in central California. *Journal of Geophysical Research*. **78**(5), pp. 832–845. 6, 25, 49, 61, 78

Savage, JC, WH Prescott, JF Chamberlain, M Lisowski and CE Mortensen. 1979a. Geodetic tilt measurements along the San Andreas fault in central California. *Bulletin of the Seismological Society of America*. **69**(6), pp. 1965–1981. 82

Sawires, R, JA Peláez, RE Fat-Helbary, HA Ibrahim and MT García-Hernández. 2015. An updated seismic source model for Egypt. *Earthquake engineering from engineering seismology to optimal seismic design of engineering structures. InTech, Croatia*. pp. 1–51. 1

Scheiber, Rolf and Alberto Moreira. 2000. Coregistration of interferometric SAR images using spectral diversity. *IEEE Transactions on Geoscience and Remote Sensing*. **38**(5), pp. 2179–2191. 23

Searle, Michael P, JR Elliott, RJ Phillips and S-L Chung. 2011. Crustal–lithospheric structure and continental extrusion of Tibet. *Journal of the Geological Society*. **168**(3), pp. 633–672. 15, 43, 56

Segall, Paul. 2010. *Earthquake and volcano deformation*. Princeton University Press. 7

Shen, Lin, Andrew Hooper and John Elliott. 2019. A Spatially Varying Scaling Method for InSAR Tropospheric Corrections Using a High-Resolution Weather Model. *Journal of Geophysical Research: Solid Earth*. **124**(4), pp. 4051–4068. 14, 29, 60, 62, 63

Sigmundsson, Freysteinn, Andrew Hooper, Sigrún Hreinsdóttir, Kristín S Vogfjörd, Benedikt G Ófeigsson, Elías Rafn Heimisson, Stéphanie Dumont, Michelle Parks, Karsten Spaans, Gunnar B Gudmundsson et al. 2015. Segmented lateral dyke growth in a rifting event at Bar [eth] arbunga volcanic system, Iceland. *Nature*. **517**(7533), pp. 191–195. 29

Simons, M and PA Rosen. 2007. *Interferometric synthetic aperture radar geodesy*. Elsevier. 19

Simons, Wims, Taco Broerse, Lin Shen, Andy Hooper, Olga Kelptsova, Julie Pietrzak, Riccardo Riva, Nicolai Nijholt, Matthew Herman, Stef Lhermitte, Marc Naeije and Rob Govers. 2021. A tsunami generated by a strike-slip event: constraints from space geodesy on the 2018 Palu earthquake [Unpublished]. 95, 96, 127, 129

Simpson, RW, JJ Lienkaemper and JS Galehouse. 2001. Variations in creep rate along the Hayward Fault, California, interpreted as changes in depth of creep. *Geophysical Research Letters*. **28**(11), pp. 2269–2272. 7

Smith, Ernest K and Stanley Weintraub. 1953. The constants in the equation for atmospheric refractive index at radio frequencies. *Proceedings of the IRE*. **41**(8), pp. 1035–1037. 24

Socquet, Anne, James Hollingsworth, Erwan Pathier and Michel Bouchon. 2019. Evidence of supershear during the 2018 magnitude 7.5 Palu earthquake from space geodesy. *Nature Geoscience*. **12**(3), pp. 192–199. 3, 9, 92, 93, 97, 109, 125, 127

Socquet, Anne, Wim Simons, Christophe Vigny, Robert McCaffrey, Cecep Subarya, Dina Sarsito, Boudewijn Ambrosius and Wim Spakman. 2006. Microblock rotations and fault coupling in SE Asia triple junction (Sulawesi, Indonesia) from GPS and earthquake slip vector data. *Journal of Geophysical Research: Solid Earth*. **111**(B8). 16, 17, 91, 92

Song, Xiaogang, Yingfeng Zhang, Xinjian Shan, Yunhua Liu, Wenyu Gong and Chunyan Qu. 2019. Geodetic observations of the 2018 Mw 7.5 Sulawesi earthquake and its implications for the kinematics of the Palu fault. *Geophysical Research Letters*. **46**(8), pp. 4212–4220. 92, 125

Sreejith, KM, PS Sunil, Ritesh Agrawal, Ajish P Saji, DS Ramesh and AS Rajawat. 2016. Coseismic and early postseismic deformation due to the 25 April 2015, Mw 7.8 Gorkha, Nepal, earthquake from InSAR and GPS measurements. *Geophysical Research Letters*. **43**(7), pp. 3160–3168. 8

Steketee, JA. 1958. On Volterra's dislocations in a semi-infinite elastic medium. *Canadian Journal of Physics*. **36**(2), pp. 192–205. 26

Sudhaus, Henriette and Sigurjón Jónsson. 2009. Improved source modelling through combined use of InSAR and GPS under consideration of correlated data errors: application to the June 2000 Kleifarvatn earthquake, Iceland. *Geophysical Journal International*. **176**(2), pp. 389–404. 101

Takagi, Hiroshi, Munawir Bintang Pratama, Shota Kurobe, Miguel Esteban, Rafael Aránguiz and Bowei Ke. 2019. Analysis of generation and arrival time of landslide tsunami to Palu City due to the 2018 Sulawesi earthquake. *Landslides*. **16**(5), pp. 983–991. 91, 92, 131

Takeuchi, Christopher S and Yuri Fialko. 2012. Dynamic models of interseismic deformation and stress transfer from plate motion to continental transform faults. *Journal of Geophysical Research: Solid Earth*. **117**(B5). 6

Tape, Carl, Pablo Musé, Mark Simons, Danan Dong and Frank Webb. 2009. Multiscale estimation of GPS velocity fields. *Geophysical Journal International*. **179**(2), pp. 945–971. 137

Tapponnier, Paul, GLDAY Peltzer, AY Le Dain, Roland Armijo and P Cobbold. 1982. Propagating extrusion tectonics in Asia: New insights from simple experiments with plasticine. *Geology*. **10**(12), pp. 611–616. 57

Tapponnier, Paul and Peter Molnar. 1976. Slip-line field theory and large-scale continental tectonics. *Nature*. **264**(5584), pp. 319–324. 57

Tapponnier, Paul, Xu Zhiqin, Francoise Roger, Bertrand Meyer, Nicolas Arnaud, Gérard Wittlinger and Yang Jingsui. 2001. Oblique stepwise rise and growth of the Tibet Plateau. *science*. **294**(5547), pp. 1671–1677. 43, 57, 60, 62

Tarayre, H and D Massonnet. 1996. Atmospheric propagation heterogeneities revealed by ERS-1 interferometry. *Geophysical Research Letters*. **23**(9), pp. 989–992. 24

Taylor, Michael and An Yin. 2009. Active structures of the Himalayan-Tibetan orogen and their relationships to earthquake distribution, contemporary strain field, and Cenozoic volcanismActive structures on the Tibetan plateau and surrounding regions. *Geosphere*. **5**(3), pp. 199–214. 59, 80

Taylor, Michael and Gilles Peltzer. 2006. Current slip rates on conjugate strike-slip faults in central Tibet using synthetic aperture radar interferometry. *Journal of Geophysical Research: Solid Earth*. **111**(B12). 23, 86

Thatcher, Wayne. 2007. Microplate model for the present-day deformation of Tibet. *Journal of Geophysical Research: Solid Earth*. **112**(B1). 56, 57

Thatcher, Wayne. 2009. How the continents deform: The evidence from tectonic geodesy. *Annual Review of Earth and Planetary Sciences*. **37**. 57

Thatcher, Wayne, Grant Marshall and Michael Lisowski. 1997. Resolution of fault slip along the 470-km-long rupture of the great 1906 San Francisco earthquake and its implications. *Journal of Geophysical Research: Solid Earth*. **102**(B3), pp. 5353–5367. 8

Thatcher, Wayne and John B Rundle. 1979. A model for the earthquake cycle in underthrust zones. *Journal of Geophysical Research: Solid Earth*. **84**(B10), pp. 5540–5556. 4

Thatcher, Wayne et al. 1993. The earthquake cycle and its role in the long-term deformation on the continental litosphere. *Annals of Geophysics*. **36**(2), pp. 13–24. 2

Tobita, Mikio, Makoto Murakami, Hiroyuki Nakagawa, Hiroshi Yarai, Satoshi Fujiwara and Paul A Rosen. 2001. 3-D surface deformation of the 2000 Usu eruption measured by matching of SAR images. *Geophysical Research Letters*. **28**(22), pp. 4291–4294. 9

Tong, X, DT Sandwell and B Smith-Konter. 2013. High-resolution interseismic velocity data along the San Andreas Fault from GPS and InSAR. *Journal of Geophysical Research: Solid Earth*. **118**(1), pp. 369–389. 6, 14, 16

Tung, Sui and Timothy Masterlark. 2016. Coseismic slip distribution of the 2015 Mw7. 8 Gorkha, Nepal, earthquake from joint inversion of GPS and InSAR data for slip within a 3-D heterogeneous domain. *Journal of Geophysical Research: Solid Earth*. **121**(5), pp. 3479–3503. 9

Ulrich, Thomas, Stefan Vater, Elizabeth H Madden, Jörn Behrens, Ylona van Dinther, Iris Van Zelst, Eric J Fielding, Cunren Liang and A-A Gabriel. 2019. Coupled, physics-based modeling reveals earthquake displacements are critical to the 2018 Palu, Sulawesi Tsunami. *Pure and Applied Geophysics*. **176**(10), pp. 4069–4109. 92, 93

USGS. 1924a. M 7.0, southern Xinjiang, China [Online]. *Available from: https://earthquake.usgs.gov/earthquakes/eventpage/iscgem911007/executive.* . 59

USGS. 1924b. M 7.2, southern Xinjiang, China [Online]. *Available from: https://earthquake.usgs.gov/earthquakes/eventpage/iscgemsup911023/executive.* . 59

USGS. 1932. M 7.9, southern Xinjiang, China [Online]. *Available from: https://earthquake.usgs.gov/earthquakes/eventpage/iscgem906530/executive.* . 59

USGS. 2018. M 7.5, 70km N of Palu, Indonesia [Online]. *Available from: https://earthquake.usgs.gov/earthquakes/eventpage/us1000h3p4/executive.* . 17, 91, 107, 108, 125

Valkaniotis, S, A Ganas, V Tsironi and A Barberopoulou. 2018. A preliminary report on the M7. 5 Palu 2018 earthquake co-seismic ruptures and landslides using image correlation techniques on optical satellite data [Online]. *Available from: https://zenodo.org/record/1467128.* . 102

Vallone, P, MS Giammarinaro, M Crosetto, M Agudo and E Biescas. 2008. Ground motion phenomena in Caltanissetta (Italy) investigated by InSAR and geological data integration. *Engineering geology*. **98**(3-4), pp. 144–155. 21

Van Laarhoven, Peter JM and Emile HL Aarts. 1987. Simulated annealing. In *Simulated annealing: Theory and applications*. Springer pp. 7–15. 108

Van Zwieten, GJ, RF Hanssen and MA Gutiérrez. 2013. Overview of a range of solution methods for elastic dislocation problems in geophysics. *Journal of Geophysical Research: Solid Earth*. **118**(4), pp. 1721–1732. 26

Vernant, Philippe. 2015. What can we learn from 20 years of interseismic GPS measurements across strike-slip faults? *Tectonophysics*. **644**, pp. 22–39. 60, 62, 85

Vilotte, Jean-Pierre, M Daignieres and Raul Madariaga. 1982. Numerical modeling of intraplate deformation: Simple mechanical models of continental collision. *Journal of Geophysical Research: Solid Earth*. **87**(B13), pp. 10709–10728. 57

Wallace, Kali, Guanghua Yin and Roger Bilham. 2004. Inescapable slow slip on the Altyn Tagh fault. *Geophysical Research Letters*. **31**(9). 60, 62

Walpersdorf, A, C Vigny, C Subarya and P Manurung. 1998. Monitoring of the Palu-Koro fault (Sulawesi) by GPS. *Geophysical Research Letters*. **25**(13), pp. 2313–2316. 17, 91, 92

Walters, RJ, B Parsons and TJ Wright. 2014. Constraining crustal velocity fields with InSAR for Eastern Turkey: Limits to the block-like behavior of Eastern Anatolia. *Journal of Geophysical Research: Solid Earth*. **119**(6), pp. 5215–5234. 5, 78

Walters, RJ, JR Elliott, Z Li and B Parsons. 2013. Rapid strain accumulation on the Ashkabad fault (Turkmenistan) from atmosphere-corrected InSAR. *Journal of Geophysical Research: Solid Earth*. **118**(7), pp. 3674–3690. 10, 11, 15, 29

Wang, H and TJ Wright. 2012. Satellite geodetic imaging reveals internal deformation of western Tibet. *Geophysical Research Letters*. **39**(7). 60, 62, 88, 137

Wang, Hua, Caijun Xu and Linlin Ge. 2007. Coseismic deformation and slip distribution of the 1997 Mw7. 5 Manyi, Tibet, earthquake from InSAR measurements. *Journal of Geodynamics*. **44**(3-5), pp. 200–212. 3, 53

Wang, Kelin, Ray Wells, Stephane Mazzotti, Roy D Hyndman and Takeshi Sagiya. 2003. A revised dislocation model of interseismic deformation of the Cascadia subduction zone. *Journal of Geophysical Research: Solid Earth*. **108**(B1). 4

Wang, Teng, Liqing Jiao, Paul Tapponnier, Xuhua Shi and Shengji Wei. 2020. Space imaging geodesy reveals near circular, coseismic block rotation during the 2016 Mw7. 8 Kaikōura earthquake, New Zealand. *Geophysical Research Letters*. p. e2020GL090206. 14

Wang, Wei, Xuejun Qiao, Shaomin Yang and Dijin Wang. 2017. Present-day velocity field and block kinematics of Tibetan Plateau from GPS measurements. *Geophysical Journal International*. **208**(2), pp. 1088–1102. 58, 60, 62

Washburn, Zack, J Ramón Arrowsmith, Guillaume Dupont-Nivet, Wang Xiao Feng, Zhang Yu Qiao and Chen Zhengle. 2003. Paleoseismology of the Xorxol segment of the central Altyn Tagh fault, Xinjiang, China. *Annals of Geophysics*. **46**(5). 60, 62, 85

Watkinson, Ian M and Robert Hall. 2017. Fault systems of the eastern Indonesian triple junction: evaluation of Quaternary activity and implications for seismic hazards. *Geological Society, London, Special Publications*. **441**(1), pp. 71–120. 16, 91, 92, 104

Watkinson, Ian M and Robert Hall. 2019. Impact of communal irrigation on the 2018 Palu earthquake-triggered landslides. *Nature Geoscience*. **12**(11), pp. 940–945. 122

Wei, Meng, David Sandwell and Bridget Smith-Konter. 2010. Optimal combination of InSAR and GPS for measuring interseismic crustal deformation. *Advances in Space Research*. **46**(2), pp. 236–249. 10, 29

Weiss, Jonathan R, Richard J Walters, Yu Morishita, Tim J Wright, Milan Lazecky, Hua Wang, Ekbal Hussain, Andrew J Hooper, John R Elliott, Chris Rollins et al. 2020. High-resolution surface velocities and strain for Anatolia from Sentinel-1 InSAR and GNSS data. *Geophysical Research Letters*. p. e2020GL087376. 16, 67

Wesson, Robert L. 1988. Dynamics of fault creep. *Journal of Geophysical Research: Solid Earth*. **93**(B8), pp. 8929–8951. 7

Weston, J, AMG Ferreira and GJ Funning. 2011. Global compilation of interferometric synthetic aperture radar earthquake source models: 1. Comparisons with seismic catalogs. *Journal of Geophysical Research: Solid Earth*. **116**(B8). 8

Weston, Jennifer, Ana MG Ferreira and Gareth J Funning. 2012. Systematic comparisons of earthquake source models determined using InSAR and seismic data. *Tectonophysics*. **532**, pp. 61–81. 8

Weston, JM, AM Ferreira and GJ Funning. 2010. Global Compilation of InSAR Earthquake Source Models: Comparisons with Seismic Catalogues and the Effects of 3D Earth Structure. In *AGU Fall Meeting 2010*. 8

Wicks, Charles W, Daniel Dzurisin, Steven Ingebritsen, Wayne Thatcher, Zhong Lu and Justin Iverson. 2002. Magmatic activity beneath the quiescent Three Sisters volcanic center, central Oregon Cascade Range, USA. *Geophysical Research Letters*. **29**(7). 13

Williamson, Amy L, Diego Melgar, Xiaohua Xu and Christopher Milliner. 2020. The 2018 Palu Tsunami: Coeval Landslide and Coseismic Sources. *Seismological Society of America*. **91**(6), pp. 3148–3160. 92, 93, 97, 125

Wright, Tim, Barry Parsons and Eric Fielding. 2001. Measurement of interseismic strain accumulation across the North Anatolian Fault by satellite radar interferometry. *Geophysical Research Letters*. **28**(10), pp. 2117–2120. 6

Wright, Tim J. 2002. Remote monitoring of the earthquake cycle using satellite radar interferometry. *Philosophical Transactions of the Royal Society of London. Series A: Mathematical, Physical and Engineering Sciences*. **360**(1801), pp. 2873–2888. 4

Wright, Tim J. 2016. The earthquake deformation cycle. *Astronomy and Geophysics*. **54**(7), pp. 4–20. 1, 2

Wright, Tim J, Barry Parsons, Philip C England and Eric J Fielding. 2004. InSAR observations of low slip rates on the major faults of western Tibet. *Science*. **305**(5681), pp. 236–239. 9, 60, 62

Wright, Tim J, John R Elliott, Hua Wang and Isabelle Ryder. 2013. Earthquake cycle deformation and the Moho: Implications for the rheology of continental lithosphere. *Tectonophysics*. **609**, pp. 504–523. 6, 7, 8

Xu, Caijun and Sen Zhu. 2019. Temporal and spatial movement characteristics of the Altyn Tagh fault inferred from 21 years of InSAR observations. *Journal of Geodesy*. **93**(8), pp. 1147–1160. 60, 62, 85

Xu, Wenbin, Rishabh Dutta and Sigurjón Jónsson. 2015. Identifying Active Faults by Improving Earthquake Locations with InSAR Data and Bayesian Estimation: The 2004 Tabuk (Saudi Arabia) Earthquake SequenceIdentifying Active Faults by Improving Earthquake Locations. *Bulletin of the Seismological Society of America*. **105**(2A), pp. 765–775. 3

Xu, Xiwei, Feng Wang, Rongzhang Zheng, Wenbin Chen, Wentao Ma, Guihua Yu, Guihua Chen, P Tapponnier, J Van Der Woerd, AS Meriaux et al. 2005. Late Quaternary sinistral slip rate along the Altyn Tagh fault and its structural transformation model. *Science in China Series D: Earth Sciences*. **48**(3), p. 384. 62

Xu, Xiwei, Xibin Tan, Guihua Yu, Guodong Wu, Wei Fang, Jianbo Chen, Heping Song and Jun Shen. 2013. Normal-and oblique-slip of the 2008 Yutian earthquake: evidence for eastward block motion, northern Tibetan Plateau. *Tectonophysics*. **584**, pp. 152–165. 88

Yalciner, Ahmet C, Rahman Hidayat, Semeidi Husrin, Alessandro Annunziato, Gozde Guney Dogan, Andrey Zaytsev, Rachid Omira, Chiara Proietti, Pamela Probst, Maria Ausilia Paparo et al. 2018. Field Survey on the Coastal Impacts of the September 28, 2018 Palu, Indonesia Tsunami. In *AGU Fall Meeting 2018*. 91

Yamasaki, Tadashi, Tim J Wright and Gregory A Houseman. 2014. Weak ductile shear zone beneath a major strike-slip fault: Inferences from earthquake cycle model constrained by geodetic observations of the western North Anatolian Fault Zone. *Journal of Geophysical Research: Solid Earth*. **119**(4), pp. 3678–3699. 6

Yang, Youqing and Mian Liu. 2009. Crustal thickening and lateral extrusion during the Indo-Asian collision: A 3D viscous flow model. *Tectonophysics*. **465**(1-4), pp. 128–135. 56

Yin, An, PE Rumelhart, R Butler, E Cowgill, TM Harrison, DA Foster, RV Ingersoll, Zhang Qing, Zhou Xian-Qiang, Wang Xiao-Feng et al. 2002. Tectonic history of the Altyn Tagh fault system in northern Tibet inferred from Cenozoic sedimentation. *Geological Society of America Bulletin*. **114**(10), pp. 1257–1295. 62

Yin, An and T Mark Harrison. 2000. Geologic evolution of the Himalayan-Tibetan orogen. *Annual Review of Earth and Planetary Sciences*. **28**(1), pp. 211–280. 60, 62

Yin, Yueping, Wamo Zheng, Yuping Liu, Jialong Zhang and Xiaochun Li. 2010. Integration of GPS with InSAR to monitoring of the Jiaju landslide in Sichuan, China. *Landslides*. **7**(3), pp. 359–365. 30

Yu, Chen, Nigel T Penna and Zhenhong Li. 2017. Generation of real-time mode high-resolution water vapor fields from GPS observations. *Journal of Geophysical Research: Atmospheres*. **122**(3), pp. 2008–2025. 11

Yu, Chen, Zhenhong Li, Jiajun Chen and Jyr-Ching Hu. 2018a. Small magnitude co-seismic deformation of the 2017 Mw 6.4 Nyingchi earthquake revealed by InSAR measurements with atmospheric correction. *Remote Sensing*. **10**(5), p. 684. 10

Yu, Chen, Zhenhong Li and Nigel T Penna. 2018b. Interferometric synthetic aperture radar atmospheric correction using a GPS-based iterative tropospheric decomposition model. *Remote Sensing of Environment*. **204**, pp. 109–121. 14, 24, 54

Yu, Ze, Zhou Li and Shusen Wang. 2015. An imaging compensation algorithm for correcting the impact of tropospheric delay on spaceborne high-resolution SAR. *IEEE Transactions on Geoscience and Remote Sensing*. **53**(9), pp. 4825–4836. 11

Yue, Y, SA Graham, BD Ritts and JL Wooden. 2003. Detrital zircon provenance analysis of Oligocene sandstone in the eastern Xorkol basin and its implications for the magnitude of displacement along the eastern Altyn Tagh fault. In *AGU Fall Meeting 2003*. 62

Yue, Yongjun, Bradley D Ritts and Stephan A Graham. 2001. Initiation and long-term slip history of the Altyn Tagh fault. *International Geology Review*. **43**(12), pp. 1087–1093. 62

Yun, Ye, Qiming Zeng, Benjamin W Green and Fuqing Zhang. 2015. Mitigating atmospheric effects in InSAR measurements through high-resolution data assimilation and numerical simulations with a weather prediction model. *International Journal of Remote Sensing*. **36**(8), pp. 2129–2147. 11

Zebker, Howard A, Paul A Rosen and Scott Hensley. 1997. Atmospheric effects in interferometric synthetic aperture radar surface deformation and topographic maps. *Journal of Geophysical Research: Solid Earth*. **102**(B4), pp. 7547–7563. 24

Zhang, Pei-Zhen, Peter Molnar and Xiwei Xu. 2007. Late Quaternary and present-day rates of slip along the Altyn Tagh Fault, northern margin of the Tibetan Plateau. *Tectonics*. **26**(5). 60, 62, 76, 80, 85

Zhao, Dezheng, Chunyan Qu, Xinjian Shan, Wenyu Gong, Yingfeng Zhang and Guohong Zhang. 2018. InSAR and GPS derived coseismic deformation and fault model of the 2017 Ms7. 0 Jiuzhaigou earthquake in the Northeast Bayanhar block. *Tectonophysics*. **726**, pp. 86–99. 8

Zheng, Gang, Hua Wang, Tim J Wright, Yidong Lou, Rui Zhang, Weixing Zhang, Chuang Shi, Jinfang Huang and Na Wei. 2017. Crustal deformation in the India-Eurasia collision zone from 25 years of GPS measurements. *Journal of Geophysical Research: Solid Earth*. **122**(11), pp. 9290–9312. 60, 62

Zhu, Sen, Caijun Xu, Yangmao Wen and Yang Liu. 2016. Interseismic deformation of the altyn tagh fault determined by interferometric synthetic aperture radar (INSAR) measurements. *Remote Sensing*. **8**(3), p. 233. 60, 61, 62, 67